The Dissertation Committee for Jori Elan Ruppert-Felsot
certifies that this is the approved version of the following dissertation:

Coherent structures and two-dimensionalization in rotating turbulent flow

Committee:

Harry L. Swinney, Supervisor

David G. Bogard

John E. Gilbert

William D. McCormick

Jack B. Swift

Coherent structures and two-dimensionalization in rotating turbulent flow

by

Jori Elan Ruppert-Felsot, B.S., M.A.

Dissertation

Presented to the Faculty of the Graduate School of

The University of Texas at Austin

in Partial Fulfillment

of the Requirements

for the Degree of

Doctor of Philosophy

The University of Texas at Austin

May 2005

To my parents and to my grandparents…

Acknowledgments

First and foremost I thank my advisor Harry L. Swinney for providing a scientifically stimulating environment at the Center for Nonlinear Dynamics (CNLD) to do research. Of course, I must also acknowledge his support in keeping me employed.

I also thank Charles Baroud, John Burgess, and Brendan Plapp, all former members of CNLD who showed me the ropes when I first came to UT Austin. Thanks also go to Thomas Weber, a former CNLD member from Würzburg with whom I worked in the very early days of the experiment.

Thanks to the successive troupe of French students from École Polytechnique and who each spent three months helping out on the experiment: Benoit Camguilhem, who did a lot of initial work in getting the Sprinkler up and running, Emilie Regul who did some nice initial work using wavelets to analyze our flow, and Bruno Forrissier, who did some of the initial work with the Okubo-Weiss decomposition.

A big thanks to Eran Sharon who is a real inspiration to do physics. We worked together to set up much of the experiment. He somehow found the time to simultaneously work on three distinct and very different experiments (including working with me), take care of his three small children, and not have to come into the lab on the weekends. Thanks also go to Olivier Praud, the postdoctoral researcher who came after Eran and continued to work with me on my project while tending to his own projects.

Thanks also go to Sunghwan Jung (Sunny) for many illuminating discussions on turbulence. Further thanks go to Hepeng Zhang for helping out with the dual light sheet setup and who will take over the experiment after I leave.

Many thanks go to Marie Farge and Kai Schneider for a great deal of help and

encouragement and useful discussions utilizing the wavelet analysis we applied to our results.

Thanks to Allan Schroeder and his staff of the main machine shop and to Jack Clifford of the student machine shop for their friendly assistance while I was building and designing various pieces for the experiment. Thanks also to the guys in the cryogenics and vacuum shop who supplied us with the distilled water for our experiment.

Also thanks are owed to John England and Robert in the electronics shop for countless repairs on our stepper motor power supplies.

Additional thanks go to many other people, especially other CNLD members including Professors Bill McCormick and Jack Swift, for numerous helpful and thoughtful discussions and assistance. Thanks also go to the additional committee members, David Bogard and John Gilbert for graciously agreeing to be on my committee and to read my dissertation.

Last, but not least, the Office of Naval Research (ONR) is credited for having funded this research.

Jori Elan Ruppert-Felsot

The University of Texas at Austin
May 2005

Coherent structures and two-dimensionalization in rotating turbulent flow

Publication No. ____________________

Jori Elan Ruppert-Felsot, Ph.D.
The University of Texas at Austin, 2005

Supervisor: Harry L. Swinney

We study laboratory-produced fluid turbulence under the influence of rapid rotation. Three-dimensional (3D) turbulence is generated by strong pumping through sources and sinks at the bottom of a rotating tank (48.4 cm high, 39.4 cm diameter) filled with water. This flow evolves toward quasi-two-dimensional (quasi-2D) turbulence with increasing height in the tank. Digital Particle Image Velocimetry (DPIV) measurements were taken using tracer particles illuminated by a horizontal laser light-sheet. The quasi-2D flow near the top of the tank contains many long-lived coherent vortices and jets with a wide range of sizes near the top of the tank. The vertical vorticity field exhibits complex dynamics such as vortex birth, merger, scattering, and destruction.

Measurements using two synchronized cameras and vertically separated light sheets revealed coherent structures that were columnar and extended vertically throughout the tank. The effect of rotation greatly increased the vertical correlation of the flow, even for small rotation rates. A gradual decay in the correlation of increasingly vertically separated planes was observed, rather than a sharp transition.

The discrete wavelet packet transform (DWPT) and discrete wavelet transform (DWT) were used to extract and study the dynamics of the localized coherent structures near the top of our tank. We separated the flow into a low-entropy "coherent" and a high-entropy "incoherent" component by thresholding the coefficients of the DWPT and DWT of the vorticity field. Similar thresholdings using the Fourier transform and JPEG compression, the Okubo-Weiss criterion and Proper Orthogonal Decomposition (POD) were also tested. We found that the DWPT and DWT yield similar results and are much more efficient at representing the total flow than other methods. Only about 3% of the large-amplitude coefficients of the DWPT and DWT were necessary to represent the coherent component and preserve the vorticity probability density function, transport properties, and spatial and temporal correlations of the measured fields. The remaining small amplitude coefficients represent the incoherent component, which has near Gaussian vorticity PDF, contains no coherent structures, rapidly loses correlation in time, and does not contribute significantly to the transport properties of the flow. This suggests that one can faithfully describe and simulate such turbulent flow using a relatively small number of wavelet or wavelet packet modes.

Contents

Chapter 1

Introduction

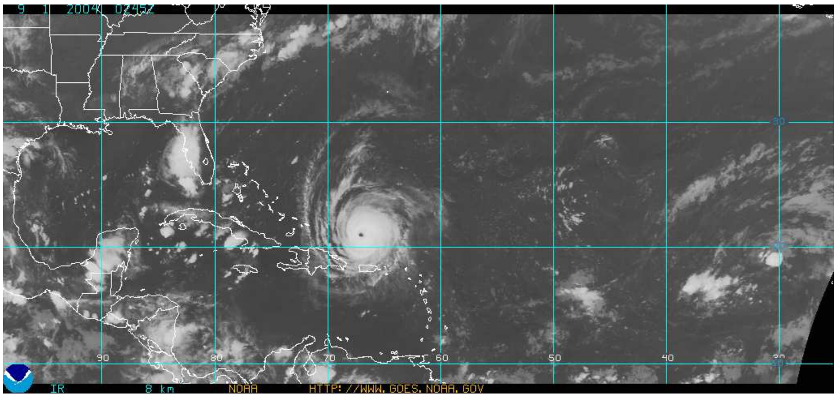

Figure 1.1: Hurricane Frances: hurricanes are an example of coherent structures that can transport significant amounts of moisture and energy. A better understanding of rotating turbulence should lead to better predictive capability of the paths these and other storm systems take. Picture taken from the GOES archive [3]

> “...even after 100 years, turbulence studies are still in their infancy. We are naturalists, observing butterflies in the wild.” [68]

1.1 Motivation

1.1.1 Impact!

In the Fall of 2004, multiple hurricanes bore down on the South-Eastern coast of the United States. Each of these hurricanes carried a large amount of moisture from the Atlantic ocean over hundreds of kilometers and unloaded it as torrential rains together with powerful 100+ mph winds on the population in Florida and neighboring Cuba and The Bahamas, resulting in billions of dollars in damage.

Prediction of hurricanes, as well as other weather systems and climate trends is highly desirable, due to the enormous human and economic impact. Weather forecasters rely on an ensemble of statistical[1] and dynamical[2] computer models to predict the evolution of hurricanes. Observational capabilities and computing power have steadily improved over

---

[1] Statistical hurricane models predict the path and intensity of the hurricane based upon historical data of hurricanes of similar characteristics.

[2] Dynamical hurricane models predict the path and intensity of hurricanes based upon computation of fluid dynamical equations of motion. Initial conditions are determined from observational measurements.

the past decades and have lead to increases in the accuracy of short-term forecasts.

However, longer-term weather prediction has remained inaccurate despite these improvements. In the case of the hurricanes, the path that they took and their intensity could not be accurately predicted. Indeed, weather forecasters can only give an expected path determined by the ensemble average of different models with an increasingly large uncertainty at future times. This is largely due to the chaotic nature of such flow which has a sensitive dependence upon initial conditions. Small scales of motion that are unresolved, due to limited computing power, can have a significant effect on the resolved larger scales. Accurate prediction remains elusive due to the question of interaction between large-scale resolved and small scales that can not be resolved. Better understanding of the flow, in particular the interaction between unresolved scales of motion and large scale motion, is needed before prediction can improve.

1.1.2 Open questions

The dynamics of planetary flows, such as that in the atmosphere or the oceans, are often highly turbulent and are heavily influenced by rotation through the Coriolis force. Coriolis dominated flows belong to a class of *geophysical flow*[3], due to their physical correspondence. Rotating turbulent flows tend towards a two-dimensional (2D) state and support the existence of stable localized large-scale *coherent structures*, such as hurricanes. Rotating turbulent flows are driven and dissipative nonlinear systems far from equilibrium. There are often many orders of magnitude separation between the largest scale of coherent motions (i.e. hurricanes, vortices), the forcing length scale (i.e. motions driven from convective plumes), and the dissipation scale (i.e. through molecular viscosity).

There are many fundamental open questions about rotating turbulence, besides the pragmatic question of prediction. What sets the length scales of such flows? How do small scale motions feed into large scale motions? Why do stable localized coherent structures emerge from seemingly chaotic turbulence? What sets the lifetimes of structures that

---

[3] Geophysical flows also include those in which Coriolis does not play significant a role. i.e. convection in the Earth's mantle, lava and glacial flow, etc.

emerge? How can we identify and separate the coherent structures from the background turbulence? How do the structures affect transport? How and why does rotation make the flow two-dimensional? What is the minimum amount of information necessary to faithfully model such flows? How can we use all of this to gain insight into the flow dynamics?

In short, rotating turbulent flows are not yet well understood. Due to their complex nature and the large separation between scales, it is difficult to directly simulate and faithfully resolve all aspects of turbulent geophysical flows. Furthermore, it is difficult and computationally expensive to directly integrate the equations of motion for highly turbulent flow. Thus, experiments with well-controlled conditions that can be varied over wide ranges are essential to answer these questions and to gain insight the behavior of turbulent flow.

1.2 Our approach to studying oceanic- and atmospheric-type flows

Flows in atmospheres and oceans are quite complex systems. They are generally large-scale turbulent flows dominated by planetary rotation. In addition to rotation, such flows are affected by thermal gradients, buoyancy and stratification, condensation and evaporation, the variation of the Coriolis force with latitude due to the curvature of the planet[4], and the distribution of land.

In the laboratory it is difficult, if not impossible, to faithfully reproduce all of the conditions of the atmosphere in a well controlled manner. However, despite the complexity of the atmosphere, the emergence of long-lived coherent structures is a universal feature of rotation-dominated flow [79, 54].

Our study focuses on the coherent features present in rotating flow and the effects of rotation. Therefore, our approach is to focus only on the effect of rotation on the fluid dynamics. We use water at a constant density and temperature in a rotating tank. We thus remove all of the additional complications mentioned above. As we shall see in chapters 4

---

[4] This is known as the β-*effect*.

and 5, even our relatively simple laboratory system still exhibits the macroscopic features as seen in the more complicated atmospheres and oceans[5], such as the existence of coherent structures.

1.2.1 Goal

We wish to understand the structure and dynamics of rotating turbulent flows. Our experiment addresses the open questions above and is an attempt to take a small step forward towards answering them.

1.3 Rotating turbulent flow

Rotation tends to drive the flow towards a two-dimensional (2D) state[6] where the turbulence is fundamentally different from that of three-dimensional (3D) flow. Despite being highly turbulent, long-lived coherent structures can exist in rotating flows. This is thought to be due to the 2D nature of the flow. In 3D turbulence, the net energy flux is from large scales towards small scales, where it is dissipated by viscosity. However, in 2D turbulence, energy proceeds from small forcing scales to the large scales; thus 2D turbulence can support long-lived large scale structures.

1.3.1 Coherent structures

Long-lived and localized intense regions, such as the hurricane in figure 1.1, are considered to be *coherent structures*. In the case of a hurricane, it is a localized region of intense wind and moisture content. Other well-known examples of coherent structures in the atmosphere are the Earth's jet stream, gulf stream, and Mediterranean eddies (meddies). Excellent extra-terrestrial examples of coherent structures in rotating turbulent flow are Jupiter's Great Red Spot (GRS) and zones and belts, shown in figure 1.2.

---

[5] The effect of rotation on fluid dynamics is not only of relevance to the atmospheres and oceans of planets; it is also important in many turbo-machinery and other engineering applications. However, in these cases it is the centrifugal force and not the Coriolis force which dominates the dynamics.

[6] n.b. the 2D state of rotationally dominated flow consists of columnar structures. This is different from the pancake-like 2D structures of stratified flows. See section 2.1.2.

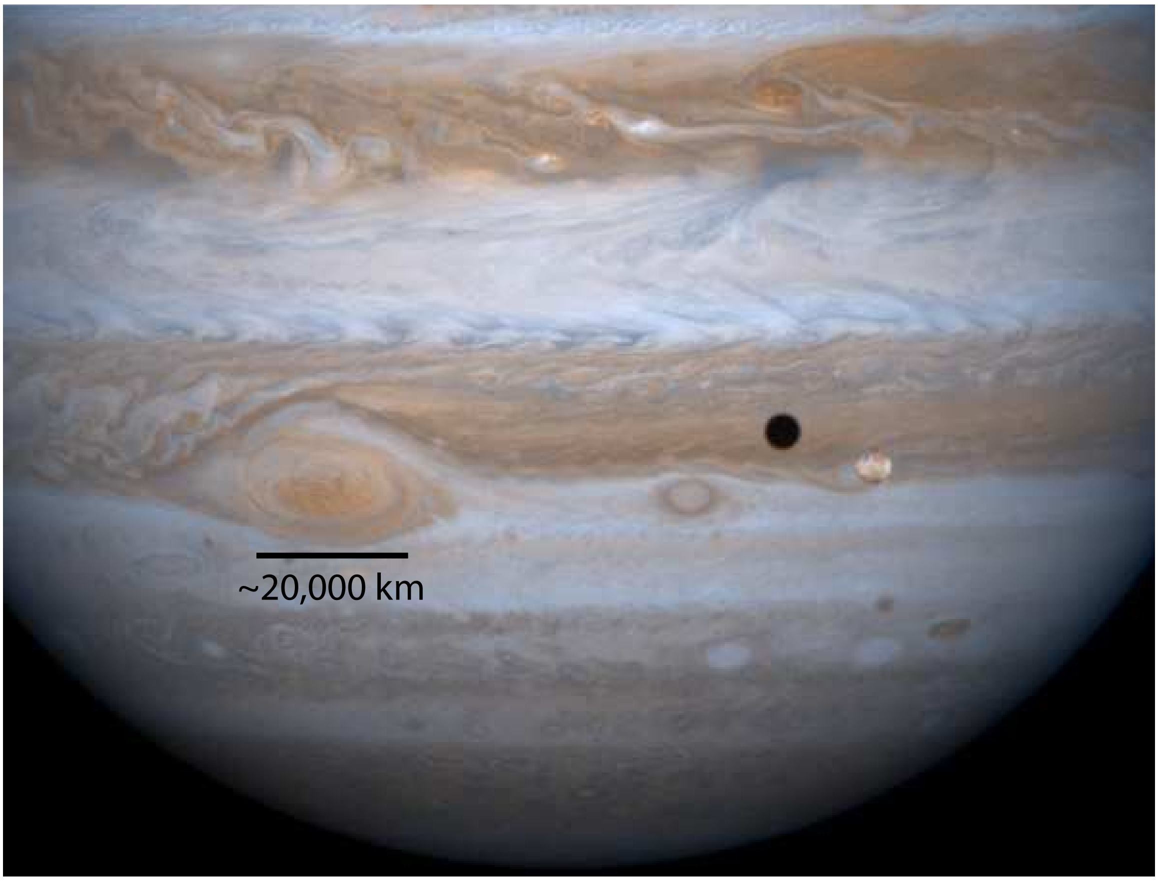

Figure 1.2: A composite true-color image of Jupiter. Jupiter's atmosphere is very turbulent, yet many stable long-lived large-scale localized coherent structures are present. These include: Jupiter's famous Great Red Spot (GRS), and the smaller white ovals, and the light (dark) bands correspond to Jupiter's zones (belts) that are regions of intense mean eastward (westward) flow which wrap around the planet. To give a sense of the large length scales of the coherent structures, the black spot is the shadow cast by Jupiter's moon, Io, which is roughly the same size as the Earth's moon. The size of the vortices were found to be roughly set by the size of the zones and belts in which they are embedded [111, 72]. However, it remains an open question as to what physics sets the length scales of Jupiter's zones and belts [72].

Coherent structures, due to their intensity and long-lifetimes, play a major role in transport of mass, momentum, and energy. For example, the Earth's jet stream enhances transport along it while inhibiting transport across it. If pollutants enter the jet stream from below, they can easily and quickly be transported across continents. The jet stream usually inhibits cold Canadian air from crossing into the Southern United States, when unperturbed from an East to West orientation. However, sufficiently strong high pressure regions[7] can disrupt the jet stream. Known as blocking events (demonstrated in experiment [125]), this causes the jet stream to dip Southward, bringing with it cold Canadian air and resulting in unseasonably cold temperatures in Texas.

In this way, the transport properties of structures like the jet stream and the Gulf stream current, which transports warm water to Northern Europe, moderating the cold temperatures, can have a large effect on weather and climate. It remains an open question as to whether or not changes in flow structure in the atmosphere can easily occur on short time scales and what the impact may be. On Jupiter, the recent merger of several white ovals (see figure 1.2) has been predicted by Marcus to result in a rapid global climate change of ~ 10 K [73].

On the Earth, a similar change in temperatures is thought to be induced by changes in the large coherent oceanic *thermohaline circulation*, known as the Ocean Conveyor[8]. The heat carried by the warm surface currents of the Ocean Conveyor warms North America and Northern Europe, and is thought to maintain the average temperature at about 6°C warmer than otherwise. Periods of cooling and rapid warming are thought to be associated with changes in the circulation pattern of the Ocean Conveyor[9], though the timescale for changes in the circulation may not be known. The possibility that the thermohaline circulation may shut down has even recently prompted the U.S. Defense Department to write a report

---

[7] High and low pressure regions in the atmosphere are also coherent structures.

[8] This is a large coherent ocean current which transports heat on the Earth. The Gulf stream forms an arm of the current which carries warm water from the equator into the North Atlantic.

[9] The last such cool period occurred approximately 10,000 years B.C. and is known as Younger Dryas, named after the arctic flower Dryas Octopetala that flourished in Europe during the time. This ended abruptly over a period of a few decades [31].

about the possible global impact [114, 104][10] and has driven interest in studying the effect of coherent structures on climate.

Simulation of such flows is typically conducted on a uniform grid. The resolution of the grid, i.e. number of grid points, required to faithfully resolve a turbulent flow scales as $Re^{9/4}$ in three dimensions, where Re is the Reynolds number[11], a measure of the level of turbulence. The computational time required scales as Re^3 (see Frisch [47], p.107 §7.4). That is, the higher the level of turbulence, the more time-intensive the calculation. Since it becomes increasingly difficult to resolve all scales of motion, the smaller scales are neglected. However, there can still be non-negligible interaction between the small and large scales.

The existence, persistence, and dominance of coherent structures in turbulent flow dynamics suggest that simplifications of the flow description may be possible. It has been hypothesized that one can decompose the flow into two components: one dynamically active, representing the coherent structures and the other dynamically passive representing the remaining parts of the turbulent flow. This raises the question of how to perform the decomposition and what can be identified with the coherent structures.

Simulation is often conducted using a spectral basis composed of Fourier modes. However, Fourier modes form a nonlocal basis in physical space (as a consequence of their localization in wavenumber space), while the coherent structures are localized. Instead of sines and cosines, Farge has proposed to use wavelets as a basis with which to analyze turbulent flows [39]. Wavelets form a compactly supported basis, meaning they are well localized in both physical and wavenumber space. As such, they are well suited to analyzing flows with localized, intermittent features.

Performing the separation using wavelets as a basis function, Farge found that only a small number of large-amplitude coefficients were necessary to represent the total flow. Furthermore, in simulating flows using a wavelet basis, Farge found that the complexity of the calculation increased as the number of coherent structures, rather than the strength

---

[10] In fact, such a doomsday scenario inspired the Hollywood science fiction action movie *The Day After Tomorrow* in the summer of 2004

[11] The Reynolds number indicates the intensity of turbulence: $Re \gg 1$ indicates increasingly turbulent flow.

Figure 1.3: Examples of two-dimensionality in a laboratory rotating flow. Side view of a Taylor column formed by a rising silicone oil droplet in a rotating experiment (from [21]). Dye injected ahead and behind of the droplet is entrained in the Taylor column.

of turbulence [41]. This approach seems promising. However, this analysis has heretofore primarily been applied to simulated flows. In this thesis, this analysis is carried out on an experimentally produced flow.

1.3.2 Two-dimensionalization

Rotation tends to cause fluid flow to become two-dimensional. i.e., under rotation, variations in the flow along the direction parallel to the axis of rotation become small compared to variations in the plane perpendicular. Thus the flow loses its spatial dependence on the direction parallel to the axis of rotation. Due to this effect, obstacles in rotating flow will produce what is known as a *Taylor column.* The obstacle may be shallow, however the Taylor column produced extends throughout the flow, parallel to the axis of rotation(see figure 1.3).

While rotation tends to two-dimensionalize the flow, such flows are ultimately forced by three-dimensional motions. One such example of forcing is the solar heating of the surface of the Earth which drives convection which becomes unstable and forms turbulent plumes. The flow is thus turbulent and three-dimensional near the forcing and undergoes a transition to two-dimensional flow far from the forcing where rotation dominates.

It has been previously thought that the stronger the rotation, the more this effect is manifest. However, recent simulations have produced the somewhat counter-intuitive result that increasing rotation may not lead to a more 2D state (e.g. [25]). The details depend on the effects of the nonlinear interactions and rotation in the fluid dynamical equations of motion. Experiments have yet to confirm this. This 3D to 2D transition is not well understood and is one of the subjects of this thesis.

1.4 Outline of the thesis

The work in this thesis focuses on the structure of the Coriolis dominated turbulence produced in our experiment. This includes the transition from three-dimensional (3D) to two-dimensional (2D) flow induced by rotation and the coherent structures present in such flows. The second chapter lays the appropriate theoretical groundwork and summarizes the relevant previous experimental and computational work regarding two-dimensionalization of turbulent flows and coherent structure extraction. The third chapter describes the experimental apparatus and techniques used to obtain, process, and analyze our data. The fourth chapter presents an overview of the flow structure observed in our experiment. The fifth chapter presents the results of our coherent structure extraction applied to our data. The sixth chapter presents preliminary results exploring the 3D to 2D transition in our flow. The seventh chapter gives concluding remarks and outlines the near and long-term course of future experiments.

Chapter 2

Theory and literature review

In this chapter we review the literature and theory relevant to understanding the scientific context of the present experiment. It is not meant to be by any means exhaustive. For instance, there is an enormous body of literature on turbulence. However, to the best of the author's knowledge, we present the most relevant work. In section 2.2 we discuss turbulence, including the difference between 3D and 2D turbulence. The effect of rotation on turbulence is discussed in section 2.3, including the transition from 3D to 2D flow. Experiment, simulation, and some recent work on the effect of rotation are reviewed. The emergence and significance of coherent structures is discussed in 2.4. The methods for coherent structure extraction are presented in more detail in section 5.3 of the coherent structure chapter. Finally, we present relevant previous work done in experiment and simulation of rotating turbulence in section 2.5. We conclude with a brief summary of the chapter in section 2.6.

2.1 Fluid motion

2.1.1 Navier-Stokes

The Navier-Stokes (N-S) equations describe the motion of an incompressible fluid and are statements of conservation of momentum and mass. They are written as

$$(\frac{\partial}{\partial t} + \mathbf{u} \cdot \nabla)\mathbf{u} = -\frac{\nabla p}{\rho} + \nu \nabla^2 \mathbf{u} \tag{2.1}$$

with

$$\nabla \cdot \mathbf{u} = \mathbf{0} \tag{2.2}$$

the additional equations describing an incompressible fluid of uniform, constant mass density ρ[1]. Here $\mathbf{u} = (u, v, w)$ is the three-dimensional velocity field, p the pressure, and ν is the kinematic viscosity. Our notation will be such that boldface indicates a vector.

The equations of motion of a fluid can be easily written but they are not easily solved. Much of the difficulty in obtaining solutions to the N-S equations is that they form a set of coupled nonlinear partial differential equations. This makes them particularly difficult to solve even numerically[2]. The nonlinearity of the N-S equations appears in the inertial terms (the terms on the left hand side of equation 2.1). Because the equations are nonlinear, the simple sum of two solutions does not necessarily form an additional solution. This nonlinearity, however, leads to the most interesting behavior including turbulence and the redistribution of energy among length scales.

Further complications in solving the N-S equations are due to the pressure term. Solving for the pressure term generally involves solving Poisson's equation. In many simulations, the use of homogeneous periodic boundary conditions allow for algebraic solutions in Fourier space. However, this can be difficult in a real fluid system with complicated boundaries.

It is possible to eliminate the complications of the pressure term, by taking the curl of the N-S equations. The result is the vorticity equation, which describes the time evolution of the swirling motions in a fluid.

---

[1] We will deal with *barotropic* flow, that is flows where surfaces of constant pressure coincide with surfaces of constant density, as in a constant density fluid.

[2] In fact, the difficulty of solving equation 2.1 is such that it is not even certain as to whether or not a solution exists or is unique! A \$ 1 millon prize from the Clay Mathematics Institute for the first person who can offer a proof of the existence and uniqueness of solutions to the N-S equations: see `http://www.claymath.org/millennium/Navier-Stokes_Equations/`

$$\frac{\partial \omega}{\partial t} + (\mathbf{u} \cdot \nabla)\omega = \omega \cdot \nabla \mathbf{u} + \nu \nabla^2 \omega \tag{2.3}$$

where $\omega = \nabla \times \mathbf{u}$ is the vorticity, i.e. the swirling motion of the fluid. However, in general, this does not completely eliminate complications as one must still solve Poission's equation for the velocity $\mathbf{u}$. In computational fluid dynamics, in practice, it is usually accounted for by satisfying incompressibility, equation 2.2. The physical argument is that any normal stresses applied to the fluid results in a pressure gradient which counteracts the stress, preventing the fluid from being compressed (thus satisfying incompressibility).

2.1.2 Two-dimensional flows

All real flows are three-dimensional (3D). However, if the variation in the third dimension (e.g. the vertical coordinate) becomes small compared to that in planes perpendicular (e.g. the horizontal coordinates), then its behavior can often be approximately described as two-dimensional (2D) (more appropriately, quasi-2D). Thus the flow field can be described as planar, i.e. only a function of horizontal coordinates.

In a fully 3D, incompressible flow, convergence or divergence in the horizontal plane will result in changes in vertical motion, i.e. the horizontal divergence $\nabla_\perp = \partial u/\partial x + \partial v/\partial y = -\partial w/\partial z \neq 0$. A purely 2D incompressible flow will have zero horizontal divergence, $\partial w/\partial z \equiv 0$. Note that this does not necessarily imply that the vertical motions vanish; the vertical velocity can be nonzero but constant. In practice a real 3D flow will have some small horizontal divergence no matter how close to a 2D state it becomes. However, if the divergence is small compared to some other characteristic quantity, such as vorticity (i.e. $|\nabla_\perp \cdot \mathbf{u}| \ll |\omega_z|$), it can be considered as quasi-2D.

There are two slightly different situations which are typically considered as conditions of 2D behavior:

(i) Motions perpendicular to the 2D plane vanish. In this case, the flow is entirely confined to move in 2D planes. This is typically manifest as "pancake"-like flow structure (i.e. large horizontal extent of correlation of motions compared to vertical extent). However, the vertical derivatives in this case are large at the top and bottom of the “pancake”. For an example, see figure 2.1 (a).

(ii) Derivatives of the flow field vanish in the direction perpendicular to the horizontal plane. In this case, the flow field is independent of the vertical coordinate. This is typically manifest as “column”-like flow structure (i.e. vertical extent of correlation of motions comparable or larger than horizontal extent). For an example, see figure 2.1 (b).

Listed below are some notable examples of situations in which a real flow can approach 2D behavior in nature and in the laboratory.

Geometrical confinement: This can be achieved by confining the system between two parallel walls separated by a small gap[3], motion in the third dimension is suppressed.

Stratification: Stable stratification consists of layers (which can be continuously stratified or stratified in discrete layers) of less dense fluid on top of more dense fluid. Due to the gravitationally stable configuration, vertical motions are thus suppressed and the flow at different heights becomes decoupled [96]. See figure 2.1 (a). Ocean and atmospheric flows are induced to 2D “pancake” behavior primarily from stratification[4].

Thin layer flows: These are flows in which the region of interest is shallow in vertical extent compared to their horizontal extent. This includes stratified flows. Strongly stratified flows are often treated as thin layers. i.e. in shallow water equations, the wavelength of motions of interest are much longer than the depth of the fluid (e.g. see Pedlosky [88]). For instance, the troposphere is $O(10)$ km deep and $O(1000)$ km wide: such an aspect ratio is justification for treating it as a 2D flow.

Applied magnetic field: A strong external magnetic field can cause an electrically conducting fluid, such as a liquid metal, mercury, or an electrolyte solution with an

---

[3] Such geometry is called a Hele-Shaw cell; besides fluid flows, this approach is also used to study 2D granular systems by confining macroscopic granular particles.

[4] However, the dynamics within a stratified layer are strongly affected by rotation via the Coriolis force.

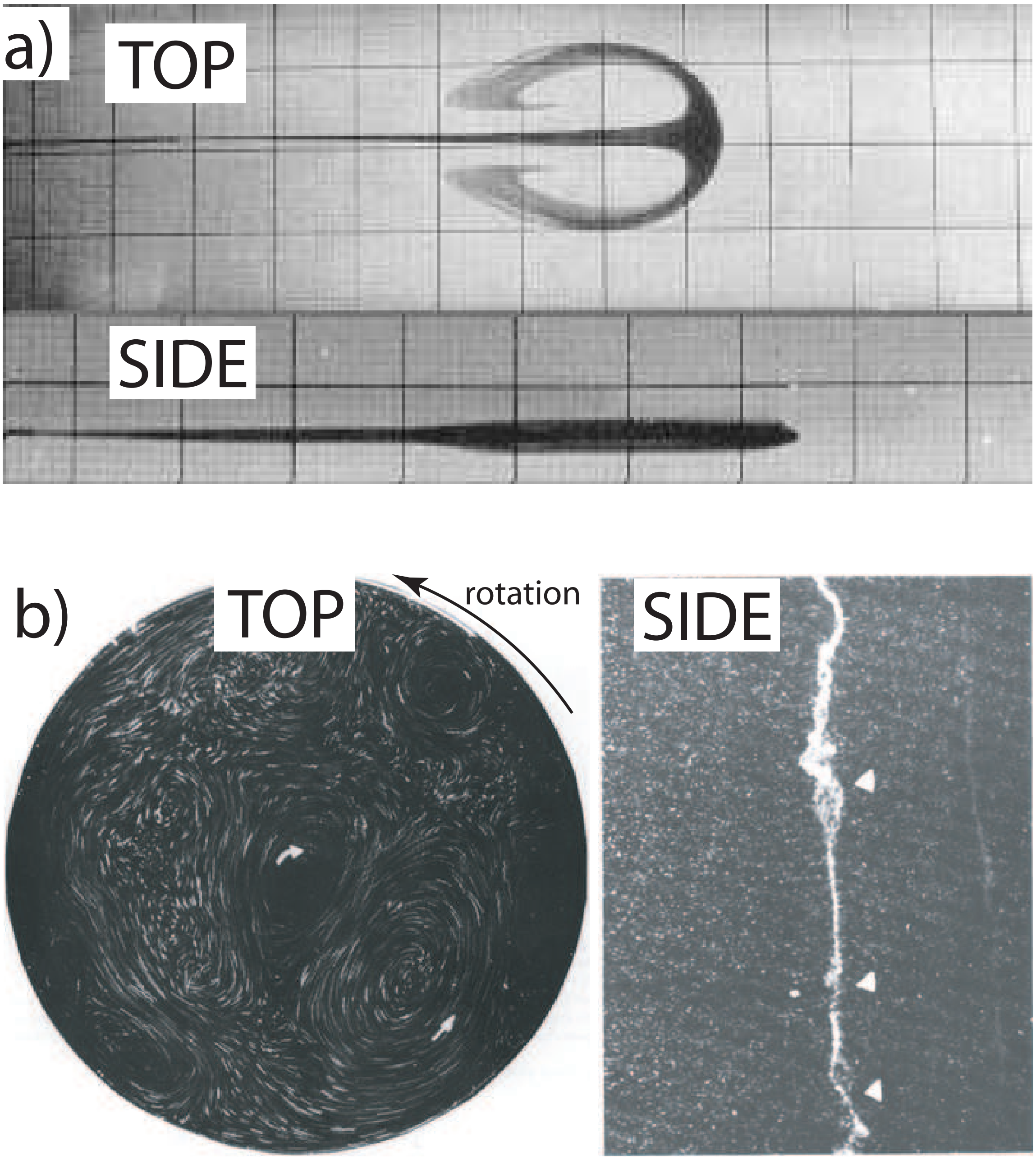

Figure 2.1: Some examples of the two types of 2D flows produced in the laboratory. (a) “Pancake”-like 2D flow produced by strong stratification. A top view of a jet of dye injected into a strongly stratified fluid shows the formation of a vortex dipole, well characterized as 2D. Comparison with the side view shows that the horizontal extent of the vortex dipole is much larger than the vertical extent. From reference [10].(b) “Column”-like 2D flow produced by strong rotation. A top view of particle streaks in the flow shows strong vortical motion and small divergence. The side view shows the columnar structure of the vortices. Air bubbles introduced at the bottom of the apparatus travel up the core of the nearly vertical cyclonic vortices. Reproduced from the rotating turbulence experiment of Hopfinger [53].

applied current, to align itself along the direction of the applied field. Under such conditions, magneto-hydrodynamic flows can behave as 2D [112].

Rotation: Presence of background rotation causes the flow to align itself along the direction of rotation. For example, see figure 2.1 (b). This is the topic of the current research.

As mentioned before, in reality there is no such thing as a purely 2D flow. Although laboratory flows can come close to approximating 2D flow (e.g. stratified electromagnetically driven flows [86]), all laboratory-produced and naturally occurring "2D" flows have some interaction with the third dimension. For instance, rotationally dominated geophysical flows are coupled to the boundary layer (see section 2.3.4), which results in significant drag on large-scale motions. Thin-layer soap-film flows, typically thought of as 2D due to their large horizontal extent relative to their vertical extent [29], also feel the third dimension through viscous drag from the surrounding air [97]), an effect which can not be completely decoupled [20]. Soap-film flows have additional problems with claims of their two-dimensionality. Even if the air were removed by placing the experiment in vacuo, there would still be significant effects due to the variation in thickness of the film. This causes a significant nonzero horizontal divergence and three dimensional motion[5].

2.1.3 Dimensionless parameters

There is some insight into the behavior of a fluid system which can be gained without solving any equations if we examine the relative magnitudes of the terms which appear in the N-S equations. Dimensionless parameters formed by taking the ratio of terms in the N-S equations are useful for giving a qualitative description of flow regimes and the relative importance of the different terms. It is possible to determine which effects will be important and which will be small or negligible for a given flow by calculating dimensionless parameters.

Dimensionless parameters can be formed by non-dimensionalizing the equation of

---

[5] Regions where fluid accumulates causes the film to swell locally, resulting in horizontal divergence.

motion.

$$\frac{L}{TU}\frac{\partial \mathbf{u}^*}{\partial t^*} + \mathbf{u}^* \cdot \nabla \mathbf{u}^* = -\frac{P}{\rho U^2}\nabla p^* + \frac{\nu}{UL}\nabla^2 \mathbf{u}^* \tag{2.4}$$

The starred variables are now dimensionless and L, T, U, and P correspond to characteristic length, time, velocity and pressure scales of the flow. The spatial coordinates all appear in the derivatives and thus the characteristic length scales will correspond to the distance over which the flow varies significantly. The velocity and length scales can be related to the time scale $T = L/U$. The coefficients of the non-dimensional terms are the resulting dimensionless parameters.

Dimensionless parameters are calculated by taking order of magnitude estimates of typical dimensional variables or constants for a given flow. The choice for scales is somewhat arbitrary. However, for suitably well chosen scales, flows of the same geometry and same dimensionless quantities will exhibit the same qualitative behavior, despite possibly having drastically different spatial and temporal scales. This is known as the principle of dynamic similarity [123]. For flows of similar dimensionless parameters, the dynamics will be dominated by the same forces and thus the dynamical behavior will be similar. This gives us confidence that our experiments done on such small relative scales in the laboratory can be relevant to the much larger scales of planetary flows.

Reynolds number

The Reynolds number Re characterizes the relative importance of the inertial forces to the viscous forces.

$$Re = \frac{inertial}{viscous} = \frac{|\vec{u} \cdot \nabla \vec{u}|}{|\nu \nabla^2 \vec{u}|} \sim \frac{\mathbf{UL}}{\nu} \gg \mathbf{1} \Rightarrow \text{Turbulent Flow} \tag{2.5}$$

Note that the same result applies for the ratio of the first term in equation 2.1 to that of the viscous term, $(U/T)/(\nu U/L^2) = (L^2/\nu)/T$. This is a ratio of the viscous diffusion timescale L^2/ν to the advective timescale T. If one takes the characteristic advective for motions as $T = L/U$, the result is also the Reynolds number.

For small values, $Re \ll 1$ the flow will remain laminar and dominated by viscosity. For large values, $Re \gg 1$, dissipation through viscosity becomes negligible and inertia dominates the flow. Depending on the system, when this number exceeds a few hundred far from any boundaries, the flow will become turbulent (see section 2.2). However, near a boundary, viscous effects are always important (e.g. see 2.3.4).

Typical Reynolds numbers for the atmosphere and ocean can be on the order of $10^9 - 10^{12}$. These flows are very turbulent and are thus often treated as inviscid.

2.2 Turbulence

Turbulent flow is characterized by large fluctuations over a wide range of spatial and temporal scales. At sufficiently high Reynolds number, typically $Re \gg 1$, flows can not be smoothly brought to rest. Instead, flows are unstable to small perturbations that quickly amplify and excite further motions. The flow can thus quickly become turbulent.

Vortex stretching, the first term on the right hand side of equation 2.3, is a process important in the production of turbulence. Gradients in velocity aligned with the vorticity can thus stretch vortex lines and increase the vorticity and cause straining to fold the vortex lines. Fluid elements of constant vorticity rapidly stretch and fold in turbulent flow. Each stretching causes vortex tubes tighten and the fluid to spin faster to conserve angular momentum[6]; each folding causes increased spatial variation of the flow. As a consequence of large fluctuations and stretching and folding of fluid elements due to turbulence, mixing and transport properties of the flow are enhanced [123]. Turbulence is thus often characterized by temporally intermittent large bursts and large gradients of intense vorticity and strain (e.g. ref [131]). A large part of the difficulty in obtaining a thorough understanding of turbulence in fluids is owed to wide range of interacting space and time scales involved.

Due to the wide range of length scales present in turbulent flow, it is thus reasonable to consider a "local" Reynolds number which is a function of a local length scale $Re(l) =$

---

[6] e.g. This is similar to an ice skater who pulls their arms inwards to spin faster.

$u(l)l/\nu$. The wide range of length scales thus implies that there will be small Reynolds number motions, corresponding to small scale motions, as well as large Reynolds number motions, both contained within a large Reynolds number flow.

In three-dimensional turbulence, at the large end of the scale, the largest motions will be limited by a length scale associated with how the motions were excited. The typical largest energy containing length scale is known as the *integral length scale.*

At the small end of the range of motions, the Reynolds number will be increasingly smaller. Where the Reynolds number is unity, the viscous and inertial forces balance and dissipation due to viscosity becomes important. In a turbulent flow, this length scale is known as the Kolmogorov length scale η.

$$\eta = \left(\frac{\nu^3}{\epsilon}\right)^{\frac{1}{4}}$$

where ϵ is the rate of dissipation per unit volume due to viscosity at this length scale and ν the kinematic viscosity. Smaller motions are quickly dissipated by viscosity. The Kolmogorov length scale is thus thought of as the size of the smallest motions in the flow. For typical conditions in our experiment, $\eta \sim 100\ \mu$ m.

In the following sections, we briefly summarize some of the understanding of fluid turbulence, particularly the difference between 3D and the special case of 2D turbulence. We will restrict ourselves to the works which are relevant to advancing the storyline of our experimental odyssey. For more detailed discussions of turbulence see the monograph of Frisch [47] or recent reviews of turbulence (e.g. [113, 68]) which are more general and illuminating than the content presented here.

2.2.1 3D turbulence

Perhaps one of the most successful (or widely quoted) theoretical treatment of turbulence is that of Kolmogorov in 1941 [62], known as K41[7]. Kolmogorov postulated that, in the limit of infinite Reynolds number, turbulent flow would become statistically isotropic and self-

---

[7] For specifics on K41 see Frisch [47]

similar (at small scales) away from the boundaries and that the flow will always have a finite dissipation rate. By small scales, Kolmogorov meant the energy containing scales which were smaller than the integral length scale and larger than the Kolmogorov length scale. Much attention has been paid to verifying Kolmogorov's hypothesis. However, experimentally, it is impossible, to achieve infinite Reynolds number. Indeed, the current experiment is limited to the largest Reynolds numbers $Re \sim 5000$.

Nonetheless, a fairly simple and useful physical picture emerges from the implications of this theory.

Turbulent eddies appear at a particular length scale at which energy is injected into the flow. For the case of grid-generated turbulence, this is typically taken to be the mesh size (i.e. the distance between bars). The energy input at large scales is balanced by energy dissipation at the very smallest scales due to viscosity. For the range of length scales of large $Re(l)$, viscosity is unimportant and energy is only transported to smaller scales. These length scales are referred to as the *inertial range* due to the dominance of the inertial terms.

Large eddies will break up into smaller eddies. These will in turn break up into even smaller eddies. This is known as the turbulent (forward) energy cascade. The whole process proceeds until the eddies reach the Kolmogorov length scale. At this scale the energy in the small scale structures is dissipated through molecular viscosity into heat. Thus the energy in the 3D turbulent flow will proceed from large scales to small scales. The distribution of energy in the flow is thus self-similar. The spectral distribution of energy, known as the energy spectrum function, $E(\mathbf{k})$ thus takes on a power law scaling. The energy spectrum is expected to take $E(k) = E(k, \epsilon) \sim \epsilon^{2/3} k^{-5/3}$ scaling, by dimensional analysis, assuming that only the wavenumber $\mathbf{k}$ and energy dissipation ϵ at small scales are important.

This cascade process, of transfer of energy between wavenumber, is mediated by interactions between triplets of modes of different wavenumber. Known as 'resonant triads'[8], they can redistribute energy from lower wavenumbers (large scale) to higher wavenumbers (small scale) [45]. The nonlinear term in the N-S equation is not a source or sink of energy.

---

[8] These 'triad' interactions arise from the nonlinear term of the Fourier transform of the energy equation, formed by the dot product of $\mathbf{u}$ with the N-S equation.

Instead, it is responsible for redistribution of the energy to different scales of motion.

2.2.2 2D Turbulence

The lack of the vortex stretching term makes 2D turbulence fundamentally different than 3D. This also means that the vorticity, which acts as an active scalar[9], and the enstrophy $Z = \int |\omega|^2$ is conserved. For a while in the history of the study of turbulence, turbulence in 2D was not thought possible[10]. This is (likely) due to the lack of the vortex stretching term, generally thought of as responsible for the production of turbulence in 3D. As a result, there was some debate as to whether or not 2D flow was to be considered turbulent or to be able to exhibit properties, such as the turbulent energy cascade.

However, Kraichnan [63], and later Batchelor [16], demonstrated that 2D flow can exhibit an inertial range cascade of energy. More specifically, it was predicted that 2D turbulence should exhibit two inertial transfer regimes, one forward and one inverse. Kraichnan showed that the 2D inertial range energy transfer has the same $\mathrm{k}^{-5/3}$ scaling as in the 3D cascade, using the same scaling arguments as in 3D, but that the triad interactions direct the energy transfer in the opposite direction, i.e. to larger scales, using the conservation of enstrophy and energy. This is thus known as the *inverse* energy cascade. Note that there is also a forward enstrophy cascade which scales as k^{-3} where enstrophy is cascaded forward to smaller scales, due to the stretching and folding by turbulent advection.

In numerical simulations, 2D turbulence can be more easily studied than 3D turbulence. This is primarily due to the simplicity of numerical calculations which are reduced in complexity by the loss of one dimension. The N-S equations can be written in terms of a single independent scalar field ψ, the streamfunction. The steamfunction is defined for 2D flow such that $\mathbf{u} = -(\nabla \times \psi \hat{\mathbf{z}})$, so that $\mathbf{u} = (u, v) = (-\partial\psi/\partial y, \partial\psi/\partial x)$. Additionally, due to the inverse cascade, most of the energy in 2D turbulence is contained at large scales, in

---

[9] It is active, rather than passive, because vorticity is coupled to the velocity field. i.e. changing the spatial vorticity distribution changes the velocity field

[10] In fact, in the turbulence presentation of the National Committee on Fluid Mechanics films, the presenter gives as part of the definition of turbulence as an isotropic distribution of vorticity in three dimensions. From this he draws the conclusion that 2D turbulence does not exist, albeit by definition; this was before Kraichnan's contribution of 1967 [63].

contrast to the cascade of energy towards the small scales in 3D, relaxing the demands of high resolution to simulate high Re flows.

The simple physical picture of 2D turbulence is the merging of small eddies to form larger eddies, ad infinitum until the process is limited by system size. If there is no dissipation mechanism to limit the inverse cascade, energy will pileup at a wavenumber that of the system size, similar to Bose condensation, (e.g. observed in a simulation of 2D turbulence by Smith *et al.* [109]). Thus, due to the inverse energy cascade, 2D turbulence can support the emergence and sustain the existence of long-lived, large scale coherent vortices. This is readily observable in the large scale turbulent atmospheric structures such as hurricanes, the jet stream, and Jupiter's GRS.

In simulation, the inverse cascade is also readily observable. McWilliams in his seminal paper, performed numerical simulations of the 2D vorticity equation [78]. Freely decaying 2D turbulence was found to contain coherent, long-lived vortices which merged to form larger vortices in time. There have been many other published numerical simulations of 2D turbulence (see the review by Tabeling for more references [117]).

In the laboratory, similar results have been obtained by Tabeling *et al.* in a close experimental approximation to 2D turbulence [87]. Tabeling forced 2D turbulence in a shallow stratified electrolyte bath. Motions were randomly forced by an array of oscillating electromagnets which drove currents in the lower layer of fluid and in turn the upper layer. If the arrangement of the magnets was such that it excited only small scale motions, the time-resolved measurements showed that this occurred through a buildup of energy starting at the forcing scale and eventually extending to the system size, consistent with an inverse energy cascade. In this case, Tabeling was able to observe a $\mathrm{k}^{-5/3}$ scaling from the forcing length scale to roughly the system size length scale with Reynolds number $O(10^3)$. If the arrangement produced large scale motions, Tabeling observed a k^{-3} scaling of the energy spectrum from large to small scales. Tabeling did not simultaneously observe the two cascades. However, it has been suggested that the simultaneous appearance of the cascades should only be a feature of an unbounded system [121].

For more detailed information on 2D turbulence, the reader should refer to the reviews by Tabeling [117] and Kraichnan [64]. While the general behavior of 2D turbulence, that of an inverse energy cascade to large scales, is applicable to experimental systems, in practice, one should always be careful when making comparisons of experiment to the results of a 2D model or numerical simulation (e.g. see section 2.1.2). For instance, Baroud and co-workers found that rotating turbulent flows, while often well described as 2D, are fundamentally different than in a 2D NS fluid (e.g. [12]).

2.3 Effects of rotation

2.3.1 Equations of motion and general behavior

We now consider the effects of rotation on the behavior of a fluid. Consider a reference frame rotating with a constant angular velocity $\Omega = 2\pi f$ about the z-axis, $\mathbf{\Omega} = \Omega\hat{z}$. Such a frame is non-inertial and additional terms appear in the Navier-Stokes equations (equation 2.1). Written in a rotating reference frame, equation 2.1 becomes

$$(\frac{\partial}{\partial t} + \mathbf{u}\cdot\nabla)\mathbf{u} = -\frac{\nabla p}{\rho} + \nu\nabla^2\mathbf{u} - 2\mathbf{\Omega}\times\mathbf{u} - \mathbf{\Omega}\times(\mathbf{\Omega}\times\mathbf{r}) \tag{2.6}$$

where the last two terms on the right hand side are the Coriolis and the centrifugal forces, respectively, that result from the transformation into the rotating frame. The centrifugal term can be written as the gradient of a scalar quantity, $\nabla(\frac{1}{2}|\Omega|^2r^2)$ and absorbed into the pressure gradient term, with $p + (\frac{1}{2}\rho(|\Omega|^2r^2) \mapsto p$. Thus the Navier-Stokes equations in a rotating frame are usually written as

$$(\frac{\partial}{\partial t} + \mathbf{u}\cdot\nabla)\mathbf{u} = -\frac{\nabla p}{\rho} + \nu\nabla^2\mathbf{u} - 2\mathbf{\Omega}\times\mathbf{u} \tag{2.7}$$

It is important to note that the Coriolis force is always perpendicular to the fluid velocity and thus does no work.

Breaking of symmetry in vorticity equation

In a rotating reference frame the vorticity equation (eqn. 2.3) becomes

$$\frac{\partial \omega}{\partial t} + (\mathbf{u} \cdot \nabla)\omega = \omega \cdot \nabla \mathbf{u} + \nu \nabla^{\mathbf{2}} \omega + \mathbf{2\Omega} \cdot \nabla \mathbf{u} \tag{2.8}$$

The symmetry between vorticity of different orientations is broken by the rotation. From equation 2.8, ignoring the viscous term, the equation for the time evolution of the vertical vorticity becomes

$$\frac{D\omega_z}{Dt} = (2\Omega + \omega_z)\frac{\partial w}{\partial z} \tag{2.9}$$

Thus, for a given background rotation and horizontal divergence $-\partial w/\partial z$, the growth rate will be larger in magnitude for cyclonic (vorticity parallel to $\mathbf{\Omega}$) than anti-cyclonic vorticity. In general, a horizontal convergence (divergence) will lead to increases in cyclonic (anti-cyclonic) motion[11].

Inertial waves

A notable characteristic of rotating fluids is that they can support plane wave oscillations for small amplitude motions. These waves are known as *inertial waves* in rotating fluids [49]. Inertial waves are similar to internal (gravity) waves in stratified fluids (e.g. see Lighthill [65]).

Plane wave solutions can be found for the linearized, inviscid form of equation 2.7. The resulting dispersion relation is $\omega = 2\Omega k_z/|\mathbf{k}| = 2\Omega cos\theta$, where θ is the angle between the background rotation and the wavevector k of the propagating inertial wave. Fast modes (limited at $\omega \approx 2\Omega$) can transport energy and propagate parallel to and at small angles to the axis of rotation; slow modes ($\omega \approx 0$) do not transport much energy and propagate larger angles from the axis of rotation.

---

[11] This can also be seen by the direction of the Coriolis force for the horizontal divergence or convergence of fluid.

2.3.2 Dimensionless numbers in rotating flow

There are two additional nondimensional numbers which can be obtained by non-dimensionalizing equation 2.7. They are the Rossby number and the Ekman number and indicate the relative important of rotation.

Rossby number

The Rossby number, Ro, is the relative importance of the inertial forces to the Coriolis forces. When this number becomes small, $Ro \ll 1$, the flow is rotationally dominated and behaves quite differently from non-rotating flows (see section 2.3.3).

$$Ro = \frac{inertial}{Coriolis} = \frac{|\mathbf{u} \cdot \nabla \mathbf{u}|}{|2\boldsymbol{\Omega} \times \mathbf{u}|} \sim \frac{U}{2\Omega L} \ll 1 \Rightarrow \text{Coriolis dominant} \tag{2.10}$$

A second Rossby number can be formed by taking the ratio of the timescales of the flow to the period of rotation.

$$Ro_T = \frac{|\frac{\partial \mathbf{u}}{\partial t}|}{|2\boldsymbol{\Omega} \times \mathbf{u}|} \sim \frac{1}{2\Omega T} \approx \frac{T_\Omega}{T} \tag{2.11}$$

Where T_Ω is the background rotation period and T is a typical timescale in the flow which can be represented as ω^{-1}, and interpreted as the typical turn-over time of vortices in the flow. Ro_T is also small if the time scale of variation of the flow is small compared to that of the background rotation period.

In our experiment we calculate a *local* Rossby number by taking the ratio of local vorticity, ω to the background vorticity of the tank, 2Ω.

$$Ro = \frac{\omega}{2\Omega} \tag{2.12}$$

A typical Rossby number for atmospheric and oceanic flows is on the order of 10^{-1}, though there is a wide range from 0.01 to > 1. In the experiment we observe flows with larger Rossby number in the range of $0.2 - \infty$[12]. However, low Rossby numbers, $Ro < 1$, indicate that rotation is significant in the dynamics of our flow.

Ekman number

The Ekman number contains the relative importance of viscosity to the Coriolis force. When this number is very small, $Ek \ll 1$, viscous terms are insignificant relative to the action of the Coriolis force.

$$Ek = \frac{viscous}{Coriolis} = \frac{|\nu \nabla^2 \mathbf{u}|}{|2\mathbf{\Omega} \times \mathbf{u}|} \sim \frac{\nu}{2\Omega \mathbf{H}^2} \ll \mathbf{1} \Rightarrow \text{Coriolis Dominant} \tag{2.13}$$

H corresponds to the vertical length scale of the flow. This is typically taken as the depth over which the flow is rotationally dominated. A horizontal Ekman number results if the horizontal length scale **L** is used. In atmospheric and oceanic flows the horizontal length scale is typically large compared to the vertical extent ($\mathbf{L} \gg \mathbf{H}$) and thus the horizontal Ekman number is much smaller than the vertical one.

Typical Ekman numbers for the atmosphere are very small, $O(10^{-9})$ due to the immense length scales. This, taken with a large Reynolds number often justifies treating atmospheric flows as inviscid.

Typical Ekman numbers observed in the experiment are $O(10^{-4})$. Both nature and experimental values are much smaller than 1, and so viscosity is negligible compared to rotation. It should be noted, however, that this does not hold near the boundaries of the flow where variations in the vertical direction become large (see section 2.3.4).

2.3.3 Taylor-Proudman: the limit of infinite rotation

We now consider the effect of strong rotation on the behavior of a fluid. In the limit of infinite rotation, $Ro \mapsto 0$ and $Ek \mapsto 0$. The Coriolis term dominates the inertial and viscous terms and is balanced by the pressure term

---

[12] It is easy to observe $Ro = \inf$ flow by not rotating!

$$2\boldsymbol{\Omega} \times \mathbf{u} = -\frac{\nabla p}{\rho} \tag{2.14}$$

This is known as the geostrophic equation. Flows which obey this are known as *geostrophic flows*. The result is the streamlines of the flow are also the isobars[13]. By taking the curl of equation 2.14, one can arrive a surprising result[14].

$$\boldsymbol{\Omega} \cdot \nabla \mathbf{u} = 0 \tag{2.15}$$

The result is know as the Taylor-Proudman theorem after the works of Taylor and Proudman [92, 119, 120]. The common interpretation of equation 2.15 is that variations in the velocity field vanish along the direction of rotation in the limit of infinite rotation. Further, if the rotating system is contained by horizontal boundaries, vertical motion along the axis of rotation will also vanish. A sufficiently rapidly rotating flow will thus be 2D.

The Taylor-Proudman theorem is often cited as the reason for the two-dimensionalization of rotation dominated flow. However, in the derivation of the Taylor-Proudman, we have assumed negligible nonlinearities in the limit of zero Rossby and Ekman numbers. As a consequence of ignoring dynamics, the result does not describe the path to two-dimensionalization. We have ignored the inertial terms, in particular the time derivative of the velocity, which can be large in rapidly fluctuating turbulent flow. For example, in our flow the turn-over time of the turbulent eddies can be less than one second, comparable to that of the rotation period of the tank. Clearly a more complete theory, including dynamics and nonlinearities is necessary to explain why rotation tends to two-dimensionalize turbulent flow.

---

[13] For example, the isobars on a weather forecast map correspond to the streamlines of the geostrophic wind.

[14] Taylor himself was quite surprised by the result, remarking, “This idea appears fantastic, but the experiments now to be described show that the true motion does, in fact, approximate to this curious type” [119]

2.3.4 Boundaries in rotating flow

Ekman layers

The effect of vertical friction in rotating flow has a relative magnitude of the Ekman number, $Ek = \nu/(2\Omega H^2)$. For most rotating flows, far from boundaries, this is on the order of 10^{-4} or smaller. Neglecting the friction terms in the N-S equations reduces the order of the differential equations by one. This means that it is no longer possible to meet all the appropriate boundary conditions on the flow. However, friction does become important near the boundaries. An estimate of the vertical extent of the horizontal boundary layer where friction is important can be made by taking the vertical viscous term to be of the same order as the Coriolis term. This is equivalent to setting the Ekman number $Ek = 1$. Taking the boundary layer depth δ as the relevant length scale for the Ekman number (and neglecting the factor of 2) [88],

$$\delta \approx \sqrt{\frac{\nu}{\Omega}} \tag{2.16}$$

This is the depth of the Ekman layer, the viscous boundary layer which appears on the horizontal boundaries in rotating flow. The Ekman layer is very small compared to the vertical extent of the geostrophic flow. The depth of the Ekman layer for our experiment is typically on the order of 0.5 mm.

The Ekman layer itself is very difficult to study experimentally due to its smallness; laminar Ekman layers can account for less than $\delta/H \approx Ek^{1/2} \approx 0.1\%$ of the total fluid depth, which for a tabletop experiment can be sub-millimeter in size. Even for 3D simulations of the atmosphere it is difficult to resolve the Ekman layer while at the same time simulating quasi-geostrophic flow. This is why, for simulations the physics of the Ekman layer on the interior flow are modeled. It is thus important to understand completely the physics of the Ekman layer and its effect on the dynamics of the geostrophic flow. While the atmospheric or ocean Ekman layers are macroscopic in size, they do not allow us to explore the dependence on various parameters.

Ekman layer instabilities

When the flow above an Ekman layer is sufficiently strong, instabilities and transition to turbulence in the Ekman layer can occur.

The Reynolds number for the Ekman layer, $Re_{Ek} = \delta U/\nu$, is characterized by the geostrophic flow velocity above the Ekman layer, U, and the Ekman layer depth, δ. Above a critical Reynolds number, the Ekman layer will become unstable. Many experiments done on Ekman layer instabilities have reported different critical Re_{Ek} ranging from 55-125 (e.g. see [118, 37, 22]).

It is known that turbulence in the Ekman layer causes an increase in its thickness, as momentum is more efficiently transferred between the boundary and the bulk flow[15]. It also changes the velocity profile and the dependence of the depth on rotation and is characterized by turbulent boundary layer parameters (see [30]; see also Schlicting [102] for more information about turbulent boundary layers).

However, the exact effect of a turbulent Ekman layer on dynamics is not well understood and most studies of the turbulent Ekman layer have focused on its velocity profile. It has been suggested that a turbulent Ekman layer modifies the drag felt by the fluid independent of the background rotation rate [35].

For moderately energetic structures in our flow, $U \sim 5$ cm/s at moderate rotation,$f = 0.6$ Hz, the Ekman layer Reynolds number ~ 25. However, for the most energetic structures which appear in our flow, $U = 25$ cm/s, the Ekman layer Reynolds number ~ 132, corresponding to a turbulent Ekman layer. It is thus quite possible that we have both regions of turbulent and laminar Ekman layer coexisting in our flow.

Ekman pumping and spin-down time

Consider a non uniform geostrophic flow such as a vortex or shear flow. In barotropic flow, the pressure field is independent of height [88]. That is, the isobars which are the streamlines of the geostrophic flow extend down into the boundary. Near the horizontal boundary, the

---

[15] This is the case for any turbulent boundary layer.

velocities decrease and so the Coriolis force, $2\mathbf{\Omega} \times \mathbf{u}$ can no longer balance the force due to the pressure gradient in the boundary. The result is that flow crosses the isobars and converges or diverges near the boundary. Because of the incompressibility of the flow and the impermeability of the boundary, fluid will turn towards the bulk from the Ekman boundary layer or be pulled into the Ekman layer from the bulk, known as Ekman injection and Ekman suction respectively. Thus the boundary in a rotating system communicates the rotation to the bulk directly by fluid transfer. Due to the Ekman injection, enhanced mixing and mass transport happens on timescales much shorter than diffusive timescales. e.g. nutrients in the ocean, such as oxygen, can be efficiently mixed.

The vertical pumping velocity, w, can be found by integrating the horizontal divergence in the vertical direction up from the boundary, assuming geostrophic flow in the interior, and matching the velocity at the edge of the boundary layer with the interior geostrophic velocity. The result for the given velocity profiles of nonuniform geostrophic flow can be given in terms of the geostrophic vorticity (see *Ekman pumping* in reference [88], section 4.5)

$$w = \frac{\delta}{2}(\frac{\partial v_o}{\partial x} - \frac{\partial u_o}{\partial y}) = \frac{\delta}{2}\omega_z \tag{2.17}$$

where u_o, v_o are the velocity components of the interior geostrophic flow. The pumping velocity is thus the vorticity of the geostrophic flow times the depth of the Ekman layer. A relative vorticity between the geostrophic flow and the background rotation gives rise to the Ekman pumping. An estimate of the predicted ratio of vertical to horizontal velocities in our experiment is about 0.1 in high vorticity regions (using 0.05 for δ and 20 s^{-1} for vorticity and 10 cm/s for u as typical values from our experiment) and less in regions of lower vorticity. However, from our measurements, this ratio is much higher (e.g. see section 4.3).

The essential effect of Ekman pumping is to provide dissipation which is independent of the scale of motion (in contrast with the viscous term) by a direct momentum transport between the bulk flow and the upper and lower boundaries. It is typically modeled in

2D geostrophic (and quasi-geostrophic) turbulence with the addition of a linear friction term $-\omega/\tau$ to the vorticity equation, (e.g. [78, 88]). This leads to an exponential decay of the vorticity with e-folding time τ in the unforced case. Though, Sansón and van Heijst proposed including nonlinear terms in modeling the laminar Ekman dissipation and found better agreement with experimental results of the decay of vortices in rotating flow [101]. However, most studies assume laminar conditions and do not account for turbulence, neither in the bulk nor in the boundary layer. It remains an open question as to how turbulence (either in the bulk or in the Ekman boundary layer) affects dissipation in rotating flows.

The dissipation time scale due to Ekman pumping can be estimated by taking the total kinetic energy in the geostrophic flow divided by the rate of work done on the fluid by the pressure force in the Ekman layer [88]. The resulting time

$$\tau = \frac{H}{2\sqrt{\nu\Omega}}$$

where H is the height of the geostrophic flow and Ω the system rotation rate, is known as the Ekman time or *spin-down* time. This is the time scale over which motions in a rotating fluid will decay (the fluid then *spins down* to rest) if they are not driven by some external forcing. This time scale was first confirmed by Greenspan and Howard in a rotating tank with a free surface [50]. The same time scale can be estimated from the loss of energy due to inertial waves reflecting off the boundaries (e.g. see reference [61]).

Duck and Foster give a review of the unforced spin-down problem, where a change in rotation rate is made to induce small motions which decay, in experiment and simulation in reference [36]. We performed similar experiments to check the theoretical spin-down time.

2.3.5 Where does dissipation occur?

To get an idea of where dissipation will be important in our flow we can make a dimensional analysis of the dissipation terms, $|\nu\nabla^2 u|$.

This is the viscous force per unit mass acting on the fluid, equivalent to the time rate of change per mass of the momentum of the flow. To get the net force, we integrate over the mass contained in the volume.

In the geostrophic flow region we have

$$\int_{\delta}^{H-\delta} \int_{0}^{2\pi} \int_{0}^{R} \rho(\nu \nabla^2 u) r dr d\theta dz \tag{2.18}$$

By order of magnitude, assuming that there is two-dimensional flow throughout the bulk, the total viscous force in the bulk is of order

$$\rho \left(\frac{\nu U}{L^2} \right) (\pi R^2 (H - 2\delta)) \tag{2.19}$$

where L is a typical horizontal length scale and R the horizontal extent. And in the Ekman boundary layers,

$$\rho \left(\frac{\nu U}{\delta^2} \right) (\pi R^2 (2\delta)) \tag{2.20}$$

The ratio of these terms is

$$\frac{\delta H}{2L^2} = \frac{\nu}{L^2} \frac{H}{2\sqrt{\Omega \nu}} = \frac{\tau_{Ekman}}{\tau_{viscous}} \tag{2.21}$$

The ratio of the viscous terms is the ratio of the timescales for Ekman dissipation $\tau_{Ekman} = H/(2\sqrt{\Omega\nu})$ to the timescale for the horizontal diffusion of momentum, due to viscosity $\tau_{diff} = L^2/\nu$. τ_{Ekman} is known as the Ekman time or *spin-down* time (see section 2.3.4 below).

Typical numbers for our system, give $\tau_{Ekman} \sim 90$ seconds (H = 48.15 cm, $\Omega = 2\pi 0.6$ Hz, $\nu = 0.0095$ cm/s^2) and $\tau_{viscous} \sim 4 \times 10^4$ seconds (using L = 20 cm, the radius of our tank). This conservative estimate yields the dissipation from Ekman effects about 30 times larger than viscous dissipation in the bulk of the flow. Ekman effects become larger as rotation is increased and the length scales of the flow increase.

Side-wall layers

Side-wall layers in a rotating fluid are known as *Stewartson layers* [88]. The main action of the side-walls is to cause the flow generated by Ekman pumping to turn away from (into) the top and bottom boundaries. Due to the no-slip boundary condition, the side-walls also exert a drag force on the perimeter of the fluid. We estimate the significance of the side-walls here in the same way as in the above section.

The sidewalls have a characteristic depth, $\delta_s = \sqrt{H\delta}$[88], where H is the depth of the geostrophic flow and δ the Ekman boundary layer depth. The ratio of the dissipation in the Ekman layers to the side-wall layers is

$$\left(\frac{(\frac{\nu U}{\delta^2})\rho V_{Ek}}{(\frac{\nu U}{\delta_s^2})\rho V_{side}}\right) \tag{2.22}$$

where the V's are the volumes of the respective layers.

Simplifying and approximating $\delta << H$, we find the Ekman to side-wall dissipation ratio to be

$$(\text{ratio}) = \frac{\delta_s}{\delta}\frac{R}{H}\left(1 - \frac{\delta_s}{2R}\right)^{-1} \tag{2.23}$$

R is the radius of the cylinder and we take H, the height as the depth of our geostrophic flow.

For the typical range of parameters used in our experiment, this ratio is usually ~ 15. This indicates that the action of the Ekman layer is stronger than the side-wall layers by at least an order of magnitude. However, this number may be a bit small and likely overestimates the dissipation occurring in the side-walls relative to the effect of the Ekman layers. This is because there is no active transport mechanism between the bulk and the side-wall boundaries; exchange of fluid between the bulk and the side-walls is due to the Ekman pumping of the Ekman layer and not the side-walls themselves [88].

This does not mean that the side-walls are always insignificant. In fact, in the current experiments we can often observe vortices shed from the side-walls. However, in the experiments where the flow is not forced, we do not observe a significant effect of the side-walls in damping the motion of the fluid.

2.3.6 Do purely 2D flows feel rotation?

In the vorticity equation 2.8, the term due to Coriolis is identically zero in a strictly 2D flow. The vorticity equation in 2D therefore has no trace of the Coriolis term.

In the equation for velocity, equation 2.7, the Coriolis term remains. However, we can write the Coriolis term as $-2\Omega \times (\nabla\psi \times \hat{\mathbf{z}})$, using the streamfunction ψ of 2D flow. Through the use of a vector identity, it can be rewritten as a gradient of a scalar, $\nabla(2\Omega\psi)$. Thus, the Coriolis term can be absorbed into the pressure term in the same way as the centrifugal force.

The answer to the question “Do purely 2D flows feel rotation?” is therefore, “No, not directly”. However, while purely 2D simulations can not directly calculate the effect of being in a rotating reference frame, modeling can bring it into the 2D equations of motion. The effect of rotation can only enter in to the calculation through the boundary conditions (i.e. rotating sidewalls) or through modeling of the Ekman dissipation by a linear drag term, $-\omega/\tau$. To include rotation effects in analysis, without the danger of modeling, it is necessary to perform a fully 3D simulation.

Simulations of 2D “rotating” flows are referred to as geostrophic and *quasi-geostrophic* simulations and are conducted to mimic oceanic and atmospheric flow. Quasi-geostrophic refers to the condition where the geostrophic equation is almost satisfied, i.e. for weak turbulence (Rossby number small but not zero). To model the effect of rotation, a linear dissipation term is included in the vorticity equation (e.g. see Pedlosky, section 4.6 [88]. Additionally a β-effect, the variation of the Coriolis with latitude, can be included in geostrophic and quasi-geostrophic models. For more on geostrophic and quasi-geostrophic simulations see the review by Read [95]

2.4 Coherent structures

We now turn our attention to the coherent structures which exist in turbulent flows.

2.4.1 Emergence of coherent structures

Large-scale ordered coherent motions occur in a wide variety of turbulent flows despite existing in a rapidly fluctuating background turbulence [59, 113]. These “coherent structures”, which are associated with localized regions of concentrated vorticity, persist for times that are long compared to an eddy turnover time. The importance of coherent structures in turbulence has become recognized through the use of flow visualization. Examples of coherent structures identified in turbulent flows include hairpin vortices in boundary layer turbulence [98], plumes in turbulent convection, and vortices in turbulent shear flows. Coherent structures play a major role in the transport of mass and momentum, thus affecting transport, drag, and dissipation in turbulent flows. Due to their long lifetimes, coherent structures in the atmosphere strongly influence the exchange of heat, moisture and nutrients between different locations. In industry, the prediction and control of transport, drag, and turbulence is important in many processes [57], and in some cases flows can be modified through the control of coherent structures [66, 67].

The emergence of coherent vortices is especially striking in geostrophic turbulence, where the Coriolis force plays a dominant role [111, 78]. Under the effect of rotation and stratification, geophysical flows develop large and robust coherent structures which can be identified and tracked for time much longer than their characteristic turnover time. Examples of such flows are high and low pressure systems, large vortical structures that are formed in Gulf Stream meander, Mediterranean eddies (Meddies), and the Earth’s jet stream; all can be observed and tracked by satellite imaging of the atmosphere or the ocean surface (e.g. see satellite imaging websites [3, 6]). Large coherent structures are not limited to the Earth; the atmospheres of other planets also reveal structures such as Neptune’s dark spot and Jupiter’s zones, belts and Great Red Spot.

Three-dimensional (3D) turbulence subjected to strong rotation develops columnar vortical structures aligned with the rotation axis, as observed in the present experiment and in previous laboratory experiments [77, 28, 53, 34]. Correlation in this direction becomes large when the Coriolis force becomes large compared to inertial forces, and the flow proceeds towards a quasi-2D state. This two-dimensionalization allows energy to proceed toward larger scales through the inverse energy cascade and toward smaller scales through the forward enstrophy cascade [63], as observed in simulation [107, 108, 48] and experiments on rotating [28, 53] and non-rotating quasi-2D flows [87]. The cascades of energy and enstrophy lead to a spontaneous appearance of intense localized coherent vortices containing most of the enstrophy of the flow. Vorticity filaments outside of those coherent structures are distorted and advected by the velocity field induced by the vortices. Thus, a rotating turbulent fluid flow can organize itself into large-scale coherent structures that are often long-lived compared to dissipative time scales. The presence of long-lived coherent structures in turbulent rotating flow has been observed in both experiment [77, 28, 53, 111] and in simulation [108, 48]. These structures are larger than the scale of the forcing. The large-scale coherent structures break the homogeneity of the flow and are thought to dominate the flow dynamics. The long lifetimes and spatial extent allow coherent structures to play a significant active role in transport processes [93, 110].

2.4.2 Coherent feature extraction

Due to the dynamical importance of coherent structures, any analysis of flow containing these structures should take into account their existence. One approach to analyze the coherent structures and the dynamics of such flow is to partition it into regions with different dynamical properties. Okubo [85] derived a criterion to separate flow into a region where strain dominates (hyperbolic region) and a region where vorticity dominates (elliptic region). The same criterion was later re-derived by Weiss [126] and is now known as the Okubo-Weiss criterion. The criterion has been widely used to analyze numerical simulations of 2D turbulence. However, as pointed out by Basdevant and Philipovitch [15], the validity of the criterion's key assumption is restricted to the core of the vortices that correspond to the strongest elliptic regions. This limitation reduces the applicability of a decomposition using this criterion.

Another method that has been found useful in analyzing flow fields is proper orthogonal decomposition (POD). This projects a field onto a set of orthonormal basis functions where successive eigenvectors are obtained by numerically maximizing the amount of energy corresponding to that eigenmode [51]. [POD is known by other names, including Karhunen-Loève decomposition, principal components analysis (PCA), and singular value decomposition (SVD); the basis functions are also known as empirical eigenfunctions and empirical orthogonal functions [51], p.86.] Linear combinations of the basis functions ideally correspond to the coherent structures in the flow. However, if the ensemble of fields is homogeneous, the basis functions become Fourier modes [51]. Furthermore, a single mode of the POD corresponds to a full field with structures in a particular spatial arrangement. If the structures in the field are not stationary, as in the case of our present flow, many modes will therefore be necessary to track the different spatial configurations. Indeed, application of POD to our data resulted in the extraction of the large scale, low amplitude mean flow structure of our field, rather than the continually moving intense coherent structures.

2.4.3 Wavelets

In chapter 5 we separate our flow into coherent and incoherent components using wavelet transforms [32] to extract localized features at different spatial scales. The most important advantage of the wavelet representation over the more usual Fourier representation is the localization of the basis functions. A Fourier analysis is not well suited to pick out localized features such as intense vortices. The basis functions of a Fourier transform are localized in wavenumber space and hence spread out over the entire domain in physical space. The basis functions of the wavelet transform consist of dilates and translates of a "mother" wavelet, which contains multiple frequencies and has compact support (non-zero values only inside a finite interval) in physical space. The basis functions are well localized in both physical and wavenumber space; hence only a few coefficients suffice to describe localized features of a signal. The coefficients of the wavelet transform contain not only amplitude but also scale and position of the basis elements. Thus the coefficients can be used to track the size and location of features that are well correlated with the wavelet bases (e.g. [105, 103]).

The discrete wavelet transform (DWT) [32] has been found to be well suited to analyze intermittent signals and systems containing localized features such as the intense vortices that occur in turbulence [39, 40, 41]. Farge has extensively applied wavelets to the analysis and computation of turbulent flows [38, 39, 40, 41, 42, 18].

The discrete wavelet *packet* transform (DWPT) [127] is a generalization of the DWT; the possible wavelet packet basis elements are a larger set which include spatial modulation of the mother wavelet. The advantage of the DWPT is that the choice of basis is adaptable to the signal to be analyzed.

Turbulent flow can be considered as a superposition of large-scale coherent motions, “fine-scale” incoherent turbulence, and a mean flow with interaction between the three constituents [58]. In numerical simulations of 2D turbulence [40, 105, 41], and more recently 3D turbulence [42], the coherent and incoherent turbulent background components have been separated using wavelet based decompositions operating on the vorticity field. The coherent part, represented by only a small fraction of the coefficients, retained the total flow dynamics and statistical properties, while the incoherent part represented no significant contribution to the flow properties [see figure 2.2 for an example of this in direct numerical simulation (DNS)]. This separation of the flow into two dynamically different components suggests that the computational complexity of turbulent flows could be reduced in simulations with coherent structures interacting with a statistically modeled incoherent background [41]. The application, however, has been heretofore primarily limited to results obtained from numerical simulations.

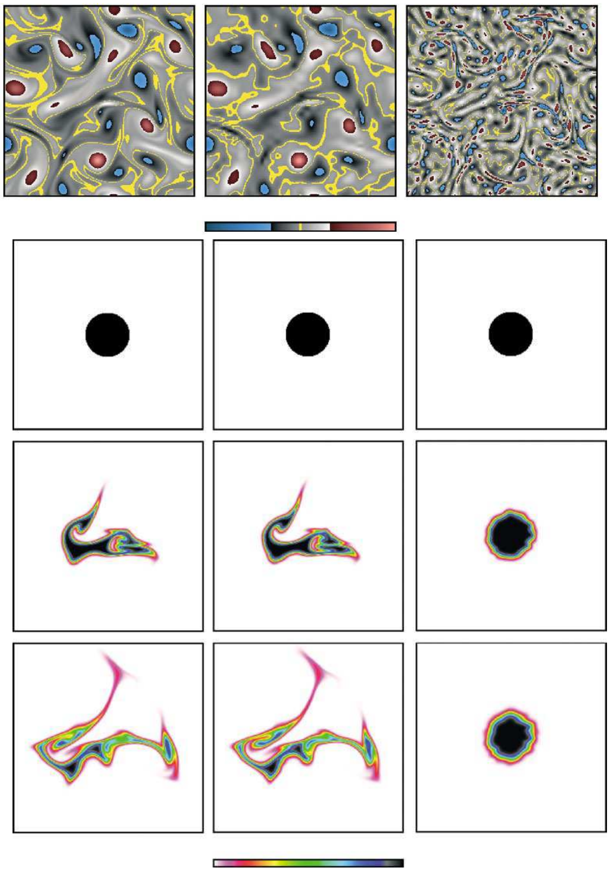

Figure 2.2: Numerically simulated 2D turbulent fields. The leftmost column corresponds to the total field produced by direct numerical simulation (DNS). The center column is the coherent field that results from the largest amplitude coefficients of the wavelet transform of the total field. The rightmost column corresponds to the incoherent field that results from the remaining small amplitude coefficients. The nine lower images show the time evolution of a passive scalar in the respective fields. The scalar is well mixed in the total and coherent fields, while it is only diffused by the incoherent field. Reproduced from separate figures in reference Beta *et al.* [17].

2.5 Rotating turbulence in the laboratory and in the computer

Many experiments and simulations have been performed on rotating turbulent flows. A summary of noteworthy rotating turbulence experiments is presented in table 2.1 and noteworthy simulations in table 2.2). However, few experiments have been performed in the last two decades which probed the effect of rotation on the dimensionality of turbulence. Though good statistical measurement techniques such as hotfilm anemometry and laser doppler velocimetry existed, experiments before the 1990's suffered from the lack of quantitative visualization tools such as digital particle image velocimetry (DPIV) [94] that would allow for detailed quantitative analysis of the structure of the flow field. Numerical simulations of fully 3D rotating flow were severely limited by lack of computational power available to compute such flows until the early 1990's.

2.5.1 Experiment

Experiments have usually been conducted in rotating tanks (cylindrical, square cross-section, or annular) or rotating pipes (without endwalls), and turbulence has been excited by a grid (either stationary or oscillating) or source-sink forcing. Surprisingly few experiments on rotating turbulence in a deep tank and forced by pumping of fluid, such as our experiment, have been performed. We discuss in more detail the experiments most relevant to ours because of the similarity of the apparatus. These include the experiments of McEwan (e.g. [77]), Colin de Verdiere [28], Hopfinger *et al.* (e.g. [53]), and Dickinson and Long [34]. The experiments of Baroud *et al.*(e.g. [12]) are also discussed in detail due to the relevance of their investigation of the transition between 3D behavior and 2D behavior of rotating turbulence.

Ibbetson and Tritton [60] performed one of the first experiments to look at the effect of rotation on decaying grid turbulence. Their apparatus was a rotating annulus filled with air. Turbulence was excited by sweeping a grid through the apparatus, and measurements

Group	Geometry	Forcing	Results
Ibbetson and Tritton [60] (1975)	annulus	dragged grid once vertically to produce decaying turbulence	anisotropy and inhibition of downscale energy transfer induced by rotation
McEwan [77] (1976)	cylinder	sources and sinks (jets)	formation of coherent cyclones with universal velocity profile
Wigeland and Nagib [128] (1978)	rotating duct	air and grid / decaying turbulence	rotation increased length scales and reduced dissipation (Ekman dissipation was negligible)
Colin de Verdiere [28] (1980)	cylinder with flat lid and different β-planes	random sources	long-lived coherent jets and vortices / primarily cyclones
Hopfinger *et al.* [53] (1982)	cylinder with flat lid	oscillating grid	cyclones oriented parallel to rotation axis
Dickinson and Long [34] (1983)	square box	oscillating grid	similar to Hopfinger et al.
Sommeria *et al.* [111] (1988)	annulus with β-plane	concentric ring of sources and sinks	long-lived coherent jet and vortices
Jacquin *et al.* [61] (1990)	rotating cylinder on its side (rotation axis horizontal) no end boundaries	airflow forced past grid down axis of cylinder	decaying grid turbulence, similar to Wigeland [128], saw increase in integral length and decrease in dissipation
Zhang et al. [132] (1997)	cylinder with inner cylinder	inner cylinder oscillates vertical, parallel to rotation axis	rotation breaks isotropy of velocity components, causes generation of mean zonal flow
Baroud *et al.* [12, 13, 14] (2002&2003)	same apparatus as Sommeria *et al.* [111]	concentric ring of sources and sinks	increasing two-dimensionality with increasing rotation, resulting quasi-2D turbulence different than theoretical 2D turbulence
Ruppert-Felsot *et al.* [100] (2005)	cylinder with flat lid	sources and sinks	long-lived coherent structures and increasing two-dimensionality
Morize *et al.* [83] (2005)	square tank with flat lid and bottom	grid raised vertically to produce decaying turbulence	decaying rotating turbulence led to large scale structures with spectral slope steeper than k^{-2}.

Table 2.1: Some previous rotating turbulence laboratory experiments.

Group	Geometry	Forcing	Results
Mansour *et al.* [70] (1992)	DNS	homogeneous	increasing rotation did not lead to Taylor-Proudman two-dimensionalization
Hossain [55] (1994)	DNS 32^3 triply periodic	3D homogeneous	high correlation after rotation applied and energy transfer to larger scales
Smith *et al.* [107, 108] (1996 & 1999)	DNS triply periodic 32^3 in [107], up to 128^3 in [108]	homogeneous 2D and 3D	2D inverse cascade / coherent cyclones
Yeung *et al.* [130] (1998)	256^3	3D isotropic	sees inhibition of energy cascade to small scales
Godeferd *et al.* [48] (1999)	DNS doubly periodic with top and bottom boundaries, typically 96^3	grid-like, localized near bottom	tendency towards 2D, cyclones

Table 2.2: Some previous rotating turbulence numerical experiments.

were taken by hotwire anemometry. When they rotated their apparatus, they observed an increased correlation length, enhanced dissipation, and inhibition of the forward energy cascade.

Jacquin *et al.* [61] performed a decaying turbulence experiment by flowing air past a grid and through a rotating pipe on its side. They improved upon a similar earlier experiment by Wigeland and Nagib [128] that suffered limitations of the experimental apparatus. Jacquin *et al.* observed a significant increase in the integral length scale of the fluctuating velocity components perpendicular to the rotation axis with increasing rotation when $Ro < 1$.

$$L_{ij} = \int \frac{< (u_i(\mathbf{x})u_i(\mathbf{x}+\mathbf{r}_j)) >_{\mathbf{x}}}{< |u_i|^2 >_{\mathbf{x}}} d\mathbf{r} \tag{2.24}$$

where $\mathbf{r}_j$ is a displacement in the x_j direction. This is a measure of the distance over which the flow is well correlated in various directions. The integral length scale parallel to the rotation axis was unaffected by rotation. They also observed a decrease in the dissipation; their experiment did not have endwalls and Ekman dissipation was negligible.

A very recent study on decaying grid generated turbulence was performed by Morize *et al.* [83]. A grid was dragged through a rotating square tank to produce roughly homogeneous turbulence as an initial condition. The decay in turbulence resulted in a corresponding decrease in the Rossby number as a function of time. They were able to verify a predicted relation between Rossby number and skewness of the vertical vorticity, and observed that the skewness reached a peak value at a moderate Rossby number[16]. The evolution of the energy spectra was also observed and they reported values steeper than k^{-2}.

McEwan [77] carried out experiments in one of the first observations of localized concentrations of vorticity (angular momentum) in a rotating flow (short tank 22.8 cm tall 29.6 cm diameter) turbulently forced by sources and sinks. McEwan remarked that the turbulence had to be sufficiently weak such that rotation could induce a 2D state and allow formation of vortices aligned along the rotation axis. In an earlier experiment, McEwan forced the flow by oscillating an rubber membrane that also acted as the lid of the apparatus. McEwan showed that it was possible for concentrations of vorticity (angular momentum) to appear in rotating flow if the forcing induced turbulence [76][17]. Arguments for and against this possibility were summarized by Bretherton *et al.* [19][18], who were unable to observe vortices although they were looking for a single vortex that would fill the entire system.

In the earlier experiment, McEwan observed apparently stationary "energization regions", locations in the tank where vortices would be "strongly energized". As vortices moved away from the locations, they would decay until they moved back to those preferred regions. This produced various inertial modes based upon the frequency of oscillation. It is possible that these locations were some complicated standing wave pattern of the inertial modes excited by the forcing in his tank. However, it seems that his observation was made only when he forced hard enough to produce turbulence (he referred to this as the breaking of inertial modes), so it is likely even more complicated. Nonetheless it produced "preferred"

---

[16] However, this experiment suffers from large stereoscopic effects that may possibly render the measured skewness meaningless.

[17] This was referred to as the breaking of inertial waves in the flow, as in the breaking of an ocean wave.

[18] The emergence of a single vortex as a departure from solid body rotation is referred to as angular momentum mixing.

locations for vortices which seemed to be stationary (not where they appear, but where they are recharged).

McEwan remarked that the method of forcing was anisotropic. Similar observations have not been made in later experiments using more isotropic forcing, by sources and sinks or by grid turbulence[19] [77, 28, 53]. However, in the present experiment, using a source-tee and sink forcing geometry, similar observations of the existence of preferred locations for coherent structures were made [100] (e.g. see chapter 4). It is not clear whether or not this is an artifact of anisotropic forcing. A few possibilities of how intense cyclones might form from turbulent forcing are summarized in the reviews of Hopfinger [52, 54]. One possibility is that at the boundary of the 3D turbulence and rotation dominated region, inertial waves propagate nearly parallel to the rotation axis and form cone-like protrusions, due to the envelope of the inertial wave, into the fluid above. This pushes fluid into the region in-between the protrusions, resulting in a strong convergence and thus driving cyclonic motion [75]. Another possibility, which dropped out of the later review, suggested by Lundgreen is that there could exist persistent suction sites in the 3D turbulent region [69].

Colin de Verdiere conducted experiments, similar to McEwan, forced by pumping near the bottom of a deep rotating tank. The experiments were conducted on a f-plane, on a β-plane, and on a sliced cylinder. The forcing was run through commutators that were switched randomly to obtain homogeneous forcing, localized at the bottom of the tank. Colin de Verdiere obtained similar results as McEwan and for his f-plane experiments. In particular, he observed a merging of smaller vortices, forming larger scale structures at the initiation of the experiment. For the experiments on a β-plane of polar geometry, he observed zonal formation. The vortices wrapped around the azimuthal direction, forming alternating "East-West"[20] mean flows.

Dickinson *et al.* [34] carried out experiments in a square rotating box of water, driven by an oscillating grid. They examined the propagation of the grid generated turbulence

---

[19] However, with grid turbulence, it is certainly possible to force a static array of vortices, corresponding to the grid geometry.

[20] With the North-pole defined as the center of the tank and the South as the outer wall.

as a function of rotation. In the absence of rotation, the disturbance was observed to propagate as $\sim t^{1/2}$. As rotation was increased, the behavior would change to $\sim t^1$ some distance from the grid, i.e. the turbulent disturbance would propagate at constant velocity. As rotation increased, the distance at which this change in behavior would occur moved closer to the grid. At more or less steady state conditions (it was specified only "after several minutes"), they observed two distinct regions in the flow, one close to the grid, dominated by the turbulence generated by the grid, and the other filling the rest of the tank, dominated by rotation. In the experiment of Dickinson, dye injected into the flow was completely mixed near the grid, consistent with 3D turbulence while it organized into elongated sheets parallel to the rotation axis, away from the grid, consistent with an increase in the vertical correlation length. The resulting flow pattern is shown in figure 2.3. The transition between the two regions was quite sharp, occurring within a only few centimeters. Similar observations in an earlier version of our apparatus were made by Weber, utilizing an oscillating grid in a square tank, that confirmed the constant velocity propagation behavior of the turbulent front and the distinction between the 3D grid dominated region and the 2D rotation dominated region [124][21].

Another grid experiment was performed by Hopfinger *et al.* who forced near the bottom of a deep cylindrical tank [53]. They were able to observe intense cyclones, with vorticity up to 40 times that of the background, i.e. a local $Ro \approx 40$ (see figure 2.4). Using laser doppler velocimetry to interrogate the horizontal velocities, they observed a sharp transition above which the mean horizontal velocities were roughly independent of height. This was interpreted as an abrupt transition between a 3D grid-dominated turbulent Ekman layer and rotation dominated 2D flow. They determined that the transition occurred at a Rossby number, $Ro_T \approx 0.2$. Hopfinger *et al.* were also able to make observations of the vortices from the side, visualizing the cores by the introduction of air bubbles, shown in figure 2.1 (b). Even for such intense vortices, they are amazingly vertically straight! The vortices rapidly filled the entire height of the tank on the order of 6-7 times that of the

---

[21] These experiments were conducted in a previous incarnation of the current experiment and also carried out by the current author.

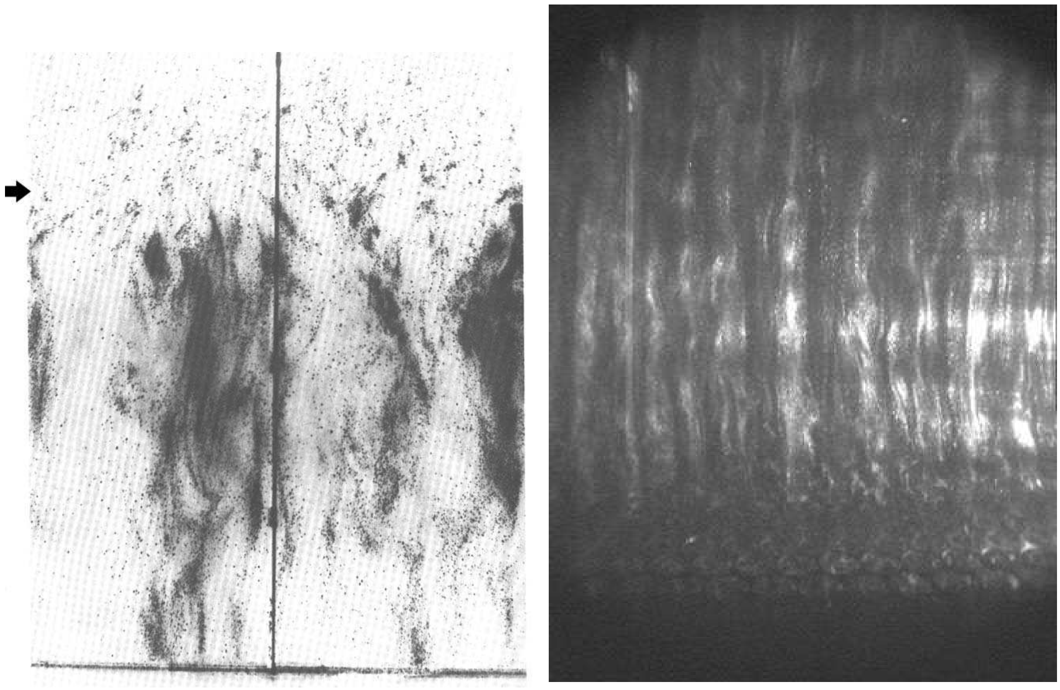

Figure 2.3: LEFT: Side view of the steady state condition achieved in the rotating turbulence of Dickinson *et al.* [34]. The forcing grid was at the top of the tank. The arrow indicates the abrupt transition region from grid dominated 3D small-scale turbulence above to rotation dominated turbulence, large curtain-like structure below. RIGHT: Side view of a previous experiment by the current author (unpublished). The flow was forced by an oscillating grid in the bottom of a square tank. A short distance from the grid, the flow is rotationally dominated as seen by the vertical column-like structures, similar to that of Dickinson *et al.* The wave structure is likely due to inertial waves propagating parallel to the axis of rotation. A little less than the entire tank is visible.

rotation period, after the start of the forcing. They observed waves that traveled along the vortex cores, a net flux upwards from the grid-dominated region, and speculated that they played a role in maintaining the strength of the cyclones.

Another experiment, which does not quite fit into the modes of forcing listed above was performed by Zhang *et al.* [132]. In it, they forced turbulence by a vertically oscillated central shaft with o-ring-like surface roughness elements attached. They were able to observe an induced mean azimuthal, anti-cyclonic flow when the system was rotating. Without rotation, no mean flow appeared. They speculated that the rotation allowed turbulent stresses initiate and to drive the mean flow.

The studies in our laboratory by Baroud *et al.* [12, 13, 14] investigated the difference in behavior of turbulence at differing rotation rates. They are the first and most careful studies of the statistical properties of rotating turbulence. Baroud *et al.* used the apparatus developed by Meyers [81] and Sommeria *et al.* (e.g. [111]) which had led to the first experimental observations of stable cyclonic vortices produced in shear flow, as a laboratory replica of Jupiter's Great Red Spot. The apparatus was a 18 cm high rotating annulus (83 cm outer diameter) with a slopped bottom (β-plane), a rigid lid, and filled with water. The flow was driven by pumping fluid between two concentric rings of holes at the bottom of the annulus. The radial flux coupled with the Coriolis force to form a strong anti-cyclonic jet that supported long-lived cyclones in the flow. Baroud *et al.* observed an inverse cascade in the form of merging structures at the start of the experiment. However, once large scale structures appeared, further merging was not observed.

More intense driving led to a more 3D state while higher rotation led to a more 2D state. This is partially indicated in the behavior of the Rossby number calculated from the experiment, reproduced in figure 2.5. However it was noted that the results from observations indicated that the flow dimensionality was not completely described by the measured Rossby number. Baroud found that, for similar Rossby number, the flow was significantly more 2D at high pumping and high rotation than at low pumping and low rotation. This effect also occurs in the measured correlation of Baroud [12]. It was not

Figure 2.4: TOP: Particle streak image from an experiment without rotation. The flow does not display any coherence. BOTTOM: Particle streak image taken from an experiment after rotation was turned on. Clearly visible are coherent vortices which have aligned along the rotation axis. See also figure 2.1 (b). Reproduced from Hopfinger *et al.* [53].

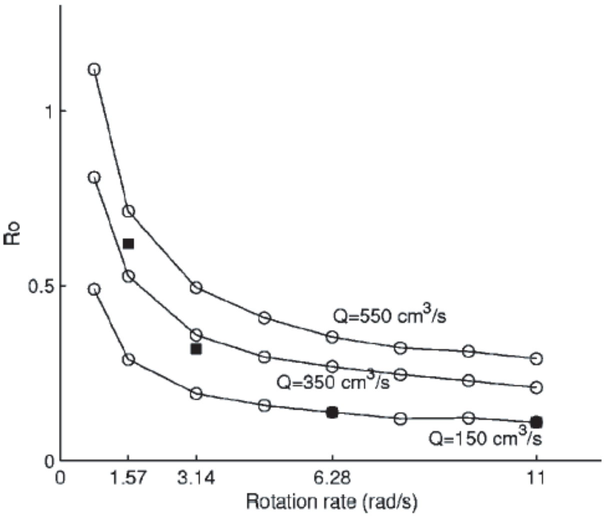

Figure 2.5: Rossby number as a function of rotation and forcing in a laboratory experiment in a rotating annulus. Increasing rotation decreases the Rossby number, making the flow more two-dimensional; increasing the forcing increases the Rossby number, making the flow more three-dimensional. Reproduced from Baroud [12].

noted that the correlations for the very low pumping cases appear to turn over and decrease slightly with increasing rotation.

Baroud also measured the two-dimensionality of the flow by measuring the correlation of velocity traces taken simultaneously at two vertically separated locations[22] (see figure 2.6). One velocity probe was near the lid of the apparatus and the other was near the bottom. For the rapidly rotating case, the two traces are nearly indistinguishable, indicating a high degree of two-dimensionality. The correlations, shown in figure 2.6, were observed to rapidly increase (higher correlations were likely not obtainable due to experimental noise, though certainly a correlation of 100% would never be reached in a real 3D flow!).

In Baroud's experiments, however, the transition from 3D behavior to rotationally dominated 2D behavior was probed by changing the control parameters (either pumping or rotation). Due to the small aspect ratio, a change in control parameter would affect the flow dimensionality throughout the entire tank. This is in contrast to the current study; we

---

[22] A hotfilm probe is an anemometer that measures the velocity component transverse to a thin element. It is similar to a hotwire probe but has a special quartz coating to allow submersion into liquids.

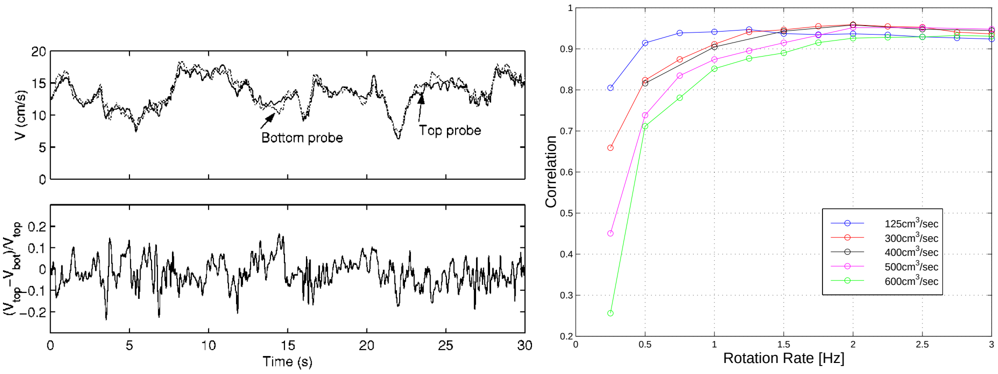

Figure 2.6: LEFT: Turbulent time series from two hotfilm probes in the experiment of Baroud [12]. The probes were placed directly above one another, one in the bottom of the apparatus and one in the lid. RIGHT: The correlation coefficient of the two curves as a function of rotation for different pumping conditions. As rotation increases, the correlation increases. The curves display a slight decrease for the low pumping (low turbulence) at high rotation. Reproduced from Baroud [12].

can probe a more 3D or more 2D region of the flow by changing our interrogation region, either near the forcing or far from it (see the experimental chapter 3.).

2.5.2 Simulation and theory

We limit our discussion here to fully 3D direct numerical simulations (DNS) and theory of rotating turbulence and of the most relevant work. Most numerical studies of rotating turbulence have confirmed the general results of experiments: the emergence of large structures and the two-dimensionalization trend for low Rossby number. Further, many numerical and theoretical studies focus on predicting or measuring the form of the energy spectrum function, so some discussion of the scaling is unavoidable.

Purely 2D flows can not directly simulate the effect of rotation (see section 2.3.6). However, we should point out the work of our colleague, Marcus (e.g. [72, 74, 73], among others). Marcus has extensively modeled planetary flows, such as that on Jupiter, with a focus on the dynamics of the vortices and zonal formation. Recently, Marcus and coworkers have turned their attention towards 3D simulations of vortices in accretion disks, with application to planetary formation. However, this astrophysical application is in the realm of compressible fluid dynamics, outside the scope of our current research[23], albeit very interesting.

Many numerical studies which have shown significant two-dimensionalization at moderate Rossby number, rather than the expected $Ro \ll 1$, in accordance with the numerous experiments (e.g. [77, 28, 53, 34, 12]). Hossain [55] observed a two-dimensionalization when rotation was suddenly turned on such that Ro = 0.1 in initially 3D DNS generated turbulence. The vertical correlation of the horizontal motions was large at low Rossby number. Smith and Waleffe also observed a two-dimensionalization (see figure 2.7), transfer of energy to large scale cyclonic motion, and suppression of vertical motions in a triply periodic DNS with rotation with initially 2D or 3D small-scale homogeneous forcing below a critical Ro of order 1 [108]. In contrast to other simulations, however, they observed a k^{-3} scaling. They interpreted this as that only the rotation and the wavenumber are important for setting the scaling of the energy spectrum, $E(k) \sim \Omega^2 k^{-3}$, by dimensional arguments. In an earlier simulation [107], however, they observed a $k^{-5/3}$ scaling, using fewer modes in the vertical direction, due to computational restrictions. In their later work, they attributed this to the lack of available nonlinear triad interactions, because of the low resolution in the vertical direction. This suggested that nonlinear interactions are important in the two-dimensionalization process.

There have been very few numerical experiments with boundaries. Godeferd and Lollini [48] carried out a DNS simulation, reproducing the laboratory experiments of Hopfinger [53]. This was novel simulation, because of the inclusion of rigid top and bottom boundaries (the simulation was periodic in the other directions) and tested a spatially localized forcing mimicking an oscillating grid, rather than homogeneously forced previous simulations. They observed the emergence of columnar intense cyclones and determined that the Ekman pumping from the top and bottom boundaries was an important process in their formation. Their simulation, however, had many problems, including their low Reynolds number, $Re \approx 18$ [71].

---

[23] Future experiments conducted in our apparatus, with modifications, are planned to test the results of Marcus' most recent simulations.

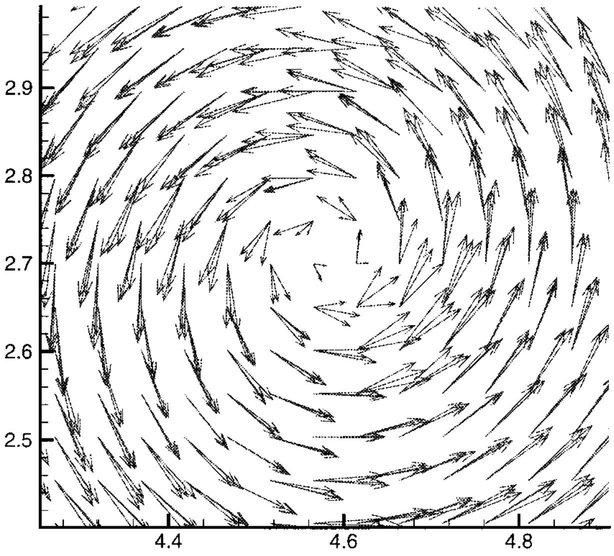

Figure 2.7: Close-up of a cyclone in the velocity field of a 3D DNS of rotating turbulence. Shown is the field at several vertically separated horizontal planes. The fields are very similar, representative of the large vertical integral length scale, due to rotation. Reproduced from Smith and Waleffe [108].

The group of Lesieur *et al.* carried out a number of numerical studies and stability analysis of cyclonic and anti-cyclonic motions under rotation (e.g. [129, 80]). They found that rotation is stabilizing for cyclonic motion in a rotating shear flow while anti-cyclonic motion is destabilized for $Ro > 0.5$. Stronger anti-cyclonic motion became stabilizing. Further, they found that the same results hold for the stability of 3D motions due to the presence of cyclonic or anti-cyclonic motions. The interpretation was that only the cyclonic motion reduces the straining of the absolute vorticity $2\Omega + \omega_z$.

Mansour *et al.* [70] have shown in DNS that increasing rotation does not lead to a 2D Taylor-Proudman state. This seems to have motivated a look at other mechanisms for two-dimensionalization. Recent theoretical attempts to account for the transfer of energy in rotating turbulence have focused on inertial waves (which are analogous to the internal waves of stratified flows) [24]. Inertial waves transport energy and in particular assist in the two-dimensionalization process by rapidly transporting energy in the direction parallel to the rotation axis. Furthermore, rotation leads to a transfer of energy towards the "slow modes". For the most recent summary see Cambon *et al.* [23]. To obtain results, they have used a closure model known as eddy damped quasi normal-Markovian (EDQNM) and various modifications thereof. Like the nonlinear term, the Coriolis term does not add or remove energy from the system (the Coriolis force does no work on the fluid). Rather it changes the phase of the interacting resonant triads. This also has the effect of redistributing the energy among different modes. For the transfer to occur, Cambon *et al.* [24] argue that a local Rossby number, based upon the RMS vorticity must be greater than one, while the Rossby number based upon the integral length scales be less than one, otherwise the inertial waves will be damped.

Zhou [133] developed a prediction for rotating turbulence using similarities to magnetohydrodynamic turbulence. Zhou reasoned that the rotation timescale, $\tau_\Omega \sim 1/\Omega$ should be compared to the time scale of energy transfer by nonlinear interactions, $\tau_{nl} \sim (k^3 E(k))^{-1/2}$. At low Rossby numbers, $Ro = \tau_{nl}/\tau_\Omega$, the dissipation rate ϵ, wavenumber, and rotation, were the important quantities for energy transfer, resulting in the scaling of the energy spectra $E(k) \sim (\epsilon\Omega)^{1/2} k^{-2}$. This scaling was later observed by Yeung and Zhou in a 3D DNS of rotating turbulence [134]. A similar scaling was also later predicted in the work of Canuto and Dubovikov [26, 25][24]. Zhou has exchanged criticisms with Canuto and Dubovikov (e.g. see [134] and response [27]).

A new non-dimensional number $N = K/\nu\Omega$ was proposed by Canuto and Dubovikov to describe the regimes of rotation dominated turbulence [26] (and in more detail in [25]). Here $K = (1/2)u^2$ is the turbulent kinetic energy. The non-dimensional number N can be written as $Ro^2/Ek \gg 1$, in our notation, if the Ekman number is based upon a horizontal length scale (rather than the vertical depth). Their claim is that for $N < 1$, rotation is dominant, but suppresses the nonlinear interactions and inhibits two-dimensionalization. Simulations carried out in this regime should not see increasingly 2D flow for increasing rotation. For $N > 1$, the nonlinearities are sufficiently strong to couple with the rotation and produce a transfer of energy from 3D modes to 2D modes. In Hopfinger's review of

---

[24] This result was presented as "new" in Canuto and Dubovikov's work, when it had been published several years earlier by Zhou.

rotating turbulence, he notes that the energy containing turbulent eddies must survive, the Ekman spin-down time $H/(2\sqrt{\nu\Omega})$must be much longer than the turnover time of the eddies L/U [54]. Both conditions are thus roughly equivalent to $Ek^{1/2} \ll Ro$.

The strongly rotationally dominated regime, $N < 1$, however, is impossible to reach in our rotating experiment. For a typical smallest value of the turbulent kinetic energy of 1 cm^2/s^2, and our highest rotation rate of 1.0 Hz, we reach $N = 8.0$. Reaching $N = 1$ would require a rotation rate of 8.0 Hz! However, in the rotating annulus of Baroud, which can rotate up to 3.0 Hz, it may be possible to come close to $N = 1$ at the highest rotation rates and lowest forcing. Indeed, the slight decrease in correlation at high rotation and low forcing from Baroud's experiment shown in figure 2.6, may be a signature of the rotation suppressing nonlinear interactions, resulting in a more 3D state for stronger rotation[25].

The Taylor-Proudman theorem is still occasionally cited as the cause for tendency towards 2D behavior in rotating flows (in the review of Hopfinger [54], for example, or in the review on geostrophic turbulence in the laboratory and atmosphere of Read [95]). Even a somewhat safer, more cautious statement that the resulting quasi-2D state is consistent with Taylor-Proudman or results “as expected from Taylor-Proudman theorem” [14] is still used. The continued use of Taylor-Proudman to describe the two-dimensionalization of rotating turbulent flows is most likely due to its simplicity.

The current consensus is that Taylor-Proudman is not adequate, but that the real route towards 2D in rotating turbulence must be due to the coupling of the nonlinear interactions with rotation.

However, it is difficult to make direct comparisons of simulation and theory to our experiment. Most simulations above use random, narrow-band in wavenumber, homogeneous or isotropic forcing. We can not control the spectra of our forcing which is broad-band (e.g. see flow description chapter 4) and definitely not homogeneous (i.e. we force locally near the bottom of our tank). Additionally, most simulation is carried out in a non-physical homogeneous periodic domain, without boundaries. In our flow the effect of the boundaries

---

[25] This is speculation, however, as the error bars on the measurements were not known.

can be significant (e.g. see the flow description chapter 4 for example of vortex shedding from the wall).

So we must be cautious when making comparisons. Nevertheless, the general results still apply to enhancing the understanding of our flow.

2.6 Summary

Fluid flow can often be considered as approximately two-dimensional (2D) if length scales of variation of the flow are small in the vertical direction compared to the horizontal. 2D flows will have small horizontal divergence and behave quite differently from their 3D counterparts. However, all real flows are three-dimensional (3D), and it is impossible to decouple the flow entirely from 3D effects such as drag at the boundaries.

In turbulent flow, viscosity is negligible for motions of Reynolds numbers $\gg 1$. Energy is redistributed among different length scales. In 3D turbulence, this energy is transferred from the large forcing scales to small scales, where it is ultimately dissipated due to viscosity by motions with $Re \sim 1$. In 2D turbulence, however, this energy transfer can proceed in the opposite direction, from small to larger scales, in what is known as the inverse energy cascade.

Strong rotation leads to a two-dimensional columnar state where derivatives of the flow field vanish parallel to the rotation axis. This has been often argued by the Taylor-Proudman theorem, valid in the limit of vanishing Rossby and Ekman numbers ($Ro \ll 1$ $Ek \ll 1$), but is more likely due to nonlinear interactions and must occur at finite, but small, Rossby number. In both experiment and simulation rotation causes a rapid growth in the vertical integral length scale and the transfer of energy from small to large scales, consistent with the inverse energy cascade in 2D turbulence. Thus rotating turbulence can support the emergence of long-lived coherent structures, intense localized features, such as vortices and jets.

Coherent structures can dominate the dynamics of the flow due to their large size, intensity, and long lifetimes. Due to their localization, analysis by non-local functions, such as Fourier modes, is not efficient. Wavelets are well suited to analyze signals with localized intermittent features, as they consist of translations and dilations of localized basis functions. Turbulent flow fields can be split into coherent and incoherent parts using wavelet-based transforms. A small number of large amplitude coefficients of the transform correspond to the coherent structures and are able to represent the total flow field. The remaining coefficients are found to have little contributions to the dynamics of the flow. Wavelets have been successfully applied to the analysis of coherent structures in turbulence simulations. However, this particular approach has not yet been applied to experimental data.

Until now, relatively few experiments have been both able to probe the flow structure quantitatively, and to study how rotation tends to two-dimensionalize flow. In the next section, we describe our experiment that shall occupy a special niche in the study of rotating turbulence.

Chapter 3

Experimental methods

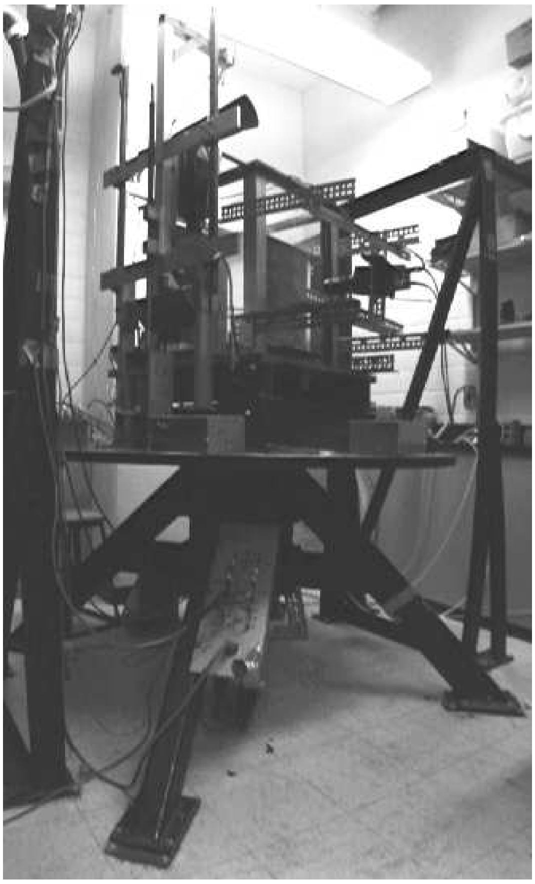

In this chapter we describe the experimental methods used. In section 3.1 we describe the apparatus hardware. A brief, self-contained overview of the apparatus is given in section 3.1.1. In section 3.2 we describe the measurement technique, primarily the digital particle image velocimetry. In section 3.3 we describe known problems of the current setup and their possible resolution. In section 3.4 we describe some numerical methods used for some of the calculations presented in chapter 5. We end with a brief summary in section 3.5.

Drawings for a new design of the system are in appendix A.

3.1 Experimental apparatus

3.1.1 Apparatus overview

An acrylic[1] cylinder (48.4 cm tall, 39.4 cm inner diameter) is fit inside a square acrylic tank (40×40 cm cross section, 60 cm tall) that has a transparent lid (Fig. 3.1) [99]. The tank is filled with distilled water at $24 \pm 1°$C ($\rho = 0.998$ g/cm^3, $\nu = 9.5 \times 10^{-3}$ cm^2/s). The tank and the data acquisition computer are mounted on a table that can be rotated up to 1.0 Hz.

Fluid is injected at the bottom of the tank by pumping water through a hexagonal array of tubes with grid spacing 2.3 cm; there are 192 sources and 61 sinks, as shown in Fig. 3.1. The source tubes are tee-shaped with a 2.5 cm shaft and 2.1 cm horizontal top (0.079 cm inside diameter) [see inset of Fig. 3.1(a)]. Each tee is screwed into the distributor. This design allows us to easily change the type of connector or change the forcing geometry by blocking or modifying sources or sinks. The tee source geometry was chosen to produce horizontal velocities so as to not directly influence the flow field at the top. The sinks are 1.27 cm diameter holes in the bottom of the distributor [Fig. 3.1(b)]. The forcing system is versatile and allows us to inject nearly homogeneous turbulence at a scale much smaller than the system size.

Flow rates can range up to 1400 cm^3/s, corresponding to flow velocities up to 8

---

[1] Do NOT use alcohol or ammonia-based products to clean acrylic!! It will cause “crazing”, small surface cracks that seriously degrade optical quality and are very difficult to remove. We learned this the hard way.

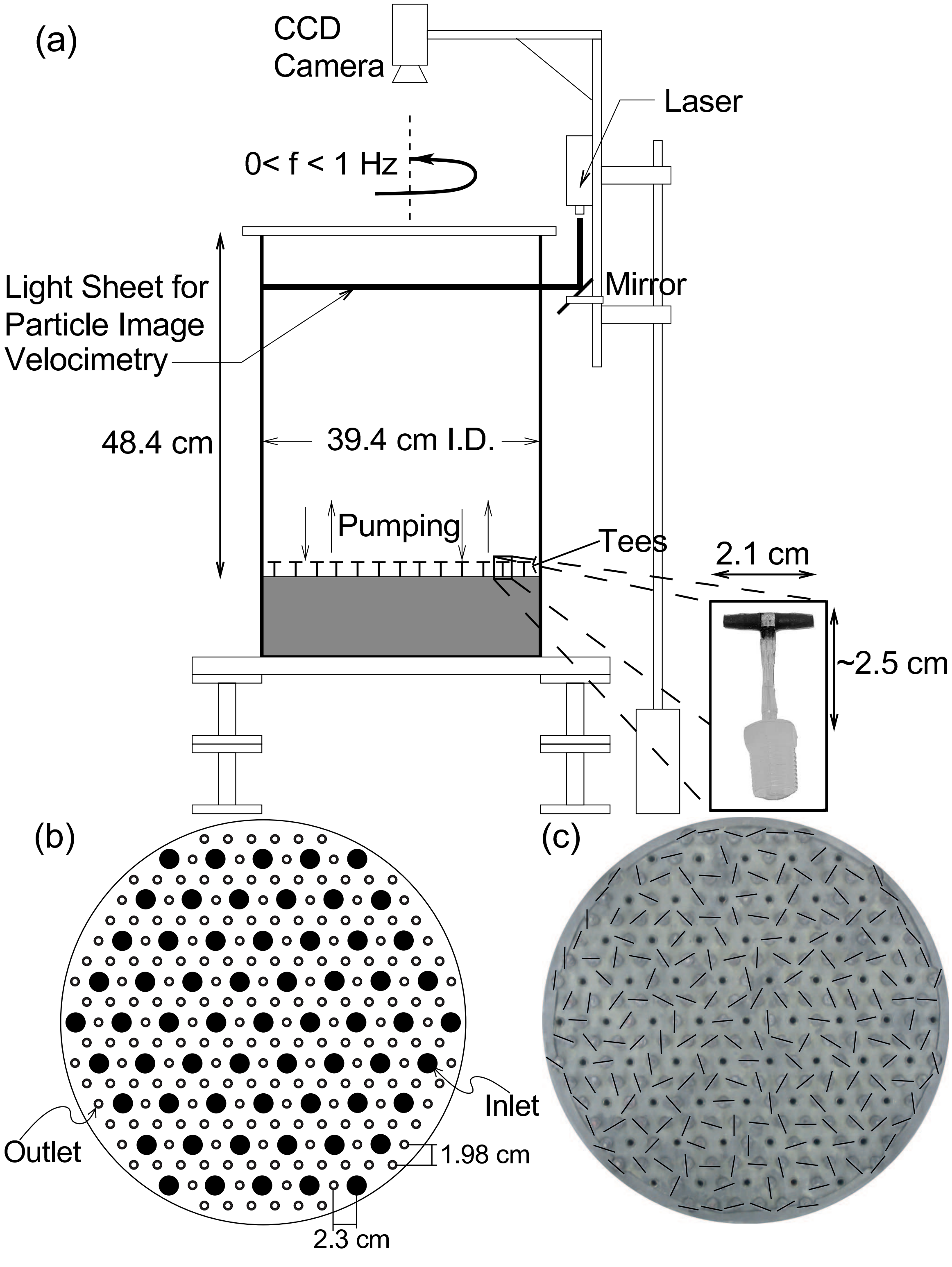

Figure 3.1: (a) A schematic of the apparatus. The height of the laser sheet is adjustable. Shown in the inset is a close-up a single tee. (b) Horizontal cross section of the distribution of pumping sources (open circles) and sinks (black dots) (positions are to scale; see text for relative size of sources and sinks and tank diameter scale). (c) Overhead image of tank bottom, showing the tees. Overlayed are lines indicating the orientation of the tees.

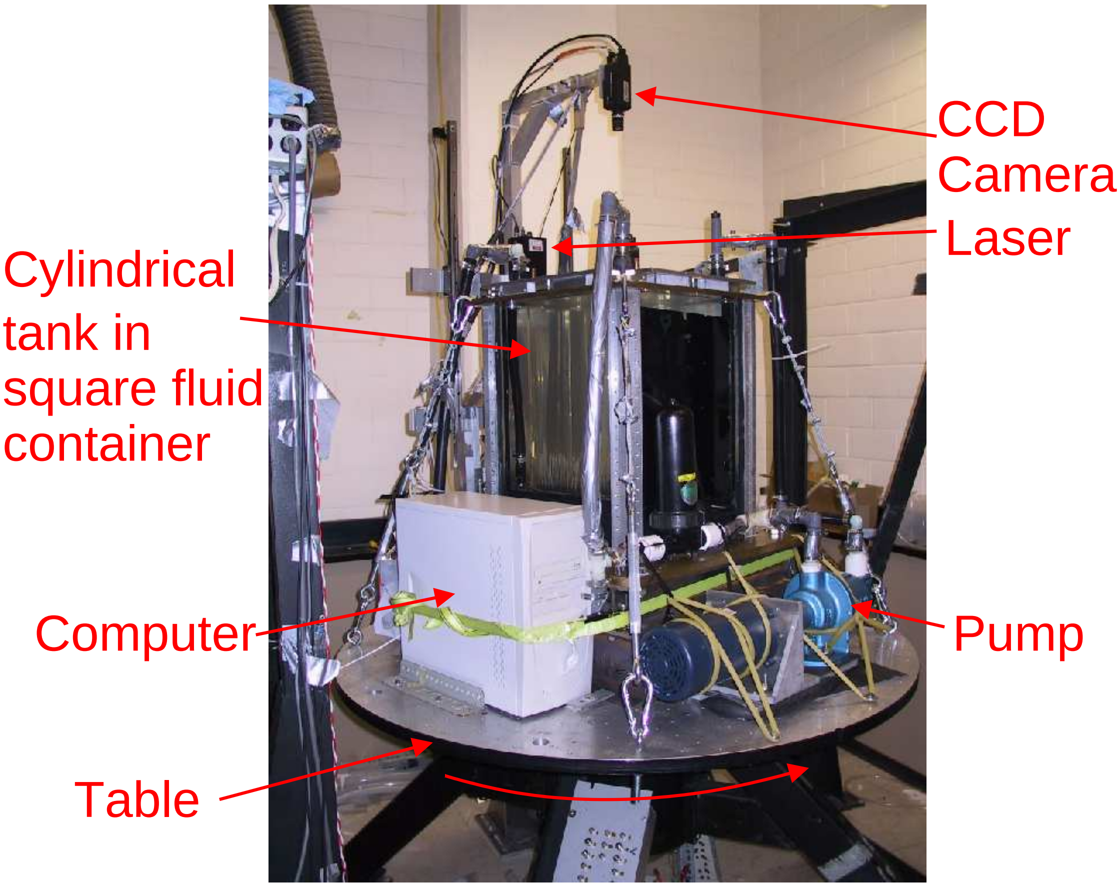

Figure 3.2: The apparatus sits on a large ≈ 1.5 meter diameter rotating table. A cylindrical tank fits inside the square box in the center of the table. The arm which holds the camera is attached to a stage which holds the laser. The stage can be moved up and down to scan the laser light sheet across the entire tank (see figure 3.1). A computer which sits on the rotating table grabs digital images from the camera. The whole apparatus is in an enclosed room within the laboratory so that we can shut out external light.

m/s out of the tees. This corresponds to a Reynolds number of order 10^5 based on the jet velocity and the grid spacing of the tees. The Rossby number, $U/2\Omega L$, based upon the same scales is order 50 near the bottom of the tank, near the forcing. However, the turbulence decays away from the forcing, with increasing height, and becomes more 2D due to the influence of rotation.

Data were taken at many different conditions. The data presented in chapter 5 are for 0.4 Hz rotation rate and flow rates of 426 cm^3/s, producing 2.4 m/s velocity jets at the forcing tees. This corresponds to Reynolds and Rossby numbers of about 6×10^4 and 20 respectively, near the forcing. Near the top the RMS flow velocity is about 2 cm/s and the maximal characteristic velocity length scale (twice the e-folding length of the velocity spatial correlation function) is about 5 cm; hence near the top the Reynolds number is about 1000. The Rossby number calculated from characteristic scales is 0.08, while the local averaged Rossby number calculated from the RMS vorticity, $(\omega_{RMS}/2\Omega)$, at such a flow condition is 0.3. The depth of our system thus allows us to observe more 3D (Rossby $\approx$ 20) or more 2D (Rossby $\approx$ 0.3) flow without changing control parameters, such as rotation or forcing.

The water is seeded with polystyrene ($\rho = 1.067$ g/cm^3) spherical particles with diameters in the range 90-106 μm. The small mismatch in density results in a sedimentation terminal velocity of 4×10^{-2} cm/s in the absence of flow, which is insignificant compared to the measured flow velocities. The density mismatch also causes a lag in the response of the particles in regions of large acceleration [94, 82]. We estimate the largest lag to be a 1% difference between the particle velocity and the flow velocity in the vortices at the top of the tank.

A 395 mW, 673 nm diode laser with attached light-sheet optics (from Lasiris) illuminates the particles in horizontal planes for flow visualization and PIV measurements. It is also possible to rotate the laser and optics by 90° to illuminate vertical planes for measurements of the vertical velocities. The thickness of the sheet is about 1 cm and varies less than 10% across the diameter of the tank. The laser is fixed to a carriage which allows

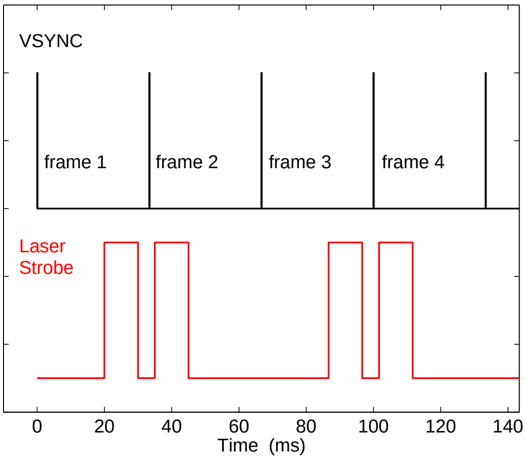

Figure 3.3: Timing diagram showing the vertical synchronization (VSYNC) pulse from the camera and the laser strobes (cf. the timing diagram in figure 3.15). The camera is operated in continuous mode and the falling edge of the VSYNC signal indicates the start of a new image frame.

us to adjust the vertical position of the light-sheet without changing the pumping rate or system rotation rate. A second laser, 1 W 532 nm (green), with light sheet optics, was added to observe simultaneously the flow in two horizontal planes (see section 3.1.10 and results in chapter 6). The position of the second laser was adjusted by hand.

Particles are imaged in the rotating frame with a CCD camera (1004 × 1004 pixels, 30 frames per second) mounted above the tank. The images are grabbed and stored into a memory buffer by a computer on the rotating table. A second, lower resolution camera with an analog output allows us to view the flow when not grabbing digital images.

The laser pulses were timed so that pairs of pulses were imaged in successive frames of the CCD camera, which had a dead time of 120 μs between consecutive frames. The pulse duration was typically 10 ms with a 2 ms dark interval between pulses.

The analog signal from the second camera and power for the equipment on the table are sent through slip rings. The entire experiment is controlled remotely with a wireless ethernet connection and remote access software (PC Anywhere[2]) by a computer in the non-

---

[2] We are currently using the built-in remote desktop software built-in to the Windows XP operating system.

rotating laboratory frame. This allows us to take multiple data sets, adjust the pumping rate, and adjust the position of the light sheet without having to stop the table.

To determine the two-dimensional projection of the velocity field we use a type of Digital Particle Image Velocimetry (DPIV) known as Correlation Image Velocimetry (CIV) [44, 43]. The CIV algorithm uses cross-correlations over small interrogation regions between a pair of consecutive images to find particle displacements over known time intervals to obtain velocities. The CIV algorithm also allows for possible rotations and deformations of the interrogation region to take into account nonlinear particle motions in between images. The resulting velocity field is interpolated to a uniform regular grid by a cubic spline interpolation. The vorticity fields are calculated from the coefficients of the spline fit.

Our maximum data rate is 15 image pairs/second, which captures the dynamics of our flow. Images were taken for 20 second periods, resulting in 300 fields in a sequence (limited by memory buffer size). Images were also taken at 1 second and 30 second intervals (longer than measured decay time for our flow) over runs of 50 minutes, sufficient for convergence of statistical quantities. Resulting velocity and vorticity fields are on a 128×128 grid with a spatial resolution of 0.3 cm and 0.19 cm when we zoom-in. We tested the CIV algorithm using simulated test particle images in known flow fields [84, 4], and found that the velocity fields determined by the algorithm have about 2% RMS (see section 3.2.1. Additional error results from perspective effects that cause apparent in-plane motions (e.g. see section 3.3.4 and references [90, 89]). The error increases with distance from the optical axis and decreases for increasing object distance. The typical velocity (vorticity) error is about 15% (35%). Given specific statistical values from measurements should therefore be taken with a grain of salt (as should all PIV measurements without corrections for stereoscopic effects). However, this systematic error does not affect our data analysis and it does not change the main results of our work.

3.1.2 A brief history of the apparatus

Our system sits on a large rotating table which was originally built circa 1981 by Andereck *et al.* for use in a Taylor-Couette experiment [11]. The table was abandoned after the Taylor-Couette experiments and was not in use throughout the 1990's[3]. The table was resurrected in 1999 by Weber[4] and the author. The objective was to build quickly a rotating turbulence experiment to observe the formation of zones from small scale isotropic forcing, in accord with the theory of Marcus [74]. However, it was found that the size of the smallest zones that would be produced were on the order of the size of the apparatus.

The experiments by Weber were conducted in a square tank with an oscillating grid [124], visualized with kalliroscope and illuminated by a LED light sheet. Measurements by ultrasound doppler velocimetry were also made[5]. Soon afterwards, an inner cylinder and laser light sheet were added, the grid was replaced by pumping to produce more turbulence and DPIV became the primary measurement technique.

During the next five years one visiting professor, two postdoctoral researchers, and two French students made contributions[6], in addition to the author. The experimental apparatus has been continually modified and improved since its resurrection. It should be noted however that, while the current incarnation of the experiment works well, there is still room for improvement (e.g. see section 3.3).

3.1.3 Table

The table is driven by a Compumotor stepper motor. The motor sits on the floor next to the table. A large pulley belt provides the transmission between the stepper motor and the table with a gear ratio of 6 : 1. A Compumotor 172 indexer provides the digital control pulses for the stepper motor. A Compumotor M106-178 stepper motor driver amplifies the

---

[3] During this time the room in which the table sits was used as storage space for equipment from other experiments.

[4] Thomas Weber was a Master's student from the University of Würzburg. He graduated from the University of Texas in 2000.

[5] However, such measurements are highly unreliable for turbulence statistics due to the volume averaging used by the ultrasound doppler velocimeter.

[6] All are acknowledged in the acknowledgements.

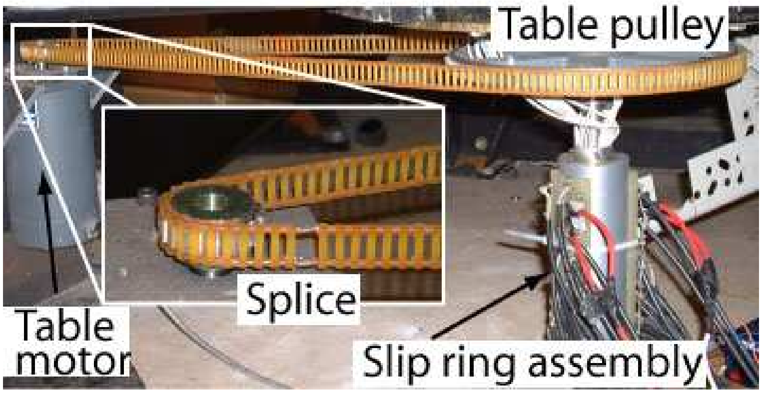

Figure 3.4: Underneath the table. The table motor drives the table via a timing belt connected to the table pulley. There is a gap in the belt where it has been spliced together that results in periodic forcing of the table oscillation (e.g. see section 3.3). The slip ring assembly is directly underneath the table pulley, connected to the shaft of the table. The bottom of the slip rings is about 4 cm from the floor.

pulses from the indexer and powers the stepper motor.

To keep the table rotating smoothly, two large bearings in the table must be greased periodically. The table has not yet been balanced due to the continual modifications to the apparatus. However, before we consistently rotate near 1.0 Hz, it is imperative that it be properly balanced.

The rotation rate of the table is not steady, shown in figure 3.5). This is due to the elasticity of the belt and the splice (see figure 3.4). We have made some effort to eliminate or reduce the table oscillation by tightening and shortening the belt. However, we have heretofore been unsuccessful in significantly reducing or changing the peak frequency of the oscillations. This is discussed in detail in section 3.3.

Getting signals to and from the table

Power and some electronic signals are transferred to and from the rotating table through a custom assembly of slip rings manufactured by Fabricast. There are 30 signal rings, 22 of which are rated for 5 amps and signals up to 20 MHz, 8 of which are rated as 75 Ohm coax. The slip ring assembly is located underneath the table (see figure 3.4.

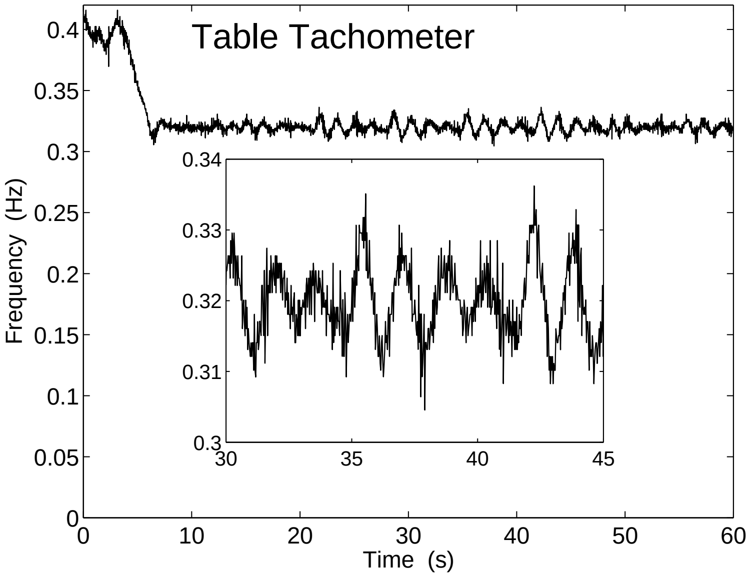

Figure 3.5: One minute time series of the table tachometer. This was taken during a spin-down experiment where the table rotation rate was decreased by 10% at about t = 4 seconds. The largest fluctuations are about 5% peak-to-peak with about 1% RMS. We attempted to decrease the oscillations by loosening and tightening the belt between the table and the motor. However, we have had limited success in eliminating the oscillations. Inset is a zoomed view of the time series from 30-45 seconds, showing the largest fluctuations. These oscillations are present in the velocity data with the same period.

The number of connections are limited so our image acquisition and laser control is done entirely on the table. Additionally the slip rings are electrically noisy[7] and thus unsuitable for transferring data signals. We control the computer on the rotating table remotely via a wireless and remote desktop software[8]. After the completion of the experiment, the table is stopped and the data are transferred to a computer in the lab frame on a LAN cable[9].

---

[7] These slip rings are also acoustically noisy, producing a whistling sound as the table rotates.

[8] We had used the commercially available software pcAnywhere$^{\text{TM}}$, however, we have recently switched to the remote desktop utility that is included in the Windows XP operating system.

[9] We had to wire specially the LAN cable as crossover cable to directly connect the two network cards.

3.1.4 Tachometers

A "homemade" tachometer for the table was made from a proximity detector. The pulley on the table has 120 teeth. By setting the proximity detector close enough to the pulley, the teeth and spaces in between can be detected as it rotates. In this way, we can get 120 pulses per revolution of the table. The period of the pulses is measured by a general purpose counter on a National Instruments PCI-6601 data acquisition (DAQ) card. Each pulse therefore corresponds to a frequency measurement ($f_{table} = 1/120 * period$) and the period is recorded as the time in between measurements.

It was found that the output of the proximity detector was jittery which produced many spurious frequency measurements. Using a DM7414 inverting Schmitt trigger to buffer the output signal eliminated this problem.

A tachometer for the pump was made from an optical interrupter. A ring was attached to the shaft of the pump and a set screw in the ring stuck out far enough to trigger the optical interrupter once per revolution of the pump shaft. The output of the optical interrupter was also buffered by a DM7414 Schmitt trigger after going through the slip rings to eliminate spurious counts due to noise.

3.1.5 The working fluid medium

The tank is filled with distilled water. The total volume of our system is about 90 liters. The density and kinematic viscosity of water at ambient laboratory temperature ($\sim 23°$) are $\rho = 0.998$ g/cm^3 and $\nu = 0.0095$ cm^2/s respectively[10]. The temperature of the water can change from the heat generated by the mechanical friction of the pump and motor. Under usual operating conditions for the experiments conducted, the water does not heat up significantly as the pump does not run continuously and the pump is allowed to cool in between experiments. However, for steady state experiments the water can heat up by a few degrees, which results in a change of the kinematic viscosity by about 5%. The temperature is not monitored, but the apparatus sits in thermal equilibrium with the laboratory which

---

[10] The values were found in tables of reference [46]

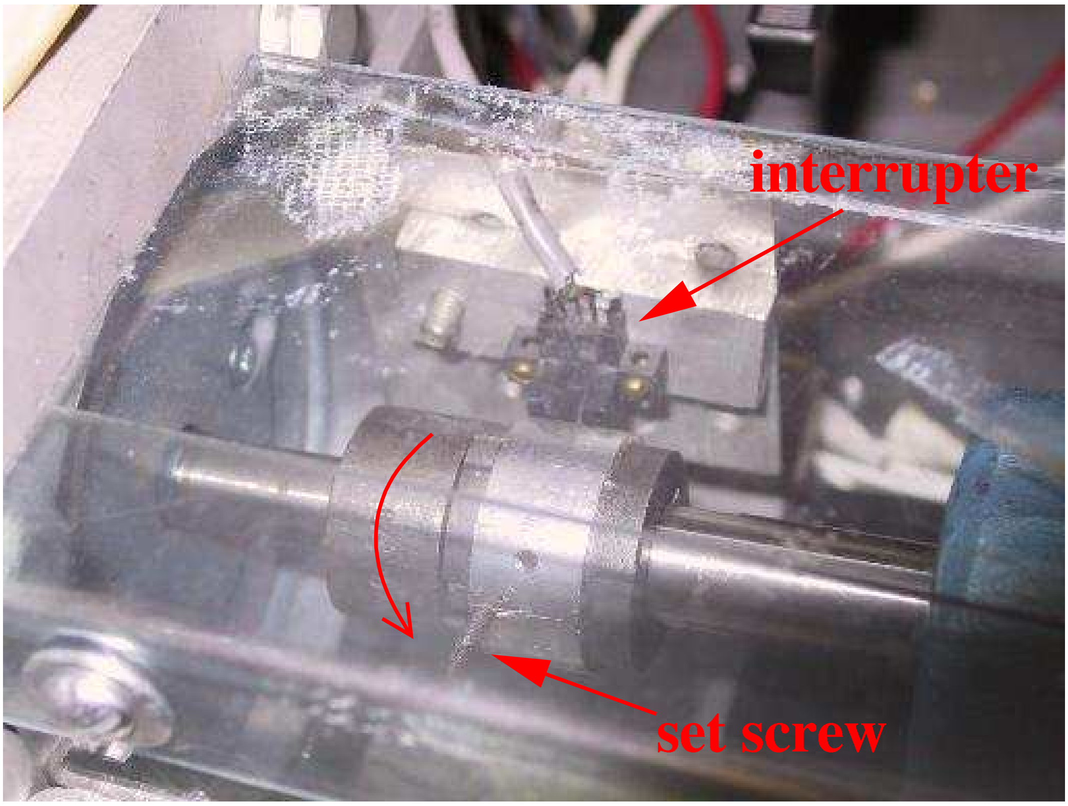

Figure 3.6: Our “homemade” pump tachometer setup. The ring with the set screw fits over the coupling between the shaft of the motor (on the left) and the shaft of the pump (on the right). The optical interrupter (black with the grey wire attached) sits on a piece of aluminum attached to the block which the motor is mounted. A transparent plastic cover is in place as a safety precaution against accidents.

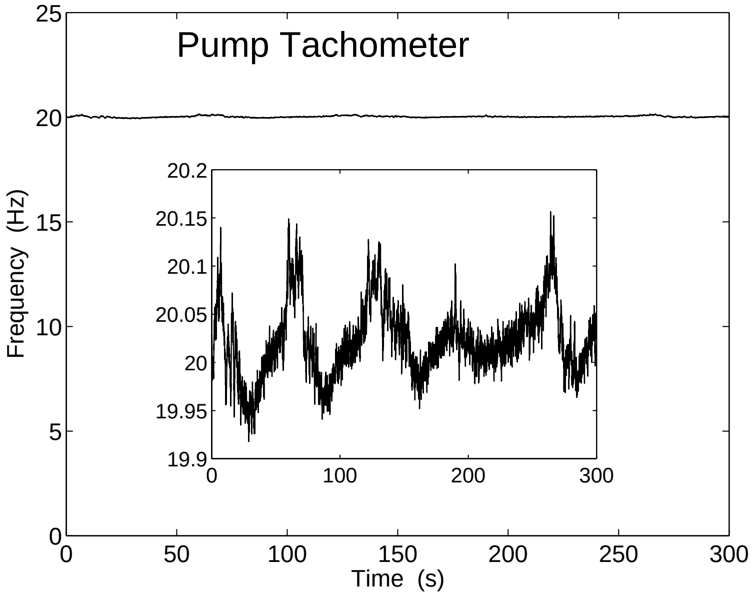

Figure 3.7: Five minute time series of the pump tachometer. Currently, there is no feedback of the pump rotation rate to the power supply. However, the fluctuations are only on the order of 1.2% peak-to-peak with a 0.7% RMS. Inset is a zoomed view of the fluctuations over the whole time series.

is maintained at a roughly constant temperature.

Typical maximal velocities achieved in our system are about 10 m/s which occur at the Sprinkler. Given the sound speed of water at room temperature as $c = 1488$ m/s, the maximum Mach number $M = V/c = 0.007 << 0.3$. This combined with the fact that there are no significant pressure variations in the cylinder itself means that we can treat our flow as incompressible.

Since our flow is incompressible and we use a homogeneous medium there will be no significant density variations. Thus stratification will also be unimportant.

The distilled water added initially contains a substantial amount of dissolved gas. Due to large differences in pressure between the Sprinkler and the cylinder (the pressure difference can be up to 35 psi), dissolved gas in the water undissolves and forms bubbles. Additionally, if the pump is run continuously at a high speed for an extended period of time, the water will heat up significantly, which also releases bubbles. These bubbles stick to the interior surfaces of the tank and interfere with visualization. In an extreme case, a maximum temperature of 39.5° C was recorded after running the pump for over 8 hours. This could possibly be used in the future as one way to increase the possible Reynolds number without changing the fluid. After changing the water in the tank, the pump is run continuously, heating the water to degas it prior to running experiments. In the future the water will be degassed by putting it in a low pressure before being transferred into the tank.

A capful of a surfactant (Kodak Photo-flo 200 solution) is added to the water to help prevent the adhesion of bubbles onto the interior surfaces of the tank. This surfactant also allows the particles to mix with the water rather than to remain stuck on the surface.

A small amount of chlorine is also added to prevent the growth of bacteria and algae. As a further precautionary step, the lights in the room with the apparatus are kept off when not in use to limit the amount of input energy available for growth.

3.1.6 The Sprinkler

The previous incarnation of the experiment was driven by an oscillating grid (see [124]). This was found to be an inefficient driving mechanism. Bars on a grid moving relative to some fluid shed vortices. These vortices contain much of the kinetic energy injected by the oscillating grid. The problem was that vortices of one orientation are produced on the up stroke of the grid are annihilated by vortices of the opposite orientation produced on the downstroke of the grid if they do not move out of the way in time. In order to inject more energy, the frequency of the grid must be increased which allows for less time for the vortices produced to migrate away from the grid before being wiped out. Thus, the majority of the energy injected into the flow by the grid was put into viscous dissipation at the grid.

With the current driving system we drive flow in the tank directly by circulating fluid through an array of sources and sinks [see figure 3.1 (b)], known as the Sprinkler. This method of driving is much more efficient at injecting energy into the flow since we control the flow rate through a known area which directly injects fluid of known kinetic energy.

We drive fluid at a known flow rate, Q, using a Moyno positive displacement 1750

RPM pump. The pump is driven by a 3/4 Hp Leeson DC motor which is powered by a Sorensen DCR150-18B DC power supply. We can control the power supply remotely by computer via a 0-10V analog input voltage generated by a National Instruments PCI-6024E data acquisition (DAQ) board.

The pump is capable of driving flow rates up to 1400 cm^3/s. At the bottom of our tank is the two chamber black box known as the Sprinkler. The upper chamber is connected to the high pressure input nozzles. The lower chamber is connected to the low pressure return sinks. Both chambers are made large so as to not create any pressure drop between the outlets; all the pressure drop occurs between the inside of the box and the inside of the tank. The fluid is forced out through nozzles (or tubes) of a known cross sectional area, A. The velocity of a jet exiting the nozzle is

$$u_{jet} = Q \cdot A \tag{3.1}$$

The total energy injection rate into the flow (of density ρ) due to our array of jets is

$$\dot{E}_{injection} = \frac{1}{2}\rho\frac{1}{A_t^2}Q^3 \tag{3.2}$$

where A_t is the total area of all the jets combined.

We do not want to impose any structure artificially on the flow. We ideally want to impose only small scale isotropic forcing. Then the physics will dictate the scales of the structures in the flow and not the geometry of the forcing. This may be achieved by placing flexible tubes over the end of the nozzles. Above a critical flow rate which depends on the flexibility and length of the tube it will become unstable and start to flip. A photograph of the tubes undergoing this instability is shown in figure 3.8. This flipping motion tends to make the forcing random in space and in time without any large scale structure. Thus we are able to provide small scale isotropic forcing.

However, it was found that we had unexpectedly large vertical velocities (e.g. see [99]). We initially thought that this might have been due to the tubes, which often point upwards.

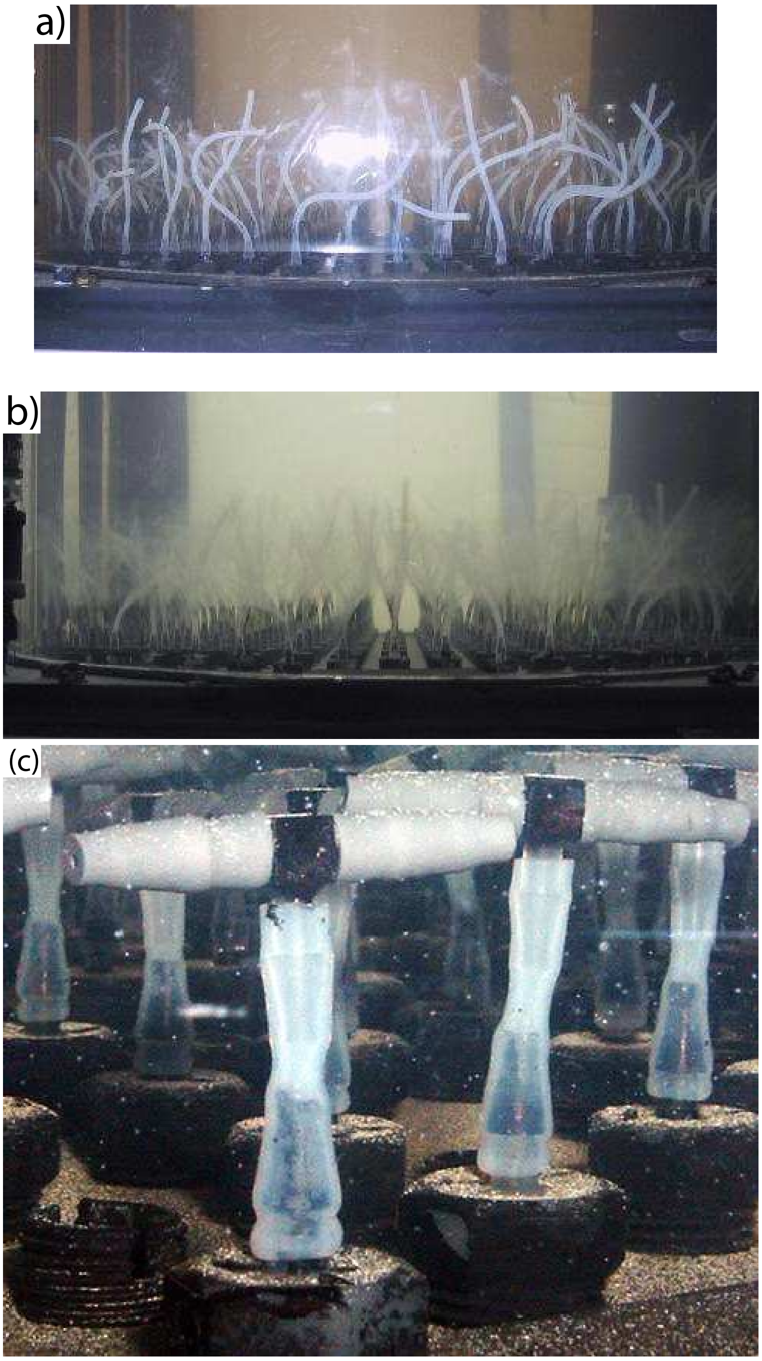

Figure 3.8: The Sprinkler's tubes: (a) 1/100 second exposure of the flexible tubes at a flow rate (typically > 1000 cm^3/s) in which the tubes are unstable, (b) 1 second time exposure of the same condition. The motion of the tubes blur them in the photograph giving an indication of how the tube instability randomizes the forcing and makes it more homogeneous. (c) Closeup of the tee connector used that produces primarily horizontal velocities [cf. figure 3.1 (c)]. To the left of the tee in the foreground is a sink (a return hole for the fluid).

Because of this we switched to tee connectors on the outlets of the Sprinkler (see figure 3.1 and 3.8). The tees have have the same interior diameter as the tubes but have twice the total output area. Most of the results presented were taken with the tee connectors. However, it was found that the tee connectors produce persistent structures in preferred locations (e.g. see chapter 4). In the future we will return to the flexible tubes.

3.1.7 Flow visualization

We visualize the flow by seeding it with small tracer particles. A horizontal light sheet illuminates the particles. The light sheet is provided by the Magnum 500 mW[11] DS model laser from Lasiris. It is a 673 nm, 380 mW diode laser with collimating optics attached to the front end to generate a light sheet. The beam profile is gaussian perpendicular to the plane of the sheet and roughly flat with large side peaks at the edge in the plane of the sheet (the side peaks were blocked out in the experiments). The focus and thickness of the light sheet can be adjusted by the optics attached. In addition, the laser can be operated in CW or pulsed mode [56].

3.1.8 Digital imaging

The camera used to grab digital images of the particles is a Cohu 7712 10-bit CCD camera. The maximum frame rate of the 7712 is 30 frames per second at a resolution is 1004x1004 pixels (in practice we are limited to 997x1004 by an incompatibility with the frame grabber). A logarithmic look up table (LUT) is used, instead of a linear LUT. This reduces problems of particles 'blinking' as they pass by the periphery of the light sheet.

The frame grabber is a National Instruments PCI-1428. The frame grabber has 4 trigger channels which can be used as triggers, drive signals (i.e. vertical sync), or generate triggered pulses. We configured line 0 to monitor the vertical sync signal from the camera. Line 1, acting as the first laser strobe pulse, was configured as a delayed pulse to be triggered by the vertical sync line (line 0). Line 2, the second laser strobe, was configured as a delayed

---

[11] "500 mW" is part of the model name and does not correspond to the actual diode output power.

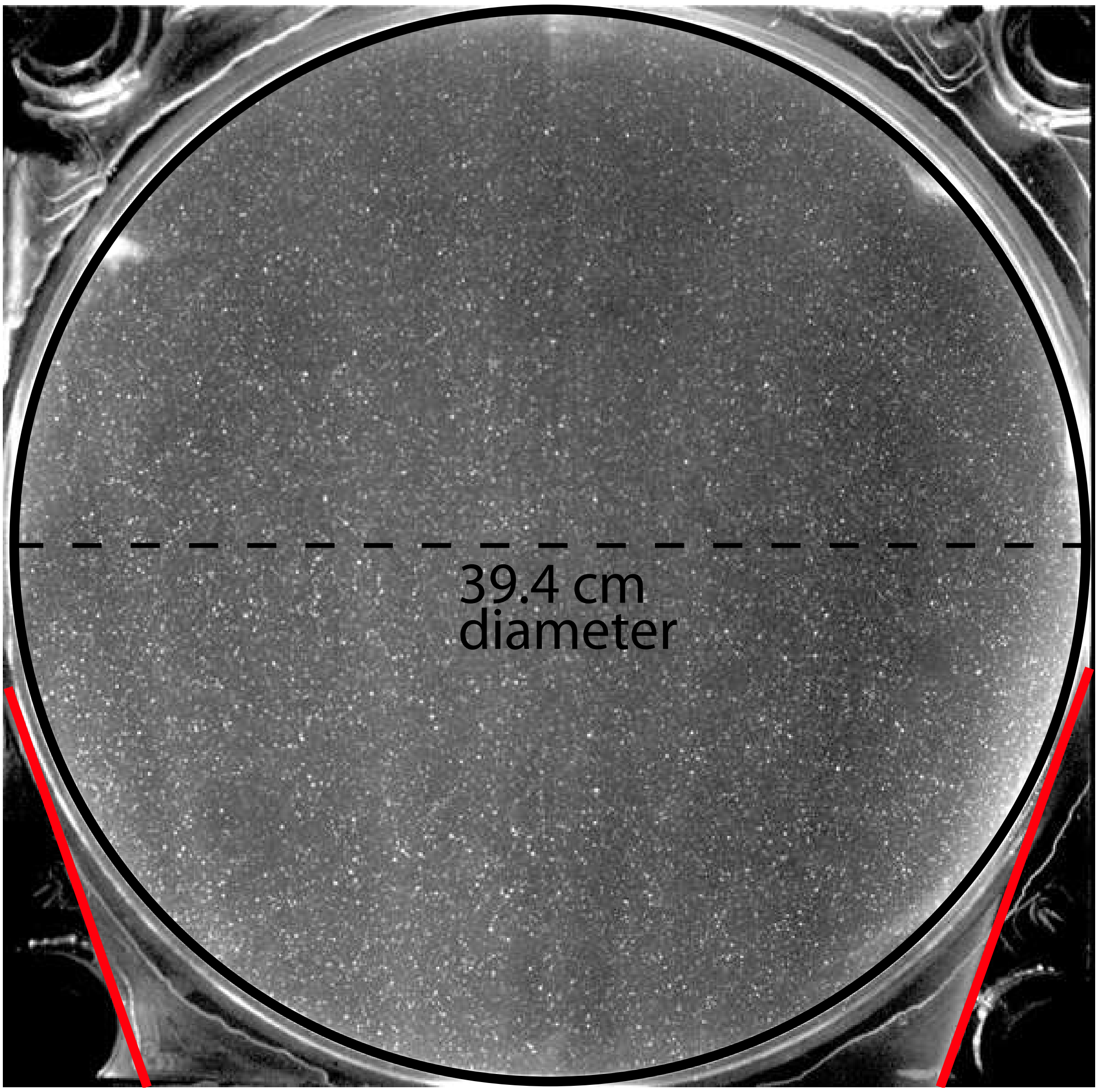

Figure 3.9: Overhead snapshot of flow with tracer particles: Size ≈ $100\mu m$, $\rho \approx 1.062$ gm/cm^3. The laser sheet enters the cylinder from the bottom of the picture. The solid black line outlines the wall of the cylinder at the height of the laser sheet. The red lines indicate the edge of the laser sheet.

pulse to be triggered off of line 1 with a delay specified as the desired separation between pulses. The desired width of the pulses is also an input parameter with 20 nanosecond resolution. Typical values were 10 ms pulse width with 12 ms pulse separation. The two pulses were then sent through a NOR gate to output the multiple pulses on a single signal line.

Additionally, we implemented the PCI-6601 counter/timer to monitor the pulses going to the laser. When grabbing starts the PCI-6601 records the times of the laser strobes to within 50 ns resolution.

The first DPIV was performed using a Cohu 6600 CCD camera with resolution of 465 × 658 pixels. However this camera, in addition to its low resolution, had timing and "jitter" problems (see [99]). The camera is now used as a video camera to observe the flow when not taking data. The analog output of the camera is sent through the slip rings and into the RCA input of a television monitor in the laboratory.

3.1.9 Tracer particles

In order to extract information about the flow, we must be able to visualize it. This can be done by seeding the flow with small tracer particles with an index of refraction different from that of surrounding medium. The tracer particles can then be illuminated by a light source and the flow can thus be observed.

An important constraint on the tracer particles is that they must faithfully follow the flow. The fluid will exert a drag force on any object which is placed in its path. The coefficient of drag C_D is defined as the ratio of the drag force F_D to the force due to the dynamic pressure on the cross sectional area A at velocity U, [46]

$$C_D = \frac{F_D}{\frac{1}{2}\rho U^2 A} \tag{3.3}$$

In the limit of an infinite drag coefficient (and thus infinite drag force or infinitesimal fluid velocity), the particles will exactly follow the flow. At low velocities, the drag force on a smooth sphere, as determined by Stokes is known. This allows us to calculate a lag velocity U_s, due to accelerations which will be [94]

$$U_s = \frac{d^2(\rho_p - \rho)a}{18\mu} \tag{3.4}$$

where d is the size of the particle with density ρ_p, ρ is the density of the fluid medium with dynamic viscosity μ, and a is the acceleration that the particle feels.

In order for the particles to faithfully follow the flow this quantity must be as small as possible. This is achieved by matching the density of the particles to that of the fluid medium ($\rho_p - \rho = 0$) and also by making the particles small. This set limits on the accelerations which we can measure in the flow. For the particles we used in the experiments an overestimate of the maximum lag velocities is about 1% of the fluid velocity while typical values are 0.01%- 0.1%.

Replacing a with the gravitational acceleration, g, in the above equation we can calculate velocity with which the particles settle to the bottom of the tank (sedimentation velocity).

Two different tracer particles were used in the experiments.

Tracer Particles # 1: Pliolite

The first tracer particles used are a white polystyrene manufactured by Goodyear, called Pliolite VT. The density of the polystyrene is $\rho = 1.026$ g/cm^3. Figure 3.10 shows some magnified Pliolite particles. These are the same particles used in Baroud's experiments [12]. The Pliolite, shown in magnification in figure 3.10, is supplied as a polydisperse powder and individual particles can be from $< 1\mu$m to ≈ 1 mm in size. We sieve the particles to obtain a size range of $100 - 140\mu$m and $140 - 180\mu$m batches. After the sieving process, the dry particles are washed with water through a 5μ m filter in order to remove smaller particles which are not eliminated by the sieve. The smaller particles are not resolvable by our camera and instead appear as “dust” which reduces the contrast of our images. Figure 3.9

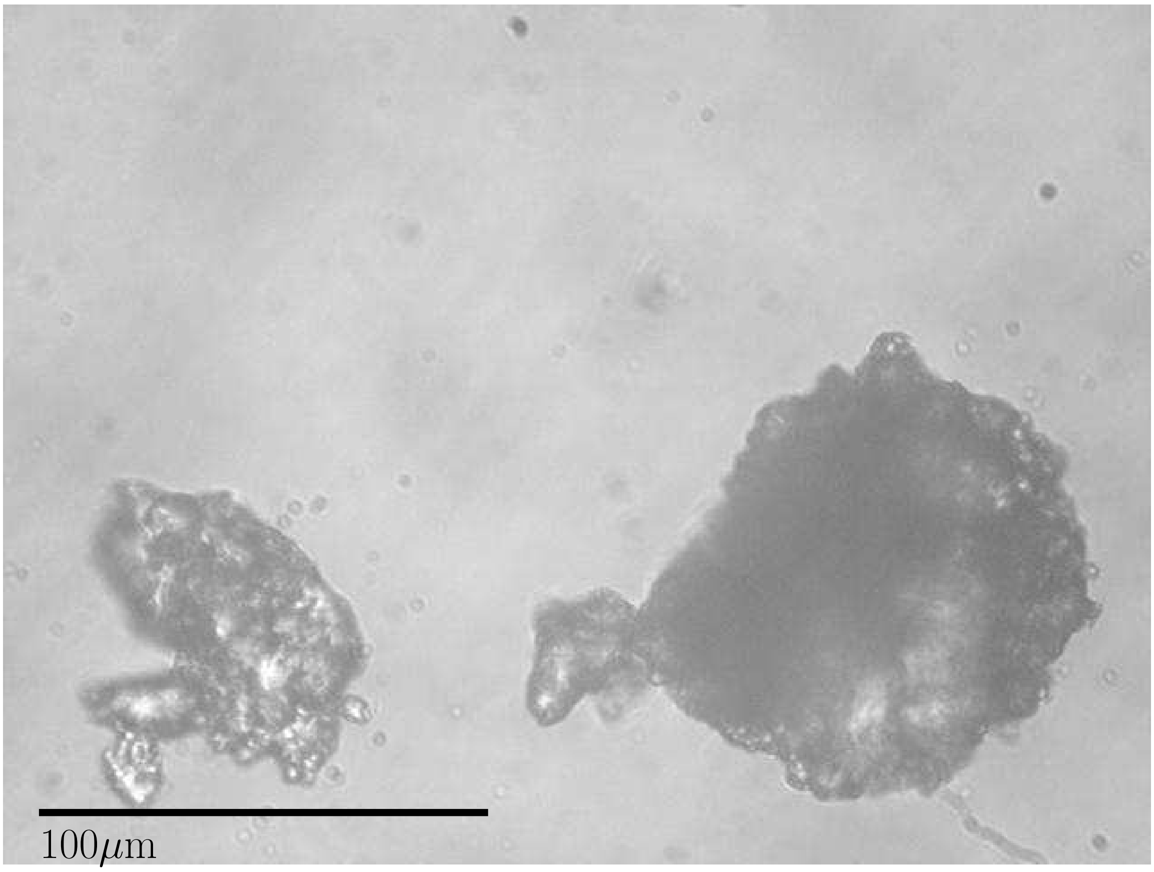

Figure 3.10: Pliolite particles under the microscope. The Pliolite particles are very nonuniform and in fact are difficult to distinguish from dust particles. These particular particles came from a batch which had been sieved to sizes $100 - 140\mu m$, however the particle on the left is obviously smaller. This indicates that the sieving process is imperfect as smaller particles remain. Notice the protrusions on the particles. It is thought that these break off, further reducing the size of the main particle and contributing to the background "dust".

shows a snapshot of a typical flow.

The particles can be segregated by their sedimentation times by carefully pouring them into a large container and then waiting for the "heavy" particles to sink to the bottom and the "light" particles to float to the top. Particles in the earlier experiments were first poured into a 500ml graduated cylinder. The particles remaining in the center after 10-15 minutes were extracted via pipette. Later experiments used a 1.5 liter glass cylinder with a stopcock attached to the bottom in place of the graduated cylinder. Particles which settled to the bottom could be slowly extracted by opening the stopcock and collecting them in a flask, leaving behind more neutrally buoyant particles.

Because the Pliolite came in a polydisperse power with a very large size range, it was extremely time consuming and difficult to obtain a sufficient quantity of $100 - 140\mu$m sized particles for a good seeding density. To speed the process, we decided to crush the larger pieces using a mortar and pestle. This allowed us to obtain far more smaller sized particles.

Using the above process allowed us to obtain good seeding densities in less time. However, several hours after adding the particles to the tank, the particles would seem to "disappear". The seeding density would decrease significantly and the background would increase. We first thought that this might be due to the particles sinking (since this would happen on a similar timescale as the settling velocity) and then sticking to the floor of the Sprinkler. So we ran the pump periodically in attempt to keep the particles stirred up. The problem, however, persisted. Finally, after using a zoom lens we noticed that the seeding density was much higher than that observed without the zoom lens. In other words, we had many particles which were not resolvable without the zoom lens. What is thought to have happened is that during the crushing process many particles were cracked or weakened. While circulating through the pump, these particles would eventually break apart into smaller and smaller particles which would then appear as "dust". Thus the seeding density would appear to decrease and the background contrast would worsen.

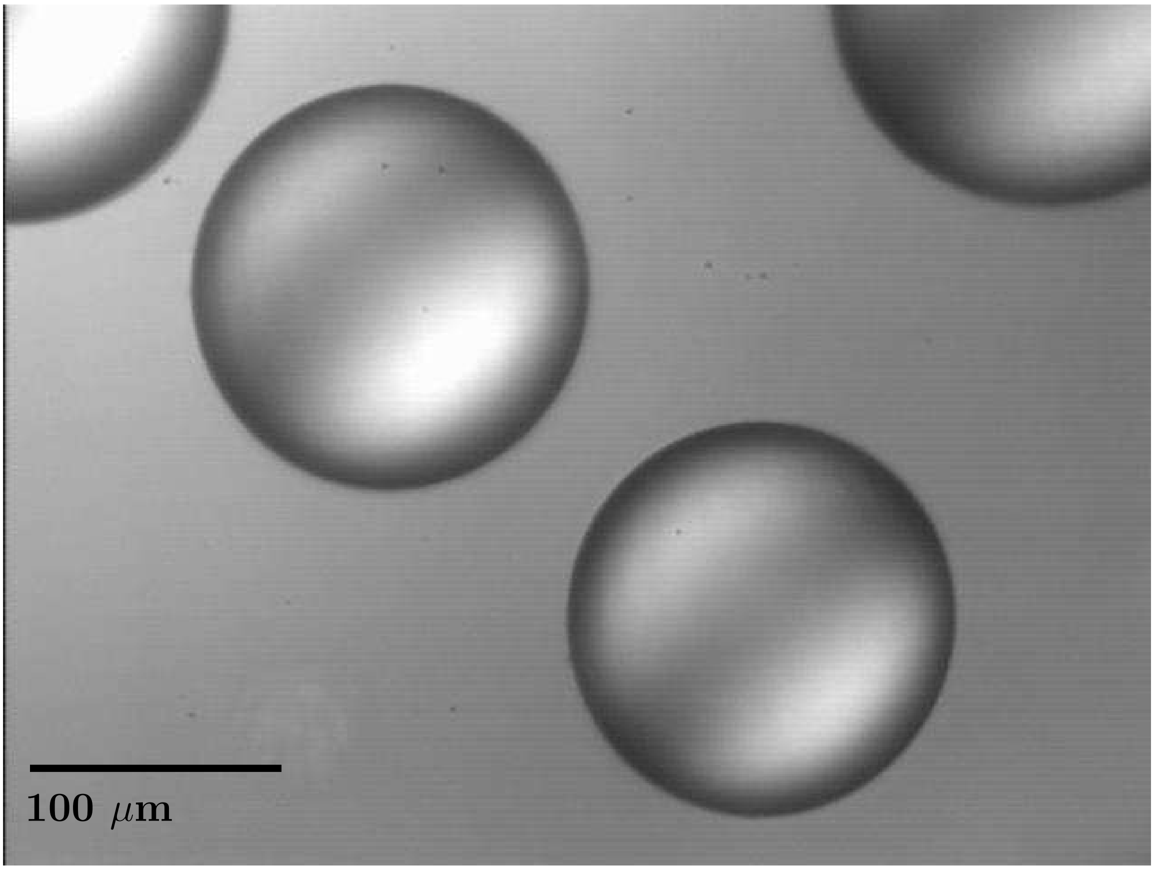

Figure 3.11: The polystyrene microsphere particles from Bangs Laboratories. These particles are very uniform in size and shape. Additionally, they are very robust and have been qualitatively empirically tested by shearing and compression as well as being circulated through our pump. Shearing by hand between two glass slides appears to do very little harm to the particles. Under extreme conditions, it can lead to cuts in some particles. Compression by hand between two glass slides tends to pancake the particles. Microspheres left in the tank for two months (which would allow for the water to circulate through the pump approximately 10,000 times) were not found to have any significant damage. The microspheres did not degrade significantly or break up over the lifetime of the experiments. Furthermore, the particles were relatively easy to stir up after they had settled to the bottom of the tank

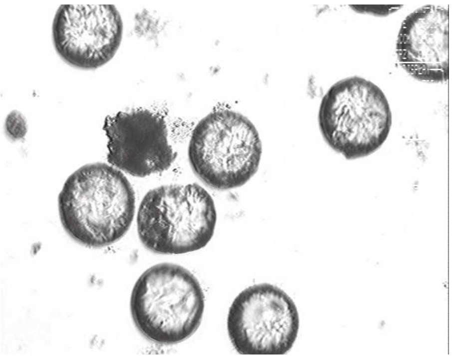

Figure 3.12: Aged polystyrene microspheres. The surfaces show scoring and some deformation. However, the microspheres are generally in good shape even after recirculating many times through the pump. cf. figure 3.11.

Tracer Particles #2: Polystyrene Microspheres

Due to the problems with the Pliolite we decided to use different particles. After a lengthy search, we found an adequate replacement. The replacement particles are polystyrene microspheres supplied by (not manufactured by) Bangs Laboratories. The microspheres, shown in Figure 3.11, are supplied as a dry powder and the particular batch obtained was pre-sieved to a size distribution between $90-106\mu$m with a mean diameter of 98μm. The microspheres have a density of 1.067 g/cm^3. This results in a sedimentation velocity of about .4 mm/s in the absence of flow. 10% di-vinyl-benzene is used as a cross-linking agent to make the microspheres more robust. The microspheres also have SO_4 groups attached which cause them to have a net negative charge. This prevents the particles from sticking together or to other surfaces, such as the bottom or the wall of the tank. Furthermore, the polystyrene microspheres were found to be fairly robust and aged well (see figure 3.12).

3.1.10 Dual light sheet

The velocity field was simultaneously determined at two vertically separated horizontal planes in the tank. The correlation of the velocity field in the two planes was computed to obtain quantitative measurements of the two-dimensionality of the flow. The apparatus was modified to make these measurements. The resulting apparatus is shown in figure 3.13.

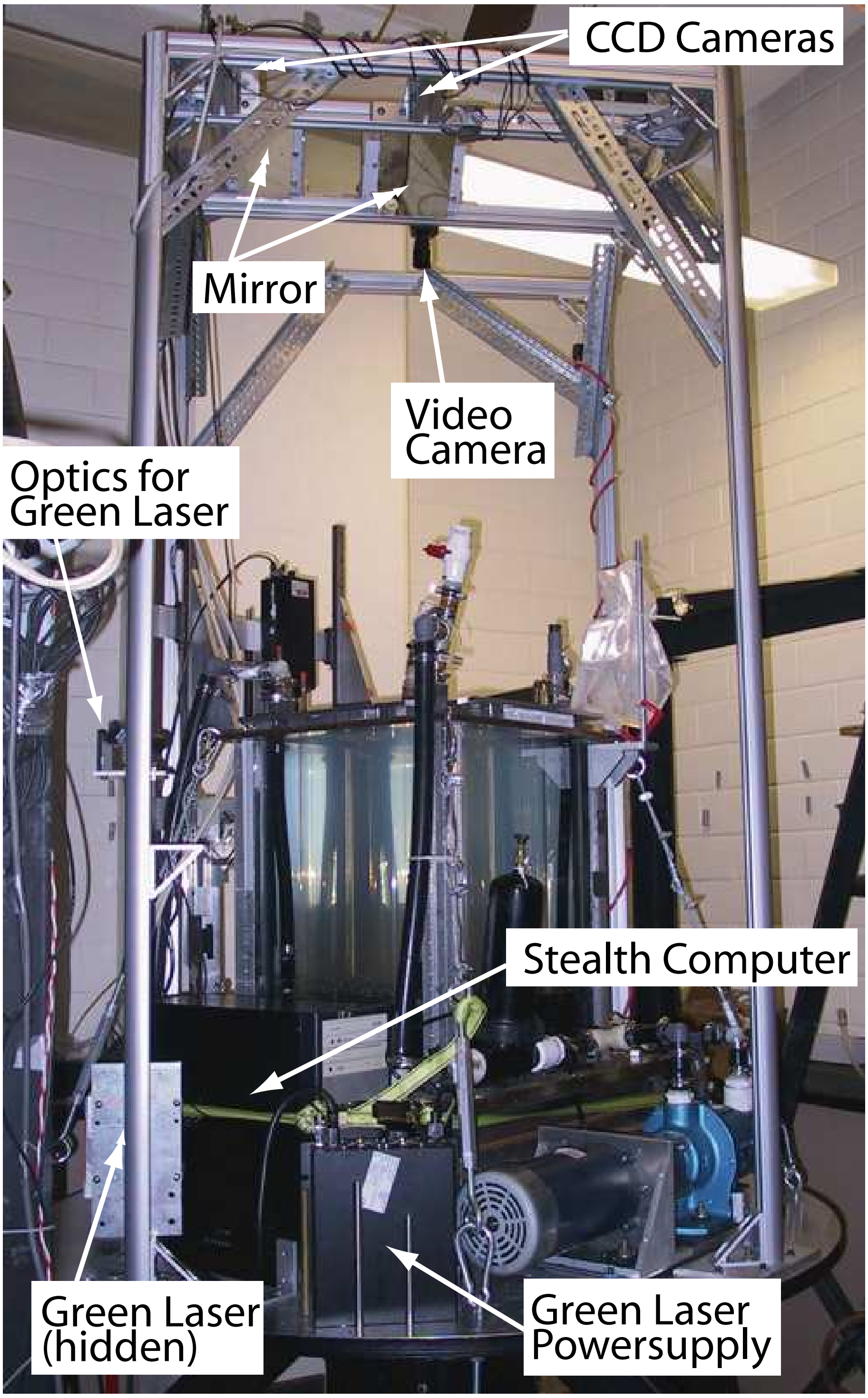

Figure 3.13: The apparatus after modifications for dual laser sheet operation. The additional support structure was added to accommodate the two cameras above the tank. The cameras (see figure 3.14), partially hidden by the support structure, view the tank via mirrors. A third video camera above the center of the tank allowed us to observe the flow when not strobing the lasers. cf. figure 3.2.

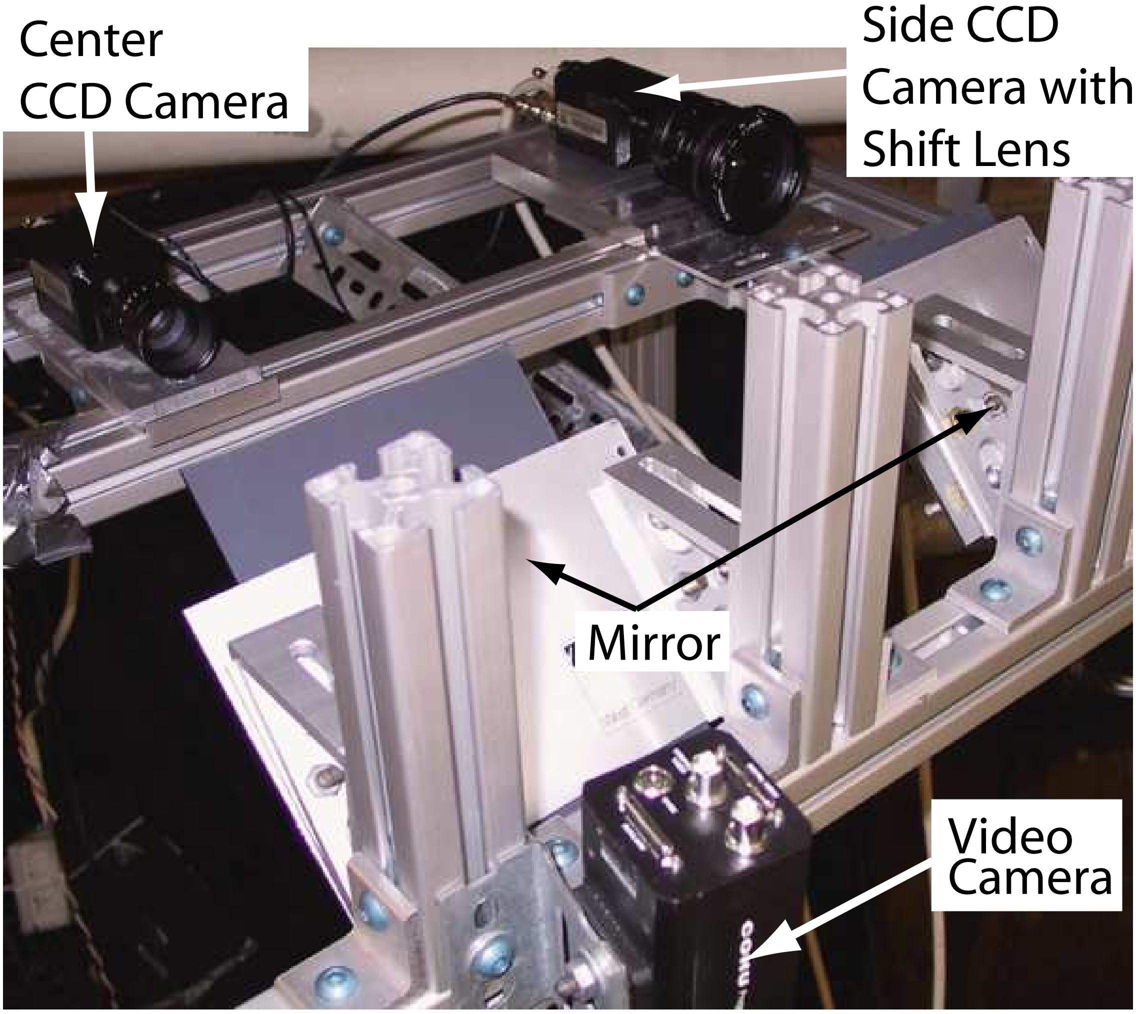

Figure 3.14: The CCD cameras above the tank. The two CCD cameras used to take data point at mirrors roughly oriented at 45 degrees to image the tank. The side CCD camera uses a special shift lens that allows the tank to be centered in the image without having to tilt the CCD image plane. The center video camera has an analog output that we send through the slip rings. This allows us to observe the flow when not taking data.

A 1 W 532 nm (green) Excel 1000 laser was added to the apparatus to provide light for the second sheet. Light sheet optics were custom manufactured and designed by Brighton Optics, Ltd[12]. The optics consisted of a single lens to expand the diameter of the laser beam and a single cylindrical lens to spread the beam out into a sheet[13].

Images were captured from the second plane using a second Cohu 7712 CCD camera and National Instruments PCI-1428 frame grabber. A support superstructure was constructed from T-slotted aluminum to hold the two cameras above the tank and to hold the optics for the green laser. The cameras view the tank from mirrors to increase the working distance and to decrease the stereoscopic error (see section 3.3.4). A shift lens allows us to place one camera off axis and still center the view of the tank without having to sacrifice pixels or to tilt the orientation of the cameras.

Wavelength selecting filters were placed in front of the cameras to segregate the light from the two laser light sheets. A short-pass (long-pass) filter was used for the camera that collected data from the green (red) light sheet. Each filter had $> 90\%$ transmission at the desired wavelength and $\approx 0\%$ transmission at the wavelength to be blocked.

It was necessary to synchronize the cameras to measure the velocity field at the same instance by both cameras. The cameras were run in "snapshot mode" which accepted trigger inputs that control the electronic shuttering. The timing diagram for triggering the cameras is shown in figure 3.15. The cameras are normally triggered by sending a trigger signal into the frame grabber which in turn sends the trigger to the camera. The frame grabber thus acts as a hardware "gate" and does additional checks to determine whether or not the camera should be ready for the trigger. However, sending triggers through the frame grabber did not result in the camera being triggered at the appropriate times, due to an incompatibility between the Cohu 7712 cameras and the National Instruments PCI-1428 frame grabbers. Instead, the frame rate was limited to 15 fps with a dead time of 1/15 seconds in between frames. To resolve this problem, the cameras were modified by rewiring

---

[12] The custom design consisted of the housing of the optics. The cost was much cheaper than similar commercially available light sheet optics from flow visualization companies such as Dantec and LaVision.

[13] The light sheet is not uniform and is much brighter in the center than at the edges. This causes a significant decrease in the signal to noise ratio outside the center of the tank.

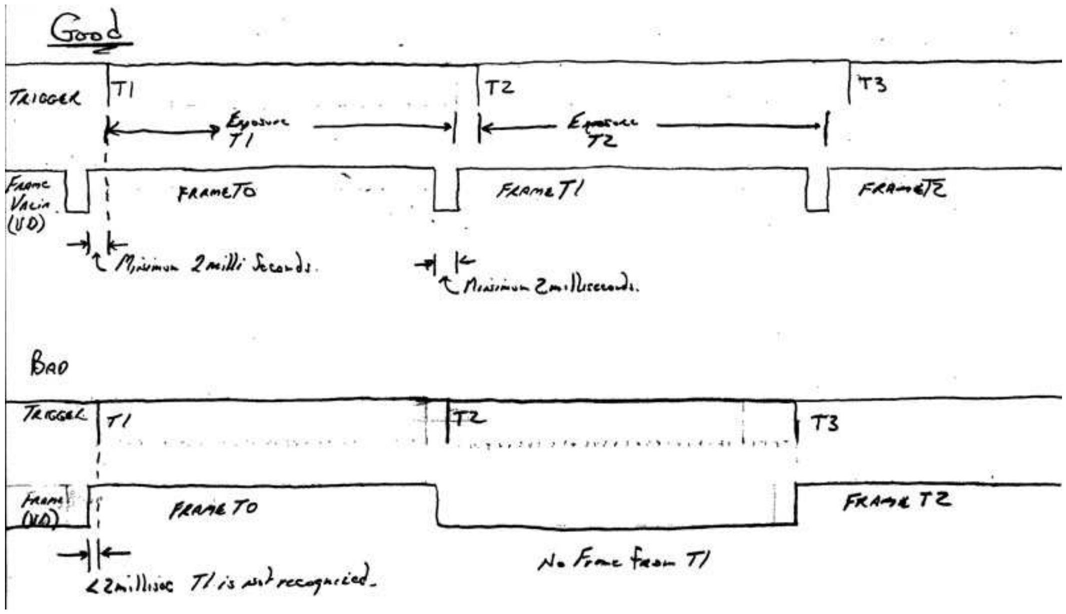

Figure 3.15: Timing diagram of the snapshot mode used to trigger the cameras. TOP: Good timing: The trigger pulses T0 (not shown), T1, T2, T3 trigger frame 0, 1, etc. The trigger must occur at least 2 ms after the rising edge of the previous frame valid (VD) pulse from the camera. The frame valid signal is high when transmitting valid data from the camera. BOTTOM: Bad timing: If the camera receives the trigger before it is ready, the trigger is ignored and the maximum frame rate is reduced by half (to 15 fps). This figure is reproduced from a correspondence from an engineer at the Cohu company.

them to accept an external hardware trigger and disconnecting them from the frame grabber trigger input.

A new computer system was built to handle the increased bandwidth requirements due to the additional data from the second camera. Each image is 998×1008 and is stored at a 16-bit depth, resulting in approximately 2 MB of information. At the maximum frame rate a bandwidth of at least 60 MB/s is therefore necessary. A SATA hard drive with a 160 GB storage capacity and capable of sustained 70 MB/s transfer rates was used. A new CPU and motherboard were required to accommodate the new hard drive. However, in practice, we were not able to capture 30 fps simultaneously from both cameras[14].

To make a relevant quantitative comparison between the two fields illuminated by

---

[14] The PCI bus is limited at and was also likely due to other drains on bandwidth, such as idle CPU activity from the Windows operating system.

the two laser light-sheets, they must be on the same grid. However, the position of the tank is different in the images from the two cameras. This is caused by alignment differences between the two cameras (i.e. verticality), and differences in spatial resolution. This results in differences in both the origin of the grids and the grid spacing. Thus the difficultly in determining the flow fields on the same grid.

3.2 Measurement techniques

3.2.1 Digital Particle Image Velocimetry (DPIV)

We use a technique known as Digital Particle Image Velocimetry (DPIV). DPIV is a statistical method to extract quantitative data from the images of flow seeded with tracer particles. Correlations are calculated over many small, local regions of the particle images obtained at two exposures of the CCD. This yields the mean displacements of particles in the local regions that can be easily converted into a velocity field representative of the flow field.

We obtain two successive exposures from our CCD camera, separated by time δt (see figure 3.3). The DPIV algorithms then calculate the cross-correlations[15] between similar regions of the two images to reconstruct the velocity field.

To get good statistical correlations, the particle seeding density must be high, yet there should also be high contrast between the particles and the background[16]. Figures 3.9 and 3.16 show examples of a good seeding density and contrast. The time between exposures should be small enough such that the velocity field does not change significantly and that the displacement of particles is small enough such that the particles do not move beyond the local correlation regions. However, the time between exposures should be large enough such that the two particle images are not identical[17]. A resulting velocity field is shown in

---

[15] DPIV can also be performed by calculating the auto-correlation function in a single image that has been double-exposed.

[16] However DPIV does surprisingly well even when the contrast appears poor by eye.

[17] The minimum displacements should typically be ≈ 1 pixel, though sub-pixel accuracy is achievable with many DPIV algorithms

figure 3.18.

We used two different DPIV algorithms for the data processing over the course of the experiment. The algorithms are briefly described below. For details of PIV theory and techniques see the book by Raffel *et al.* [94] and the review by Adrian [9].

We can measure horizontal velocities up to about 1 meter/second, by adjusting time delays and strobing the light sheet. The resolution of the resulting velocity field is ≈ 0.3 cm/velocity vector when viewing the entire tank. This can be significantly increased if we zoom in on a smaller region.

PIV algorithm

The first DPIV algorithm used was a set of MATLAB functions known as MatPIV, developed by Sveen [116]. The package is freely available to download online [116]. This was the same PIV MATLAB routine as used by Baroud [12].

The MatPIV routine works by analyzing two consecutive images separated by a known time, δt. The images are divided into smaller regions by interrogation boxes. A cross correlation is performed that is a convolution of corresponding boxes in the two images. The resulting correlation function has a peak, the location of which indicates the relative mean particle displacement between the two images. The velocity is calculated by dividing the displacement by δt. Thus one velocity vector is produced for each interrogation box. Overlap of the boxes is allowed and is typically 50%. The routine further makes multiple passes, using the results from previous passes, over the images and halves the box size on the second pass. The algorithm also includes filtering and interpolation to remove *outliers*, velocity vectors that are marked as obviously false due to poor correlation or due to a large deviation from the surrounding vectors.

For the MatPIV algorithm to produce useful results, there should be ≥ 10 particles per box (e.g. see 3.16).

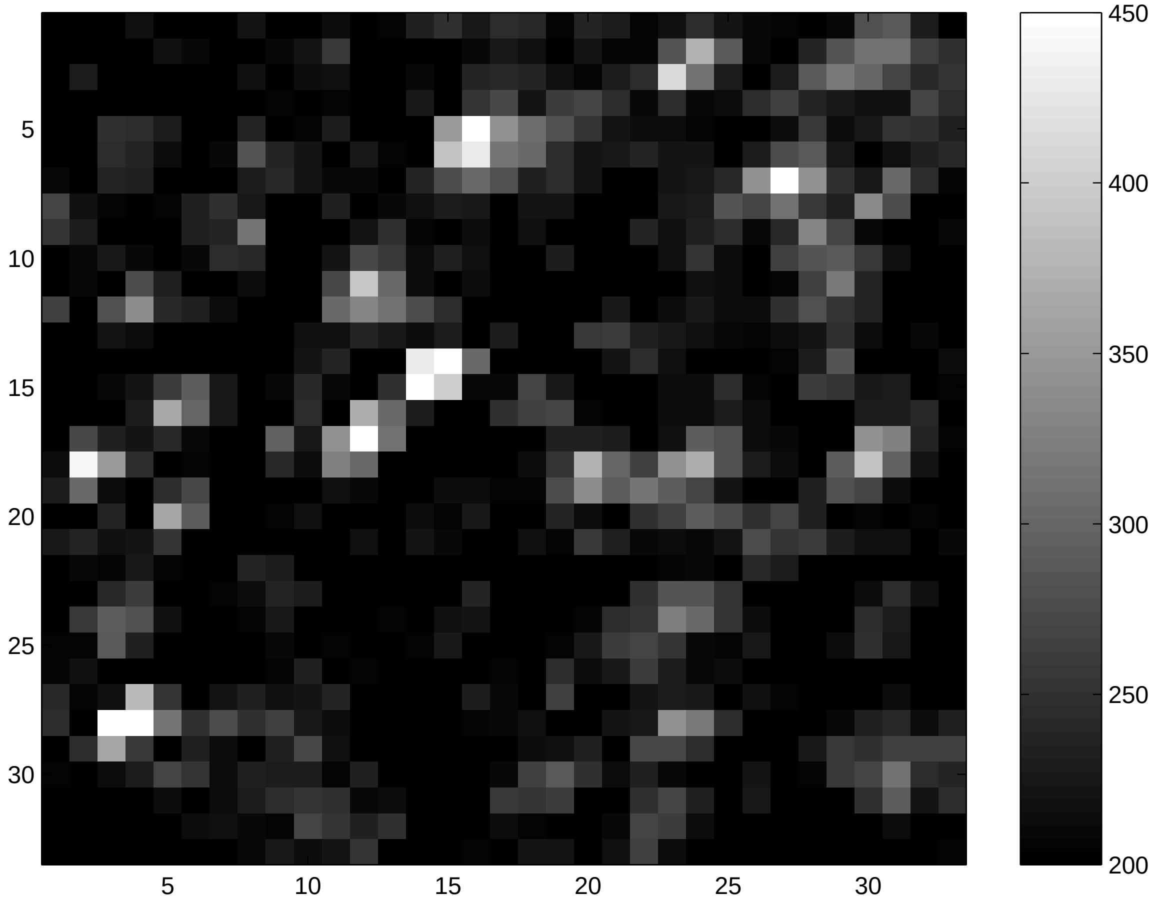

Figure 3.16: An example of good seeding in a 32×32 pixel box. There are about 8 bright particles and another 7 dim ones. Note that the DPIV does not identify individual particles.

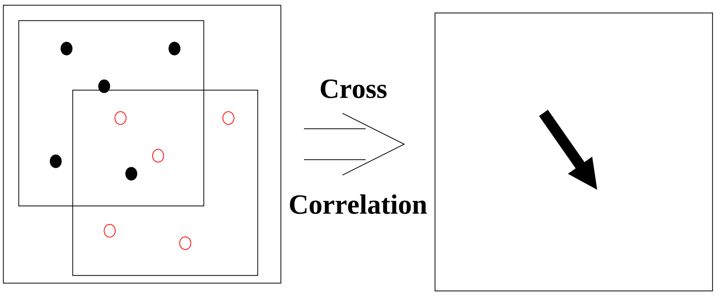

Figure 3.17: Schematic of basic PIV algorithm. The black circles represent particle images from the first frame, the red open circles are from the second frame. The relative displacement is determined from the peak in the cross correlation function applied between the two frames. The black arrow is the resulting displacement which is converted into a velocity vector by dividing by the time separation between the two frames.

CIV algorithm

Correlation Image Velocimetry (CIV), introduced in [44], is used at the Coriolis laboratory in Grenoble (LEGI), France. The algorithm is an extension of the basic PIV algorithm with features to improve its accuracy (see [43]), including local image enhancements. CIV is available for free download via the web at [33]. The first CIV algorithm used was run using a web-based interface to specify parameters to be used by Windows executables. It is now used via a MATLAB interface (and Windows executables).

The CIV consists of several sub algorithms: CIV1, "fix", "patch", and CIV2. The first pass of the CIV consists of CIV1, followed by fix and patch. Subsequent passes correspond to CIV2 followed by fix and patch.

CIV1 This is the basic correlation algorithm. The interrogation boxes allowed to move within a specified larger search window, not fixed as in the case of MatPIV.

FIX In the "fix" step false vector are identified and removed. This prepares the data for the patch step.

PATCH In the "patch" step, the velocities are interpolated using a spline function onto a

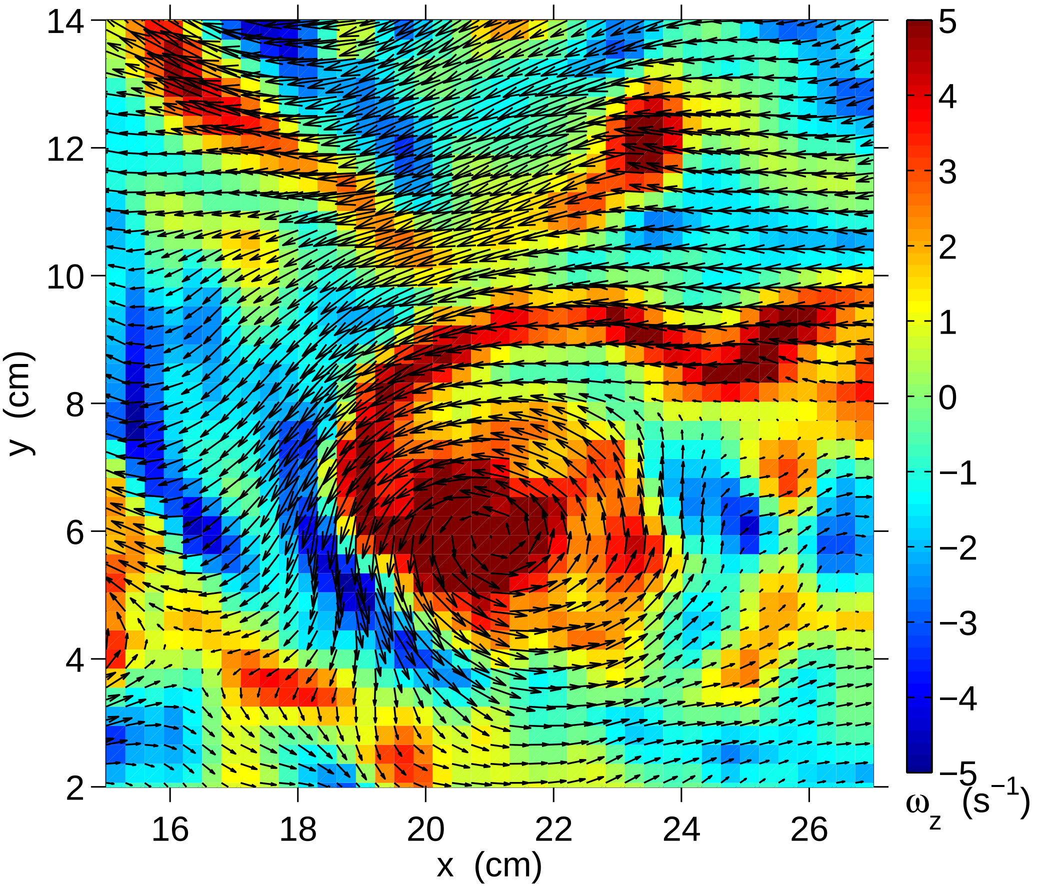

Figure 3.18: Sample velocity field calculated by the CIV algorithm plotted on top of vorticity (indicated by the colormap). Displayed is a 12 cm×12 cm region of the tank. The largest velocity is ≈ 7 cm/s; the largest vorticity is ≈ 12 s^{-1}. The colormap is saturated to render visible weaker structures. At roughly position $(x, y) = (21$ cm, 6 cm$)$ is a vortex. The vorticity is concentrated in the core and thus acts as as a reasonable tracer for the location of vortices. However, a strong vorticity filament spirals outward from the core. Thus regions of strong vorticity is not always indicative of a vortex center.

regular grid of specified size after the first pass[18]. Coefficients of the spline interpolation also yield the derivatives of the field, which are later used to calculate vorticity. A smoothing parameter can be specified for use with the spline[19]. The interpolation grid can be used specified in this step.

CIV2 This uses the results from previous passes as an initial predictor of the displacements. In this step, deformation and rotation of the correlation boxes is allow which increases the accuracy of the algorithm.

Estimation of algorithm uncertainties

Estimating the uncertainty obtained from a DPIV algorithm is difficult. The results of an algorithm are usually sensitive on a large number of parameters. This includes particle density, size, mean displacement, laser-sheet thickness, optical distortions, misalignment of the CCD image plane, and out-of-plane velocity and stereoscopic effects (e.g. see section 3.3). For non-steady flows, many of these parameters can have large fluctuations from one captured image pair to the next. It is therefore important to know how one's DPIV algorithm performs for a wide range of image parameters.

Okamoto *et al.* proposed a standard means to evaluate the results of DPIV by synthesizing particle images from a known 3-D flow velocity field [84]. The particle image fields are generated with seeding density, mean size, laser sheet thickness, and δt. The particles are then displaced according to the velocity field and δt between images. In this way, DPIV algorithms can be directly evaluated for many flow and seeding conditions on a single velocity field. Some standard images for given parameters of interest are publicly available. We have examined a moderate density, sparse seeding, thin laser-sheet (large out-of-plane displacement), large in-plane displacement, and small in-plane displacement.

We evaluated the MatPIV and CIV algorithms by comparing the results calculated

---

[18] The resulting velocities from the first pass are actually at positions shifted from a regular grid by half of the local displacement.

[19] Caution: this can make the velocity field look very appealing, however smoothing can have a significant effect on measured statistics! Be wary of over-smoothing your data.

on image pairs where the underlying velocity field is known.

The standard velocity field is taken from a 3-D numerical large eddy simulations of a jet impinging on a wall [84, 4]. Synthetic particle images were generated by displacements according to the known velocity field from the numerical simulation.

We performed a single correlation pass and an interpolation pass to test the CIV algorithm. An interrogation widow size of 21x21 was used with a search box of 55x55.

The MatPIV algorithm was run with two passes with an initial box size of 32x32 pixels which is reduced to 16x16 in the second pass. These parameters were chosen because it yields a resulting field on the same grid as the given numerically simulated velocity field and 16x16 is too small of a box size for a single pass (correlations become too small for sparsely seeded regions and particle displacements become too large for high velocity regions, i.e. too many particles enter/exit the box between frames). We can not arbitrarily choose our grid in the MatPIV algorithm (in contrast to the CIV algorithm).

To make quantitative comparisons, we calculate the mean percent RMS deviation from the real velocity field.

$$\sigma = \frac{1}{N}\sqrt{\sum_{i}^{N} \frac{[(u_i - U_i)^2 + (v_i - V_i)^2]}{[(U_i)^2 + (V_i)^2]}} \tag{3.5}$$

We also compare the distributions of the components of the velocities.

We find in general that the CIV performs much better than MatPIV, even for a single pass and non-optimized parameters of the CIV. There are several things to note:

- For image conditions typical of our experiment, the single-pass CIV RMS deviation is around 2.5% while for MatPIV it is $\approx 4\%$.
- Both the CIV and MatPIV velocity distributions differ by about %1 in standard deviation and mean values from the real field.
- MatPIV systematically calculates smaller magnitude velocities when there is a large out-of-plane displacement. The CIV does not appear to have this problem. This is

important to keep in mind for vertical light sheet measurements, where the out-of-plane velocity can become large.

- MatPIV does a better job in the regions of larger velocity (as long as the box size is not too small) and does not do as well for small displacements as the CIV.
- Both algorithms do better for high seeding density

Uncertainty in vorticity

There are two different ways to calculate the vertical vorticity which we used. For the MatPIV algorithm, we use the local circulation of the velocity field at point $\mathbf{x}_i$.

$$\omega_z(\mathbf{x}_i) = \frac{\oint \mathbf{u}(\mathbf{x}_i) \cdot d\ell}{dA} \tag{3.6}$$

Velocity differences are averaged over the eight nearest neighbors, weighted for distance from the central point. For exact algorithm see the MatPIV manual [115].

For the CIV algorithm, the coefficients of the spline interpolation during the patch stage give the derivatives of the velocity field, du_i/dx_j. The vertical vorticity is then calculated from the derivatives

$$\omega_z = \frac{dv}{dx} - \frac{du}{dy} \tag{3.7}$$

Estimating the uncertainty in the vorticity is not straightforward. Uncertainties in the vorticity field can be significantly affected by the characteristics of the flow field and the grid size. If the flow is relatively smooth across the grid spacing then the spline interpolation and local averaging of velocity differences will do a good job of calculating the derivatives. However, large local fluctuations in gradients or discontinuities over the grid will induce larger uncertainty as the averaging and interpolation will tend to smooth over fluctuations. Unfortunately, we do not have a given field of known vorticity with which to compare our results to obtain an empirical knowledge of our uncertainties. However, we can estimate that as a percentage of the calculated value the uncertainty in the vorticity will be at least twice that for the uncertainty in the velocity alone.

3.2.2 Measurement of vertical velocities

Data were taken to measure the vertical velocities in the flow. The laser was turned 90 degrees to create the vertical light sheet. A curved mirror was used to fold the light sheet to the small region. The mirror was made by carefully bending a heated piece of plastic which had been coated with aluminum by the vacuum shop. However, this special mirror was found to be unnecessary. A simple flat mirror that was mounted so as to be easily rotated was subsequently used to direct the light sheet.

Because limited space on the table restricted how far the camera could be placed from the side of the tank, only a small 9.5x9.5 cm region was imaged. The data were taken from just above the top of the tees, a region in the middle of the tank, a region just above that, and a region including the lid. In each region, the light sheet was slightly off of the center axis of the tank.

The laser sheet had to be expanded to about 1.5 cm to get good DPIV data. When zooming on a small region, particle displacements in pixels become larger; the pulse width of the laser had to be shortened to 3 ms to avoid long streaks from the particles. The separation between pulses was shortened to 5 ms to keep the particle displacements between frames small.

The uncertainty in the vertical measurements are much larger throughout the tank than those for the horizontal measurements. This is due to the large horizontal velocities that result in large out-of-plane motion. Additionally, the camera was placed closer to the light sheet plane resulting in larger stereoscopic errors (see section 3.3).

3.3 Room for improvement

The apparatus currently operates well and there are no critical problems. However, there is much room for improvements to be made and resolving some issues will improve the operation of the current apparatus. In this section we discuss some of the known problems with the apparatus.

3.3.1 Table oscillations

Due to the elasticity of the belt the rotation rate of the table is not steady, as shown in the tachometer output of figure 3.5. The amplitude of the modulation is small, about 1-3% of the table rotation rate. However, this is significant! This small amplitude can result in velocities of 0.6 - 2.5 cm/s in our flow near the boundary of our tank, whereas typical RMS velocities are on the order of 2-4 cm/s throughout the tank.

Furthermore, it is also possible that the table oscillation actively drives flow which may affect structures and dissipation in our tank. For example, since vortices are shed from the wall, differential rotation of the wall and the flow may influence the frequency of shedding.

Locking the motor pulley in place and displacing the table by hand we can measure a frequency of oscillation of about 0.75 Hz. However, there does not appear to be a persistent peak near the estimated natural frequency (see figure 3.19). Instead, there is always a peak at approximately half the table rotation frequency. For 0.4 Hz and 0.7 Hz table rotation this occurs at 0.19 Hz and 0.33 Hz respectively, with subsequent peaks at higher harmonics (and a peak at the table rotation rate). This corresponds to a ratio of ≈ 2.1. This is approximately the same ratio as the length of the belt to the circumference of the table pulley.

The belt is made from a single linear piece spliced together to form a loop. At the splice there is a gap spacing equal to twice the regular spacing between teeth on the belt (see the splice in figure 3.4). When the splice encounters the motor pulley the gap in teeth

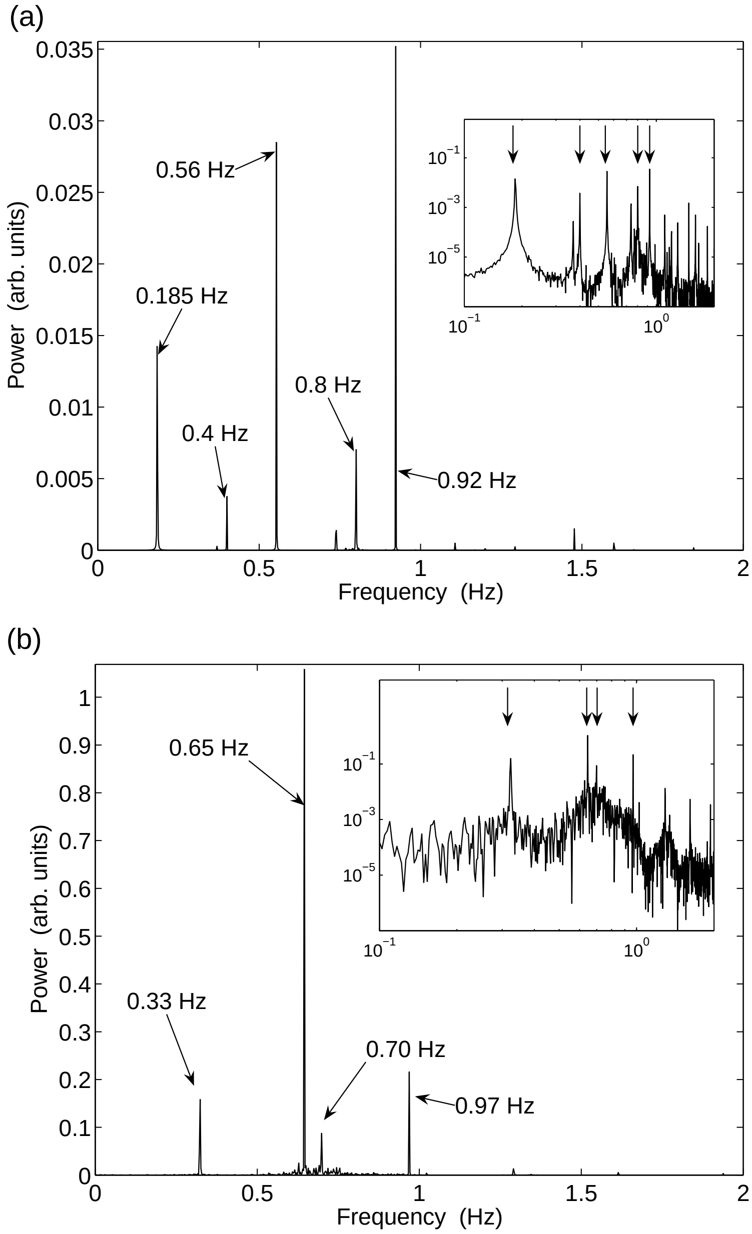

Figure 3.19: Power spectra from the tachometer for (a) 0.4 Hz and (b) 0.7 Hz table rotation rate. The large peaks correspond to roughly half the table frequency and higher harmonics. The labeled peaks are indicated by arrows in the inset on a log-log scale.

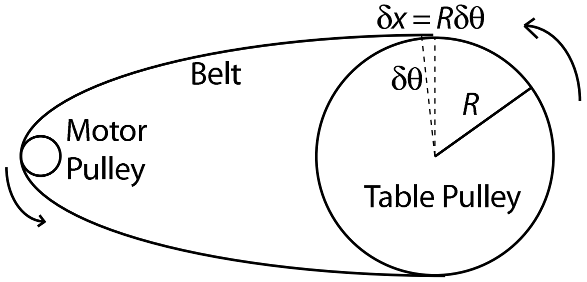

Figure 3.20: Schematic of the pulleys and belt. A lag of the table pulley by $\delta\theta$ causes an extension of the flexible belt by $\delta x = R\delta\theta$. The belt acts as a spring due to its elasticity. This leads to unwanted oscillations in the table rotation rate.

on the belt causes a lag in the extension of the belt. The belt is then extended again when the teeth of the motor pulley contact with the belt just after the splice. Thus the table is periodically forced by the splice in the belt.

Attempts were made to eliminate or reduce the table oscillation by tightening and shortening the belt by reducing the distance between the table and motor pulleys. It was thought that either or these changes would make the natural frequency higher and thus move it away from the rotation frequency. However, while tightening the belt had no effect, shortening the belt made the oscillations much worse. This is due to the splice. Shortening the belt makes the contact angle between the motor pulley and the belt much larger and as a result fewer teeth on the pulley are in contact with the belt. Thus there is a larger lag in motion when the splice encounters the motor pulley.

The angular velocity of the table is modulated in time such that it consists of a constant plus an oscillatory component (approximately sinusoidal). We want to eliminate the oscillatory component so that the table rotation is constant, equal to the rate at which we drive it.

A simple model of our table-pulley-belt system is a damped-driven harmonic oscillator.

$$I\ddot{\theta} + 2\gamma\dot{\theta} + kR^2\theta = At \tag{3.8}$$

Where I is the moment of inertia of the table and pulley system, γ is the coefficient of linear damping, k is the spring constant of the system, R is the radius of the table pulley, and At is the driving of arbitrary amplitude necessary to maintain a constant angular velocity.

The solution is a piece constant in time (from the inhomogeneous part) that corresponds to the constant angular velocity, and an oscillating transient

$$\omega(t) = \dot{\theta}(t) = Ae^{-\frac{\gamma}{I}t}[A_1' e^{(\sqrt{(\frac{\gamma}{I})^2-\omega_o^2})t} + A_2' e^{-(\sqrt{(\frac{\gamma}{I})^2-\omega_o^2})t}] + \Omega \tag{3.9}$$

where Ω is now the desired driven angular velocity and $\omega_o = \sqrt{kR^2/I}$ is the natural frequency of oscillations of the belt-table system.

For a critically damped solution, we expect

$$(\frac{\gamma}{I})^2 = \omega_o^2 \tag{3.10}$$

We estimate the moment of inertia of the table system as $I \approx 100$ kg m^2. Using the measured natural frequency of $\omega_o = 4.7$ s^{-1} ($f = 0.75Hz$) results in $\gamma = 471$ Nms. This would requires about 2950 Nm of torque ($\gamma\omega$) for a table rotation rate of 1.0 Hz! Our current motor can only supply about 5 Nm of torque maximum.

The flexible drive belt is known to cause problematic oscillations. However there is no replacement available[20].

The best possible solution would be to directly drive the table with a motor connected to the table axis. However, since the slip-rings occupy the space underneath the table, this would require lifting the entire apparatus and extending the shaft. To do this, the table must be disassembled which may be prohibitive. Another solution would be to drive the table by directly coupled gears. However, this would also require disassembling the table.

In the future, it may be possible to control oscillations through closed-loop feedback on the pulses sent to the table motor.

---

[20] From a communication with the manufacturer: The design of the belt has been discontinued due to this problem that causes oscillations.

3.3.2 Pump vibration

The rotor of the positive displacement pump is not axisymmetric due to its helical shape. As a result there can be significant mechanical vibrations of the pump. This vibration is transmitted to the table, tank, and the support structure for the cameras to vibrate. This can result in significant error in the DPIV due to the vibration-induced relative motion of the CCD and the particles.

This problem can be reduced by isolating the mechanical vibrations from the pump. We have placed vibration damping pads and (an old bicycle inner tube seemed to work reasonably well). Further, we avoid pump rotation rates that induce mechanical resonance.

An ideal solution to this problem would be to have the pump completely isolated from the table. Rotating pump couplings do exist, however there is not sufficient space under the table.

3.3.3 Bubbles, bubbles everywhere

It is difficult to close the apparatus without trapping some air on the inside of the lid. Furthermore, to remove the lid we must disconnect the pipes (the pipes enter through the lid). This introduces air into the system which must be removed. If there is any air in the pipes or Sprinkler, bubbles will form, rise and stick to the lid, interfering with the flow visualization.

As another source of air in the tank, the distilled water contains a significant amount of dissolved gas when it is first put into the tank. If the pump is run continuously for more than a few hours, the heating of the water will cause the gas to appear as bubbles on the surfaces of the tank. This is avoided by running the pump before completely closing the tank to allow the dissolved gas to escape.

Bubbles that are trapped on the lid they will eventually dissolve into the water. Smaller bubbles are less of a problem than large bubbles as they tend to disappear faster due to their larger surface area to volume ratio. However, this can take up to a few weeks for the bubbles to be completely eliminated.

In the new design, the pipes enter the Sprinkler through the sides, rather than through the top. This will allow us to easily remove bubbles by reposition the lid without having to introduce air into the Sprinkler. Thus, the problem of bubbles should be significantly reduced, if not completely eliminated with the new apparatus design (see appendix A).

3.3.4 Uncertainty in PIV due to out of plane motion

The flows that we observe in our tank are three-dimensional, as with any real flow. We will not be able to resolve the motions perpendicular to our light-sheet with a single camera. Furthermore, there will be errors due to out-of-plane motions.

Error in DPIV due to out-of-plane motions has two primary causes:

(i) Particles leave the light sheet or travel across a large vertical gradient of light intensity. This can decrease the correlation by either causing the particle to appear brighter in one frame of an image pair or appear only in one frame. This effect is reduced by making the time separation between successive laser strobes short enough. For an extreme case of a 10 cm/s vertical velocity, and a strobe separation of 12 ms, the particles will travel 0.12 cm. This upper limit is still only about 20% of the thickness of our light sheet. We therefore do not expect a large error from this effect.

(ii) The vertical motions of particles are manifest as apparent horizontal motions due to perspective. Relations between the vertical and horizontal motions view through an objective lens can be derived [89]

$$\delta x = M\left(\Delta X + \Delta Z \frac{x}{d_o}\right) \tag{3.11}$$

$$\delta y = M\left(\Delta Y + \Delta Z \frac{y}{d_o}\right) \tag{3.12}$$

where the upper case (X,Y) refer to the real location of the particle and the lower case (x, y) is the distance of the particle image from the optical axis at the time of the first exposure

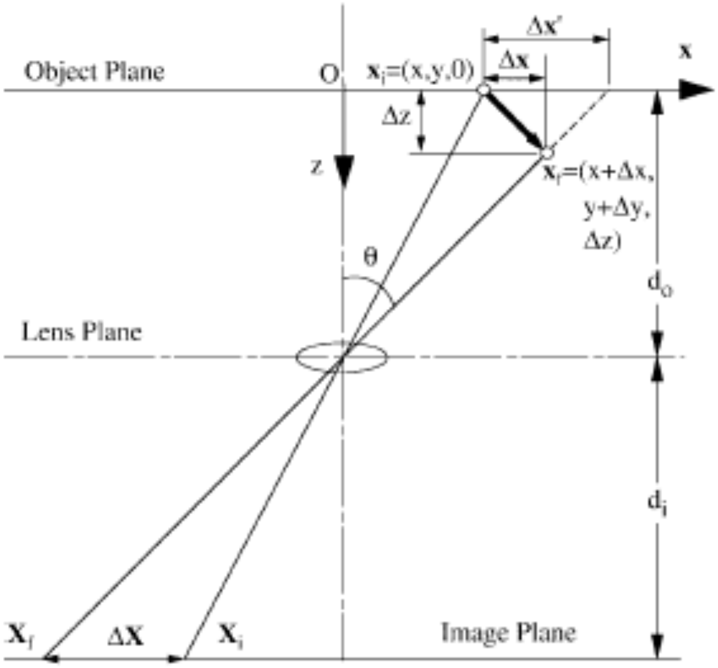

Figure 3.21: Schematic of the stereoscopic effects. From reference [89].

. The deltas, $\Delta X, \Delta Y, \Delta Z$, indicate the real displacement of particle or its image image between exposures. The M is the magnification and d_0 is the distance from the objective lens to the illumination plane. This effect is larger for larger distances off the optical axis (x, y). Thus the typical error due to this effect is zero at the center of the tank. The error becomes smaller for larger separation of the camera and light-sheet, and smaller for smaller displacements transverse to the light-sheet. For our PIV system, Near the top of the tank, our mean vertical velocities are typically of order 10% the horizontal velocities. With $d_o = 120$ cm, $x = 20$ cm (the radius of the tank) this will induce about 2% error near the wall of the tank. However, in more 3D flow, and in the core of some vortices the vertical velocities can be of the same order of the horizontal velocities. In this case the error can increase up to 16% at the boundary[21].

This effect can be used to measure the vertical velocities. The technique is known as

---

[21] This is a sizeable effect. In single camera PIV the error due to out-of-plane motions is typically $> 10\%$, yet it is rarely mentioned as a source of uncertainty in results presented in the literature!

stereoscopic[22] PIV [90, 89]. For a single camera, the above relations result in 3 unknowns for 2 equations. With the addition of a second camera focused on the same light-sheet, two additional equations are added. There are then 4 equations and 3 unknowns and the system is over-determined. Experimental uncertainty allows us to solve the system of equations for the vertical displacement. This remains a subject of future work and is beyond the scope of this dissertation.

3.3.5 Lack of good particles

Finding good particles for use in our system was a difficult process. There is a limited supply of the currently used microspheres. Currently, Bangs Laboratories is out of stock of the particles now in use.

Sources of other particles exist. For example, hollow ceramic (or glass or metallic coated) microspheres can be obtained for free as samples. However, we did not use them because they are easily crushed and will be pulverized in our positive displacement pump. Pine pollen has also been used in experiment as it absorbs water and becomes neutrally buoyant. However, it reflects light poorly and it is organic and thus has a limited lifetime. Although pine pollen is commercially available, it is very expensive[23].

New sources of cheap particles must be found in the future.

3.4 Numerical methods

3.4.1 Passive scalar advection

To study the transport and mixing properties of our flow we examine numerically the motion of passive scalar point particles and passive scalar fields in the velocity fields obtained from the experiment. The velocity fields that we measure are a two-dimensional projection of a three-dimensional incompressible flow field. Therefore, they have a non-zero divergence

---

[22] This same effect is how our brain can distinguish depth at short distances using two eyes.

[23] It is perhaps better to obtain free samples from nature when your allergies are acting up.

and do not satisfy any fluid dynamical equation of motion. Nonetheless, they can give us useful information regarding the transport properties of the flow.

Initial locations are chosen for the point particles, the positions of the particles are updated corresponding to the velocity fields such that $\mathbf{x}_{n+1} = \mathbf{u}_n \Delta t + \mathbf{x}_n$ where $\mathbf{x}_n$ is the position of the particle at time-step n, and $\mathbf{u}_n$ is the velocity of the flow field at time-step n at the location of the particle. Each velocity field is interpolated in space by a cubic-spline to calculate the field at the location of a given particle. The timestep, Δt, is chosen by the Courant condition[24] [91], which avoids particles jumping over grid points or going too far at a given iteration. For our data this condition means $\Delta t < 0.02$ s $< 1/15$ s; therefore, fields must also be interpolated in time. The measured velocity fields vary slowly in time compared to our temporal resolution 1/15 s (measured correlation time is ≈ 2.4 s; see chapter 5 and 5.4.1). We therefore justify the use of a cubic spline interpolation in time to achieve $\Delta t \ll 1/15$ s (typically $\Delta t = 0.001$ s).

We also examine the time evolution of a passive scalar field advected in the experimental velocity field by numerically integrating the advection-diffusion equation,

$$\frac{\partial c}{\partial t} = -\mathbf{u} \cdot \nabla c + \kappa_D \nabla^2 c, \tag{3.13}$$

where $c = c(\mathbf{x}, t)$ is the passive scalar concentration and κ_D is a diffusion coefficient, chosen as necessary for numerical stability of the solution. The values of κ_D used correspond to Schmidt numbers (κ_D/ν) near 0.05. The numerical integration is performed using a pseudo-spectral method in polar coordinates based upon methods given in [122]. The grid is 128 Chebyshev modes in the radial direction and 256 Fourier modes in the azimuthal direction. The velocity field obtained by the CIV measurement is interpolated via a cubic spline onto the simulation grid. The numbers of radial and azimuthal modes were chosen so as to not under-resolve our velocity fields on the nonuniform polar grid.

The singularity at the origin was avoided by choosing Chebyshev modes for the radial direction. The collocation points for Chebyshev modes have unit spacing on a circle,

---

[24] This is also known as the Courant-Friedrichs-Levy (CFL) condition.

$x_i = \cos(\pi i/(N-1))$, where x_i is the i^{th} gridpoint, and N the total number of gridpoints. The gridpoints are clustered at the boundaries and sparse in the center of the domain. By defining the radial coordinate $r \in [-1, 1]$ and using only the $r > 0$ values, the radial grid points are sparse near $r = 0$ and clustered at the boundary $r = R$. For an even number of modes the origin, $r = 0$, is skipped. However, the azimuthal grid is still dense at the origin, which requires us to use a very short time step $\Delta t \approx 2 \times 10^{-4}$ s to avoid numerical instability. The experimentally determined velocity fields are then interpolated in time by the method described above for the tracer particle simulation.

The diffusive term is calculated implicitly by a Crank-Nicholson scheme, separately for the radial and azimuthal directions. The advection term is calculated explicitly by a predictor-corrector scheme using a third-order Adams-Bashforth step followed by a fourth-order Adams-Moulton step [91].

To perform the numerical analysis on the decomposed fields we construct a velocity field from a vorticity field. We make the assumption of 2D flow that the total vorticity is given by the measured vertical vorticity, $\omega = \omega_z$. We then use the 2D streamfunction-vorticity relation $\nabla^2\Psi = -\omega_z$ and solve Poisson's equation for the streamfunction Ψ using MATLAB's PDE solver. The derivatives of the streamfunction are then used to calculate the velocity field by the relation $\nabla \times (\Psi \mathbf{z}) = \mathbf{u}$, where $\mathbf{z}$ is the unit vector in the vertical direction.

The assumption above is clearly not valid close to the source tees, where the flow is 3D. However, close to the top of the tank the assumption becomes valid as the flow is quasi-2D. To test the reconstruction and the validity of the 2D approximation, we compare the original measured velocity fields to velocity fields reconstructed from the vorticity fields. A region of an original velocity field and the reconstructed field is shown in Fig. 3.22. The RMS difference in the magnitudes of the original and reconstructed fields is about 2%. The reconstruction calculation does well in regions where there is a strong uniform flow. It does less well where there are large gradients in the velocity, in particular near vortices. However, on the whole the reconstructed velocity field follows the same behavior as the original field.

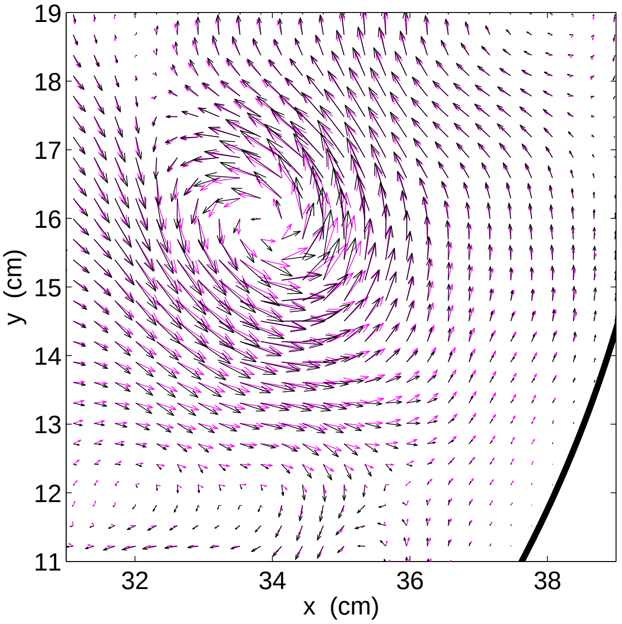

Figure 3.22: Close-up of a vortex in our tank near the boundary (bold line). The original field is represented by black vectors and the reconstructed field by light-colored (purple) vectors. The original and reconstructed fields are indistinguishable in the regions of uniform flow. The largest vectors correspond to 6.7 cm/s. The center of the tank is at (x,y) = (19.2 cm, 18.9 cm).

3.5 Summary

Our experimental apparatus is a deep rotating tank. We locally force 3D turbulence near the bottom by circulating water through sources and sinks. We can easily change the forcing geometry. We visualize the flow by scattering light off of neutrally buoyant tracer particles. We determine the velocity field in planes using digital image velocimetry techniques.

The apparatus has several non-critical problems. These includes oscillations from the table drive system, mechanical vibration from the pump, and errors in the DPIV due to stereoscopic effects. We offered suggestions for the resolution of such problems. Resolving the problems will improve the operation of the apparatus.

We also described numerical methods used to reconstruct the velocity field from the vertical vorticity field and to calculate the advection of a passive scalar. We found that near the top of the tank, the field appears to be well described by the measured horizontal projection of the velocity field.

In the next sections we describe some results obtained from the experiment.

Chapter 4

Flow description

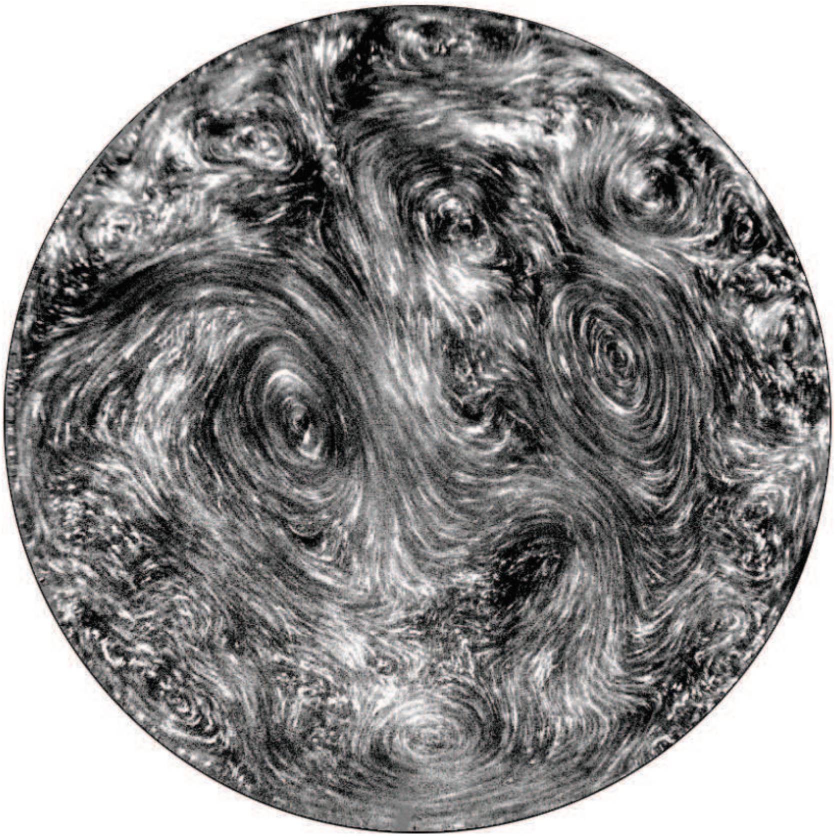

In this chapter we describe the flows produced in our rotating tank. Some of the flow description has been taken from [100]. When referring to quantities such as velocity, vorticity, and divergence, it is typically meant the components that we can observe from the plane of measurements. i.e. for the horizontal PIV, we mean the horizontal projection of the velocity field (u, v), the vertical vorticity ω_z, and the horizontal divergence. For all of the fields presented, the cyclonic direction is out of the paper (counter-clockwise) unless otherwise noted.

4.1 Flow structure

Near the forcing sources (tees) at the bottom of the tank, the flow is very turbulent (Reynolds number $\sim 6 \times 10^4$) and three dimensional (Rossby number $\gg 1$). However, moving vertically away and up the tank from the forcing, the turbulent velocities decay. The Reynolds number near the top of the tank is order 1000, based upon the RMS velocities of 2 cm/s and typical structure size of 5 cm (estimated from the velocity correlation function). The relative influence of rotation also becomes larger so that the Rossby number becomes about 0.3 for moderate rotation rates (dependent upon specific control parameters). In this rotationally dominated region near the top of the tank, we see many long-lived structures aligned along the rotation axis.

4.1.1 Particle image streaks

The particles in a plane near the top of the tank are confined primarily to the plane of the horizontal light sheet. The particle streaks follow persistent coherent jets, cyclones (a vortex with rotation in the same sense as the tank), and anti-cyclones without crossing, similar to a 2D streamline flow [figure 4.1 (a) and (b)].

The instantaneous flow structure changes drastically from the top of the tank, near the lid, to the bottom, near the forcing tees. In contrast, the motions of the particles near the bottom of the tank are much less organized; particles pass through the plane

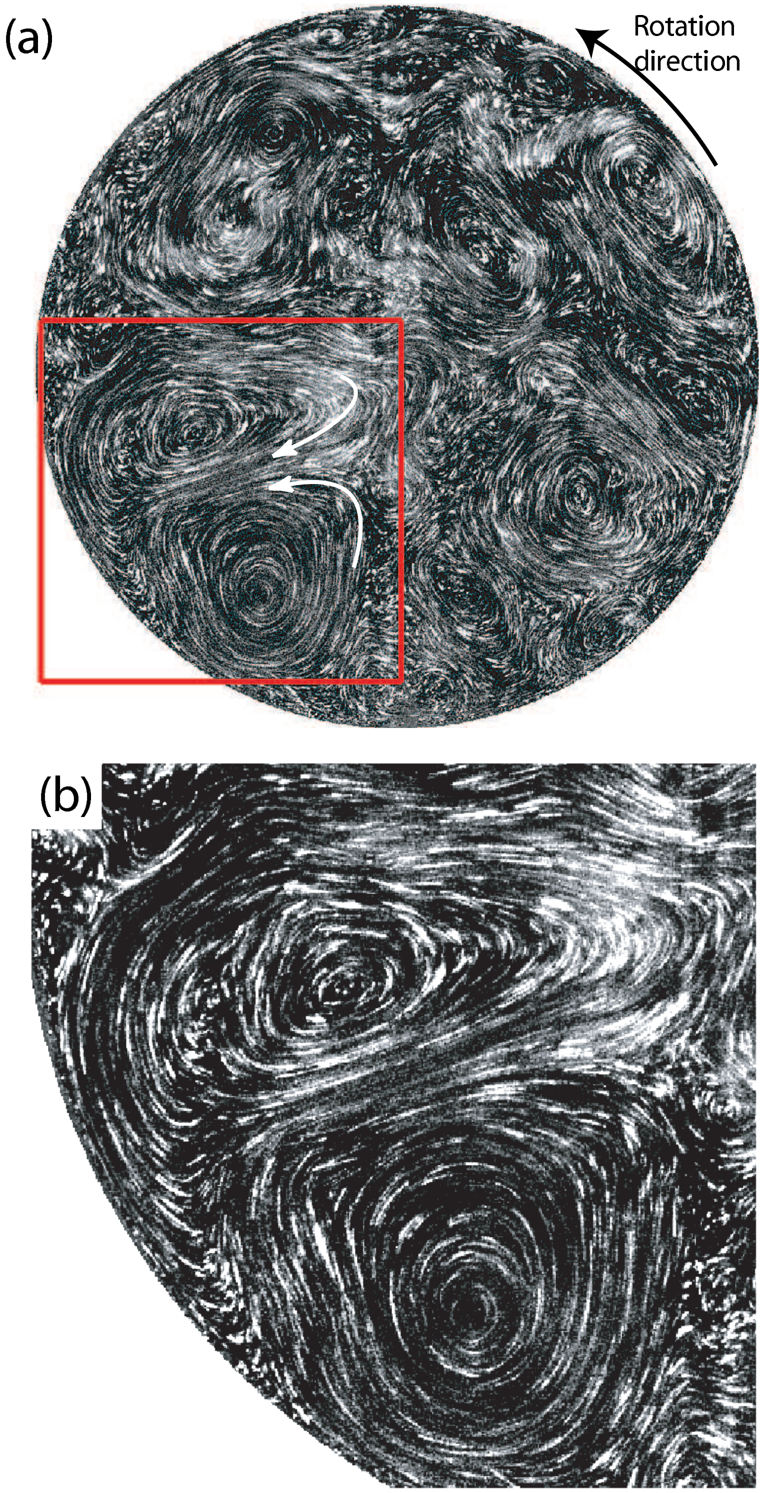

Figure 4.1: (a) Streak photo of the particle image fields in a horizontal plane 4 cm below the lid of the tank. The exposure time was 400 ms. (b) Close-up of the boxed region (18.7 cm × 18.7 cm) showing a cyclone (circular closed particle streaks) and an anti-cyclone (elliptical closed particle streaks to the upper-left of the cyclone). The time average of many fields has been subtracted to account for non-uniformities in the illumination. From reference [100]. cf. the figure on the first page of this chapter.

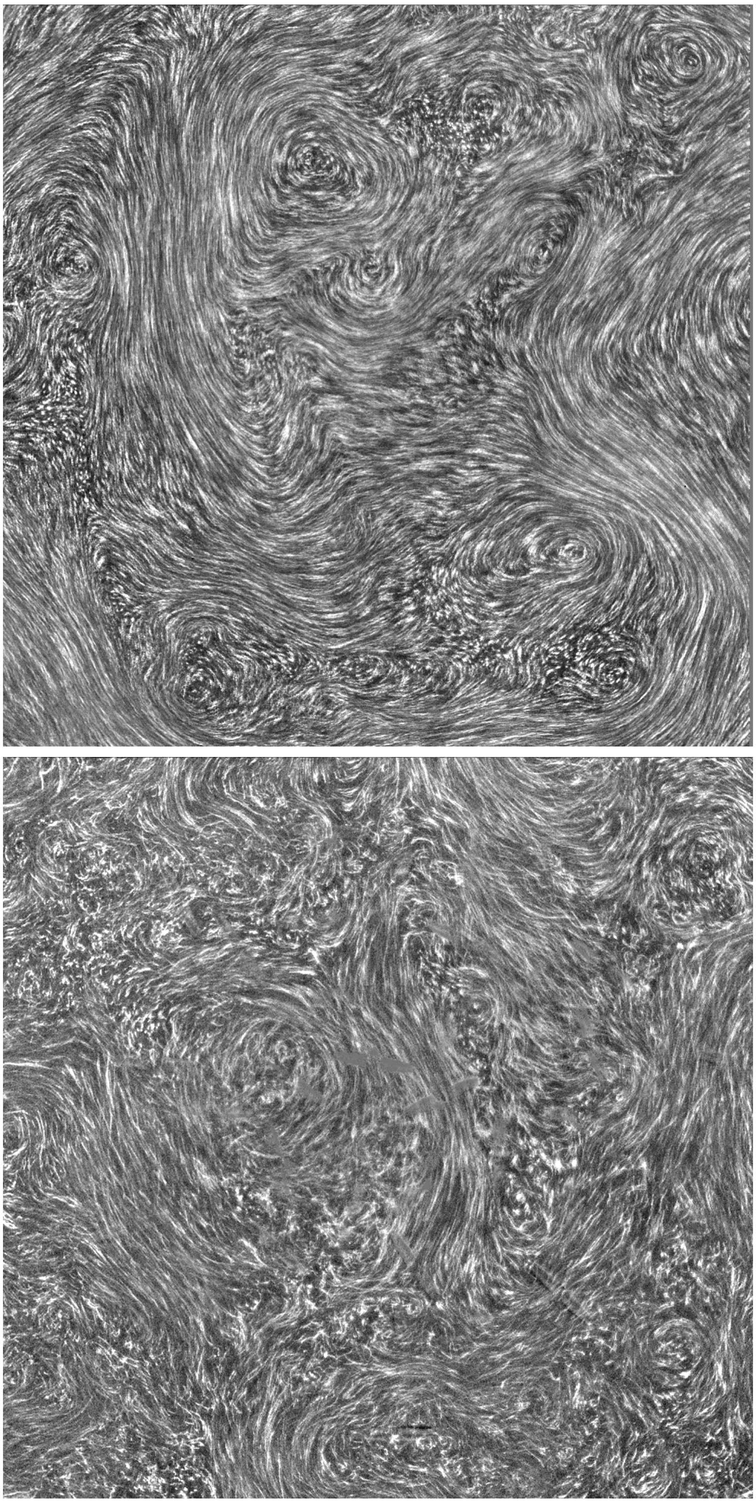

Figure 4.2: Streak images from a zoomed region near the top (top image) and bottom (bottom image). The time average has been subtracted from the images. In the image near the tees (bottom image), the “ghost” of the tees can be seen. For particle images taken simultaneously from the top and bottom of the tank see chapter 6.

frequently and the particle streaks can cross and exhibit small fluctuations, indicative of larger horizontal divergence. This can be seen in figure 4.2, streak images of the particles are shown for a zoomed region of the tank. This is due to increased three-dimensionality and turbulence near the forcing tees.

4.1.2 Persistent coherent structures

Localized coherent structures are apparent as regions of strong rotation in the measured velocity field near the top of the tank (see figure 4.3. These structures include the large compact regions of intense vorticity and wispy filaments of intense vorticity are evident in figure 4.4 (a) and (b). We observe more cyclones (rotation in the same sense as the tank) than anti-cyclones, in accord with observations in similar previous experiments on rotating turbulent flows [77, 28, 53]. The amplitudes of vorticity at the core of the intense cyclones are typically more than ten times that of the surrounding flow [see figure 4.4 (b) for a close-up of an intense cyclone]. The anti-cyclones, however, have a typical core vorticity amplitude only a few times that of the background.

The cyclones, anti-cyclones, and vorticity filaments are long-lived and are active dynamically. The vortices and vortex filaments can be tracked by eye as the flow evolves in time (figure 4.6 and figure 4.5). Vortices are also shed from the wall and travel across the tank and interact with one another (top of figure 4.6).

Vortex filaments occasionally peel from vortices, advect with the flow, and sometimes roll up to form new vortices. Structures may disappear by merging with other structures or by stretching in a jet region between opposite sign vortices. Many of the small intense vortices with very short turn around times (< 1 s) live on the order of a characteristic decay time (~ 10 s, see section 4.2) before shearing apart or merging with neighboring structures.

Additionally, we see persistent structures such as the large cyclone (red) and anti-cyclone (blue) that appear in figure 4.4. Such structures often appear in a preferred location in the tank. Presumably such preferred locations exist because of inhomogeneities in the forcing by the tees [cf. figure 3.1 (c)]. A vortex can be kicked off its preferred location

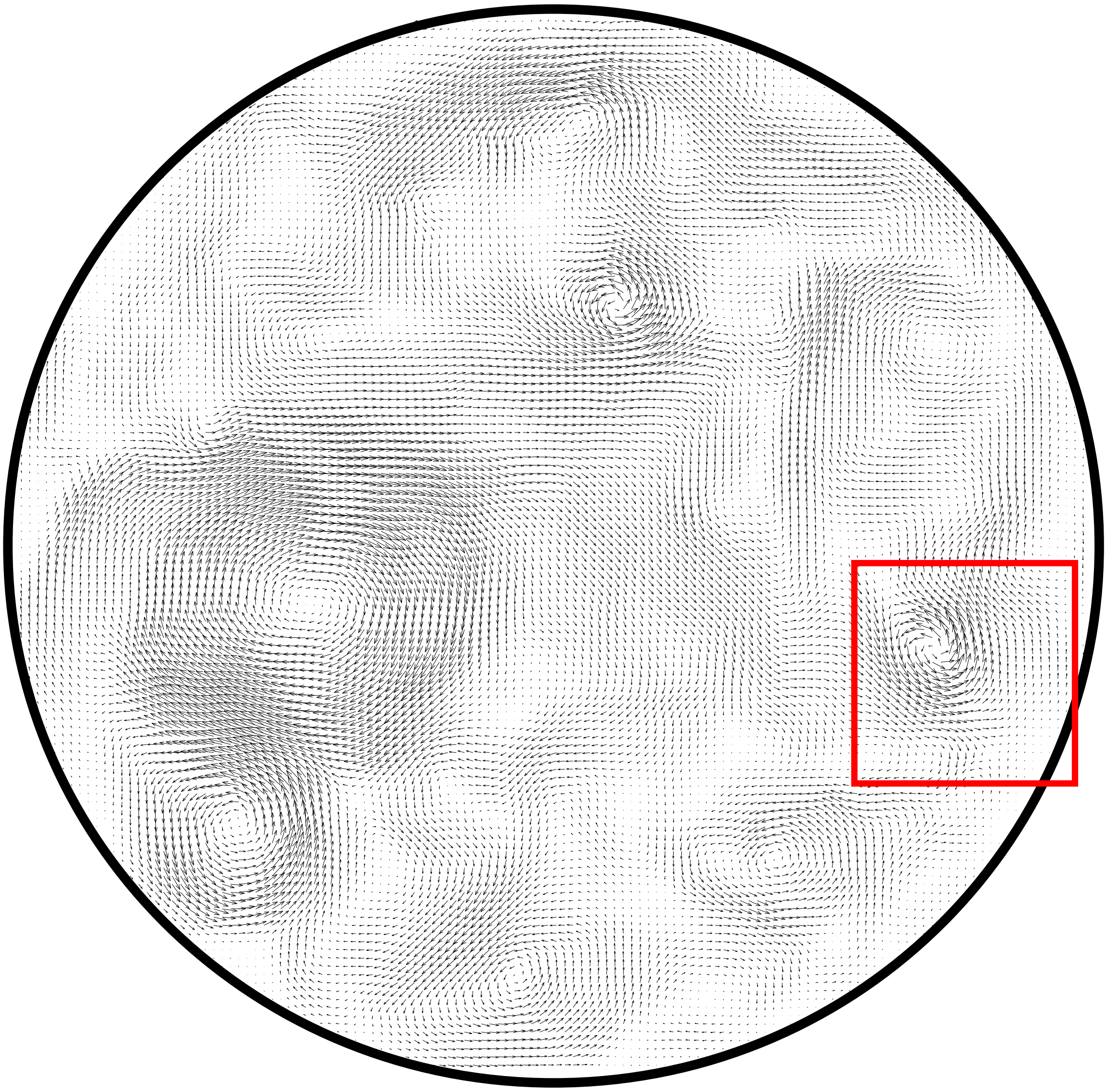

Figure 4.3: A whole velocity field determined at 0.4 Hz rotation and 426 cm^3/s pumping. Immediately apparent are a large anti-cyclone and several small cyclones. The longest vector corresponds to ≈ 8 cm/s. The box indicates the zoomed region in figure 4.4 (b).

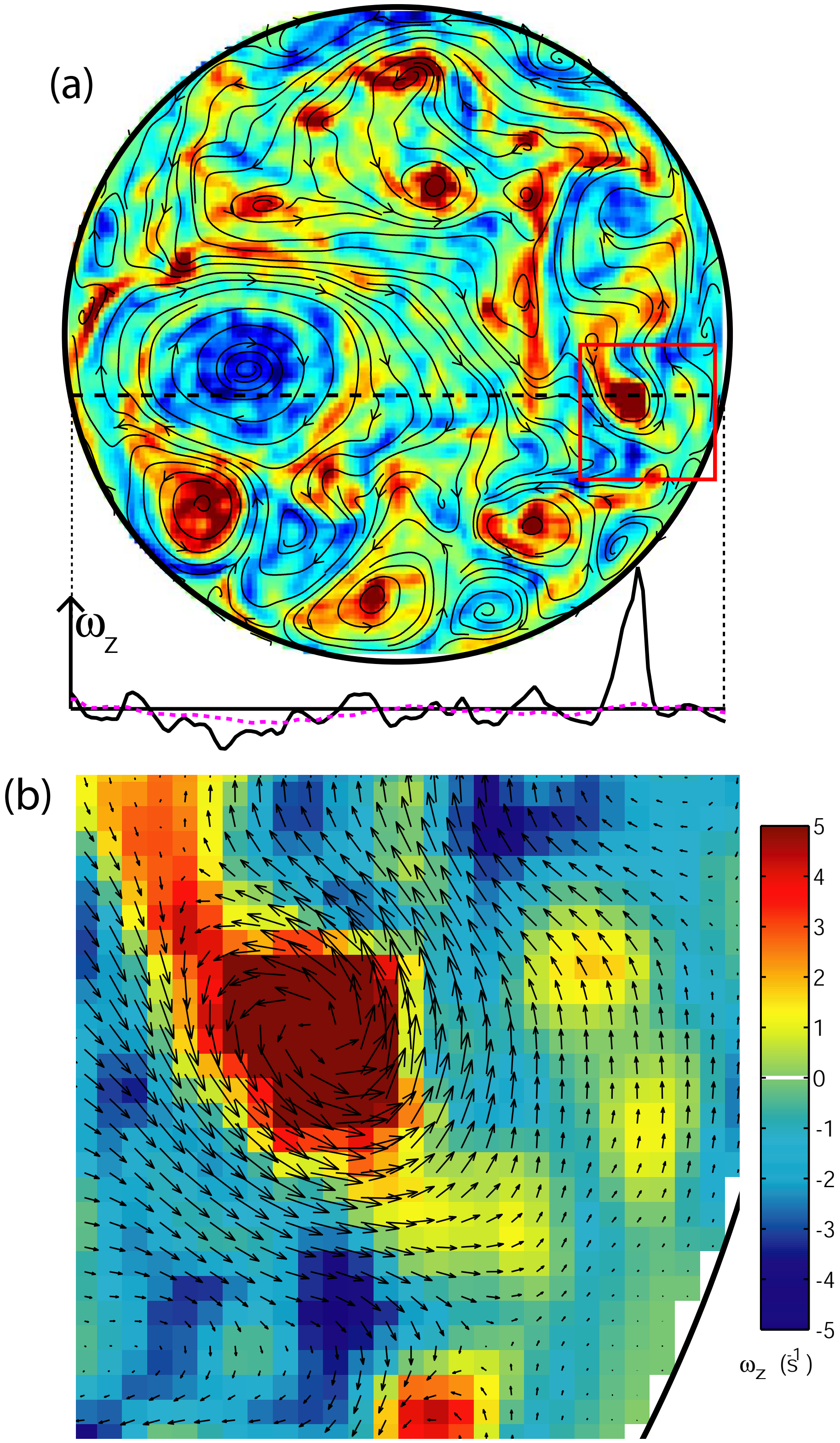

Figure 4.4: (a) Vertical vorticity field ω_z with the value along the dashed line shown in the trace below the field. The dashed line in the trace indicates the mean field value. (b) Close-up of the velocity and vorticity fields in a 8 cm × 8 cm region near the boundary. The longest velocity vector corresponds to 6.7 cm/s. The vorticity is indicated by the color map, where vorticity values are clipped at 5 s^{-1} to render visible weaker structures; the vorticity in the core of the strongest cyclone is 22 s^{-1}. The data were taken at 0.4 Hz and 426 cm^3/s.

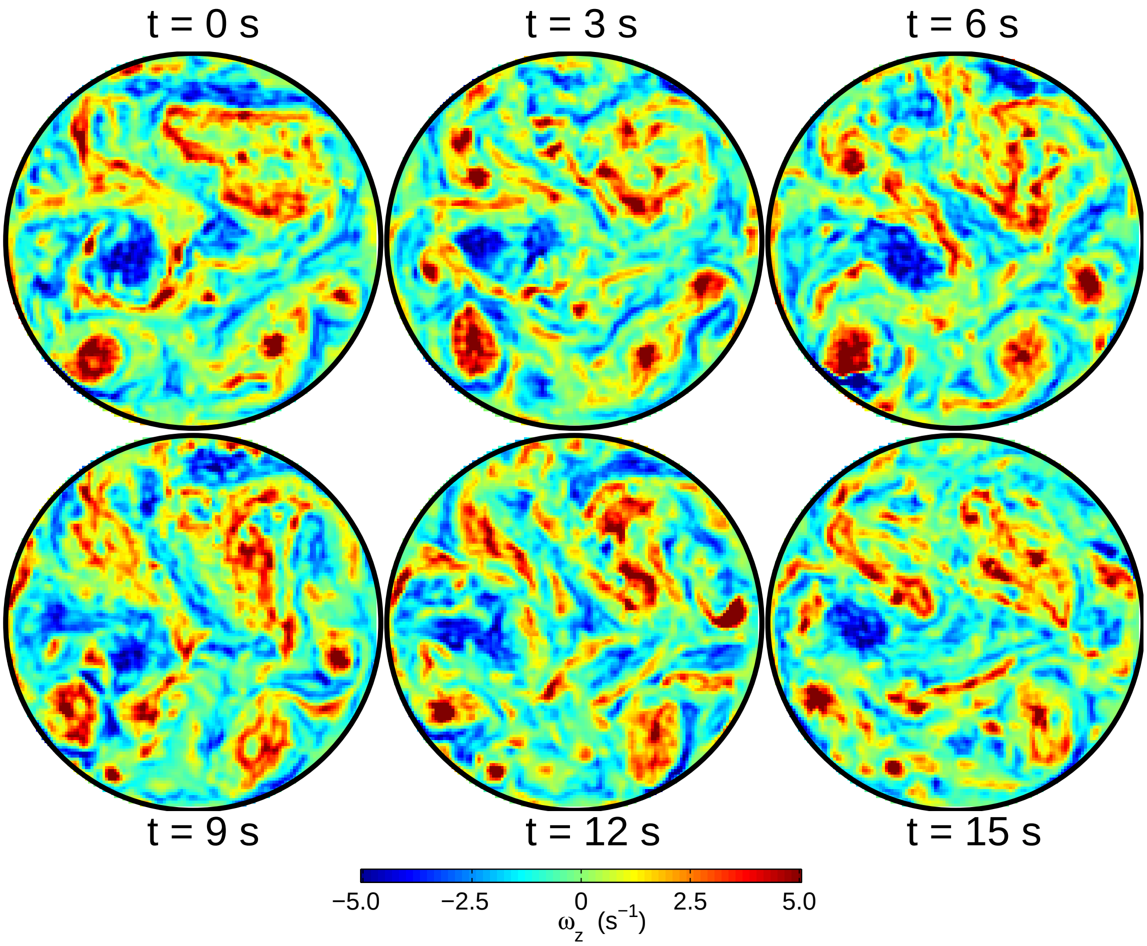

Figure 4.5: Time evolution of the vorticity field over 16 seconds, near the top of the tank. The data were taken at 0.4 Hz rotation and 426 cm^3/s pumping. The localized intense regions of vorticity persist between successive snapshots. The same colorscale is used as in figure 4.4.

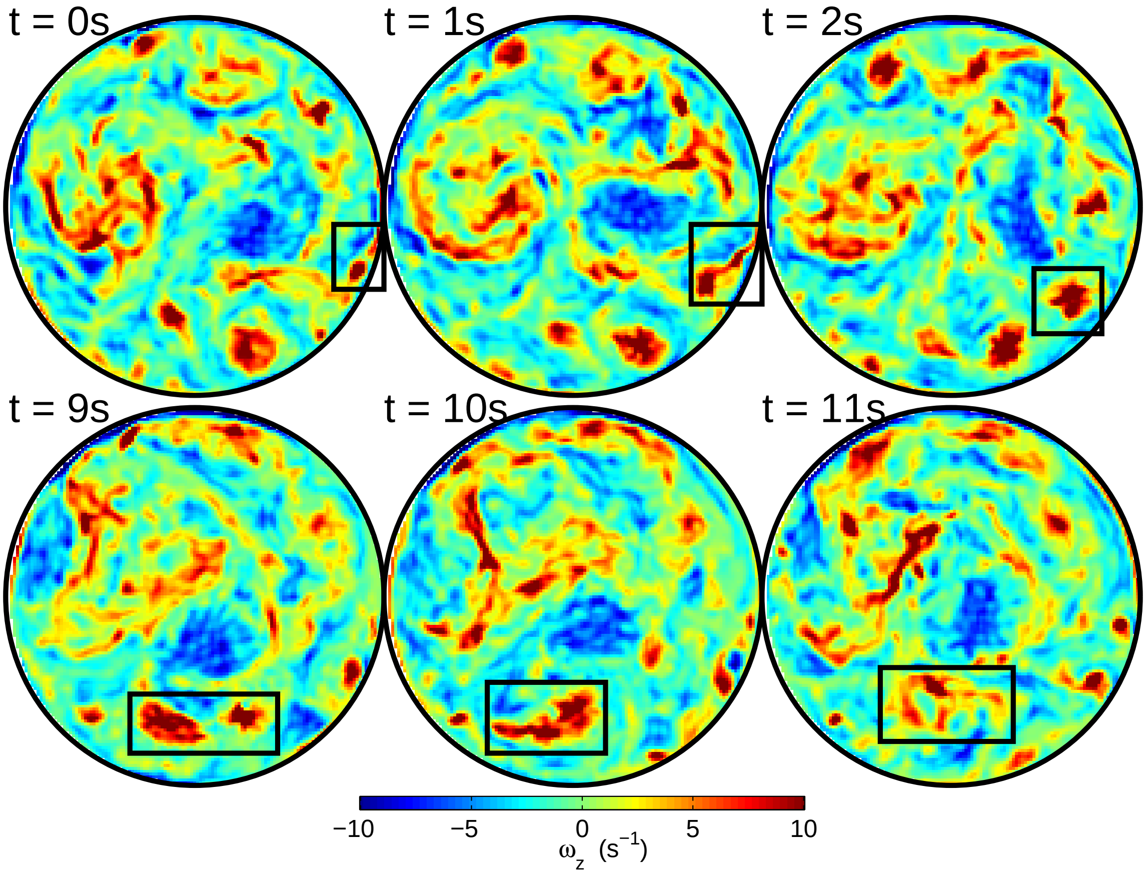

Figure 4.6: Time elapsed fields from 0.6 Hz table rotation and 20 Hz pumping. This shows a vortex being shed from the wall (top row) and a merger event (bottom row). Time progresses from left to right and the fields are separated by 1.0 second.

by a large perturbation when it interacts with neighboring vortices. If it begins to wander around the tank, it will generally disappear within a few characteristic decay times unless it returns to the preferred location. If a structure moves off its preferred location and disappears, a new structure will typically form, replacing the pre-existing one within a few decay times. Some long-lived coherent structures occasionally persist throughout the entire duration of an experimental run (~ 5000 vortex turnover times). Further, we observe persistent structures as low as 5 cm above the tees. Observations closer to the tees are difficult because the three-dimensional turbulent flow rapidly moves particles into and out of the laser sheet. However, these structures show up in the mean fields (cf. figure 4.11)

A wide range of spatial scales is visible in the velocity and vorticity fields [figure 4.4 (a) and (b) and figure 4.6]. The largest features, approximately 10 cm in size, are coherent vortices that have a much larger amplitude than their surrounding region. There are also large amplitude vortex filaments that stretch up to ≈ 10 cm; these can be as thin as the grid resolution, ≈ 0.3 cm in the transverse direction. Small scale persistent structures less than 1 cm in size yet large in amplitude are also observed. The region between the various large amplitude coherent structures is occupied by relatively low amplitude vorticity [see the vorticity trace in figure 4.4 (a)].

4.1.3 Correlations

The spatial correlations of the fields are plotted in figure 4.7. We take as the e-folding distance of the correlation curve as the correlation length of the corresponding field. This roughly corresponds to the radius of average structure size. The correlation length of the velocity field is typically more than twice that for the vorticity field. This can be seen in that the vorticity is typically concentrated in the core of a structure, while the velocity extends to its edges [see for example figure 4.4 (b)].

The time correlation of the vorticity field is shown in figure 4.8. The curves show good correlation for longer than a few seconds, though this is much shorter than the dissipation time scale and that of the long-lived vortices. However, the correlation curve is a measure

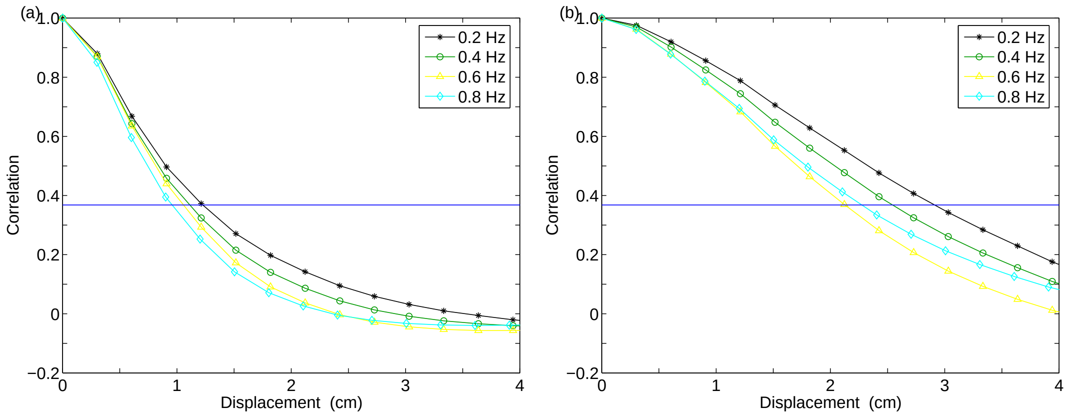

Figure 4.7: Spatial correlations of the flow fields at 426 cm^3/s pumping. The different curves correspond to different rotation rates. In general, higher rotation rate leads to more rapid decorrelation. (a) Spatial correlation of the vorticity field. The horizontal line indicates the e-folding length, $1/e \approx 0.37$. (b) Spatial correlation of the velocity field, averaged for a single horizontal component.

of the Eulerian field and can not track the structures. Therefore, if a structure moves from its original position, the overall calculated correlation of the field will decrease, despite the fact that the structure may still exist in future snapshots (albeit at a different location). Nevertheless, the time correlation give an idea of how rapidly the flow changes at a fixed location.

4.1.4 Mean flow fields

Mean vorticity fields for some characteristic conditions are shown in figure 4.9 and 4.10. Streamlines with arrows indicating the direction of circulation are plotted to render the corresponding mean velocity fields.

If the forcing were completely homogeneous and isotropic, the mean vorticity fields would have an amplitude much smaller that that of an instantaneous field and would also be devoid of structure. Instead, the mean fields have amplitudes which can be of order half of the instantaneous fields (but is typically much smaller than the most intense structures). This is indicative of the anisotropy of our forcing and the mean flow that it drives. The structure which appears in the mean fields reflects the persistent coherent structures [see

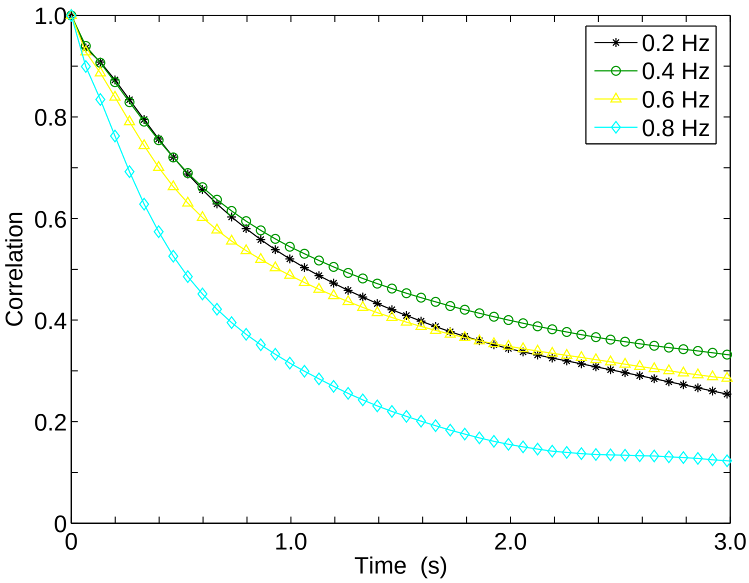

Figure 4.8: Time correlations of the vorticity fields at 426 cm^3/s pumping. The different curves correspond to different rotation rates.

the trace in figure 4.4 (a)].

Despite the anisotropy of our forcing, the mean flow structure can change drastically under different conditions[1]. Consider in figure 4.9 the changing pumping rate at fixed rotation rate. The amplitude of the mean fields increases with the pumping, reflecting the increase in energy input. However, the flow structure also changes. For the two conditions close to each other (272 cm^3/s and 426 cm^3/s pumping), the mean flow structure is similar. Both consist of a large anti-cyclonic region in the center of the tank with cyclonic regions on the periphery. This is possibly due to the shear between the anti-cyclonic center and the wall of the tank. Increasing the pumping a little further (to 580 cm^3/s) causes the anti-cyclonic center to break up and the mean flow structure looks much different. At the highest pumping rate (1248 cm^3/s), the anti-cyclonic region disappears completely and is replaced by a cyclonic circulation. The change in the mean flow structure for varying rotation rates at a fixed pumping is shown in figure 4.10. The changes are similar (but not the same as) to

---

[1] This can have implications in global climate change. i.e. what would happen if a change in some control parameter caused the jet stream or the gulf stream to change directions or disappear?

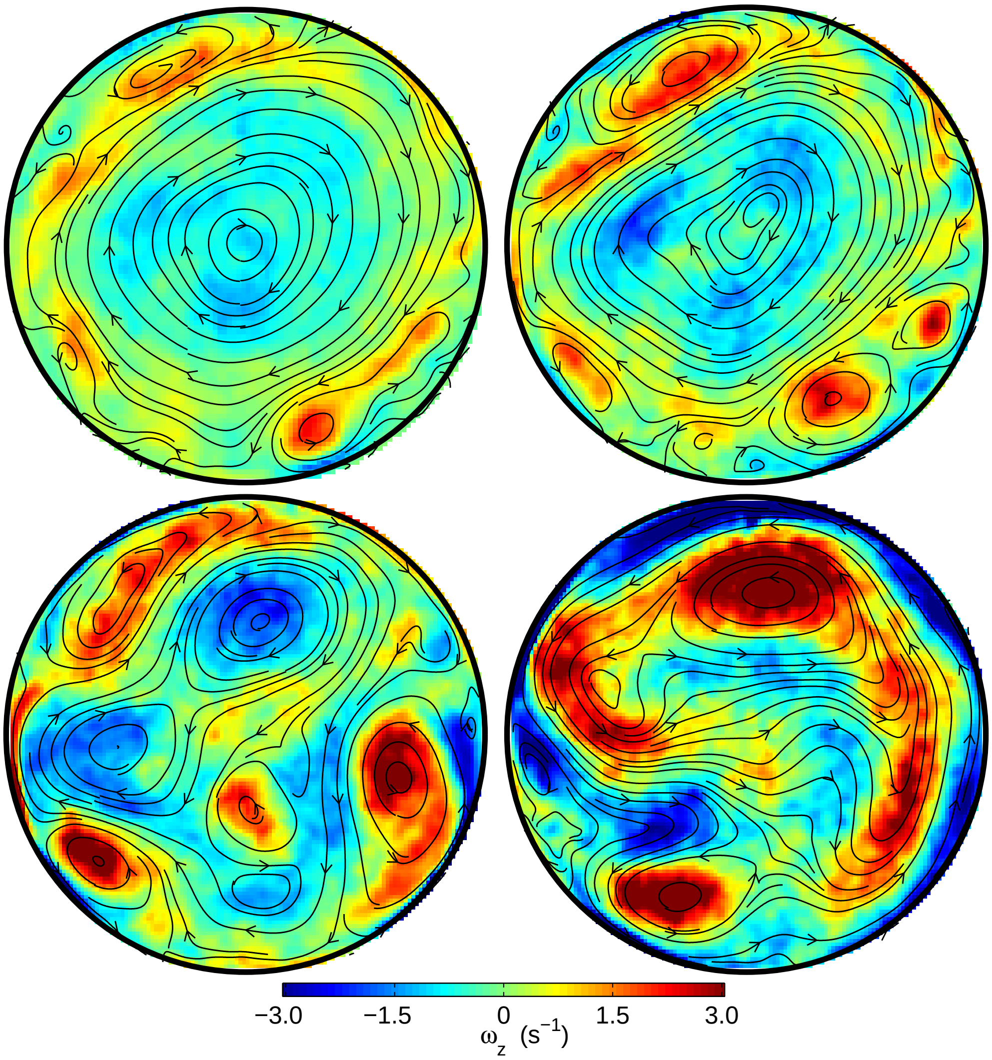

Figure 4.9: Average vorticity fields as a function of pumping rate. The rotation is fixed at 0.8 Hz. Top row: 272 cm^3/s and 426 cm^3/s pumping. Bottom row: 580 cm^3/s and 1248 cm^3/s pumping. The colorscale is the same for all plots and saturates at a value of ±3 s^{-1}.

those observed for varying pumping rates if one considers increasing rotation as analogous to decreasing the pumping rate. i.e. increasing rotation increases the dissipation and thus the relative strength of the forcing to the dissipation also decreases, for a fixed pumping rate. In all cases, the mean flow structure observed at a given forcing and rotation rate is robust. Hysteresis depending on the initial conditions of how the flow was set up was not observed.

Just how large a change in control parameter leads to a change in mean flow structure should be a subject of future study.

4.1.5 Dependence upon control parameters

4.1.6 Near the bottom

In figure 4.11 we compare the instantaneous and mean fields near the top and at a location near the forcing tees (30 cm below the top position) and for a fixed pumping and rotation rate. The instantaneous fields appear to contain very different structure, however the distribution of cyclonic and anti-cyclonic vertical vorticity is similar. The most striking difference is that closer to the forcing tees contains much more small-scale structure in the vertical vorticity field. This is likely due to the increased vertical motions near the tees.

Despite the large difference in flow structure, however, the mean horizontal statistical quantities do not change drastically. The mean fields also look surprisingly similar. For instance, the same cyclone anti-cyclone dipole is present in the mean fields in figure 4.11, which is difficult to see in the instantaneous fields. This may be due purely to the anisotropy of our forcing, however this supports the assertion that the flow structures observed near the top of the tank exist throughout the bulk, down to close by the forcing tees. The results of further investigation into the two-dimensional structure of our flow are presented in chapter 6.

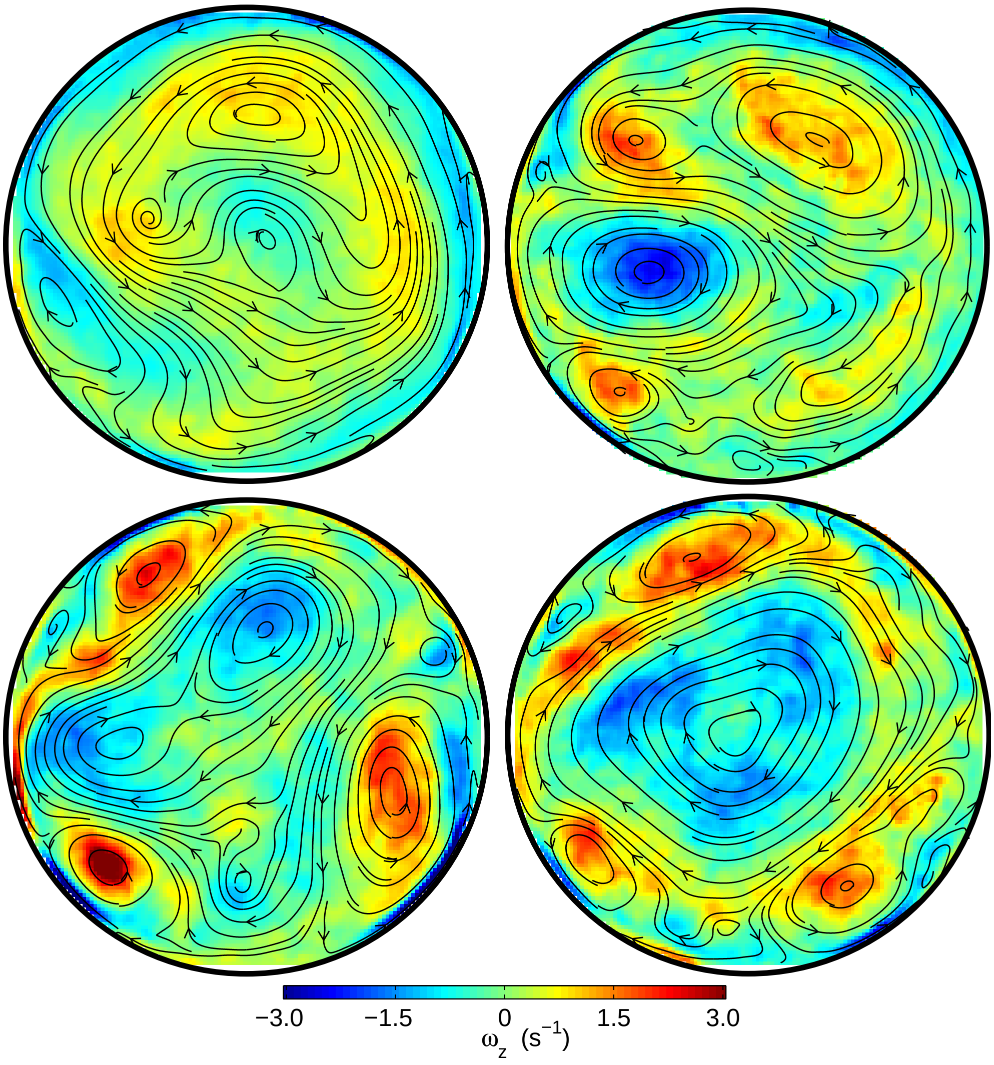

Figure 4.10: Average vorticity fields at a fixed pumping rate of 426 cm^3/s and varying table rotation rate. Left to right, top to bottom: 0.2 Hz, 0.4 Hz, 0.6 Hz, 0.8 Hz table rotation. The colorscale is the same as that used in figure 4.9 which saturates at ±3 s^{-1}.

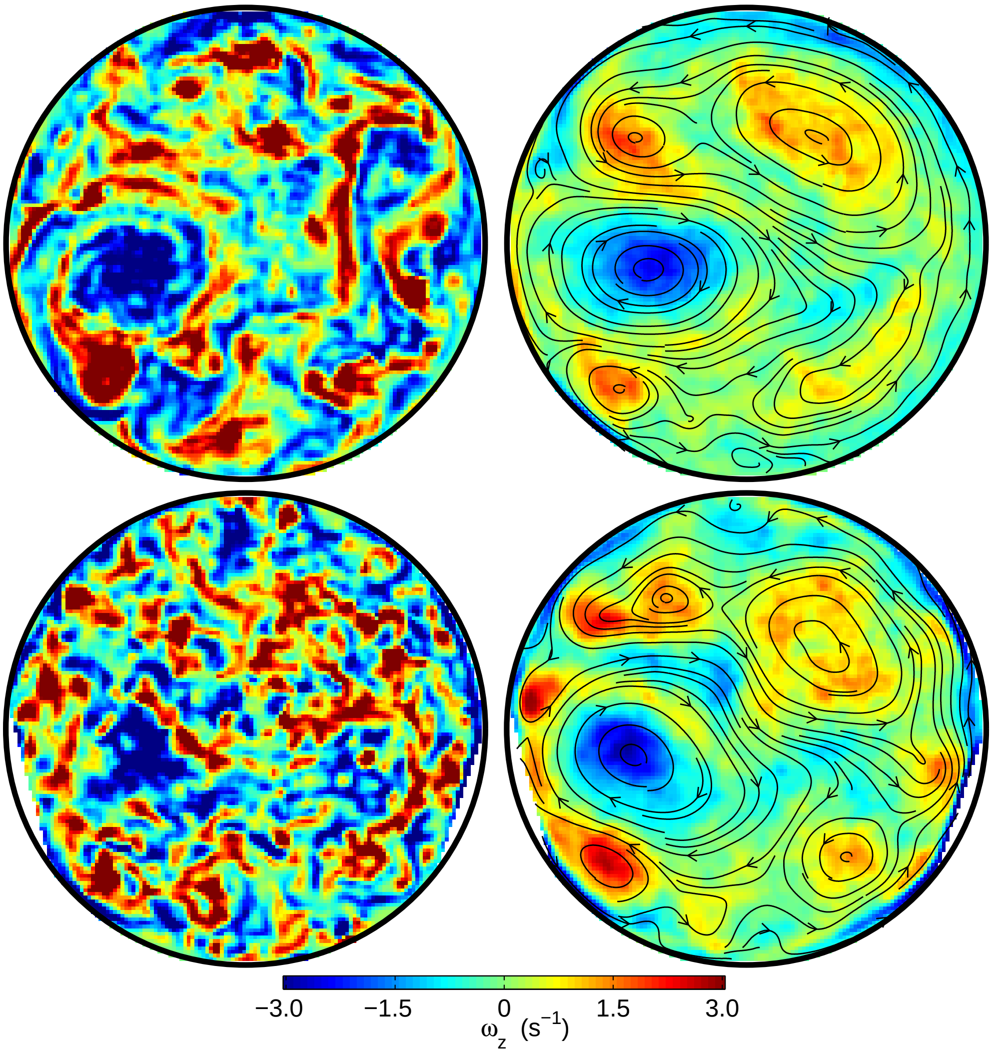

Figure 4.11: Dependence of fields upon height. Top row: near the top of the tank, bottom row: near the forcing tees. Left column: instantaneous fields, right column: mean fields. The rotation and pumping rate are fixed at 0.4 Hz and 426 cm^3/s.

4.2 Decay and dissipation

Characteristic decay times for our flow were measured by three different types of experiments. In each experiment, the measured decay time was taken as the e-folding relaxation time of the mean kinetic energy in the flow. The measured decay times are presented in figure 4.12. The numbers presented below are for the 0.4 Hz table rotation and 426 cm^3/s pumping condition data presented in chapter 5.

(i) Laminar (no forcing) *spin-down* experiments were conducted with the tees removed and replaced with a flat horizontal boundary. The tank was subjected to a sudden 10% decrease in rotation rate after the flow had reached solid-body rotation (no motion in the rotating tank frame). The predicted decay time of motions in laminar rotating flows with rigid, flat horizontal boundaries subject to small step changes in rotation is given by the *Ekman* dissipation time, $\tau = H/(2\sqrt{\nu\Omega})$, where H is the depth of the fluid, ν is the kinematic viscosity and $\Omega = 2\pi f$ is the angular frequency of the container [88]. The corresponding decay time for the energy in the flow is $\tau = H/(4\sqrt{\nu\Omega})$. For our closed cylindrical tank without topography of depth H = 48.4 cm, $\nu = 0.0095$ cm^2/s, and a rotation rate of 0.4 Hz, this gives a decay time of the energy as 78 s; the measured time was 64 s.

(ii) Laminar spin-down experiments were conducted in the same way as in (i), except that the tees were installed in the bottom of the tank. The characteristic decay time measured with the tees installed in the bottom of the tank for our flow was 18±3 s. The reduced laminar spin down time is due to the tees, which cause extra drag and secondary circulations that quickly bring the fluid to solid-body rotation.

(iii) Turbulent decay experiments were conducted by abruptly shutting off the forcing. For these experiments, the flow was allowed to reach a steady turbulent state (waiting many decay times) under a constant pumping rate of 426 cm^3/s and rotation rate of 0.4 Hz before abruptly turning off the forcing. The measured decay time of 13±3 s is still long compared to the typical vortex turnover time of 1 s.

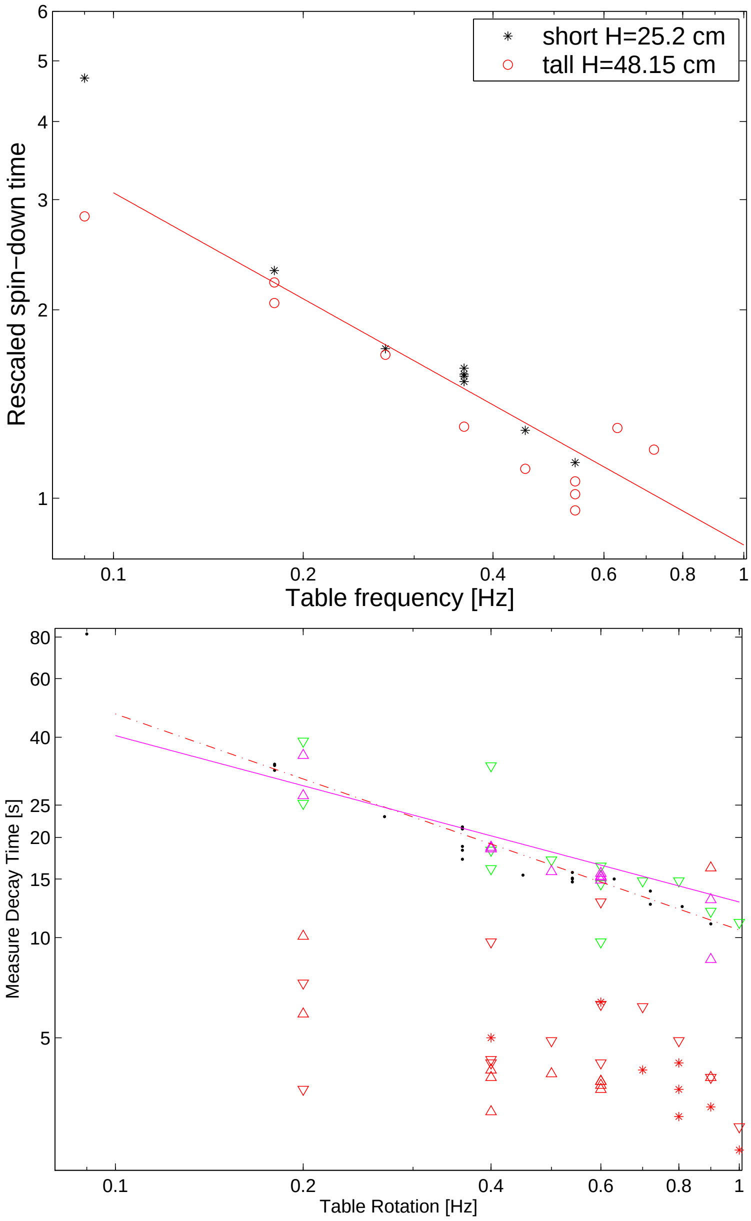

Figure 4.12: Results from spin-down and decay experiments. Top: Classical spin-down measurements with no bottom topography. The measured spin-down time has been rescaled by $[H/(2\sqrt{2\pi\nu})]^{-1}$. Bottom: Spin-down and decay experiments with the tees installed. The dots are the measured spin-down times. The green and magenta triangles are the measured “long” time decay exponents, as measured from the asymptotic decay behavior, from various driving conditions (pointing up for “high” driving and pointing down for “low” driving). The red symbols are all of the measured “short” decay times, as measured from the decay at very short times. The asterisks are for driven spin-down measurements (step change in rotation made while forcing). The dash-dotted line is the fit through the long decay time data. The fit has slope -0.61 ± 0.06 and corresponds to an effective height of about 10.6 cm. The solid line has $f^{-\frac{1}{2}}$ dependence and is about 20% of the laminar Ekman spin-down times. The long time decay data are grouped together along the curve fairly well and indicates that the relaxation of the flow at long times is similar to the process of relaxation after a small perturbation induced by changing the rotation rate of the system. The short decay times may have a weak dependence on rotation rate. Taken from reference [99] (see this reference for more on the decay experiments).

4.3 Vertical velocities

Particle streak images taken in a vertical plane are shown in figure 4.13. Near the bottom forcing tees, the flow is quite 3D and the particle streaks do not display much organization. Near the top in the quasi-2D flow region, the particle streaks are more organized. In particular they move primarily in the horizontal direction, producing streaks from left to right. However, we also observed particle streaks that stream upwards towards the lid (e.g. the top image in figure 4.13). These streaks also appear to turn over and return downward in other parts of the flow. This may act as an additional circulation on top of the Ekman pumping, enhancing the dissipation. At low rotation rates (< 0.1 Hz) we did not observe this behavior.

If our flow were rotationally dominated as per Taylor-Proudman and ideally 2D, the vertical velocities would be zero[2]. However, we observe large vertical velocities as shown in figure 4.14. Indeed, the vertical velocities can be on the order of the horizontal (e.g. the largest vertical velocities in figure 4.14 are 10-12 cm/s[3]).

The large vertical velocities appear more intermittently at larger rotation rates (cf. 0.1 Hz and 0.6 Hz in figure 4.14). Furthermore, they appear to be associated with the coherent structures. The vertical velocities transport momentum and energy to the boundaries of the tank, where it is dissipated. Typical Ekman pumping velocities are of the order of the Rossby number times the vertical vorticity. This may be the cause of the faster decay times than predicted by the Ekman spin-down time (see sections 4.2 and 2.3.4).

4.4 Mean quantities and variation of control parameters

In figure 4.16, 4.17, and 4.18, we show how various mean statistical quantities of the flow fields change as a function of the control parameters and location in the tank. In figure 4.16 the dependence upon pumping rate, in figure 4.17 the dependence of the quantities on

---

[2] Strictly speaking the vertical gradient of the velocity field should be zero. However, since we have a rigid lid this puts the boundary condition of zero vertical velocity at the top of the flow.

[3] n.b. this is for a very high forcing condition where the horizontal velocities are up to 20 cm/s

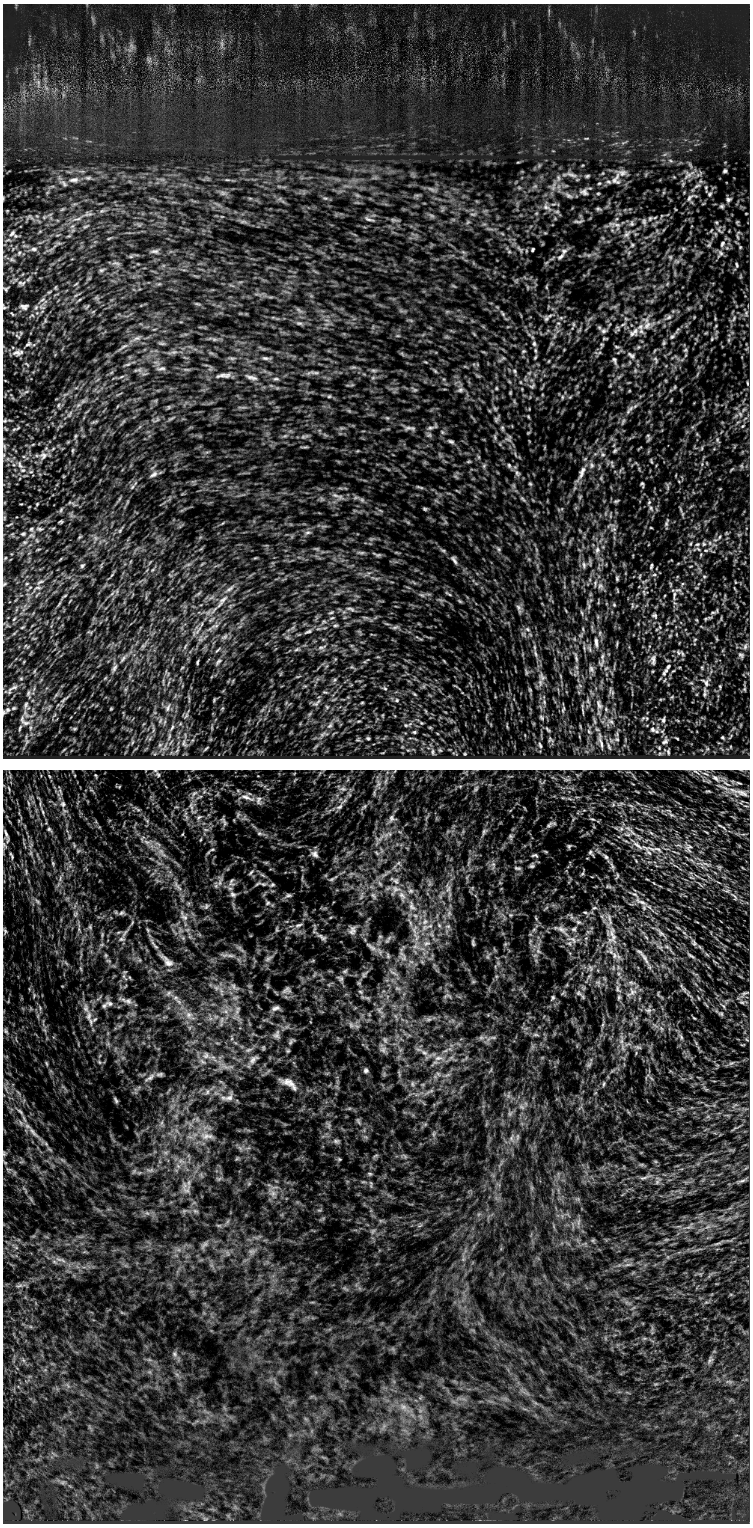

Figure 4.13: Particle streak images of the vertical velocities at 0.6 Hz rotation and 1042 cm^3/s pumping. TOP: Near the lid. A vertical "fountain" can be seen. Particle streaks appear to be broken because of the large velocities transverse to the light sheet. BOTTOM: Near the forcing tees, the ghost of which can been seen at the bottom of the image. The particle paths are disorganized, due to the 3D turbulent forcing. Consecutive images were averaged to produce an effect exposure time of 0.4 seconds. The regions are roughly 11.5 cm × 11.5 cm.

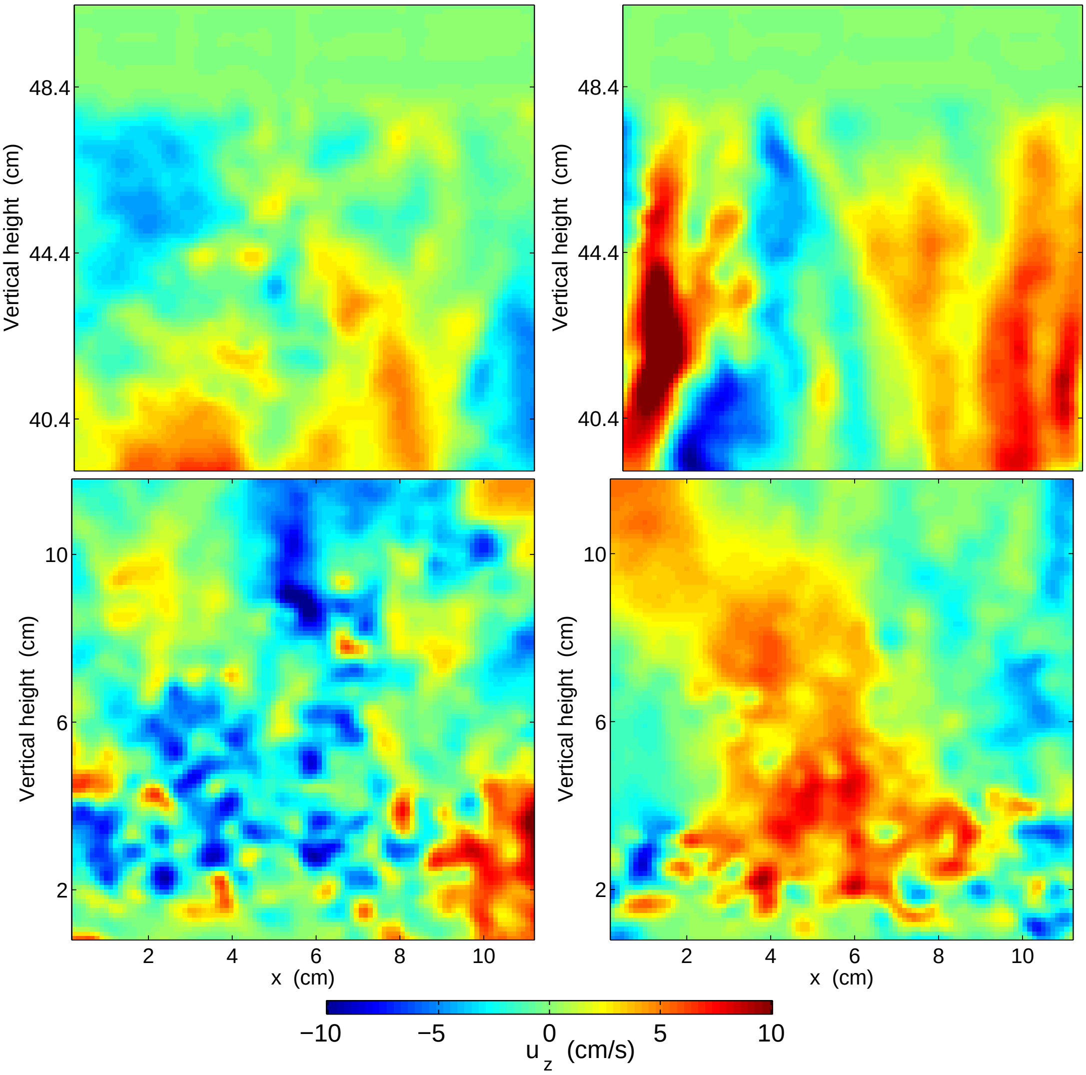

Figure 4.14: Four snapshots of vertical velocities measured from the vertical light sheet. The top row are from near the top of the tank, just below the lid. Each snapshot corresponds to an approximately 10 × 10 region. The bottom row are from data near the forcing tees at the bottom of the tank. The left column corresponds to low rotation (0.1 Hz) and the right column to moderate rotation (0.6 Hz). The colorscale indicates the magnitude of the vertical velocity.

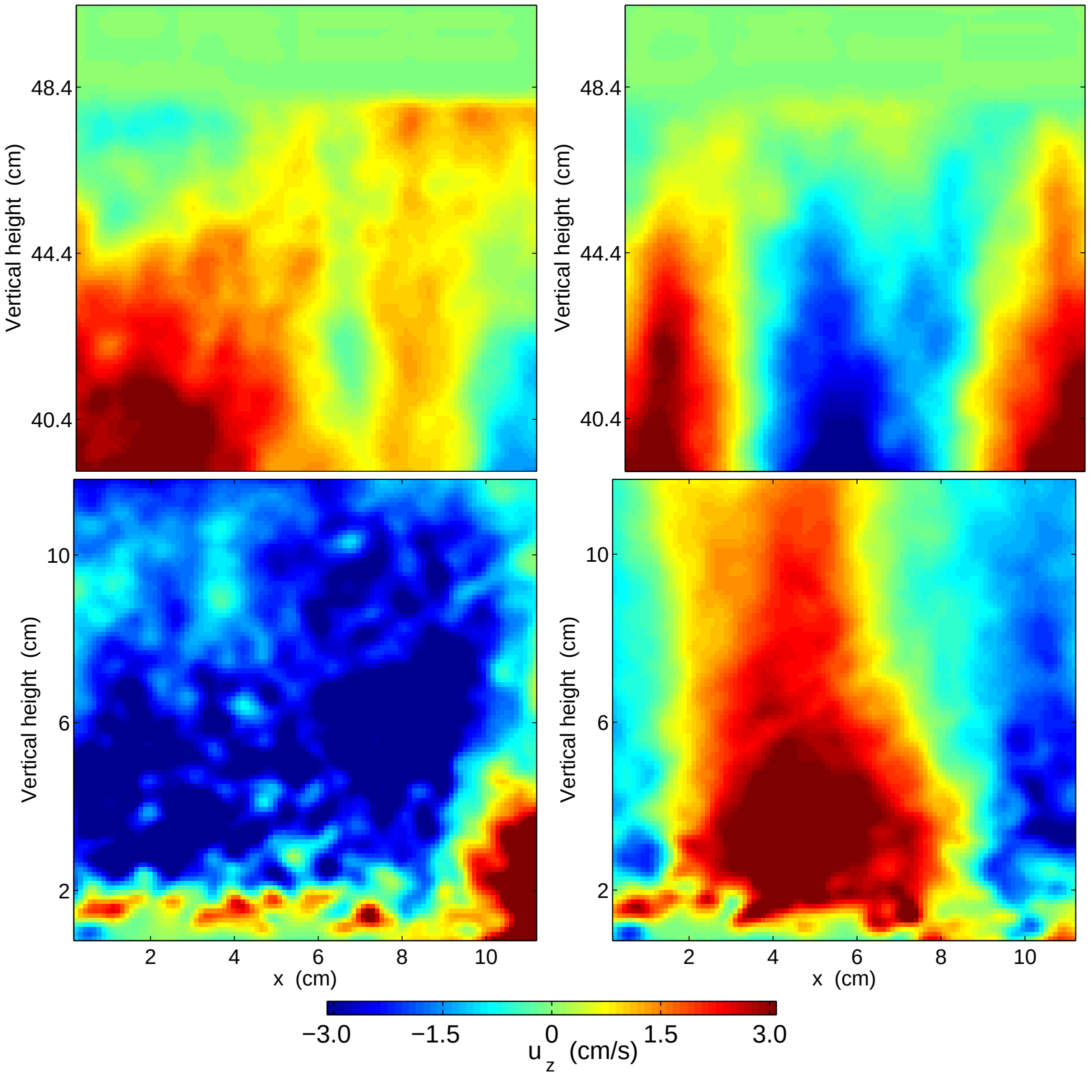

Figure 4.15: Mean vertical velocity fields measured from the vertical light sheet. The top row are from near the top of the tank, just below the lid. Each snapshot corresponds to an approximately 10 × 10 region. The bottom row are from data near the forcing tees at the bottom of the tank. The left column corresponds to low rotation (0.1 Hz) and the right column to moderate rotation (0.6 Hz). The colorscale indicates the magnitude of the vertical velocity.

the table rotation rate, and in figure 4.18 the dependence upon the height in the tank is shown. We plot the RMS velocity, RMS vorticity, RMS divergence, and the Rossby number (computed from the RMS vorticity). In each figure, the statistical quantities were calculated from the mean-subtracted fields, except for the RMS divergence. Similar symbols correspond roughly to similar conditions (taken at different times). Some of the data for the same condition is scattered, however there are noticeable consistent trends which emerge.

The effect of increasing the pumping rate is to increase the amount of energy injected into the flow. The increase in energy appears to make it to the top of the tank. One effect is to produce larger, more energetic flow structures (see figure 4.9 and spectra). This also results in larger velocity scales. The RMS quantities all increase almost linearly with increasing pumping rate. This implies that the increase in the velocity scale is more rapid than that of the length scale with increasing pumping.

The RMS velocity increases slowly with increasing rotation (figure 4.17) This is likely due to the enhanced two-dimensionalization of the flow from the increased influence of rotation. As the rotation increases, the flow tends to become more 2D and the transport of energy from the bottom forcing is more efficient. This results in larger energy, and thus larger velocities near the top for a fixed pumping rate.

The RMS vorticity also increases slowly with increasing rotation rate. However, this increase is more rapid than the RMS velocity. This is consistent with smaller structures due to enhanced dissipation at higher rotation rates (see section on dissipation and spectra). i.e. for a fixed velocity scale and smaller length scale, the vorticity scale will be larger ($\omega \sim U/L$). This is also apparent in the similarly slow increase in RMS divergence (figure 4.17). The increase in the RMS vorticity is slower than linear, and thus the Rossby number decreases slowly with increasing rotation ($Ro = \omega_{RMS}/2\Omega$). This is typically interpreted as increasing two-dimensionality. The ratio of the RMS divergence to the RMS vorticity is typically close to the Rossby number (e.g. at 0.4 Hz rotation and 426 cm^3/s, RMS divergence / RMS vorticity = 0.55/1.66 = 0.33, which is the same as the Rossby number calculated from the RMS vorticity).

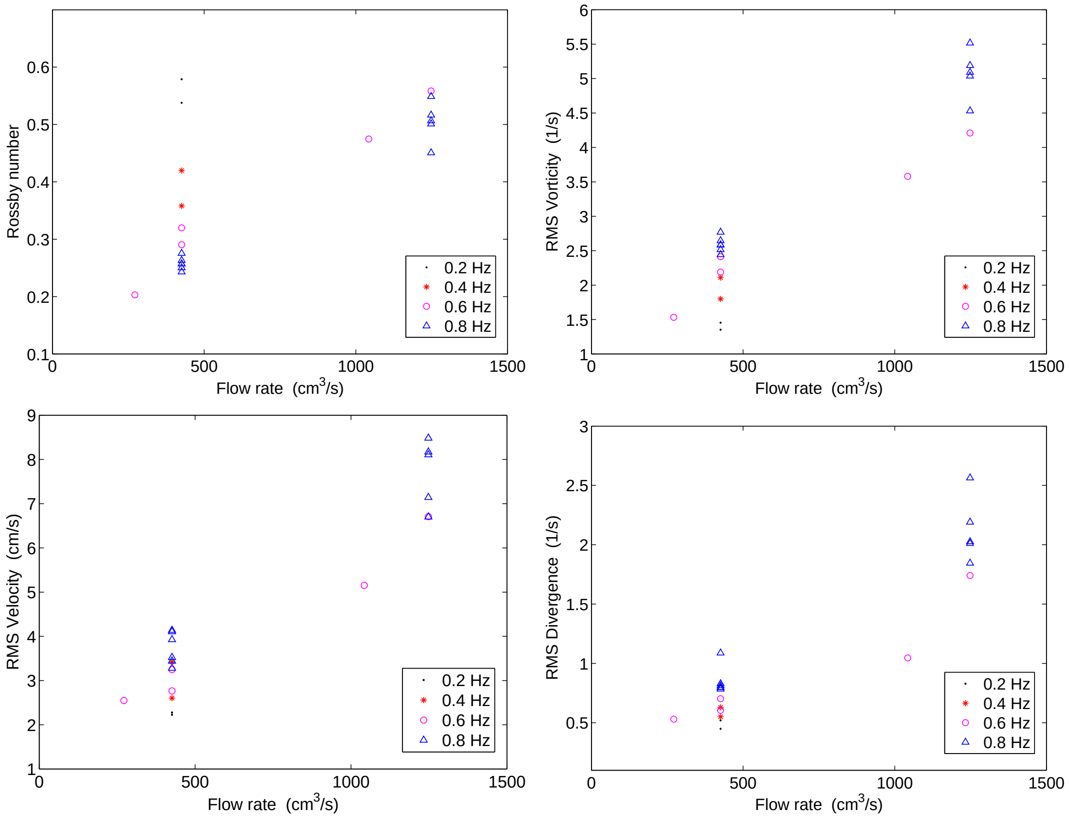

Figure 4.16: Statistics versus pumping rate. The pumping rate is related to the amount of energy injected into our flow (see equation 3.2, relating Q to energy input). Left to right, top to bottom: Rossby number, RMS vorticity, RMS velocity, RMS divergence.

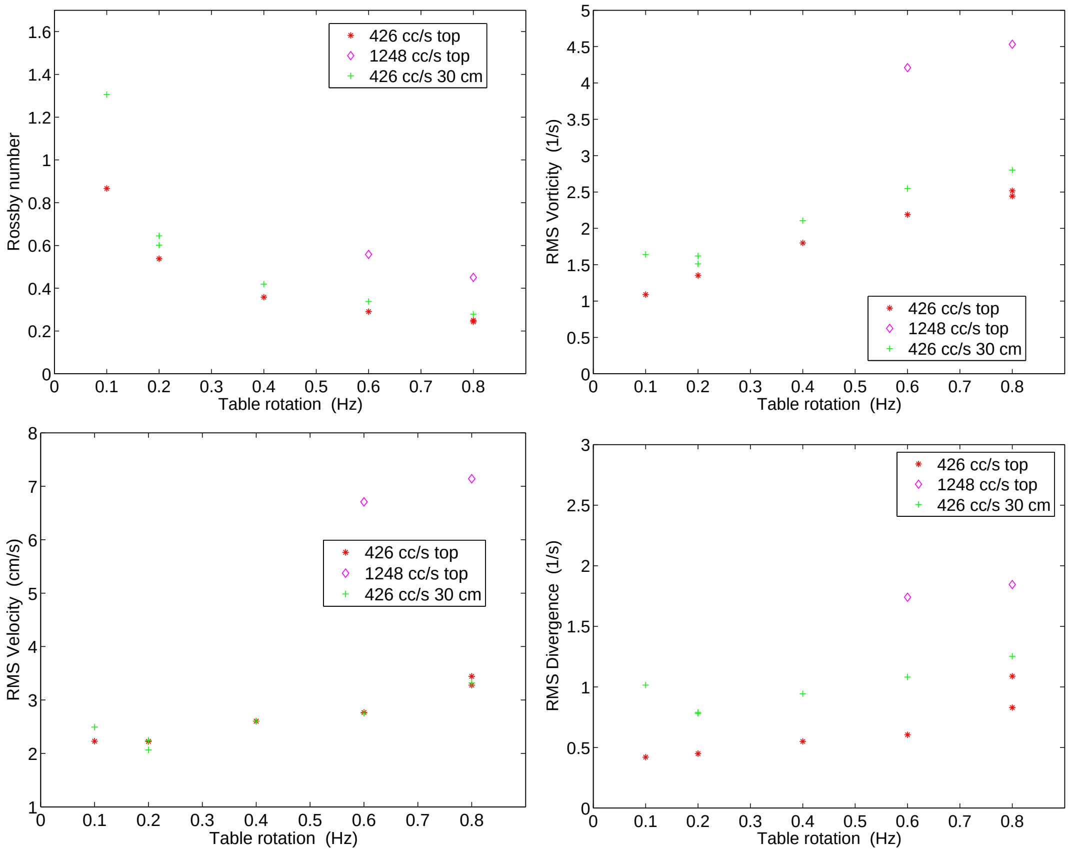

Figure 4.17: Statistics versus table rotation frequency. Left to right, top to bottom: Rossby number, RMS vorticity, RMS velocity, RMS divergence.

As a function of height, the RMS velocity does not seem to change much (figure 4.17 and 4.18). The vertical velocities, however increase closer to the tees (see section 4.3). This implies that the flow becomes more 3D closer to the tees as the ratio of energy in horizontal to vertical components becomes more isotropic.

This is interpreted as an increase in the three-dimensionality of the flow as the rotation becomes relatively less dominant closer to the forcing tees. However, the increase in the Rossby number is not as drastic as one might expect. This is likely due to the fact that we calculate the Rossby number from only the vertical component of the vorticity. The Rossby number from the full three-component vorticity is likely to be much larger (i.e. approximately $\sqrt{3}$ times larger for a more isotropic distribution of vorticity) as $< |\omega_x| >$ and $< |\omega_y| >$ components become $\approx < |\omega_z| >$.

4.4.1 Vorticity PDFs

Some sample vorticity and divergence PDFs are plotted in figure 4.19. Figure 4.19 (a) compares the magnitude of the divergence and vertical vorticity of the flow in our tank at two different heights. The divergence in our flow fields is small relative to the vorticity and 2Ω ($\approx$ 5 rad/s). The divergence field consists of small length-scales near the top and has a weak correlation with the vorticity field. The ratio of the RMS divergence to the RMS vorticity is 0.2, of the same order as the Rossby number. Near the bottom forcing, however, the divergence field becomes larger in amplitude, length-scale, and more strongly correlates with structure in the vorticity field. The inset in figure 4.19 (a) shows the ratio of the divergence to vorticity increases near the forcing, where the flow is more 3D and decreases near the top, where the flow is more 2D.

The vorticity PDFs are non-Gaussian. They are both skewed (asymmetrical) and have broad tails. In the inset of figure 4.19 (b), the PDFs are normalized by their respective RMS values (e.g. the RMS vorticity and divergence in figure 4.17). After normalizing, all of the vorticity (and divergence) PDFs collapse upon one another near small values. Some difference still occurs at the tails, which contain the large amplitude coherent structures.

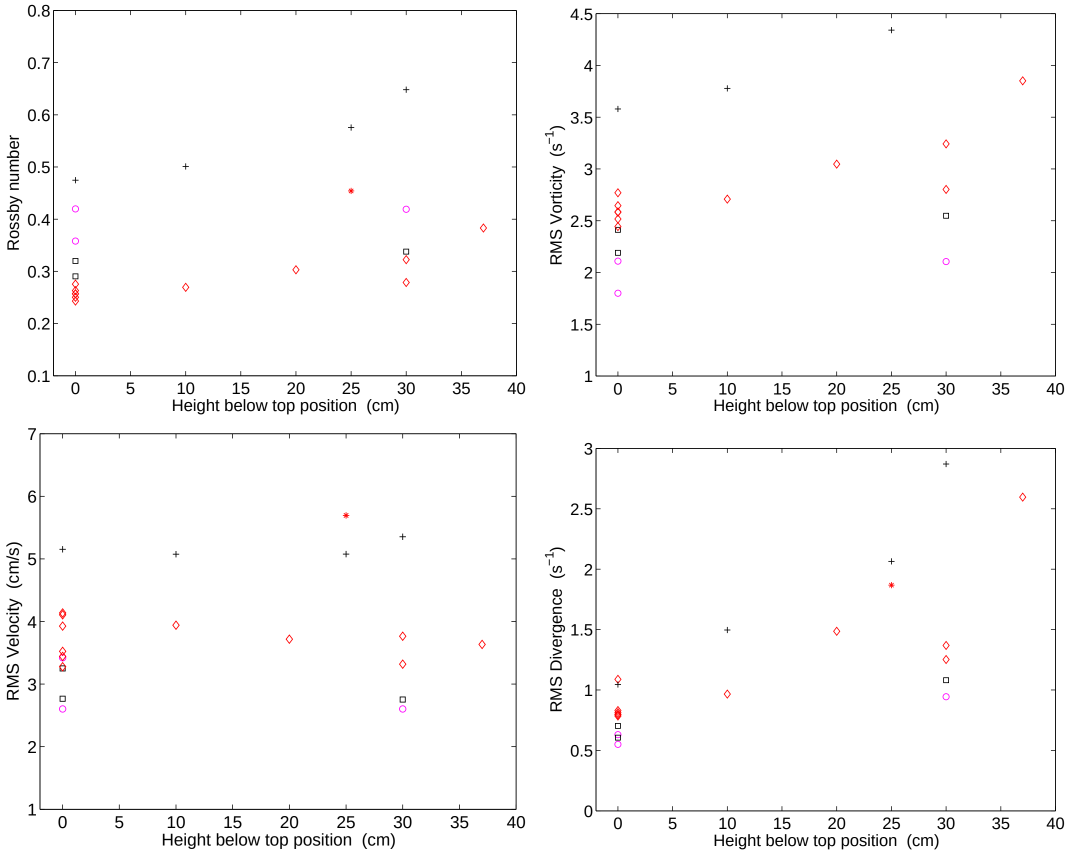

Figure 4.18: Statistics versus height below the top position. Similar symbols correspond to similar flow conditions with the larger, more open symbols corresponding to higher pumping and rotation rates. Circles, squares, and diamonds correspond to 0.4, 0.6, and 0.8 Hz rotation at 426 cm^3/s pumping; "+" corresponds to 0.6 Hz rotation at 1246 cm^3/s pumping. Left to right, top to bottom: Rossby number, RMS vorticity, RMS velocity, RMS divergence.

The conditions of higher driving have larger tails which do not collapse upon the rest of the curves, due to the larger values of intensity in the coherent structures. The divergence PDFs are much more symmetric and closer to Gaussian. However, deviations become increasing large for larger pumping rates.

4.4.2 Spectra

Some of the resulting energy and enstrophy spectra are shown in figure 4.20 (a-b) for the fields near the top of the tank for low (426 cm^3/s) forcing and in figure 4.21 for high (1248 cm^3/s) forcing conditions. Spectra for the fields near the bottom of the tank at the low forcing condition are shown in figure 4.21 (c-d).

In all cases, it can be seen that most of the energy and enstrophy resides in the large-scale, at small wavenumber, k. This is consistent with the intense large-scale structures present in our fields. This is also consistent with an inverse cascade of energy from a small-scale forcing towards large-scale structure. However, our forcing must be broad-band, as evidenced by the large-scale structure in the mean flow fields (figure 4.9 and figure 4.10). Additionally, the forcing is inhomogeneous (at the bottom as opposed to uniform through the tank).

There energy spectra has a scaling of roughly $\mathrm{k}^{-2.5}$ which may become shallower at lower rotation and closer to the tees. As rotation becomes more dominant and with sufficient nonlinear interactions, the energy spectrum is expected to scale as k^{-3}. As more energy is transferred into 2D modes from 3D modes due to rotation, the spectra should begin to follow this scaling. Near the tees [figure 4.20 (c-d)], the influence of rotation is less and the scaling appears weaker.

In the enstrophy spectra, however, there is no clear scaling Though the enstrophy spectra for the high driving near the top has a kink around $1/\mathrm{k} \approx 0.7$ cm (figure 4.21). The spectra are split into a region of exponent roughly -1.3 in front of the kink and a steeper region around -4 after the kink. The low driving enstrophy spectra do not have a scaling region and instead gradually turn over from a shallow -1.4 to a steeper -5 slope.

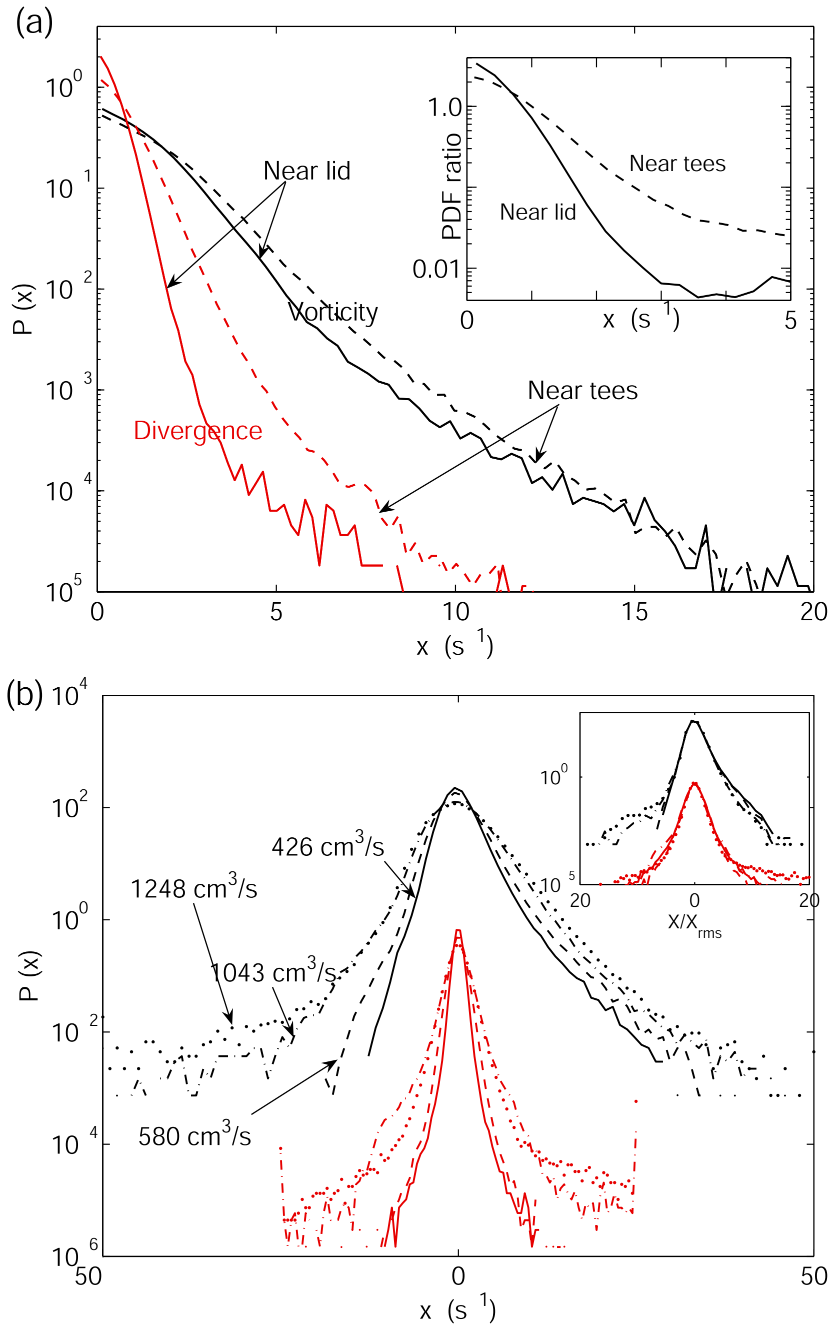

Figure 4.19: (a) The PDF of the magnitude of vertical vorticity and divergence at two different heights in our tank, 4 cm below the lid (solid curves) and 10.4 cm above the top of the tees (dashed curves). Inset: the ratio of the divergence PDF to the vorticity PDF, showing the increase in the relative magnitude of the divergence near the forcing. (b) PDFs of vorticity and divergence for 0.8 Hz rotation and various pumping rates (1248 cm^3/s, 1043 cm^3/s and 426 cm^3/s). The vorticity PDFs are shifted upwards. The inset shows the collapse of the PDFs near their center after normalizing by the RMS.

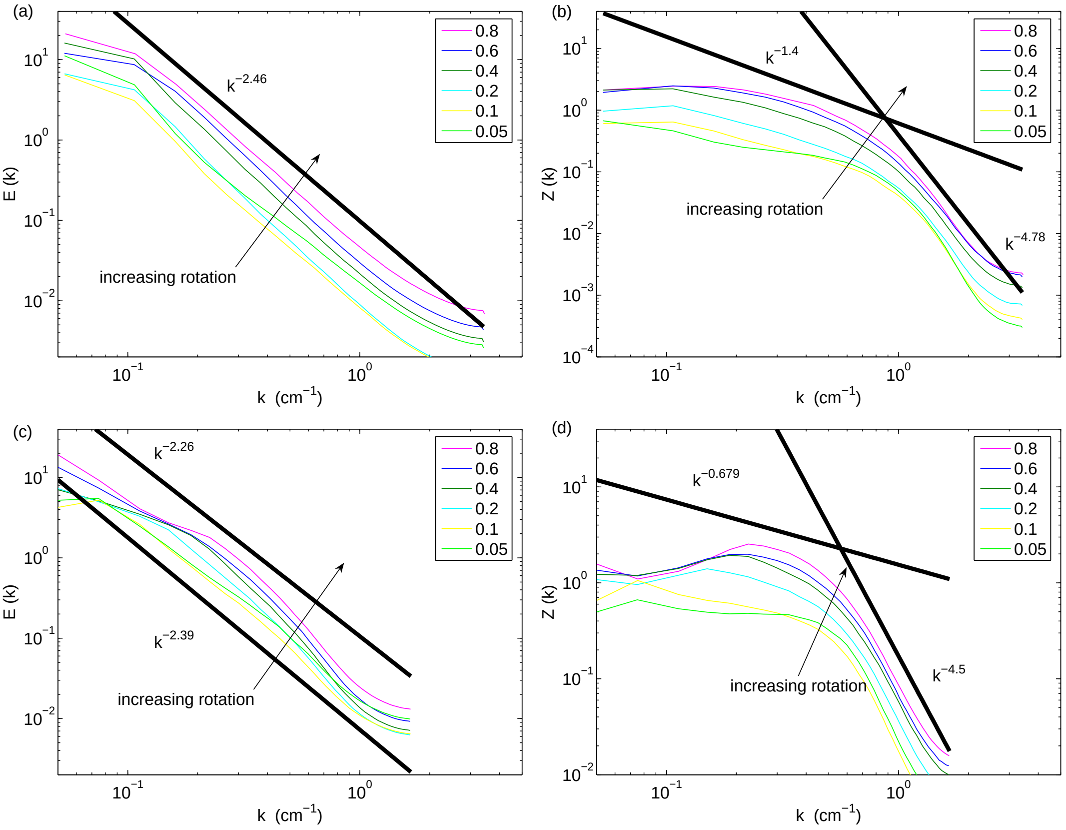

Figure 4.20: Energy (left column) and enstrophy (right column) spectra (a-b) near the top and (c-d) 30 cm below the top position at low pumping (426 cm^3/s) and various rotation rates. The spectra were calculated for a 27 cm by 27 cm square subset of the full tank. Note: $k = 1/L$ (no 2π)

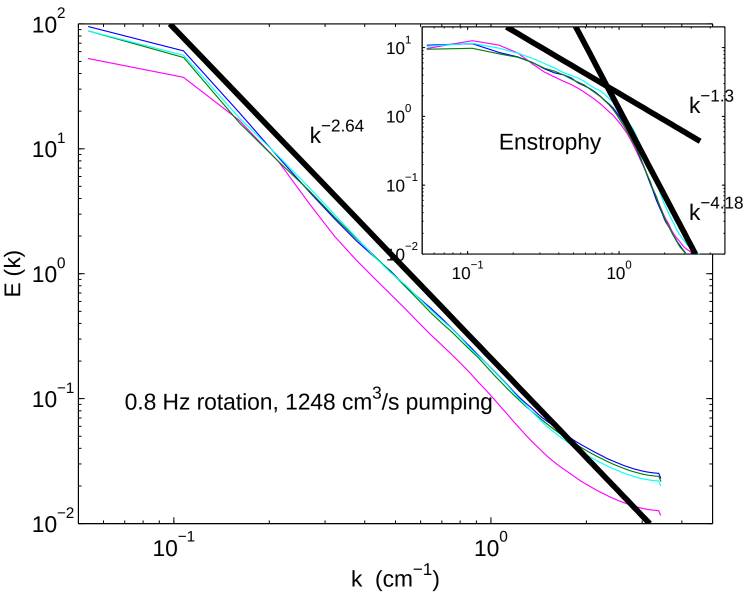

Figure 4.21: Energy and enstrophy (inset) spectra at the top of the tank and at high pumping (1248 cm^3/s) and 0.8 Hz rotation. The spectra were calculated for a 27 cm by 27 cm square subset of the full tank. Note: $k = 1/L$ (no 2π)

The spectra near the bottom, shown in figure 4.20 (c-d), reflect the increased three-dimensionality structure in the fields. As the flow is less rotationally dominated and more 3D, less energy inverse cascades and more forward cascades towards the small scales. Thus, the slopes of the spectra are shallower and relatively more energy is contained in the small scales. This can be seen in the increased relative intensity of the small scales in the vorticity field near the bottom figure 4.11.

However, we should be careful not to over-analyze these spectra for a number of reasons. (i) We do not have the narrow-band forcing assumed by most turbulence models and simulations. (ii) We do not have access to the full 3D fields. And (iii) what scaling appears to exist is only over a small region, much less than a decade.

4.5 Summary

We can generate large-scale, long-lived structures in our tank. The structures are coherent vortices and jets which have amplitudes much larger than the background flow. The lifetimes of the persistent coherent structures is large compared to the timescales in the flow, e.g. rotation: 1 second, advective: 1 second[4], dissipative: 20 seconds. The structures dominate the flow dynamics and lead to skewed, broad winged vorticity PDFs. The structures appear to exist throughout the volume of the tank, but are most prominent features near the top where the flow looks increasingly 2D.

In general, higher rotation rates lead to smaller flow structures. This is likely due to the increased dissipation from the stronger Ekman pumping at the higher rotation. This decreases the overall amount of energy which makes it up the inverse energy cascade to the large scale structures. As a result, more small scale structures remain and the spatial correlation is correspondingly shorter.

By a similar argument, higher forcing in general leads to larger flow structures. At higher pumping rates, the amount of energy injected into the flow is larger. Thus there is more energy available to be transferred to the large-scale structures.

The real story, however, is more complicated. The interaction between the anisotropy of the forcing and the control parameters combine to produce different flows which do not simply depend upon the forcing and rotation rate.

---

[4] Order of magnitude estimated by U/L.

Chapter 5

Coherent structure extraction

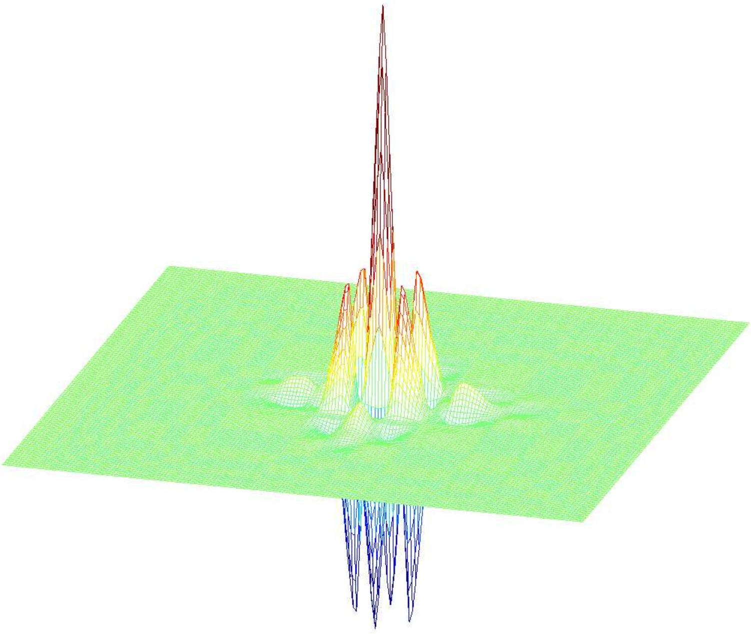

In this chapter we present the results of coherence structure extraction applied to our flow field and the results of advection of a passive scalar in the resulting fields. For the presented analysis, we use a single flow condition at 0.4 Hz table rotation and 426 cm^3/s pumping, which corresponds to a state with long-lived persistent coherent structures (for more details of the flow conditions, see chapter 4). Much of the contents of this chapter are taken verbatim from [100], with the appropriate modifications to fit into the content of the dissertation.

5.1 Wavelets and wavelet packets

5.1.1 Overview

The discrete wavelet transform (DWT) is a multi-resolution analysis that successively decomposes the signal into coefficients which encode coarse and fine details at successively lower resolution [127]. The basis elements of the transform $\psi_{p,s}$ correspond to dilations and translations of a mother wavelet function ψ, where p is the position (translations) of the wavelet and s its the scale (dilations). Successive levels of the transform continue to split the coarse detail coefficients, effectively analyzing the signal at coarser and coarser resolution.

The discrete wavelet *packet* transform (DWPT) is a generalization of the discrete wavelet transform. The basis elements of the wavelet packet transform include, in addition to dilations and translations, spatial modulation of the mother wavelet at different resolutions. The basis elements $\psi_{p,s,k}$ take on an additional parameter k that roughly corresponds to the modulation of the wavelet packet. In contrast to the DWT, the choice of basis of the DWPT is not unique [32]. The wavelet basis is contained within the possible choices of wavelet packet bases. To select the particular basis to use, a natural choice is the wavelet packet basis into which the coefficients of the transform most efficiently represent the signal. This is known as the “best basis”. The best basis is typically calculated based upon the minimization of an effective entropy measure of the coefficients [127], thus minimizing the "information cost" of the coefficients in the best basis. The flexibility in basis choice of the DWPT allows the transform to adapt the basis to the particular signal being analyzed. For example, if the signal contains regions of rapid fluctuations, the basis choice will reflect that by including more basis elements with high modulation.

We use the DWT [$O(N)$ operations] and DWPT [$O(N \log_2 N)$ operations] on our experimentally obtained vorticity fields, as previous authors have done using 2D turbulent flow data from numerical simulations in a periodic square domain (e.g. [40, 105, 41]). We use the MATLAB wavelet toolbox and the coiflet 12 (coif2 in MATLAB notation) as the analyzing wavelet. The coiflet family of wavelets (see reference [32], p. 258) has both compact support and can generate an orthogonal basis. These two properties allow one to select the localized features of the coherent structures and to treat the decomposition of the vorticity field as two orthogonal components. The choice of wavelet does not alter the results significantly as long as the basis is sufficiently smooth [41].

5.1.2 Mathematical details of discrete wavelet transforms

An arbitrary signal f can be decomposed and written as a sum of a set of basis functions, ϕ_n

$$f = \sum_n c_n \phi_n \tag{5.1}$$

The coefficients c_n's correspond to the inner product of the signal and the n^{th} basis such that $< f|\phi_n >= \sum_i f(x_i)\phi_n(x_i)$. If the basis functions are orthonormal, they satisfy the relation $< \phi_n|\phi_m >= \delta_{mn}$.

For example, the usual functions for decomposition are the sine functions, i.e. $\phi_n(x) = \exp(-2\pi inx)$ in Fourier analysis (i.e. sines and cosines). However, we will be using wavelets and wavelet packets for our transforms, in particular what MATLAB refers to as the coif2 family of wavelet (see figure 5.2).

For the continuous wavelet transform

$$\hat{f}(p,s) =< \psi_{p,s}|f >= \int \psi_{p,s}(x) f(x) dx \tag{5.2}$$

where the $\hat{f}$ indicates the transform of the function. The subscripts on the wavelets $\psi_{p,s}$'s are defined as

$$\psi_{p,s}(x) = s^{-1/2}\psi(\frac{x-p}{s}) \tag{5.3}$$

where the p corresponds to the translations and s to the dilations of the wavelet basis function. The $\hat{f}(p,s)$'s thus correspond to the coefficients of the transform at a particular scale and position.

The continuous transform results in a function of more variables than the original function! The continuous representation of the wavelet transform is thus not orthogonal. However, we will be using the discrete orthogonal transform with discrete orthonormal wavelets and wavelet packets for our transforms (see figure 5.2 for the coif2 family of wavelet).

The wavelet, $\psi(x)$ an oscillating function with $\int \psi(x)dx = 0$, and its associated scaling function, $\phi(x)$ a low pass equivalent with $\int \phi(x)dx = 1$, can be defined by the two-scale dilation equation

$$\begin{aligned} \phi(x) &= \sqrt{2}\sum_p h_p \phi(2x+p) = H\phi & (5.4)\\ \psi(x) &= \sqrt{2}\sum_p \tilde{h}_p \phi(2x+p) = \tilde{H}\phi & (5.5) \end{aligned}$$

where the h_p's are the coefficients of a low pass filter H (i.e. the Fourier transform of the filter at zero frequency, $\hat{H}(0) = 1$) and the $\tilde{h}_m$'s are the filter coefficients of the *conjugate mirror filter* (CMF), $\tilde{H}$ defined as

$$\tilde{\mathrm{H}} = [\tilde{h}_p] = (-1)^p \bar{h}_{1-p} \tag{5.6}$$

where the tilde represents the conjugate mirror and the over-bar is the complex conjugate. The CMF sends the low (high) pass filter into its high (low) pass equivalent. The wavelet family is uniquely determined by the coefficients of the associated filter H. The restriction on orthogonality being that the filter satisfies the relation

$$\frac{1}{2}(|\hat{H}|^2 + |\hat{\tilde{H}}|^2) = 1 \tag{5.7}$$

Thus the two-scale dilation equation tells us that we can obtain the mother wavelet or the scaling function by the scaling function and filter at a particular resolution. Because the filter H is low pass, the scaling function is a low frequency function (i.e. the Fourier transform $\hat{\phi}(0) = 1$). The high pass CMF $\tilde{H}$ that produces the wavelet ensures that the wavelet is a high frequency function (i.e. $\hat{\psi}(0) = 0$).

The convolution of two finite sequences, h of length M and f of length N is calculated by

$$(h \circ f)_j = \sum_{k=-M/2+1}^{M/2} h_k f_{j-k} \tag{5.8}$$

The coefficients of the wavelet and wavelet packet transforms are computed by filtering and then down-sampling $(\downarrow 2 \circ H)$. The down-sampling operation, $\downarrow 2$, corresponds to discarding every other point, effectively halving the resolution of the original signal. The convolution operation corresponding to a wavelet transform is thus

$$(\downarrow 2 \circ H)f = \sum_{k=-M/2+1}^{M/2} h_k f_{2j+1-k} \tag{5.9}$$

The coefficients of the transform are obtained depending upon which filter, H or $\tilde{H}$, was applied. The low pass filter H produces the "approximation" coefficients that encode the coarse details of the signal. The high pass filter $\tilde{H}$ produces the "detail" coefficients that encode the fine details of the signal. Successive application of the filters on the coefficients result in a branching tree-like structure. An example is shown in figure 5.1. As a result

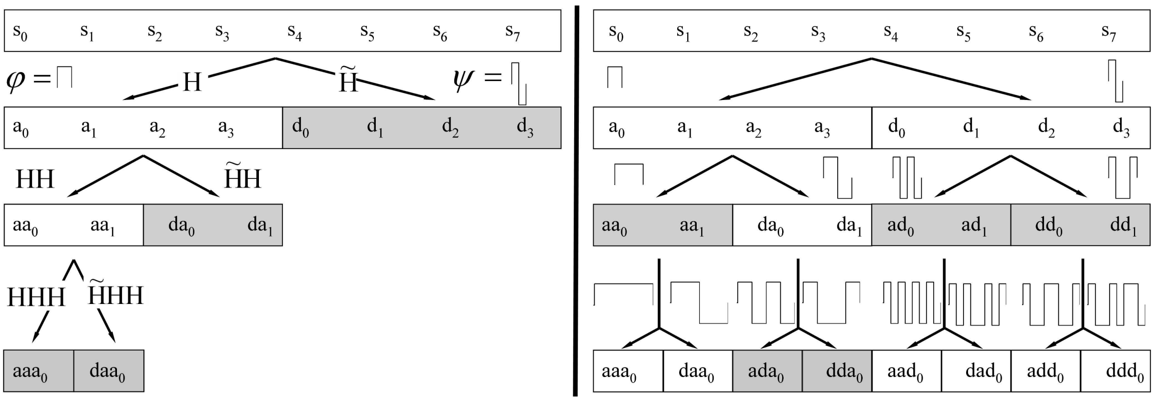

Figure 5.1: LEFT: A wavelet decomposition tree for a one dimensional signal analyzed by the Haar wavelet. i.e. H is taken as the Haar filter ($H \equiv h_m = [1/\sqrt{2}, 1/\sqrt{2}]$ for $m = 0, 1$; $h_m = 0$ for $m \neq 0, 1$). RIGHT: A wavelet packet decomposition tree. In both, the shaded branches of the tree indicate the basis coefficients. Notice that the wavelet basis is contained within the wavelet packet decomposition tree. The "a" and "d" correspond to approximation and detail. Shown on the wavelet packet tree are the basis elements in physical space. By splitting the detail coefficients, the wavelet packet basis functions include modulations on top the mother wavelet. Moving top to bottom in the tree is equivalent to increasing the dilation of the basis elements or decreasing resolution of the transform. Moving left to right in the coefficients of the tree adjusts the location of the basis elements. In the representation of the decomposition, branching to the left is the result of convolution and down-sampling of the sequence in the branch directly above by the low pass filter H. Branching to the right is the result of the same operation with the CMF high pass filter $\tilde{H}$. Thus, branchings to the left correspond to analyzing with the scaling function and to the right, analyzing with the mother wavelet.

of the down-sampling, branches farther down the tree consist of coefficients at successively coarser scales which represent successively larger dilations of the mother wavelet.

The synthesis (reconstruction) of the transform is also computed via convolutions. The parent node in the decomposition tree is reconstructed from its children by superimposing the results of up-sampling[1] and convolving the coefficients of the transform with their respective filter (either H for the approximation coefficients or $\tilde{H}$ for the fine detail coefficients).

Since the wavelet transform uses convolution, the operation count of the wavelet transform is $O(CN)$, where N is the number of elements in the signal. C is a constant multiplier which corresponds to the number of elements in the filter; we use the coif2 of MATLAB which has $C = 12$ elements.

5.1.3 Wavelet packets and "best basis"

For the wavelet analysis, only the approximation coefficients are successively reanalyzed and split. The resulting wavelet basis is composed of all the terminal nodes of the decomposition tree (the shaded nodes on the left hand side of figure 5.1).

For the wavelet packet analysis the detail coefficients are also reanalyzed, resulting in the full branching structure shown in figure 5.1. The wavelet packet basis functions can be defined in a similar way as the wavelet was defined

$$\psi_0 \equiv H\psi_0 \quad = \quad \phi \tag{5.10}$$

$$\psi_{2k} \equiv H\psi_k \tag{5.11}$$

$$\psi_{2k+1} \equiv \tilde{H}\psi_k \tag{5.12}$$

where k is an additional index which is loosely associated with the "frequency" of the wavelet packet and ϕ is the scaling function. The index k indicates the location of the

---

[1] Up-sampling is defined such that the value 0 is added in between every point. Thus the number of elements in the signal is doubled after an up-sampling.

wavelet packet in the decomposition tree representation, increasing from left to right across the nodes of the tree. See figure 5.2 for an example of the coif2 wavelet packets in 1D.

The choice of basis is not unique for the wavelet packet. The "best basis", is selected by finding which basis best represents the signal according to a given criterion. As a criterion we minimize the entropy $H(f)$ for a discrete signal, $f = [f_i]$, defined as

$$H(f) = -\sum_{i=1}^{N} p_i \log p_i \tag{5.13}$$

where $p_i = |f_i|^2/||f||^2$ is the normalized square modulus of the i^{th} element of the signal, with N the number of elements and $||f||^2 = \sum_i |f_i|^2$. Minimizing the entropy of the representation of the signal ensures that the best basis is that basis into which the signal is most efficiently compressed.

The operation count of the full wavelet packet decomposition tree is $O(CN \log N)$. Calculation of the best basis adds another $O(N \log N)$ operation count. The total operation count for the wavelet packet is still $O(N \log N)$.

5.1.4 Extension to two-dimensions

In two-dimensional signals, the basis elements are tensor products of the wavelets (or wavelet packets) and the scaling functions:

$$\begin{aligned}
\phi(x,y) &= (H \otimes H)\phi(x)\phi(y) = \phi(x)\phi(y) && (5.14)\\
\psi_h(x,y) &= (\tilde{H} \otimes H)\phi(x)\phi(y) = \psi(x)\phi(y) && (5.15)\\
\psi_v(x,y) &= (H \otimes \tilde{H})\phi(x)\phi(y) = \phi(x)\psi(y) && (5.16)\\
\psi_d(x,y) &= (\tilde{H} \otimes \tilde{H})\phi(x)\phi(y) = \psi(x)\psi(y) && (5.17)
\end{aligned}$$

for the coarse, horizontal (i.e. x-direction), vertical (i.e. y-direction), and diagonal (i.e. x- and y-directions detail wavelets respectively. The first "factor" of the tensor product acts

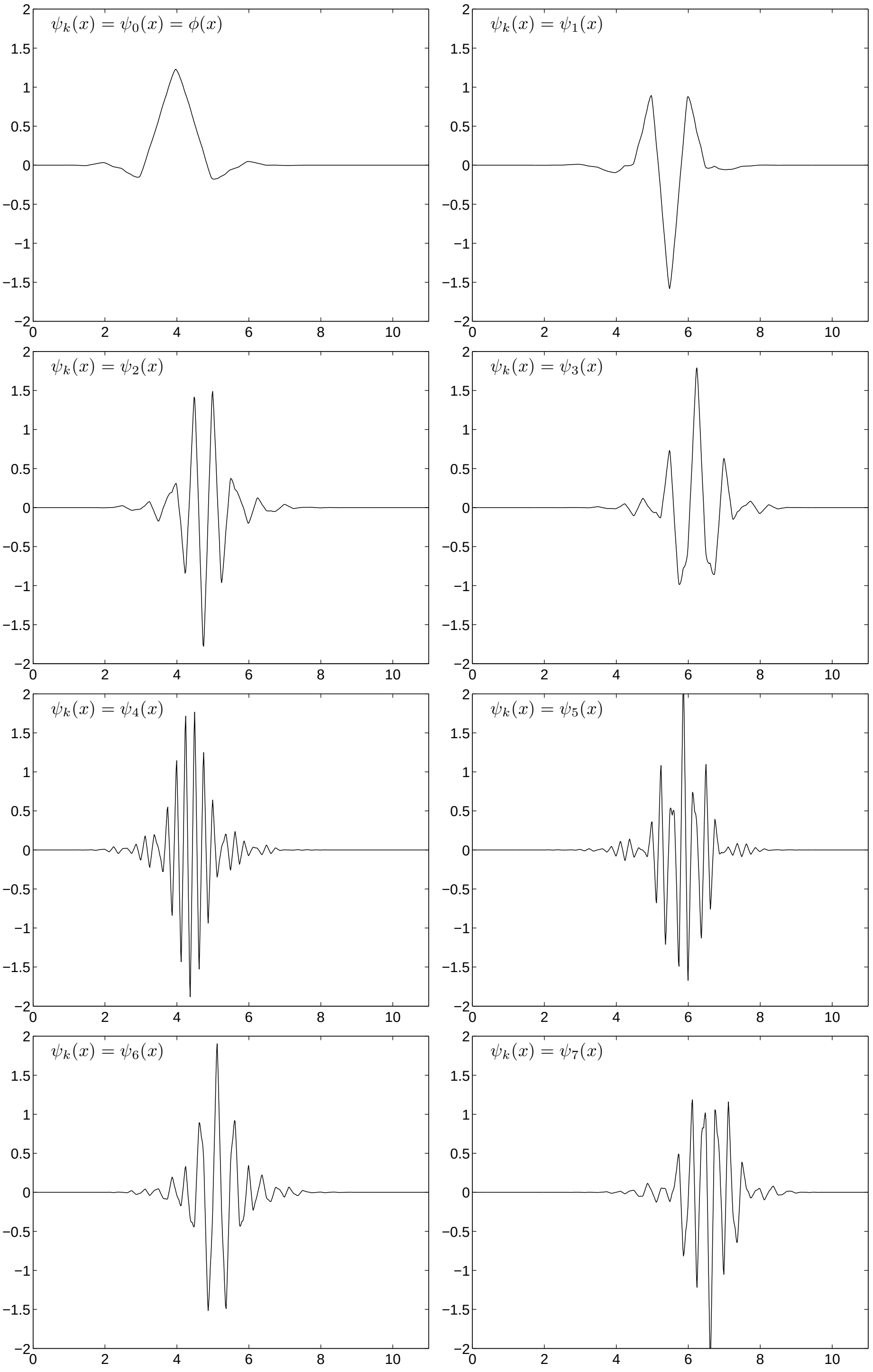

Figure 5.2: The first 8 ($n = 0 - 7$) wavelet packets for the coif2 family which we use in our analysis. The top two plots are the scaling function and the wavelet which forms the basis of the wavelet tree. The other plots are the higher order wavelet packets which form the possible bases of the wavelet packet tree.

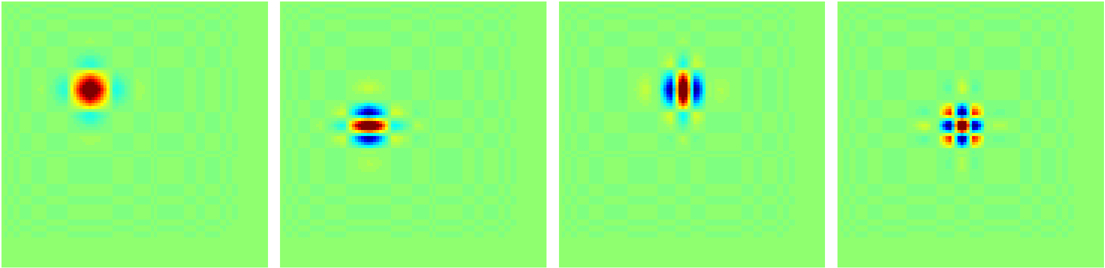

Figure 5.3: An example of the scaling function and mother wavelets in two-dimensions using the coif2 wavelet family. From left to right: The scaling function. The horizontal details wavelet, the vertical details wavelet, and the diagonal details wavelet. The colormap indicates amplitude, red is positive, blue is negative.

only on the first variable x and the second on the second variable y. The resulting structure is such that each parent node produces four children, one each for the approximation, horizontal, vertical, and diagonal detail coefficients. he resulting coif2 wavelet basis functions in two dimensions are shown in figure 5.3.

The analysis and synthesis of the transform in 2D are carried out by convolutions in the same manner as the 1D case, using tensor products of the filters. A representation of the tree structure of a two-dimensional wavelet decomposition is shown in figure 5.4.

5.2 FFT, JPEG compression, Okubo-Weiss, and POD techniques

To examine the relative efficiency of the wavelet-based decompositions, we compare the DWPT and DWT to three other algorithms; one based upon a Fourier transform, a second on basic JPEG compression, and a third on the method developed by Okubo [85] and Weiss [126].

5.2.1 FFT based technique

For the Fourier transform algorithm we threshold the coefficients of a 2-dimensional fast Fourier transform (FFT) of our vorticity. The coherent fields are then constructed via an inverse FFT of the largest amplitude coefficients. The incoherent remainder fields are

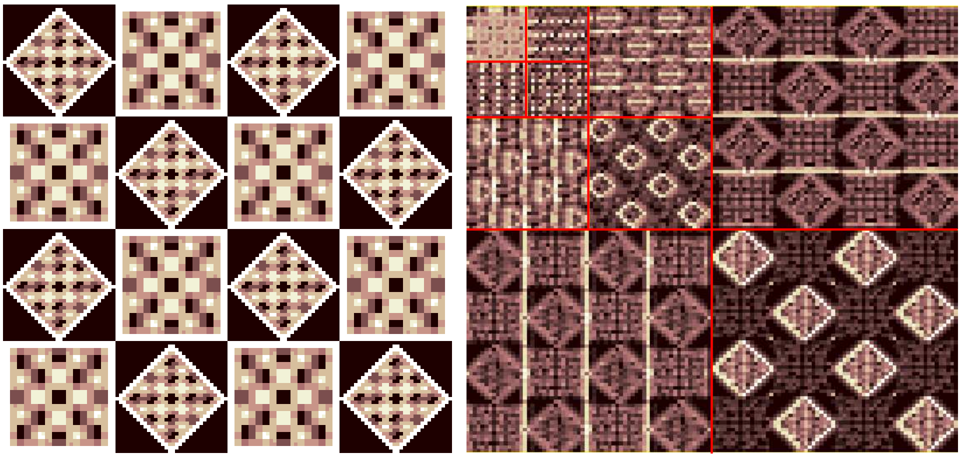

Figure 5.4: LEFT: A sample image (MATLAB's "tartan" image). Right: Coefficients of the 2D wavelet transform of the figure on the left. The coefficients are arranged in a common 2D representation of the wavelet tree decomposition. The coefficients are divided into quadrants with the upper leftmost sector (-,+) corresponds to the approximation coefficients. The approximation coefficients are then successively divided further into smaller quadrants. The other quadrants, correspond to the horizontal (+,+), vertical (-,-), and diagonal (+,-) detail coefficients, respectively.

constructed by subtracting the coherent fields from the original fields.

5.2.2 JPEG

The basic JPEG algorithm consists of subdividing an image into 8×8 blocks and taking the discrete cosine transform over the sub-blocks. The coefficients are arranged based upon the global average of the amplitudes among the sub-blocks. The average of the amplitudes is used to determine which modes to keep. After the threshold, each sub-block retains the same number of modes, each in the same position. Thus the number of modes retained must be a multiple of the number of sub-blocks which compose the image (for our 128×128 fields, this is 256). For more information on the JPEG image compression standard see reference [8], chapter 3.

5.2.3 Okubo-Weiss

The Okubo-Weiss criterion splits the fields into elliptic and hyperbolic regions, dominated by vorticity and strain respectively. The regions dominated by vorticity and strain are then separated and taken to be the coherent and incoherent fields.

From the inviscid Euler equation one can obtain the following equation for the evolution of the vorticity gradient

$$\frac{\partial \nabla \omega}{\partial t} + \nabla U(\nabla \omega) = 0 \tag{5.18}$$

If the velocity gradient varies slowly relative to the vorticity gradient then this is just an eigenvalue equation [126]. The eigenvalues determine the behavior of the vorticity gradient. The parameter Q

$$Q = s^2 - \omega^2 \tag{5.19}$$

is the square root of the eigenvalues, where $s = (\partial u/\partial y + \partial v/\partial x)$ is the strain and $\omega = (\partial v/\partial x - \partial u/\partial y)$ is the vorticity of the flow field. In regions where the strain dominates the velocity field, Q is positive and the eigenvalues are real (one positive and one negative). The velocity field is hyperbolic in these regions and the vorticity gradient should be distorted exponentially (exponentially grow in one direction and shrink in the orthogonal direction). In these regions the vorticity gradient rapidly becomes large and thus vorticity should tend to be stretched out and coherent structures destroyed. Conversely, in regions where the vorticity dominates, Q is negative and the eigenvalues become imaginary. The velocity field is elliptic in these regions and the vorticity gradient has an oscillatory solution. In these regions, the vorticity should tend to rotate rather than to be stretched, thus preserving the coherent structures.

Using the Weiss criterion, we separate the flow into these hyperbolic and elliptic regions. $Q = 0$ is the cutoff which determines the distinction between the two regions in the field. Thus, areas where the vorticity dominates are designated as coherent since the elliptic character of the velocity field should preserve the coherent structures while areas where the strain dominates are left as the background since the hyperbolic character of the velocity field should destroy coherent structures.

Basdevant and Philipovitch checked the assumptions of the Weiss criterion. They found that the assumption of a slowly varying velocity gradient was valid only in regions where the pressure field was nearly isotropic. On numerically simulated data, they found that this restricted the validity to a small region of the flow corresponding to the cores of the strongest vortices [15]. However, they noted that despite the invalidity of the hypothesis over most of the field, splitting the flow into vorticity-dominated and strain-dominated regions is relevant to dynamical analysis.

Results of the Okubo-Weiss decomposition showing the restriction of the validity to the very cores of the vortices are presented in appendix B. For further details on the Okubo-Weiss criterion see reference [15].

5.2.4 POD

Proper orthogonal decomposition (POD) is a general term for decomposition of a signal into an arbitrary orthogonal basis. In practice it refers to a basis where the fewest number of modes contain the largest amount of variance (or energy).

For an arbitrary spatially extended signal $f(\mathbf{x}, t_i)$ we can construct empirical eigenfunctions as follows using the method of snapshots [106]. The correlation matrix

$$C_{ij} = \frac{1}{M} \sum_{\mathbf{x}} f(\mathbf{x}, t_i) f(\mathbf{x}, t_j) \tag{5.20}$$

where M is the total number of snapshots of the signal. Each snapshot corresponds to a particular realization of the field, i.e. a single snapshot is one vorticity field in a set of data from the same conditions. The sum, is over all spatial points of the signal. In our case, the $f(\mathbf{x}, t_i)$'s correspond to our snapshots of the vertical vorticity. The correlation matrix is diagonalized by solving the eigenvalue problem

$$C\mathbf{a} = \lambda\mathbf{a} \tag{5.21}$$

The eigenvectors are orthogonal in the familiar way

$$\sum_n a_i^n a_j^n = \delta_{ij}\lambda^n \tag{5.22}$$

In the case of M snapshots, there will be M resulting eigenvalues, each corresponding to the variance contained in a particular eigenfunction. The n^{th} eigenfunction $\phi^n(\mathbf{x})$ can then be constructed

$$\phi^n(\mathbf{x}) = \sum_i^M a_i^n f(\mathbf{x}, t_i) \tag{5.23}$$

The eigenfunctions obey the familiar orthonormality

$$\sum_{\mathbf{x}} \phi^i(\mathbf{x})\phi^j(\mathbf{x}) = \delta_{ij} \tag{5.24}$$

The original signal can thus be reconstructed by summing the eigenfunctions

$$f(\mathbf{x}, t_k) = \sum_n a_k^n \phi^n(\mathbf{x}) \tag{5.25}$$

Each eigenfunction corresponds to an entire field. The POD was not found to be a useful or efficient decomposition for our data. Results are shown in appendix B and are not included in the analysis in this chapter.

5.3 Coherent structure extraction

We use an algorithm for coherent structure extraction based upon a de-noising algorithm (e.g. chapter 11 of reference [127]). In the de-noising, the assumption is that the original signal can be represented by a few large amplitude coefficients of an orthogonal transform using an appropriate set of basis functions, while the noise is contained in the many remaining coefficients of small amplitude. The de-noising is then performed by applying a threshold to the resulting coefficients of the transform. Coefficients above the threshold amplitude are assumed to correspond to the signal while coefficients below the threshold correspond to the “noise”. The few large amplitude coefficients are called the “coherent” coefficients, while the many small amplitude coefficients are “incoherent”. The coherent and incoherent parts of the vorticity are then reconstructed by the inverse transform.

The choice of the threshold separating the coherent and incoherent parts of the signal is based upon a measure of the number of significant coefficients N_o, which is the theoretical dimension of the signal, defined by

$$N_o(f) = e^{H(f)} \tag{5.26}$$

where $H(f)$ is the entropy of a discrete signal $f = [f_i]$ (where $[f_i]$ is the set of discrete values of an arbitrary signal f), defined in equation 5.13. In our case, the f_i's correspond to the discrete values of our vertical vorticity measurements. N_o indicates how many of the largest coefficients should be retained to give an efficient, low entropy, representation of the signal.

Thus, the decomposition algorithm is the following. We take the transform of an individual measured vorticity field. For the DWPT, the best basis is used. Then we find the number of significant coefficients N_o of the transformed vorticity field in the transform basis. The threshold is therefore based upon the value of the N_o^{th} largest coefficient. Coefficients whose modulus is larger (smaller) than the threshold correspond to the coherent (incoherent) part of the vorticity field. We then take the inverse transform to get the coherent part in physical space. The incoherent field is reconstructed by subtracting the coherent from the total field. The process is then repeated for each of our vorticity fields. Our algorithm contains no adjustable parameters other than the selected wavelet and is based upon the assumption that the flow field has a low entropy component, corresponding to the coherent structures, and a high entropy component, corresponding to an incoherent background.

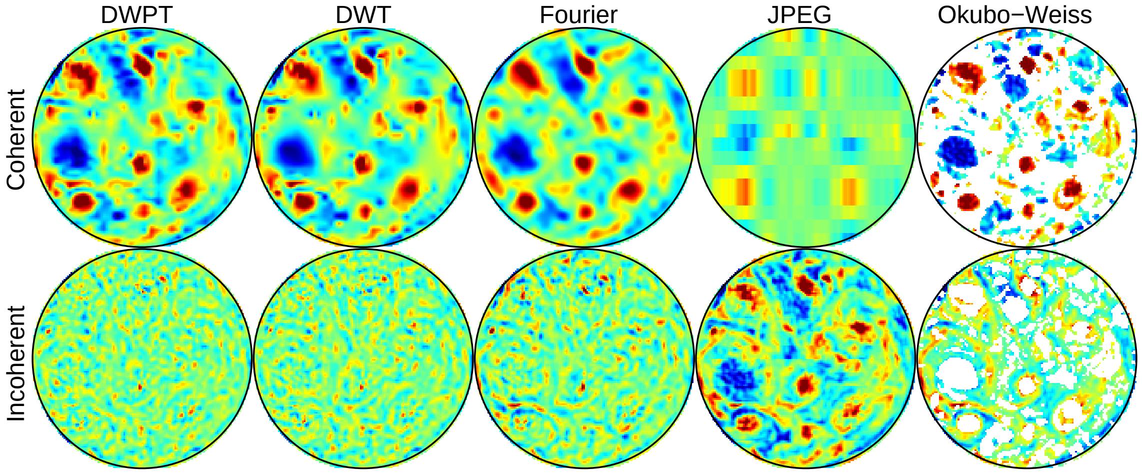

Figure 5.5: Decomposed vorticity fields, TOP: Coherent BOTTOM: Incoherent remainder fields, all for the same number of coefficients retained, roughly 2.4% (except for Okubo-Weiss and approximate for JPEG). The colormap corresponds to the intensity of vorticity and is the same for all images and the same as used in figure 4.4. [MOVIE [2]]

Our algorithm is different than the various iterative algorithms of Farge *et al.* [41] and others [127, 105]. In the de-noising algorithm described in [127, 105], successive iterations extract a fraction of the coherent coefficients until a stopping criterion is met. The fraction of retained coefficients at each step and stopping criterion are adjustable parameters. However, the basis of the DWPT can change at each iteration. The number of coefficients retained therefore loses its meaning since coefficients can be selected from completely different bases. Therefore, we only perform a single iteration without changing the basis for the DWPT. In the algorithm of Farge [41], an a priori assumption is made of Gaussian white noise incoherent component superimposed upon a non-Gaussian component of coherent vortices. The threshold is then iteratively found to separate the two without adjustable parameters.

5.4 Results

5.4.1 Decomposed vorticity fields

The resulting coherent and incoherent vorticity fields obtained from the wavelet packet, wavelet, Fourier, and JPEG techniques are compared in figure 5.5. The Okubo-Weiss criterion was also tested for comparison with the other decomposition methods. The fields shown are constructed with the same number of coefficients for the DWPT, DWT, and Fourier transforms, and the closest approximate number for JPEG.

The coherent fields in figure 5.5 appear to retain the large scale coherent structures [cf. figure 4.4(a) and (b)]. The DWPT, DWT, and Fourier preserve the structure of the total vorticity field. The Okubo-Weiss criterion excises primarily the regions of large amplitude vorticity, which generally corresponds to the cores of vortices. However, it extracts only the cores and leaves behind the peripheries. The JPEG does poorly with so few coefficients; it barely picks out some of the stronger vortices in the field.

For the same number of coefficients, 2.4%, the DWPT and DWT do a better job of extracting structure in the fields than the Fourier decomposition, which leaves more structure behind in the incoherent field (e.g. figure 5.5 [MOVIE [7]]). The JPEG incoherent field is large amplitude because of the few coefficients retained in the coherent field. The incoherent fields resulting from the DWPT, DWT, and the Fourier are mostly devoid of large-scale structures and are much smaller in amplitude. The incoherent fields are also poorly correlated in time and are devoid of large scale structures or any other feature which can be tracked by eye (e.g. see figure 5.5 and associated movie).

The Okubo-Weiss criterion selects the centers of the vortices where vorticity dominates strain. This accounts for a large portion of the enstrophy. It extracts about 74% of the enstrophy in the vorticity dominated regions, which cover about 40% (not coefficients) of the area of the flow. However, the method leaves behind holes in the vorticity field that act as coherent structures and are often surrounded by large values of vorticity. The resulting “incoherent” field thus retains coherent properties. The Okubo-Weiss criterion also does poorly in recovering the statistics of the total field, as shown in table 5.1. Furthermore, the decomposition shown in figure 5.5 was performed without regard to the Okubo-Weiss validity criterion, which restricts the application of the criterion to the very centers of the vortices or regions of very large vorticity [15]. If the validity criterion is applied, much less is retained in the coherent field, and the incoherent field ends up with large values of vorticity (see Appendix B).

Statistical properties of the decompositions are shown in tables 5.1 and 5.2. Table 5.1 lists the results from setting the threshold of the various transforms based upon the number of significant coefficients calculated from equation 5.26. On average about 2-3% of the large-amplitude coefficients of the wavelet-based decompositions were retained in the coherent fields, which account for about 85% of the total enstrophy of the flow. The Fourier retains roughly the same enstrophy but requires more coefficients, about 4%. The JPEG decomposition retains only 67% of the total enstrophy with about 13% of the large-amplitude coefficients.

Owing to the compact support of their basis functions, fewer coefficients were needed for the DWPT and DWT, based upon the entropy criterion in equation 5.13, than for the Fourier and JPEG decompositions. Compression curves for enstrophy of the various decompositions applied to our vorticity fields are shown in figure 5.6. The DWPT and DWT both do similarly well at extracting the enstrophy in the fields with only a small number of coefficients. The DWPT probably does slightly better due to the adaptability of its basis. The Fourier based methods do not converge as rapidly as the wavelet-based methods. This is likely due to the non-locality of the basis functions when applied to a field which has localized structures and sharp features.

The wavelet-based algorithms also do a better job preserving the skewness and kurtosis of the total vorticity in the coherent component, while the incoherent components are much closer to a Gaussian distribution (skewness = 0, kurtosis = 3). Table 5.2 displays the results from setting the threshold on the transforms so that each method retains 2.4% of the coefficients in the coherent component (since the coefficients JPEG must be a multiple

Decomposition		Wavelet packet		Wavelet		Fourier		JPEG		Okubo-Weiss	
Quantity	Total	coherent	incoherent	coherent	incoherent	coherent	incoherent	coherent	incoherent	coherent	incoherent
coefficients retained (%)	100	2.4	97.6	2.7	97.3	4.1	95.9	13.1	86.9	40.2	59.8
Enstrophy/field ($s^{-2} \times 10^4$)	4.33	3.63	0.63	3.67	0.62	3.68	0.56	2.92	1.33	3.21	1.12
Vorticity skewness	0.78	0.80	0.02	0.85	0.04	0.62	0.20	0.53	0.24	1.22	-0.07
Vorticity kurtosis	7.09	7.03	3.88	7.58	3.42	5.37	7.85	5.27	6.55	11.81	8.28

Table 5.1: Statistical properties of the decomposed vorticity fields using entropy criterion.

Decomposition		Wavelet packet		Wavelet		Fourier		JPEG	
Quantity	Total	coherent	incoherent	coherent	incoherent	coherent	incoherent	coherent	incoherent
coefficients retained (%)	100	2.4	97.6	2.4	97.6	2.4	97.6	3.0	97.0
Enstrophy/field ($s^{-2} \times 10^4$)	4.33	3.63	0.63	3.60	0.69	3.28	0.92	0.96	3.18
Vorticity skewness	0.78	0.80	0.02	0.86	0.04	0.51	0.32	0.06	0.72
Vorticity kurtosis	7.09	7.03	3.88	7.62	3.47	4.77	7.85	4.84	7.08

Table 5.2: Statistical properties of the decomposed vorticity fields retaining the same number of modes, 2.4%, as the DWPT decomposition (approximate for JPEG).

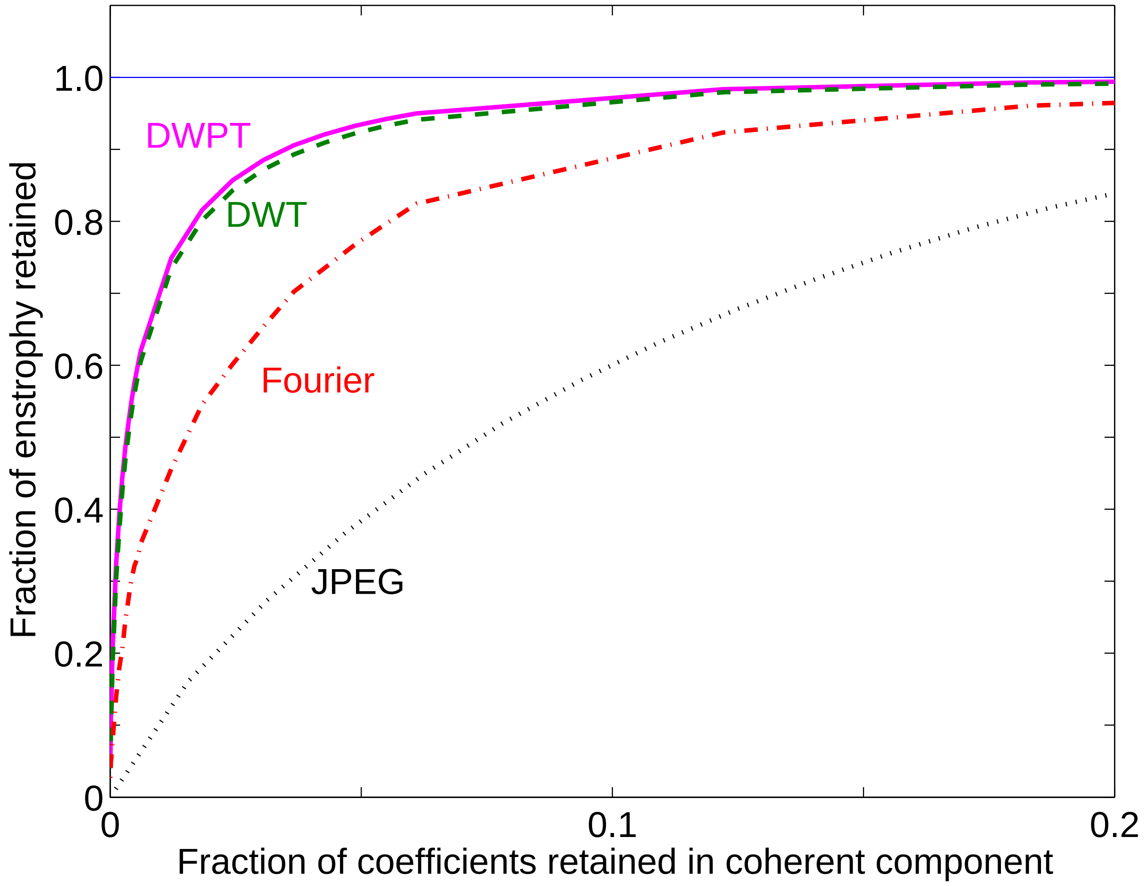

Figure 5.6: The percent enstrophy retained in the largest amplitude coefficients as a function of the number of coefficients kept. In order from best (most efficient) to worst: wavelet packet, wavelet, Fourier, JPEG.

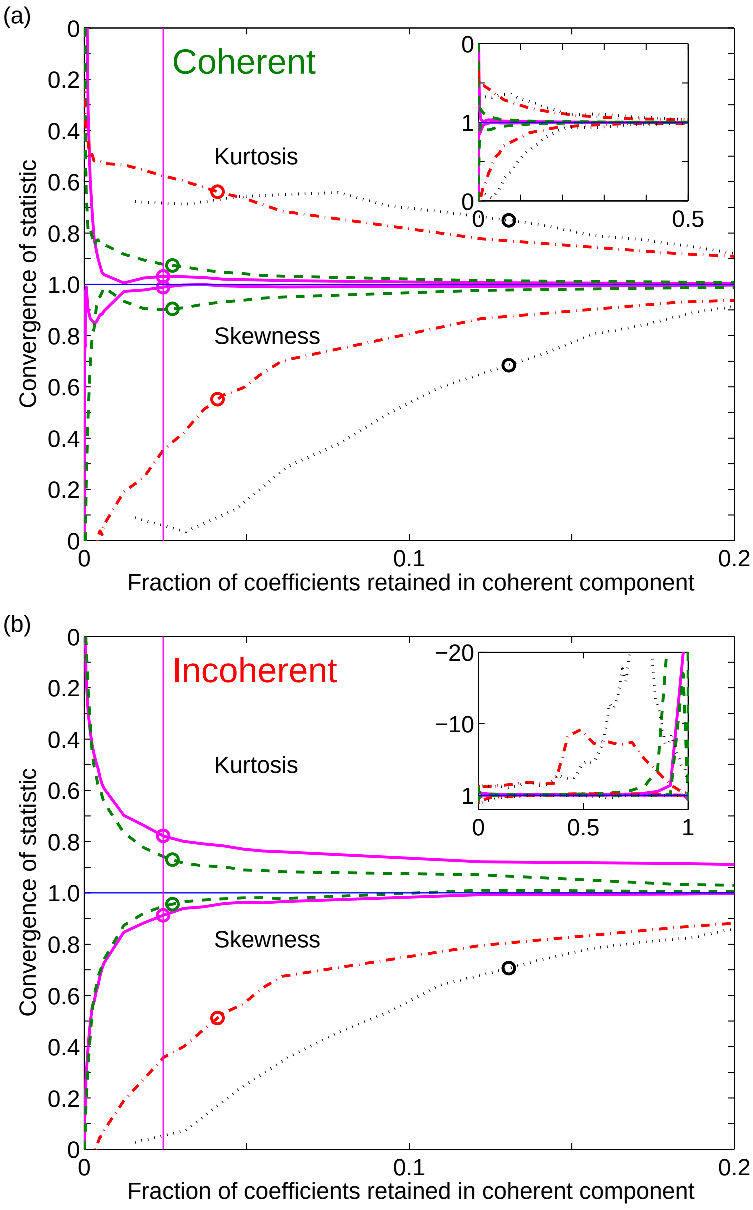

Figure 5.7: Convergence of the skewness and kurtosis of the vorticity PDFs for the various decompositions, plotted with quantities defined so that they approach unity as they converge. The vertical line indicates the fraction of coefficients retained in the wavelet packet decomposition. (a) Convergence of the coherent component. Plotted: kurtosis ratio: $|k_{\text{coh}}/k_{\text{total}}|$, skewness ratio: $|s_{\text{coh}}/s_{\text{total}}|$. (b) Convergence of the incoherent component. Plotted: kurtosis ratio: $2 - k_{\text{incoh}}/3$, skewness ratio: $1 - |s_{\text{incoh}}/s_{\text{total}}|$. Note that unity on the graph represents the respective statistic for a Gaussian distribution: skewness $= 0$, kurtosis $= 3$. The kurtosis of the Fourier and JPEG incoherent field is large and off the main plot. The insets show the convergence behavior at large numbers of retained coefficients. The open circles on the curves correspond to the fraction of coefficients retained for the corresponding techniques using the entropy criteria as a threshold.

of the number of 8 × 8 blocks, 256, this restriction is relaxed). For the same number of retained coefficients, the DWT and DWPT clearly outperform the Fourier method in terms of preserving the statistics of the total vorticity field.

Figure 5.7 shows that the coherent fields from the wavelet packet and wavelet decompositions rapidly converge to the statistics of the total vorticity field. The coherent fields preserve the non-Gaussianity of the vorticity PDF without having to extract many coefficients. The respective incoherent fields also rapidly converge to Gaussian statistics. This suggests that wavelets and wavelet packets do a good job of extracting the coherent structures from the vorticity field. The near-Gaussianity of the incoherent field suggest that the transforms have left the remainder without coherent structure.

The coherent components of the Fourier and JPEG decompositions, however, converge to the statistics of the total fields much more slowly. To obtain the same level of fidelity, both the Fourier and JPEG must extract many more coefficients. This inefficiency would result in over-transformed fields. Further, the insets in figure 5.7 (b) show that the kurtosis of the incoherent component never converges to anything small, but increasingly deviates from Gaussian. This suggests that the Fourier decomposition is not separating the coherent structures from the background.

The probability density function (PDF) of vorticity has broad wings (see figure 5.8), which correspond to the large vorticity values that occur in the coherent vortices and vorticity filaments. The preference for cyclonic (positive vorticity) structures over anti-cyclonic structures appears as a large positive skewness (see also table 5.1 and 5.2). While the PDF for the DWPT and DWT coherent vorticity field are nearly the same as that for the total vorticity field, the PDF for the corresponding incoherent field is narrower and more symmetric, indicating the lack of high intensity structures.

Consider the enstrophy spectrum of the vorticity fields, as shown in figure 5.8 (b). It is clear from the enstrophy spectra of the total field that most of the enstrophy is contained in long wavelengths (small k). This agrees well with the observation of the vorticity fields and the dominance of large structures with large amplitude vorticity. The enstrophy spectrum,

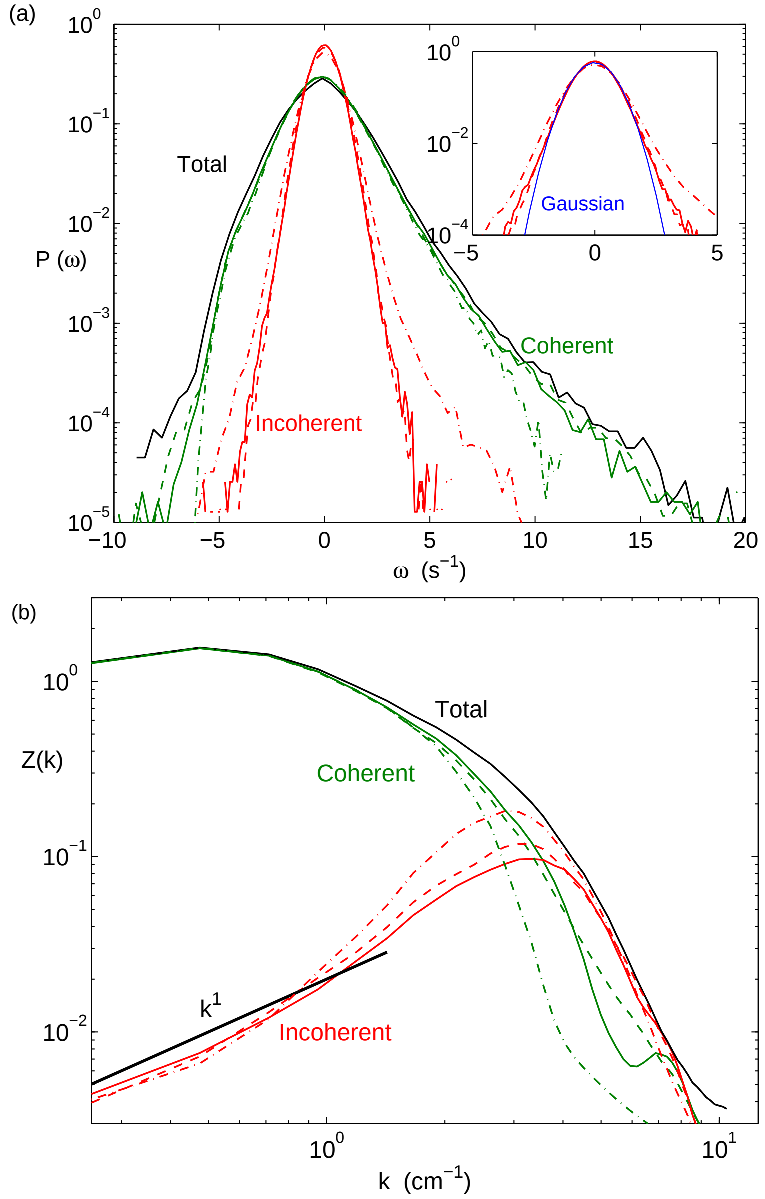

Figure 5.8: (a) Vorticity PDFs of the total field, coherent field, and incoherent field, where the inset shows the incoherent PDFs plotted together with a Gaussian fit to the wavelet packet results. (b) Enstrophy spectra Z(k) of total, coherent, and incoherent fields, calculated on a square subsection of our circular domain. The solid, dashed, and dash-dotted lines correspond to the wavelet packet, wavelet, and Fourier decompositions respectively. The k^1 line is the spectral slope for Gaussian white noise in 2D. The wavenumber is defined as $k = 2\pi/L$.

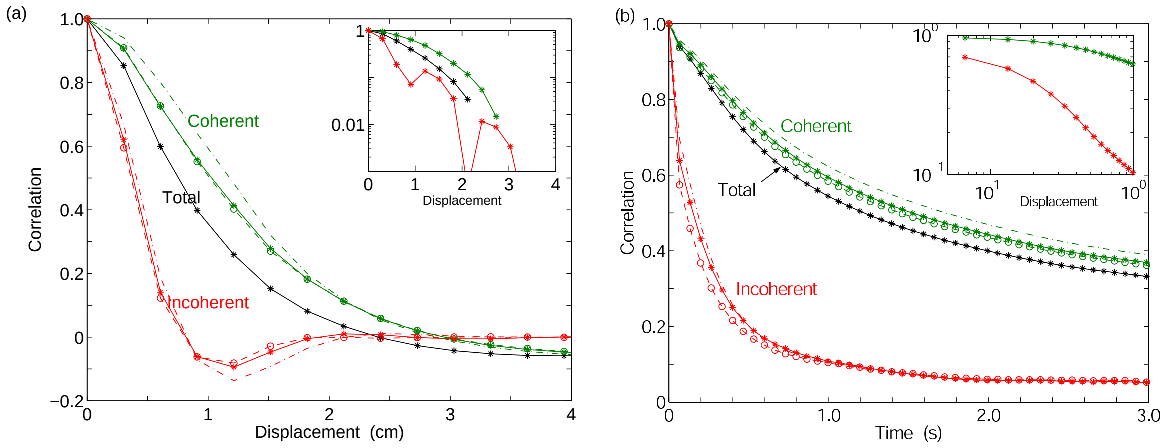

Figure 5.9: (a) Space and (b) time correlations of the decomposed vorticity fields. The solid, dashed, and dash-dotted curves correspond to the DWPT, DWT, and Fourier decompositions.

shown in figure 5.8, does not contain a well defined scaling region corresponding to a cascade of enstrophy. A cascade would not be expected for our quasi-2D flow, which is forced by the broad-band 3D turbulence in the bottom of the tank rather than by injection of energy at a single well-defined wavenumber. The presence of large structures which extend well into the 3D region alone tells us that we must have a broad spectrum energy injection.

The coherent field contains the same large structures that are present in the total field. Accordingly, the enstrophy spectrum of the coherent field matches that of the total field at long wavelength [figure 5.8 (b)]. The incoherent field contains negligible enstrophy at large scales, indicating the lack of large scale features. This is apparent in the vorticity decomposition (see figure 5.5). The incoherent field has only small structures and is the dominant contribution to the enstrophy at large k.

The wavelet-based and the Fourier decompositions also retain the spatial and temporal correlations in the coherent field, as figure 5.9 illustrates with the DWPT and DWT yielding almost the same results. The long time correlation is in part due to the presence of long lived coherent structures. In contrast, for the incoherent field the spatial and temporal correlations are short ranged, indicating the absence of large scale and long-lived structures.

5.4.2 Transport of passive scalar particles and concentration fields

Paths computed for some passive scalar "particles" in the measured velocity fields are shown in figure 5.10 (a). Over the 20 s duration of the measurement, the particles are advected around a large portion of the tank. The motion of the particles depends on their location in the flow. For example, a particle can spend time caught in a vortex, following the motion of the vortex as it meanders slowly in a localized region of the tank [path in upper right of figure 5.10 (a)]. Occasionally the particle will escape from a vortex and then be carried by a high velocity jet, which can transport a particle large distances in a short time. A particle may then be captured by a vortex [e.g. path ending in lower right of figure 5.10 (a)].

The resulting mean squared displacement of the tracer particles in the velocity fields obtained by experiment is shown in figure 5.10 (b). It exhibits approximately t^2 scaling at short times, which looks "flight-like[2]" [110]. At long times the finite size of the tank becomes significant and the scaling exponent becomes smaller.

Both the wavelet and wavelet packet coherent fields disperse the tracer particles similarly around the tank; the scaling behavior of the mean squared displacement, not shown in this paper, is also the same. Differences in the paths are due to the sensitive dependence upon initial conditions of a turbulent flow field.

We find a striking difference in the behavior of a numerically integrated passive scalar particle in the coherent and incoherent fields. The incoherent fields make no significant contribution to the transport properties; rather, particles are confined to a small region, as shown in the inset in figure 5.10 (a). This is due to the rapid decorrelation in time of the incoherent fields. The rapid fluctuations cause the tracers to jiggle around and the scaling of the mean squared squared displacement of the tracers in the incoherent fields approaches that of a random walk.

The evolution of the passive scalar field in the measured velocity field is similar to that for tracer particles. Results for the coherent and incoherent fields produced by the

---

[2] A "flight" is an extended period of ballistic transport, i.e. the tracer particle is purely advected by the flow, without being locally stuck.

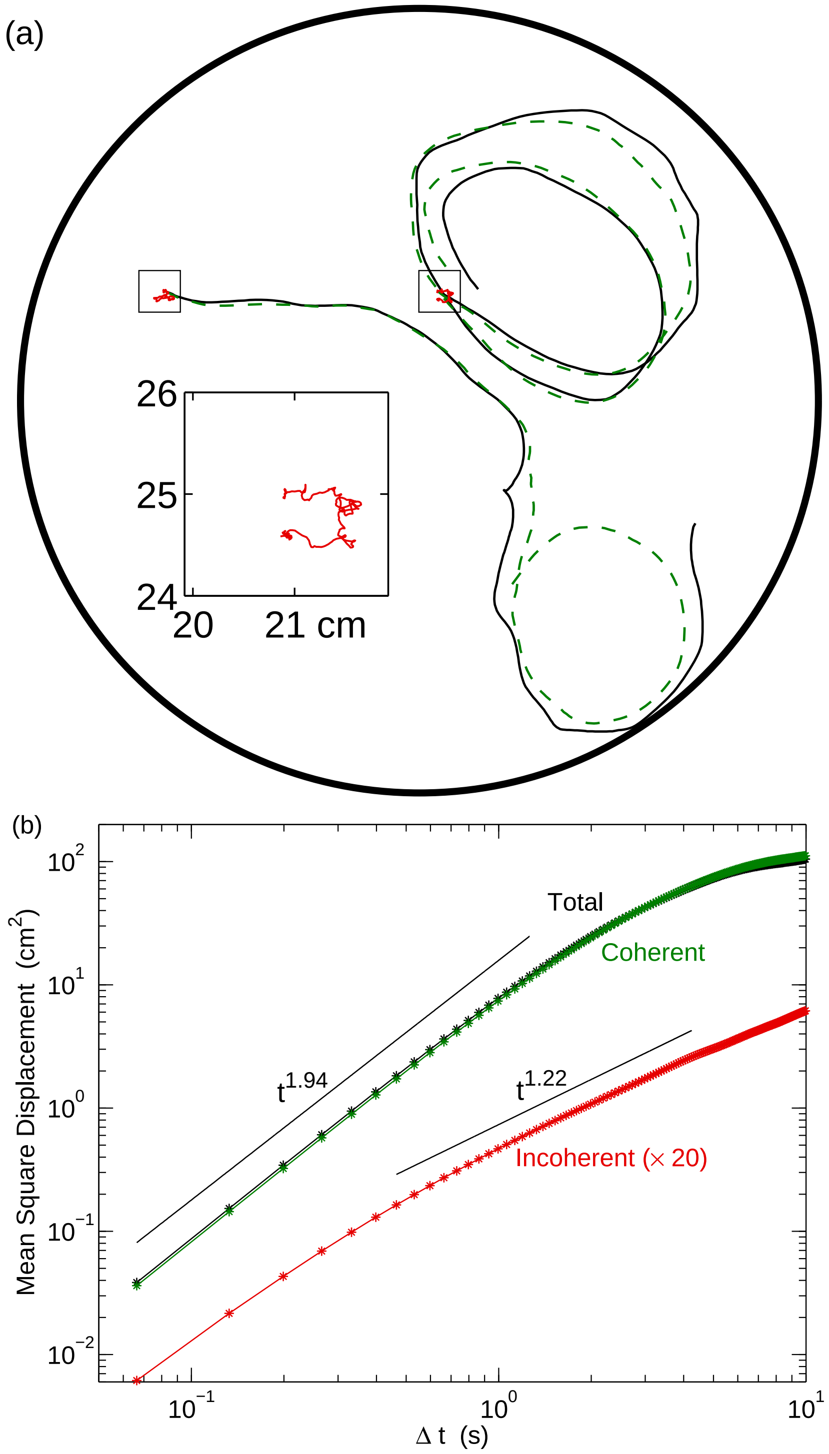

Figure 5.10: (a) Simulated paths of numerical tracer particles in the total field (solid curves) and in the coherent (dashed curves) and incoherent field (red) for the DWPT (total time 20 s). The inset shows an expanded view of the path in the incoherent field. (b) Mean squared displacements for the tracers in the total, coherent, and incoherent velocity fields. The exponents for the total and coherent fields are 1.94 while for the incoherent remainder the exponent is 1.22 over the range indicated. Both results are for the wavelet packet.

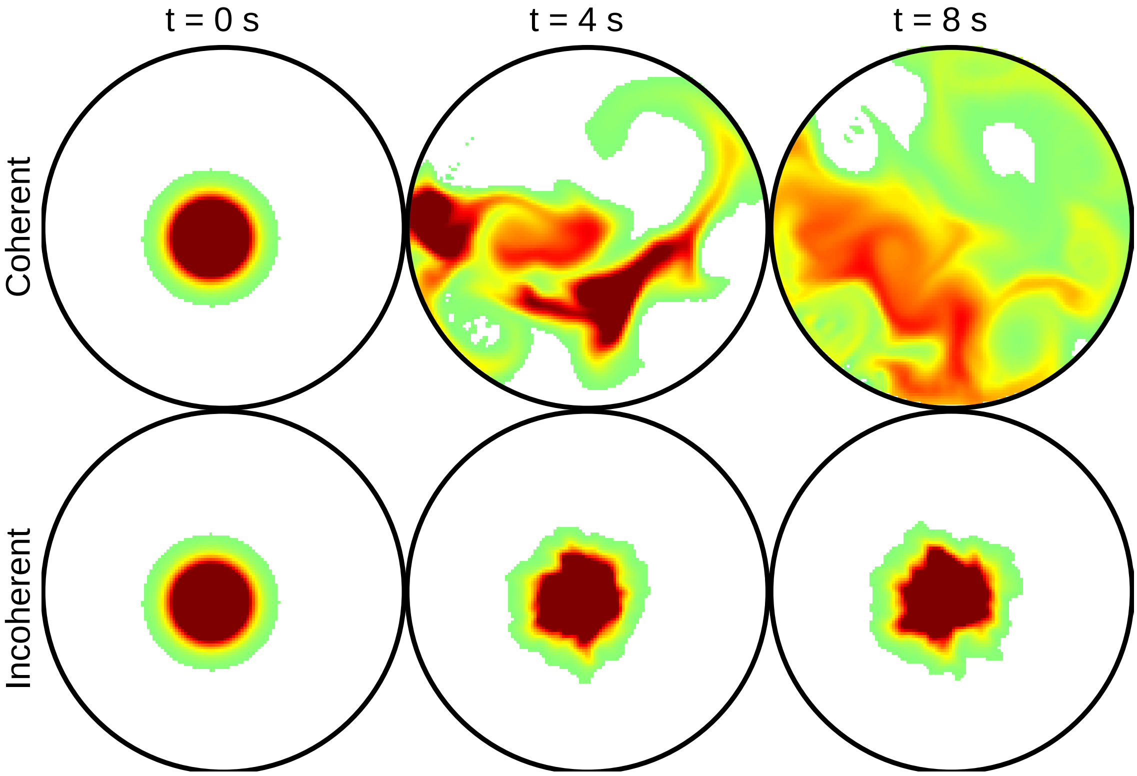

Figure 5.11: [MOVIE [5]] Advection of a passive scalar field in the velocity field of the DWPT, as computed from the advection-diffusion equation (3.13). By eight seconds the scalar field has been significantly mixed by the coherent field, while it appears only to have been diffused in the incoherent field.

DWPT are shown in figure 5.11, which illustrates the stretching and folding; the results for the total field are similar to that of the coherent field. By four seconds the scalar has already been significantly stretched by the velocity fields. There is no significant advection in the incoherent fields and is similar to results obtained with pure diffusion (no advection term). This is expected from the short time and space correlations of the incoherent fields (see figure 5.9). Similar results were obtained for the DWT and Fourier methods. Our results agree well with those of Beta *et al.* [18] who, using the DWT, found that the coherent field is responsible for the mixing in a numerically simulated 2D turbulent flow.

5.5 Summary

We have shown that wavelet based transforms can be used to separate our quasi-2D turbulent flow into a non-Gaussian coherent component represented by as few as 3% of the large-amplitude, low entropy coefficients of the transform and a nearly Gaussian incoherent component, represented by the remaining small-amplitude, high entropy coefficients. We are able to obtain this result without an *a priori* assumption on the particular distribution of the two components and without any arbitrary free parameters.

The discrete wavelet packet transform (DWPT) and the discrete wavelet transform (DWT) yield very similar results, despite the adaptability of the DWPT basis. The coherent components of the DWPT and DWT retain all of the properties of the total field, including the large-scale structures, shape of the vorticity PDF, long spatial and temporal correlations, and transport properties. The coherent component contained the large skewness and kurtosis of the PDF, which are due to the coherent structures. In contrast, the incoherent remainder has only small-scale short-lived features and does not contribute significantly to the transport. Thus in analysis of flow dynamics and transport, it may be sufficient only to consider the coherent component.

The localized basis functions of the DWPT and DWT outperformed the Fourier and JPEG decompositions. Both the DWPT and DWT have more rapid convergence of the statistics of the extracted coherent component toward that of the total flow. The rapid convergence of the skewness and kurtosis of the vorticity PDF suggest that the wavelet based methods have efficiently captured the coherent structures. The Fourier and JPEG converge much more slowly and are thus unable to efficiently capture the large higher moments of the vorticity PDF. This suggests that the Fourier and JPEG methods did not really extract the coherent structures despite the appealingly smooth visual appearance of large-scale structures in the coherent field. The incoherent remainder of both the DWPT and DWT converge rapidly towards Gaussian statistics, while the incoherent remainders of the Fourier and JPEG do not converge to any value.

Chapter 6

Dual light sheet

In this chapter we present results from the dual laser light-sheet in our rotating tank. Data were taken using vertically separated light-sheets that illuminated horizontal planes. This allowed us to correlate the flow structure in the vertical direction, a measure of its two-dimensionality. The vertical correlation of the horizontal projection of the velocity field and of the vertical vorticity field were determined as a function of separation and rotation rate for a fixed pumping rate. This allowed us to quantify the two-dimensionality of our flow.

6.1 Measurements and methods

Data were taken at (i) varying separation at fixed rotation and pumping rates, and (ii) varying rotation rate at fixed pumping and separation.

(i) The position of the red laser sheet was fixed near the top of the tank, approximately 4 cm below the lid, while the height of the green laser sheet was varied. We used separations of 0, 2, 10.5 16.0, 22.1, and 33.1 cm. At the 33.1 cm position the green laser is approximately 10 cm above the tops of the forcing tees. For most data, the tank was rotated at 0.4 Hz and the pump was set to 426 cm^3/s. This condition produces a local averaged Rossby number $Ro = 0.3$[1] near the top of the tank.

(ii) Fixed separation measurements were made at varying table rotation rate and at low (426 cm^3/s) and high (1046 cm^3/s) pumping. The red laser was at the same height as previous and vertical separations were 2, 10, and 33.1 cm.

Typically 50 instantaneous snapshots of the field were determined to calculate the correlation. In some data sets only 10 snapshots were obtained.

Typical instantaneous and mean vorticity fields of the conditions presented are shown in figures 4.11, 4.9, and 4.10.

The particle images from the red and green sheets were each cropped according to a mask which defined the boundary of the tank at the respective heights. The images were then interpolated one onto the other and CIV was used to calculate the fields on the same

---

[1] $Ro = \omega_{RMS}/(2\Omega)$

grid. The centroid of the mask was also calculated to determine the location of the center of the tank. The resulting velocity and vorticity fields were then interpolated onto the same grid[2]. Rotational orientational differences were found by determining the orientation of a grid placed on the lid of the tank in both cameras. Differences in orientation were found to be less than 0.5°[3].

6.2 Correlation calculations

We quantitatively make a comparison between the fields measured in the respective light-sheets by calculating a correlation coefficient. The correlation can be calculated by two slightly differing methods

$$R_1 = \left\langle \frac{\mathbf{u}_1(\mathbf{x},t)\cdot\mathbf{u}_2(\mathbf{x},t)}{|\mathbf{u}_1(\mathbf{x},t)||\mathbf{u}_2(\mathbf{x},t)|} \right\rangle \tag{6.1}$$

$$R_2 = \frac{<\mathbf{u}_1(\mathbf{x},t)\cdot\mathbf{u}_2(\mathbf{x},t)>}{\sqrt{<|\mathbf{u}_1(\mathbf{x},t)|^2><|\mathbf{u}_2(\mathbf{x},t)|^2>}} \tag{6.2}$$

where $\mathbf{u}_1$ and $\mathbf{u_2}$ are the measured projections of the velocity fields onto the plane of the respective horizontal laser sheets with $\mathbf{u_1} = (u_1, v_1)$ and $\mathbf{u_1}\cdot\mathbf{u_2} = u_1u_2 + v_1v_2$. The vector $\mathbf{x} = (x, y)$ corresponds to the position in the horizontal plane. The $<>$ denotes an average over space and time (i.e. over all the spatial points and snapshots of the measured fields). Similar relations were used for the vertical vorticity field, replacing the velocity vector field $\mathbf{u}$ with the scalar vertical vorticity field ω.

$$R_1 = \left\langle \frac{\omega_1\omega_2}{|\omega_1||\omega_2|} \right\rangle \tag{6.3}$$

$$R_2 = \frac{<\omega_1\omega_2>}{\sqrt{<|\omega_1|^2><|\omega_2|^2>}} \tag{6.4}$$

---

[2] The higher resolution field was interpolated onto the lower resolution field.

[3] This did not cause significant differences in the correlation and thus was not corrected for.

The first correlation, R_1 in equations 6.1 and 6.3, has the geometrical interpretation as the pointwise correlation of the angle between the two fields. i.e.

$$\cos\theta(\mathbf{x},t) = \frac{\mathbf{u}_1 \cdot \mathbf{u}_2}{|\mathbf{u}_1||\mathbf{u}_2|} \tag{6.5}$$

and thus

$$R_1 =< \cos\theta > \tag{6.6}$$

is the mean cosine of the angle between $\mathbf{u_1}$ and $\mathbf{u_2}$. For the vorticity, this is the angle in one-dimension, i.e. the correlation of the sign (+/-).

The second correlation, R_2 in equations 6.2 and 6.4, is similar but is weighted by the pointwise magnitude of the fields. i.e. the numerator is $\mathbf{u}_1 \cdot \mathbf{u}_2 = |\mathbf{u}_1||\mathbf{u}_2| \cos\theta(\mathbf{x},t)$ and the denominator in each is just a normalizing constant so that

$$R_2 \propto< |\mathbf{u}_1||\mathbf{u}_2| \cos\theta(\mathbf{x},t) > \tag{6.7}$$

Both R_1 and R_2 are bounded between -1 and 1.

6.3 Results

6.3.1 Flow field observations

Simultaneous observations made in the vertically separated light-sheets confirmed our notion of the basic flow structure: the vortices and other flow features extend throughout the vertical extent of the tank, even for moderate rotation rates. A representative pair of particle streak images for a large (20 cm) vertical separation and moderate rotation (0.4 Hz) and pumping (426 cm^3/s) is shown in figure 6.1.

The strong vortices cross horizontal planes at nearly the same locations, even for large separations. In particular, the vortices of the dipole present[4] in the lower left of figure 6.1

---

[4] This is the same location of the dipole in figure 4.1.

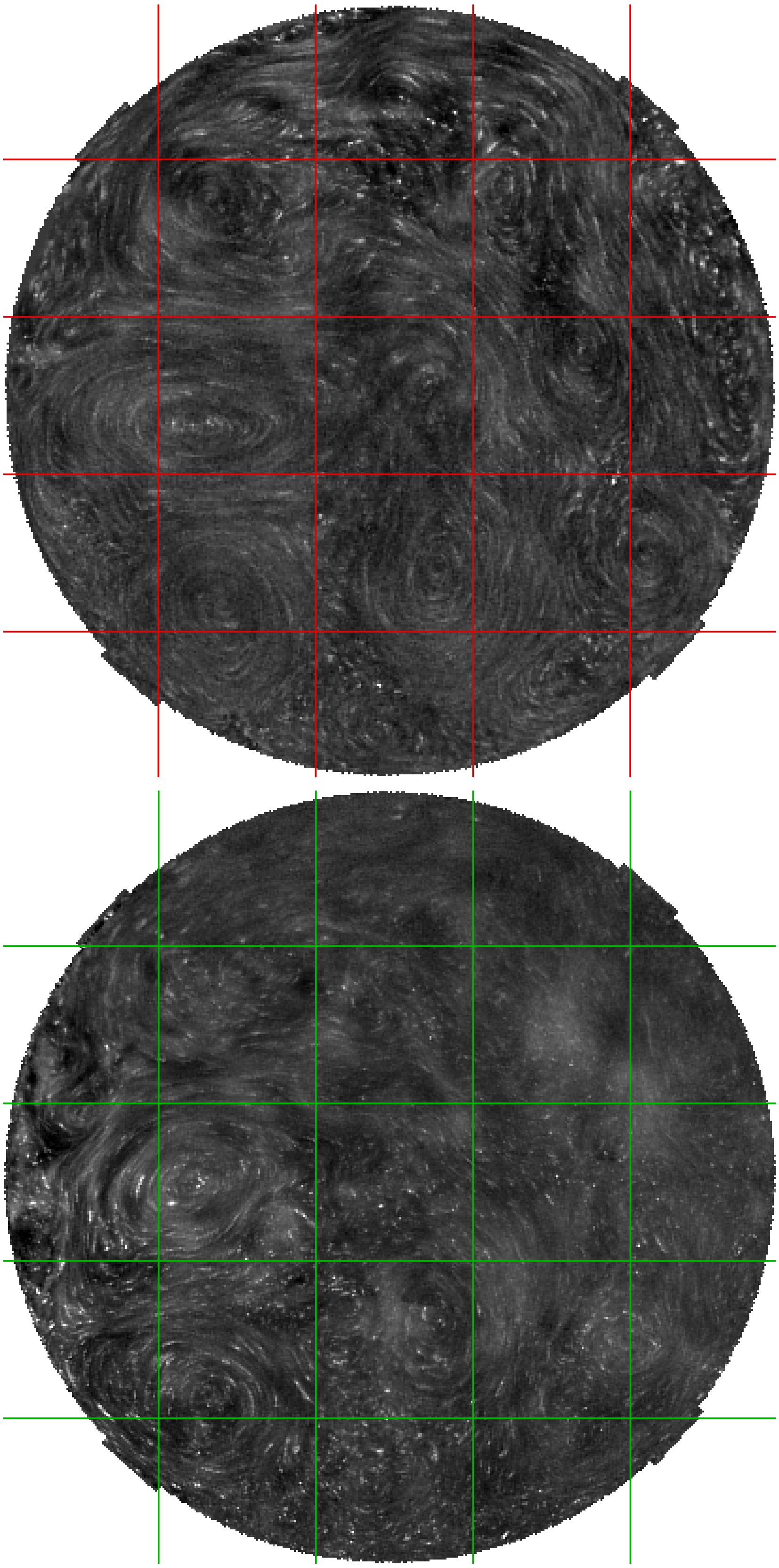

Figure 6.1: Simultaneous particle streak images in two light-sheets vertically separated by 20 cm. The grid lines, to guide the eye, are separated by 8 cm. The vortex dipole in the lower left (cf. figure 4.1) and other structures extend throughout the tank and therefore appear in nearly the same location at different heights (cf. figure 6.3). Multiple images are averaged to produce an effective exposure time of approximately 0.6 seconds.

appear to have been only shifted and deformed slightly between the two planes. We were able to observe the vertical extent of the vortices for a separation of 33 cm (at a lower light-sheet position 10 cm above the tees). We were not able to take quality measurements closer to the tees due to poor contrast of the resulting images from scattering of light. However, the extent of the vortices is likely even farther, as we were able to observe the strong vortices (such as the dipole pair) at a height 4 cm above the tees, using the video camera and a single light-sheet[5]. This indicates that the flow is quite columnar.

It is possible that some jets also extend vertically, such as the jet that meanders around the top of figure 6.1. However additional flow structure in the upper right of the lower sheet is difficult to resolve from particle streak images alone, due to poor contrast which smears out regions of the particle streak image.

The behavior of the flow field is quite different at very small or no rotation. At very small rotation or without rotation, a mean global flow was quickly induced by the pumping. The mean flow dominated what could be observed by eye. However, the flow did not appear correlated in separated horizontal planes, other than the mean flow, and no long-lived coherent structures were observed without rotation.

6.3.2 Measured fields and correlations

The correlation was calculated with the light sheets coincident near the top of the tank to determine the uncertainty in our measurements. A sample region of a resulting field is shown in figure 6.2 (a). The results were surprising[6] and a bit sobering. The mean pointwise percent difference between the two fields when the light sheets were coincident was found to be 25-27%For the small region shown in figure 6.2 (a), the mean pointwise difference between the fields is 13-18%. Despite the large percent difference between the two measured fields, there is still a high correlation of the instantaneous fields: 0.95 over the entire field and 0.97 in the region shown[7]. This indicates that the correlation is actually

---

[5] The contrast was poor, yet we were able to integrate for a long time with our eye to pick out the vortical motions.

[6] Though they should not have been: see section 3.3.4.

[7] It actually takes quite a large magnitude of noise to affect the correlation.

fairly robust against noise and uncertainties in the measurement. The uncertainty of the velocity correlation was roughly estimated to be no larger than ±0.05.

The vorticity is much more sensitive to spatial variations and noise because it is a derivative. For the vertical vorticity determined in the same plane, the percent difference over the whole field is 62% and over the region in figure 6.2 (a) is 43%. The vorticity correlation over the whole field was 0.82 and 0.92 for the region in the figure 6.2 (a), despite the large percent difference in the two fields. The uncertainty of the vorticity correlation was roughly estimated to be ±0.10.

The uncertainty due to the DPIV algorithm (about 2-3%, see chapter 3) and the amount of the uncertainty due to the different volumes illuminated by the two light sheets (the red is 1 cm thick; the green is less than 5 mm thick) is small compared to that due to the stereoscopic effects. In regions where the vertical velocity is comparable to the horizontal velocity and regions off of the center optical axis, the largest uncertainty is 13% (estimating from the stereoscopic formulae, see equations 3.11 and 3.12 in section 3.3.4); the uncertainty in the measured vertical vorticity is larger[8]. The uncertainty in the DPIV taken by a single camera is less than the 25-27% difference stated above (the difference comes from the fact that the two cameras are separated off of the optical axis, like our eyes). The difference in the two fields is physically significant and corresponds to vertical velocities[9]. However, from looking at the difference fields, it is difficult to pick out any clear structure associated with the structures. There may be only a weak correlation with cyclonic structures. However, measurements with calibrated stereoscopic PIV are necessary before we can make any robust statements regarding the correlation of the structures with vertical velocities.

Sample regions of the instantaneous velocity fields separated by 2 cm, 10 cm, and 33.1 cm are shown overlaid in figure 6.2 (b), (c), and (d), respectively. At a small separation, and with rotation, the fields look similar. In regions of strong uniform velocity the fields still

---

[8] n.b. This probably makes the specific values of the measured moments of vorticity meaningless(!), however the convergence of the measured statistics in the wavelet analysis still retains its significance.

[9] This is an important subject of future study.

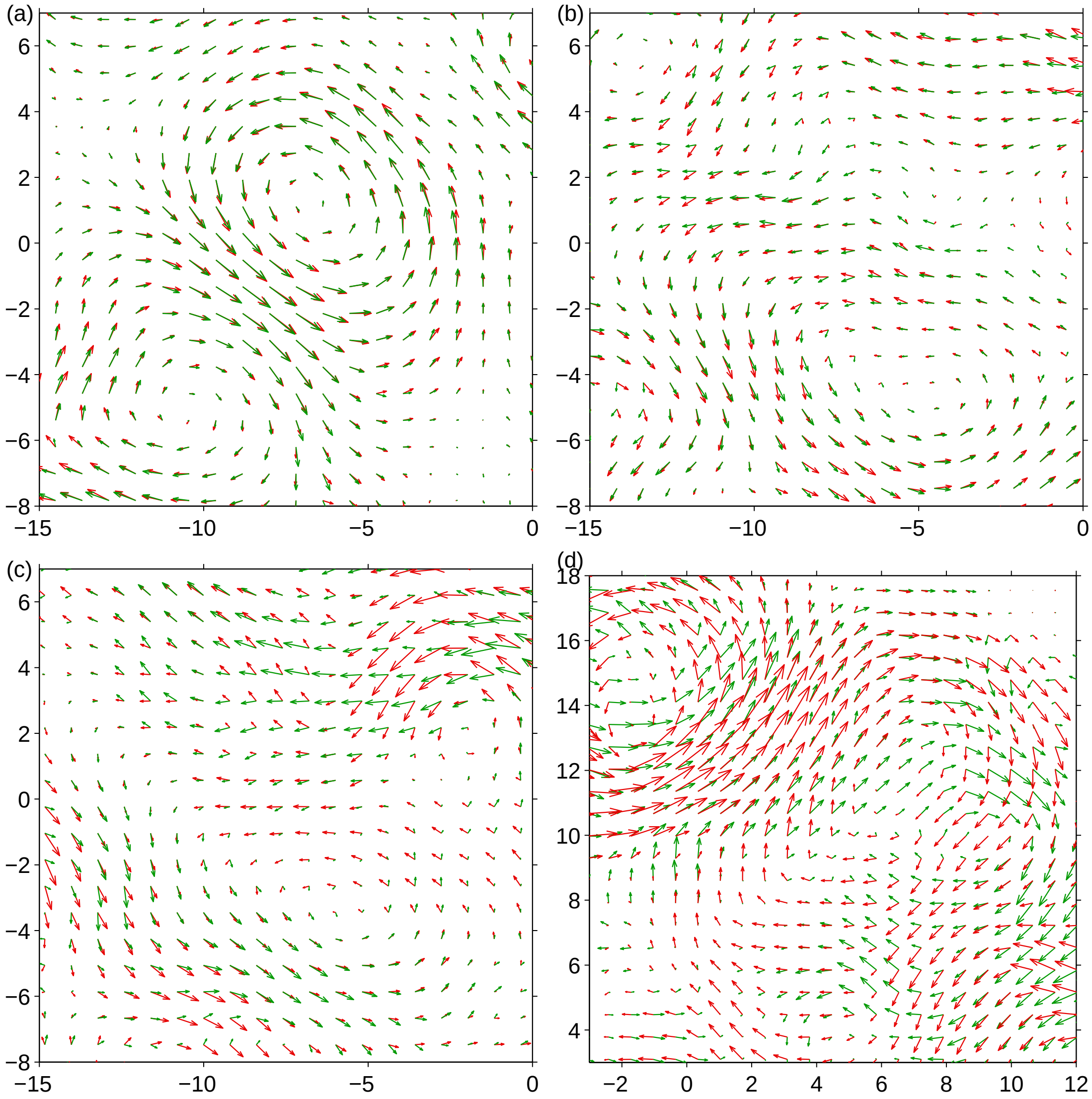

Figure 6.2: Separated velocity fields for fixed 0.4 Hz rotation and 426 cm^3/s pumping. The red light sheet, indicated by red vectors, was fixed at 4 cm below the lid. Vertical separations are (a) 0 cm, (b) 2 cm, (c) 10 cm, and (d) 33.1 cm. Large differences can be seen in the fields at 10 cm and 33.1 cm, however the same vertically extended structures are present (see figure 6.3). The center of the tank is at (0,0); units on the axis are cm.

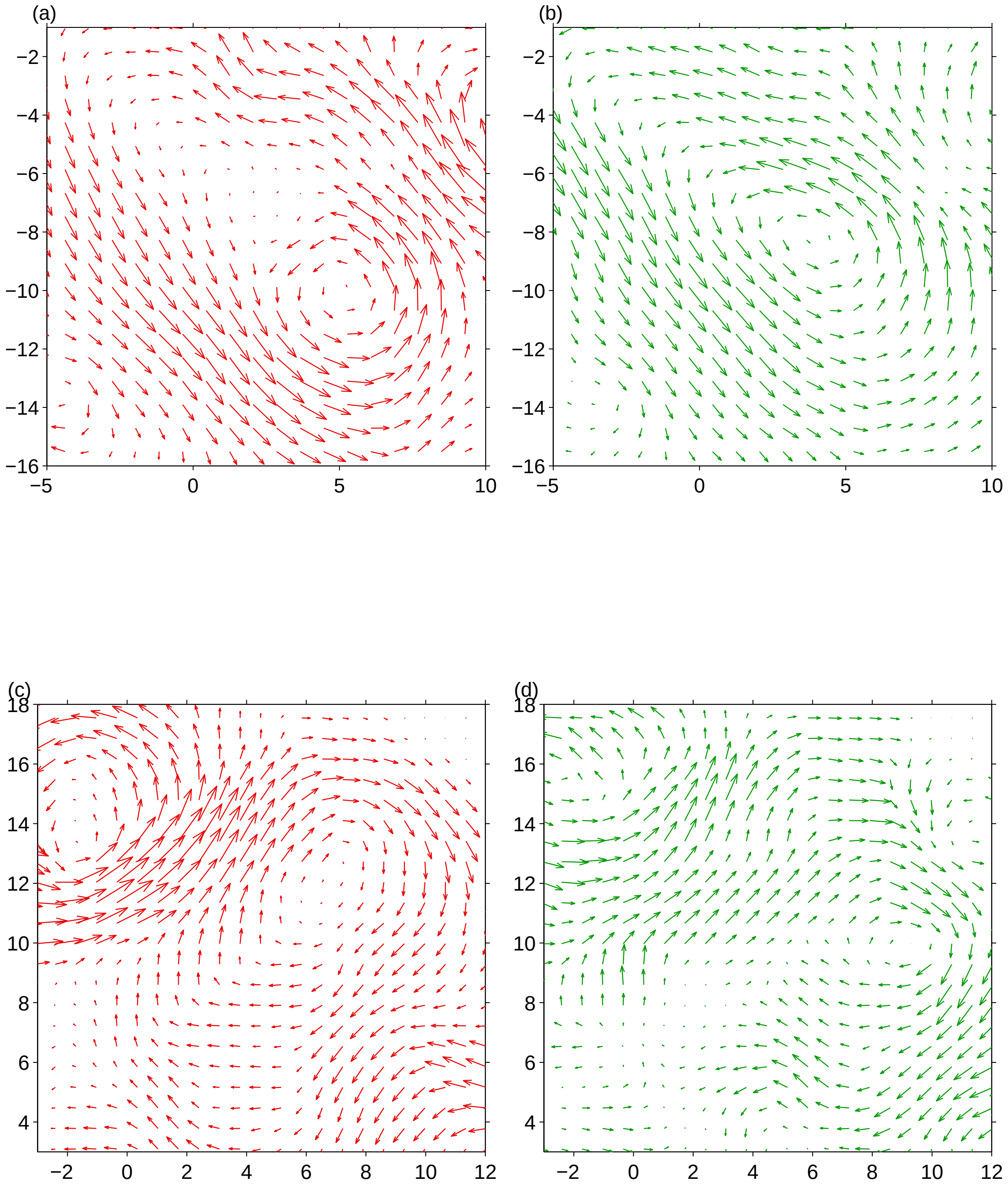

Figure 6.3: A side-by-side comparison of a close-up of velocity fields measured for large separations. (a-b) 10 cm separation (c-d) 33.1 cm separation. In (c-d), the fields are the same shown in figure 6.2 (d). If the fields were plotted on top of one another they would not appear to be correlated [e.g. figure 6.2 (d)]. However, in this side-by-side comparison, it is apparent that the flow structure is quite similar. e.g. the cyclone and anti-cyclone in (c) and (d).

look similar at a separation of 10 cm. Noticeable differences in the velocity fields emerge in regions of smaller velocity or where the velocity gradient is large. For larger separations, 33.1 cm, the overlaid fields look very different and uncorrelated [e.g. see figure 6.2 (d)].

However, the fields contain the same structures at large separations despite the uncorrelated appearance of the overlaid fields at large separations. The velocity field from separate heights is plotted side-by-side in figure 6.3 (a-b) for 10 cm, and (c-d) for 33.1 cm. The fields that look uncorrelated when plotted directly on top of one another now display a high degree of correlation of the structure, in particular the vortices, albeit not at exactly the same locations nor the same shape and orientation. For example, the center of the cyclone near the top of the tank in figure 6.3 (a) is shifted and elongated at a plane 10 cm below. This is consistent with our observations of the particle streaks (see figure 6.1). Even at the largest separations, the same vortices are present, but at shifted locations and deformed. Thus small shifts in the columnar structure along the vertical direction can cause the apparent correlation to decrease at large separations.

The resulting correlations are plotted in figures 6.4 and 6.5. In figure 6.4, the resulting correlations calculated using the two different methods, R_1 (equations 6.1 and 6.3) and R_2 (equations 6.2 and 6.4) were plotted. The correlation R_1 was consistently smaller than R_2. For a given difference in velocity, there is a larger contribution to the difference in angle in regions of small flow velocity. i.e. In regions where the vorticity or velocity is small, a small difference can significantly change the sign or angle. Thus weighting the correlation by the magnitude is less sensitive to error and is the more appropriate correlation to calculate.

We calculated the correlations for the instantaneous fields, the mean fields, and the mean-subtracted fields. The mean fields exhibit a much slower decrease in correlation. This is likely due to a combination of the flow structure that is forced by the pumping in addition to the 2D nature of the flow (e.g. see mean fields in figures 4.11, 4.9, and 4.10). In particular, at very low rotation or at no rotation, the pumping drives a large mean flow. At low rotations the mean flow dominates the instantaneous flow field throughout the tank,

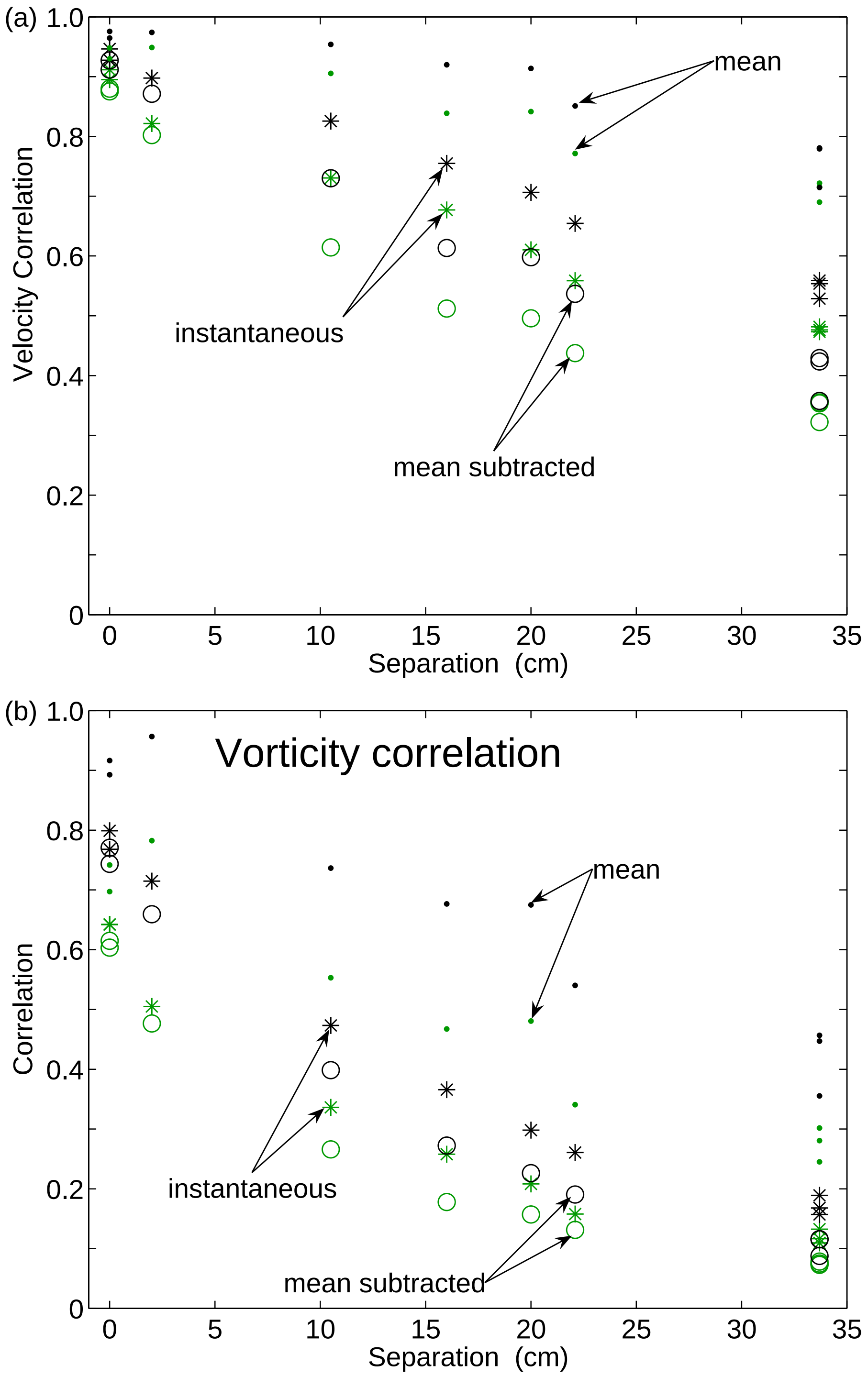

Figure 6.4: (a) Velocity correlation and (b) vorticity correlation as a function of separation. Data fixed rotation rate at 0.4 Hz and pumping rate at 426 cm^3/s. The dots correspond to the correlations of the mean fields, the asterisks to the instantaneous fields, and the open circles to the mean subtracted fields. The lighter color symbols correspond to the R_1 correlations (equations 6.1 and 6.3, not weighted by the magnitudes) and are consistently smaller than the R_2 correlations (equations 6.2 and 6.4).

causing the correlation to be larger than expected (this is an artifact of the tee forcing geometry).

We computed the correlation of the mean-subtracted fields to account for artificially high correlation induced by our forcing. Without rotation, the velocity correlation at a separation of 33.1 cm was found to be 0.962 (0.928) for separated instantaneous fields and 0.008 (0.003) correlation for the mean-subtracted fields (this is our global flow without rotation) for R_2 (R_1). For the rotating cases, the flow is not dominated by a mean global flow. Subtracting the mean fields reduced the correlation, though the effect was not as large as for the non-rotating case (e.g. see figure 6.4).

In all cases, we see a steady monotonic decrease in the correlation for increasing separation. The trend is not sharp and we did not observe a plateau in the correlation or any well defined transition or break points. The vertical vorticity [figure 6.4 (b)] correlation is consistently smaller than the velocity correlation, likely due to a larger uncertainty, but exhibits the same trend. For the 0.4 Hz rotation and 426 cm^3/s pumping in figure 6.4, the *e*-folding length of the velocity field is approximately 33 cm. This can be interpreted as the vertical integral length scale of the flow. This is much longer than the horizontal integral length scale, 4 cm at the same condition (from the calculation of the correlation in the horizontal plane of the flow field near the top of the tank). This is consistent with the effect of rotation, increasing length scales parallel to the rotation axis.

The resulting correlations as a function of the table rotation rate and at several separations are shown in figure 6.5. For small (i.e. 2 cm) separations there is a weak dependence upon the rotation rate of the correlation of the instantaneous, mean (not plotted), and mean subtracted fields at this separation. For larger separations (i.e. 33.1 cm) there is a stronger dependence upon the rotation rate. The trend is consistent with the effect of rotation increasing the vertical integral length scale of the flow.

However, the dependence of the correlation of the mean-subtracted fields upon rotation appears to be non-monotonic with a peak measured at a moderate rotation rate, 0.4 Hz. This is contrary to what we would expect, i.e. increasing correlation as rotation

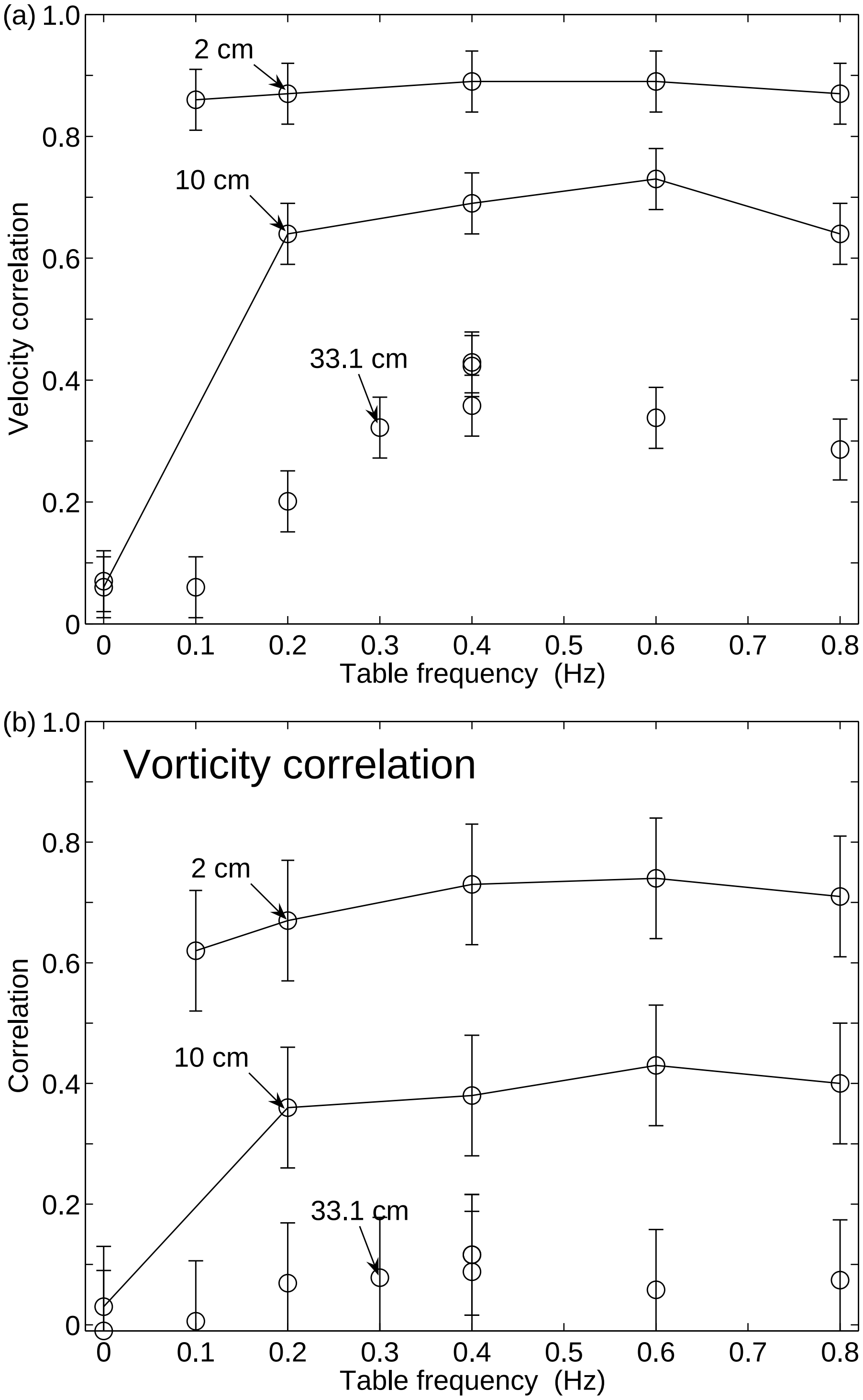

Figure 6.5: (a) Velocity correlation and (b) vorticity correlation at different separations as a function of table rotation rate. The pumping rate was fixed at 426 cm^3/s. Plotted are the correlations, R_2 in equations 6.2 and 6.4, of the mean subtracted fields. The lines connecting points are plotted to differentiate the data taken at different separations.

is increased. A possible explanation might be the interplay of rotation and dissipation in our flow. The large coherent structures, such as the vortices, dominate the correlation. At higher rotation rates, for the same forcing, the structures are smaller due to enhanced dissipation (e.g. see chapter 4). Thus the smaller vortices may not contribute as much to a large correlation. This may be the cause of the decrease in correlation at the very high rotation rates. However, more careful measurements are necessary before reaching such a conclusion.

6.4 Summary

The fields are surprisingly well correlated at moderate rotation and for large vertical separation. We observed the same structures, such as vortices, simultaneously present in vertically separated horizontal planes. This was consistent with the picture of the flow vertically extended throughout the tank in a quasi-2D column-like state [e.g. see figure 2.1 (b)].

For the conditions presented where the separation is varied, there does not seem to be a sharp spatial transition where the correlation rapidly decreases. Instead, the velocity correlation drops off almost linearly. The vorticity decreases more rapidly, but does not appear to suddenly decrease at a well defined transition point.

There appears to be a non-monotonic change in the correlation as a function of rotation at large separation. Surprisingly, the correlation peaks at low rotation (0.4 Hz) and decreases for higher rotation. This seems to be just outside our estimated uncertainty, but we need to take better data to confirm this trend.

Chapter 7

Discussion

The work in this thesis was a study on coherent structures and the effect of rotation on turbulence in a laboratory experiment. In this final chapter we discuss the significance of the present work and outline future directions and experiments.

7.1 Contributions

We have designed and built an apparatus to study rotating turbulence. We can achieve a large range of rotation and forcing rates to study the effect of rotation on turbulent structure. The geometry of the forcing, consisting of pumping near the bottom of the tank, can be easily modified to produce a wide range of flow conditions. The tank was designed to be deep so as to allow us to probe the dimensionality of the flow by changing the vertical location of our horizontal light-sheet; the flow near the bottom is dominated by the localized turbulent forcing which spatially decays such that the flow near the top is dominated by the rotation. We were also able to obtain vertical velocity measurements by changing the orientation of our light sheet and illuminating vertical planes. This is in contrast to most other rotating turbulence experiments that are shallow and typically constrain observations of the flow to a fixed horizontal plane. We implemented a second camera and light-sheet, synchronized to the first. This allowed us to correlate simultaneously the flow at different vertically separated planes, not previously done in experiment. The construction of the apparatus, designed to be versatile and easily modifiable for future experiments, is a major contribution of our work.

We found that flow strongly forced near the bottom of our deep rapidly rotating tank evolves with increasing height in the tank from 3D turbulence into rotation-dominated turbulence. This is due to the competition between the turbulent forcing which is 3D, and the rotation which tends to two-dimensionalize the flow. Near the forcing, the turbulent velocities are large and the flow is 3D. Away from the forcing, the spatial decay of the turbulent velocities allows the rotation to become increasingly important with increasing height. Motions of the particles in the flow were observed to be more organized in the horizontal plane near the top, consistent with two-dimensional columnar vortices. The flow in the rotationally dominated (Rossby number $< O(1)$) region of our tank has a strongly non-Gaussian vorticity PDF and exhibits properties of 2D turbulence, such as large-scale long-lived coherent vortices, vortex filamentation, and merger.

We found that the presence of even moderately turbulent flow significantly enhances the decay rate at which the flow responds to perturbations, compared to the laminar response. For a high enough initial turbulence level, we found that the decay could be described by a sum of two decaying exponentials with two well separated decay rates. The short time decay is responsible for the decay of most of the energy in the flow and indicates that the turbulence is responsible for the overall enhanced decay. The long time decay agreed well with the decay times found in the laminar experiments and appeared after a significant amount of the turbulence had decayed. We also observed significantly larger vertical velocities than expected. The largest vertical velocities appeared to be present in the large coherent structures and were similar in magnitude to the horizontal velocities. Since large vertical velocities increase the momentum exchanged between the interior and the boundaries, this indicated the possibility that the coherent structures present in quasi-2D turbulent flow may be responsible for enhanced dissipation rates. Further work is required to verify this claim, however. It remains to be seen whether or not the enhanced dissipation is due to a turbulent Ekman layer or due to vertical velocities induced by the coherent structures (or a combination of both).

The vertical component of vorticity describes the flow well near the top where the flow is quasi-2D as a consequence of the rotation. We were thus able to use the projected flow field as measured in a horizontal plane for analysis with wavelet and Fourier-based decompositions. Because our flow fields contain compact structures, the localized basis functions of the discrete wavelet packet transform (DWPT) and discrete wavelet transform (DWT) outperform Fourier and JPEG decompositions. The DWPT and DWT yielded very similar results, despite the adaptability of the DWPT basis. The DWT is therefore made preferable by its faster computation [$O(N)$ versus $O(N \log_2 N)$ operations].

Both the DWPT and DWT have more rapid convergence, relative to other methods, of the statistics of the extracted coherent component toward that of the total flow. The rapid convergence of the skewness and kurtosis of the vorticity PDF suggest that the wavelet based methods have efficiently captured the coherent structures. The Fourier and JPEG converge much more slowly and are thus unable to efficiently capture the large higher moments of the vorticity PDF. This suggests that the Fourier and JPEG methods have not really extracted the coherent structures despite the appealingly smooth visual appearance of the structures in the coherent field of the Fourier. Indeed, the superior performance of the DWT over the JPEG is exploited by the emerging next generation JPEG2000 image compression standard, which uses a bi-orthogonal DWT [1, 8]. The incoherent remainder of both the DWPT and DWT converge rapidly towards Gaussian statistics, while incoherent remainders of the Fourier and JPEG do not converge to any value.

We have shown that wavelet based transforms can be used to separate the coherent structure-containing quasi-2D turbulent flow into a non-Gaussian coherent component represented by as few as 3% of the large-amplitude, low entropy coefficients of the transform and a nearly Gaussian incoherent component, represented by the remaining small-amplitude, high entropy coefficients. We are able to obtain this result without an a priori assumption of Gaussianity or non-Gaussianity of the two components.

The coherent components of the DWPT and DWT retain all of the properties of the total field, including the large-scale structures, shape of the vorticity PDF, long spatial and temporal correlations, and transport properties. Further, the coherent component contains the large skewness and kurtosis of the PDF which are due to the coherent structures. In contrast, the incoherent remainder has only small-scale short-lived features and does not contribute significantly to the transport. Thus in analysis of flow dynamics and transport, it may be sufficient to consider only the coherent component. These results suggest that it is reasonable to reduce the computational complexity of turbulent flows by considering only the low-dimensional coherent structures, which interact with a statistically modeled incoherent background.

We observed that the coherent structures, in particular the vortices, are vertically extended throughout the flow. They reach to just above the forcing and are surprisingly columnar, undergoing small shifts in their location and deformation of their cross section. The vortices appear in similar locations in vertically separated planes, consistent with a tendency of structures to align themselves along the rotation axis.

We found a gradual decrease in the correlation of increasingly vertically separated horizontal velocity and vertical vorticity fields, rather than a sharp transition. We found that even moderate rotation significantly increases the vertical correlation length of turbulent flow. This is perhaps due to the dominance of the coherent structures.

We also observed a non-monotonic change in correlation for increasing rotation rate. For large separations, the correlation peaked at moderate rotation and decreased for stronger rotation. This could be due to the effect of the enhanced dissipation at higher rotation rates on the coherent structures. However, we must correct for stereoscopic effects to obtain the most accurate possible measurements of correlation of vertically separated horizontal projections of the velocity field. This will require 4 cameras (2 cameras per light sheet) and new grant monies(!).

7.2 Future work

Not being selfish, we have left a fair amount of work for future graduate students and postdoctoral researchers. A key feature of our apparatus is its versatility. This will allow future research to address many aspects of rotating turbulent flow.

7.2.1 Improvements on the current apparatus

Though the apparatus is in a good working condition, there are still many improvements to be made, as already outlined in section 3.3. Resolving these issues will improve the operation of our apparatus.

7.2.2 Effects of forcing configuration

The forcing geometry of the tees was chosen to reduce vertical velocities. However, this resulted in preferentially forced coherent structures. The specific flow configuration was dependent upon a combination of the pumping and rotation rates and rotation direction. The pumping also injected energy at large scale into the flow by forcing the large persistent structures. This creates large inhomogeneities in the flow structure. This may have influenced our measurements such that we were probing a combination of the effect of rotation and the forcing geometry.

Careful DPIV measurements probing the flow structure have not yet been taken with the flipping tubes or other geometries. The modularity of our apparatus allows us to examine the effect of different forcing configurations. Ideally, we do not want the forcing geometry to constrain the resulting flow structure. Rather, we want the physics to determine the flow structure. Can an array of nozzles or flipping tubes produce more homogeneous flow? How many sources and sinks are necessary to produce small scale forcing? Is it even possible to force only small scale motions by pumping in a closed tank?

7.2.3 Stability of coherent structures

The stability of coherent structures in rotating turbulent flow is of great interest in climate dynamics. Questions such as how large of a perturbation is necessary to destabilize a structure such as the jet stream or hurricane can be addressed in our apparatus. The modularity of our apparatus allows us to hook up our sources to relay switches that can modulate the forcing configuration. How much of a change in forcing or rotation is necessary to destabilize our structures?

7.2.4 Stereoscopic PIV

Stereoscopic effects in our apparatus can be large (e.g. section 3.3.4). This affects the measured velocities: they are a combination of in-plane and out-of-plane motions. We must use properly calibrated stereoscopic PIV, to achieve higher accuracy in our measurements (this is a challenge in itself!). This will be particularly useful closer to the forcing and for measurements in the vertical light sheet, where the out-of-plane motions are comparable to in-plane motions.

We can also determine the vertical velocities in the plane of our horizontal light sheet using stereoscopic PIV. This will allow us to correlate the coherent structures with the large vertical velocities. Are they in the cores of the coherent vortices, or just outside in the jets? Is there a relation between the strength or vorticity of a structure and vertical velocity?

7.2.5 Future dual light sheet

Many measurements remain to be taken with the dual light sheet setup. Exploring the vertical integral length scale as a function of control parameters is one of the most physically significant set of measurements. So far, only limited data have been taken, due to (graduation) time constraints.

Further measurements should investigate the non-monotonic dependence of the correlation between two vertically displaced horizontal fields on the rotation rate. We should measure the vertical integral length scale as a function of rotation rate. Will we see the same trend in the vertical integral length scale? What is the cause of the non-monotonic dependence of correlation on rotation?

Additional measurements should be performed for small vertical separations at various heights in the tank. We could then examine the correlation as a function of the local Rossby number, typically though of as a measure of the flow two-dimensionality. Is the Rossby number an accurate indicator of the level of two-dimensionality of the flow?

Further, it is best to repeat the measurements with different forcing configurations. The tees used in the current measurements preferentially forced structures that may dominate the correlation. Will different forcing configurations lead to more homogeneous flow structure and have the same degree of vertical correlation?

Of course, to obtain the most accurate measurements, we will need 4 cameras. This will allow us to correct the correlations for stereoscopic effects and to correlate the vertical velocities (for 2D flow, the $\partial w/\partial z = 0$).

Vertical sheet

The advantage of using two light sheets extends not only to simultaneous measurements in two horizontal planes. Using intersecting horizontal and vertical light-sheets will allow us to correlate vertical velocities along the depth of the tank with the coherent structures. This is complementary to stereoscopic PIV measurements that yield vertical velocities in the plane. When structures observed in the horizontal plane pass through the vertical sheet we should be able to determine the extent of the associated vertical velocities. This will help to resolve the question of whether or not enhanced dissipation is due to pumping from the coherent structures.

An exciting possibility of the dual light-sheet configuration can be realized using 4 cameras and a very small vertical separation. Then we may determine all 3 components of the velocity and all 3 components of the vorticity field in a plane. Even with 2 cameras we may be able to estimate the full 3D field (we can calculate $(\partial w/\partial z)dz$ for a sufficiently small separation). We can then calculate the angle between the vorticity and the rotation axis as a function of control parameters. How vertical are our structures?

7.2.6 Future work with wavelets

We should attempt to understand the physical significance of wavelet transformed data. Most uses of wavelets until now have focused on reducing noise or extracting coherent parts. Once we trust that the wavelet technique is able to faithfully extract the dynamically significant component of the flow field, the next step is to understand the physics of the coherent field. One thing we can measure is the global and local fluxes of conserved quantities (i.e. energy and enstrophy). By observing these quantities in the coherent and incoherent remainder fields, we hope to understand the dynamical difference between the two components. The transform should be tested on simulated data of well characterized flow solutions, to understand exactly what those quantities mean.

It will be interesting to use the wavelets to analyze hotfilm probe data of the rotating annulus of Baroud (and possibly data from a Taylor-Couette apparatus). The coherent structures likely play different roles and have different distributions depending on whether the flow is 2D or 3D. It would be interesting if we could observe that indeed the coherent structures are somehow responsible for non-Gaussian PDFs, even if by indirect observations of more structures in 2D where the PDFs are more non-Gaussian. Can we appropriately identify coherent structures using some time series data? What can we learn about the distribution of such structures in flow of varying degrees of turbulence and two-dimensionality?

7.2.7 Vorticity probe

We can realize a novel vorticity probe using the region of interest (ROI) function of the frame grabber. We can obtain small subregions of images by specifying a ROI. This allows us to achieve a much higher frame rate, as the amount of data stored from a single image can be significantly reduced.

This local probe can be used to obtain long time series of local velocity and vorticity data. Potentially all three components of the velocity can be measured, using stereoscopic PIV. This provides several benefits over hotfilm probes which can not distinguish the components of velocity measured transverse to its sensing element. There is also no need to rely on the Taylor frozen turbulence hypothesis to convert temporal data into spatial data.

With these measurements it will be interesting to test the local isotropy of our flow and compare local temporal averages to global spatial averages (obtained by DPIV measurements over the entire flow field). As energy dissipation plays an important role in determining the statistics of velocity differences, enstrophy dissipation in 2D flows affects on the statistics of vorticity. Geophysical and rotating turbulent flow is very inhomogeneous and anisotropic. In our tank, the flow is very inhomogeneous, containing many coherent structures. However, the flow may be considered as more homogeneous over a small region. Are there regions where the flow can be considered locally homogeneous?

7.2.8 Zonal formation

Another interesting problem is the genesis of zonal flow. A test of the theory of zonal formation given in [74] can be carried out in our apparatus. A β-plane will be added which mimics the variation in the Coriolis force due to planetary curvature. The β-plane, a Plexiglas cone, has been specially made for our apparatus and will fit just below our top lid, but has not yet been used. The effect of the β-plane is to inhibit radial (North-South on a planet) motion in our tank so that coherent structures, such as vortices, will wrap around in the azimuthal direction (East-West) and eventually merge into concentric zones. We will have all the ingredients needed: small scale homogenous forcing (using the flipping tubes), Ekman-like dissipation and a rotationally dominated quasi-2D system with a β-plane. We expect to be able to see zones, though preliminary calculations have suggested our system size may be too small to see more than one or two zones.

7.2.9 Simulations

An ambitious project would be to simulate numerically the full three-dimensional flow produced in our apparatus. This is not a simple weekend project (nor perhaps even a summer project)! No realistic numerical simulations have been carried out for large Reynolds number, due to computational difficulties. Simulation becomes increasingly ambitious if the appropriate boundary conditions and domain geometry are realized, such as our rigid top and bottom boundaries and cylindrical sidewalls. It is not clear how to model the localized forcing or whether the resulting flow will depend upon the details of the modeling.

7.3 The end

We could go on forever, but at some point the author must graduate. We conclude with the hope that our experimental apparatus will live a long and happy life in the Center for Nonlinear Dynamics at the University of Texas at Austin!

Appendix A

New Sprinkler Drawings

In this appendix we present the design drawings for the new Sprinkler construction.

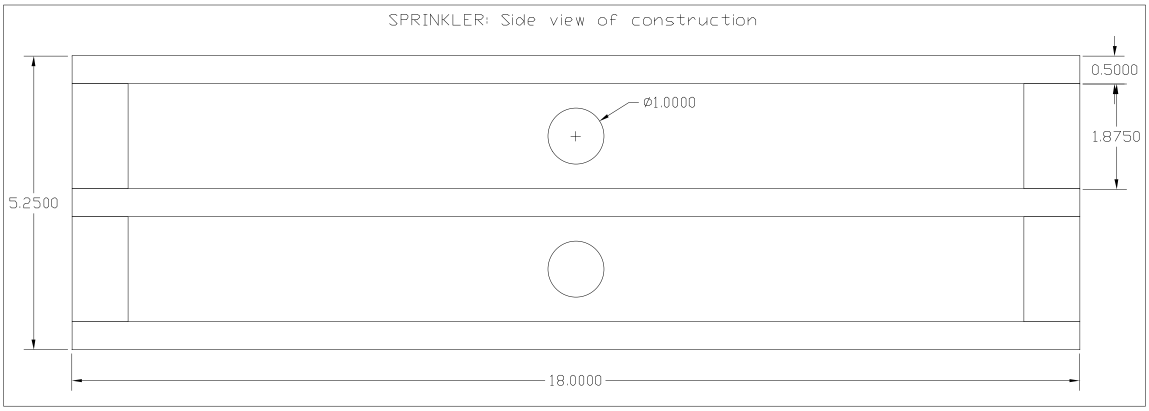

Figure A.1: Side view of the Sprinkler. The upper chamber is the high pressure manifold, the lower chamber is the low pressure return. The two chambers are are sealed by o-rings between the top, middle, and bottom plates and the sidewalls. The plates are made from 0.5 inch acetal copolymer stock. The sidewalls are made from acrylic stock that was milled flat.

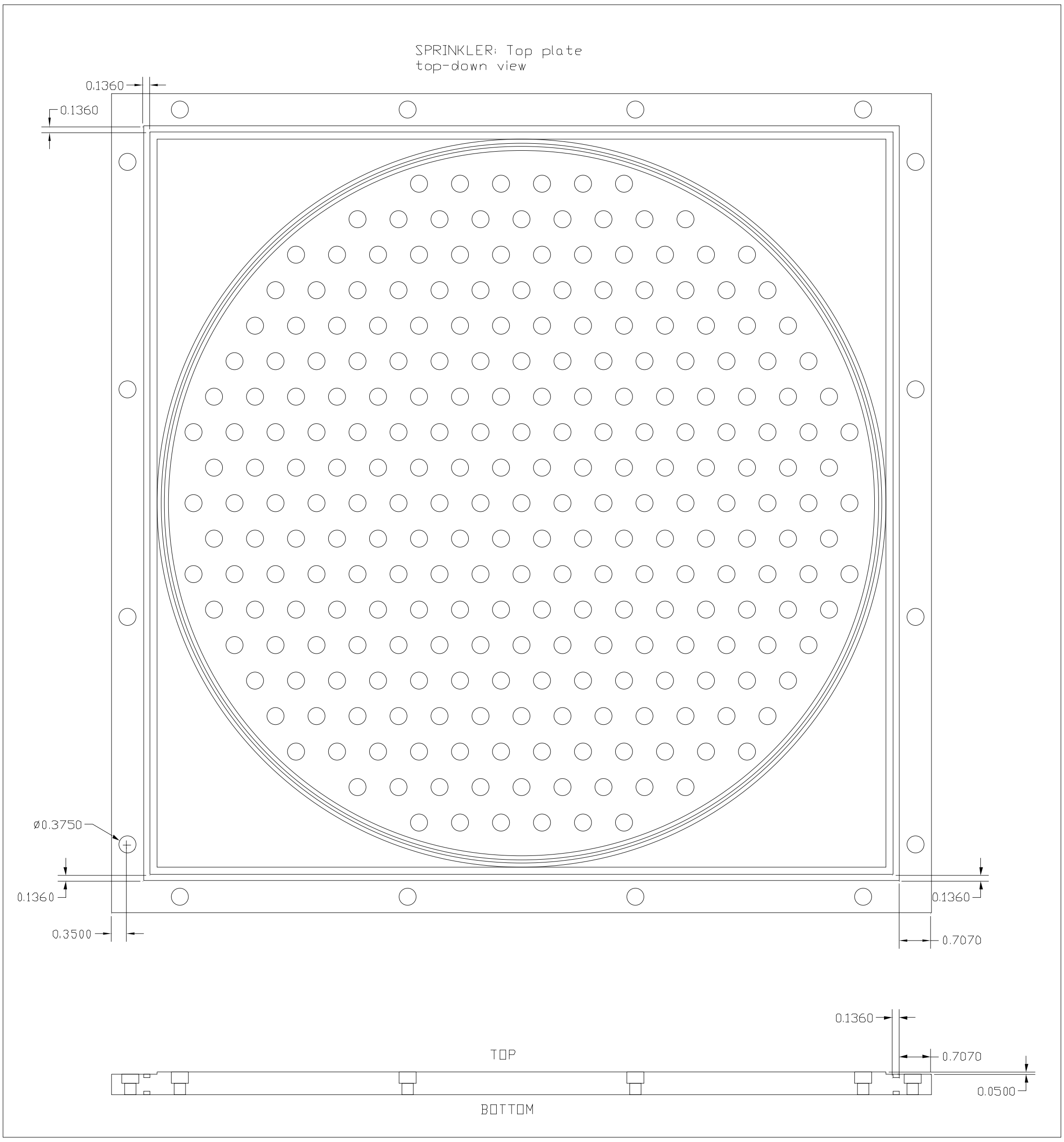

Figure A.2: The top plate of the Sprinkler shown with all the holes. The 61 holes that align with the ones in the middle plate are clearance and chamfered so that o-rings can seal against the nipples that connect to the lower chamber. The remaining 192 holes are tapped for nozzle connectors. A circular o-ring groove allows the cylinder to be sealed. The o-ring groove along the periphery of the top surface allows the acrylic box to be sealed.

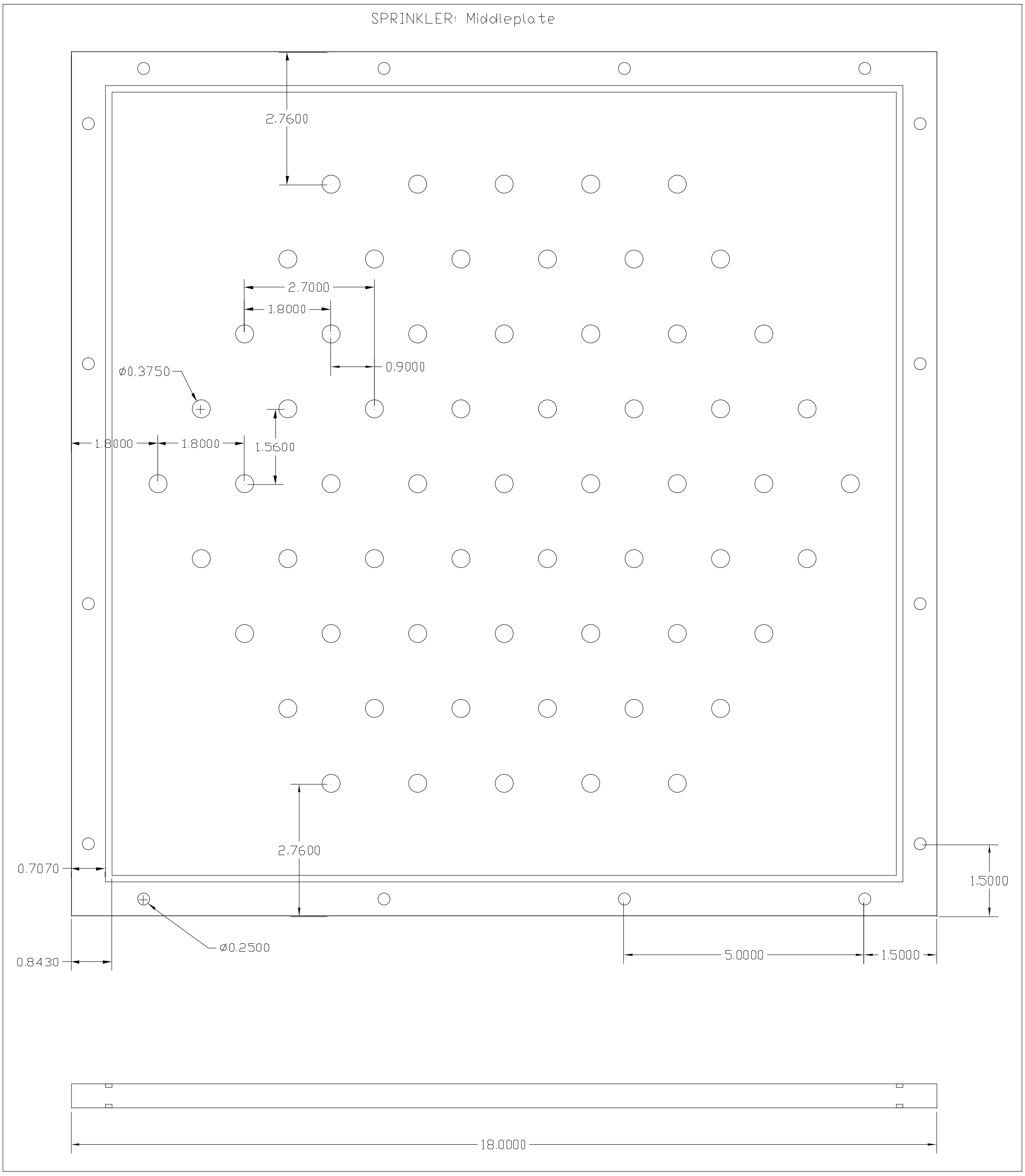

Figure A.3: The middle plate of the Sprinkler. Nipples connect to the NPT tapped holes to connect the sinks to the lower chamber of the Sprinkler.

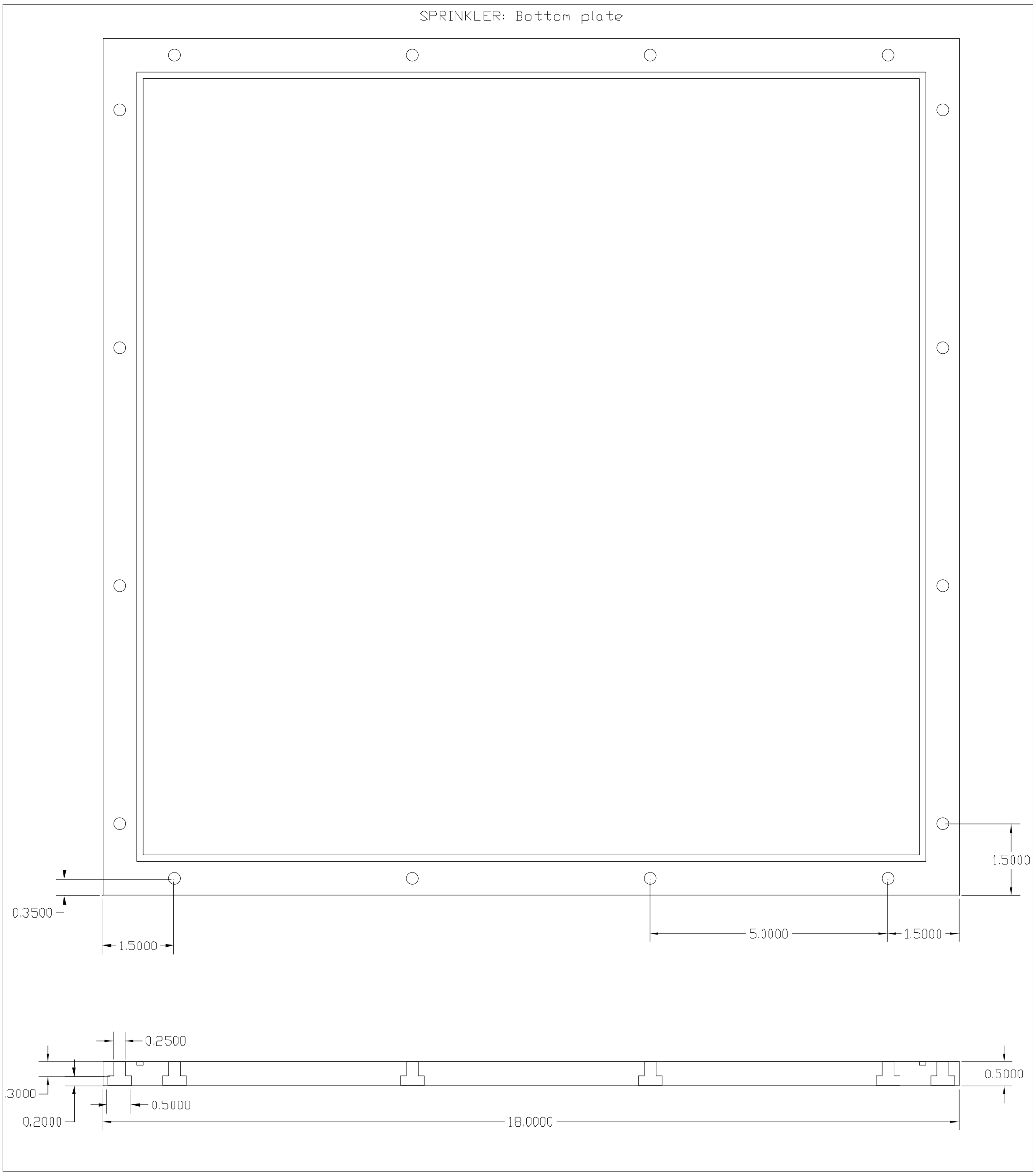

Figure A.4: The bottom plate of the Sprinkler. The bottom clearance holes along the edge are counter bored to allow for nuts to be fastened underneath the surface of the plate and to the bolts that hold the Sprinkler together.

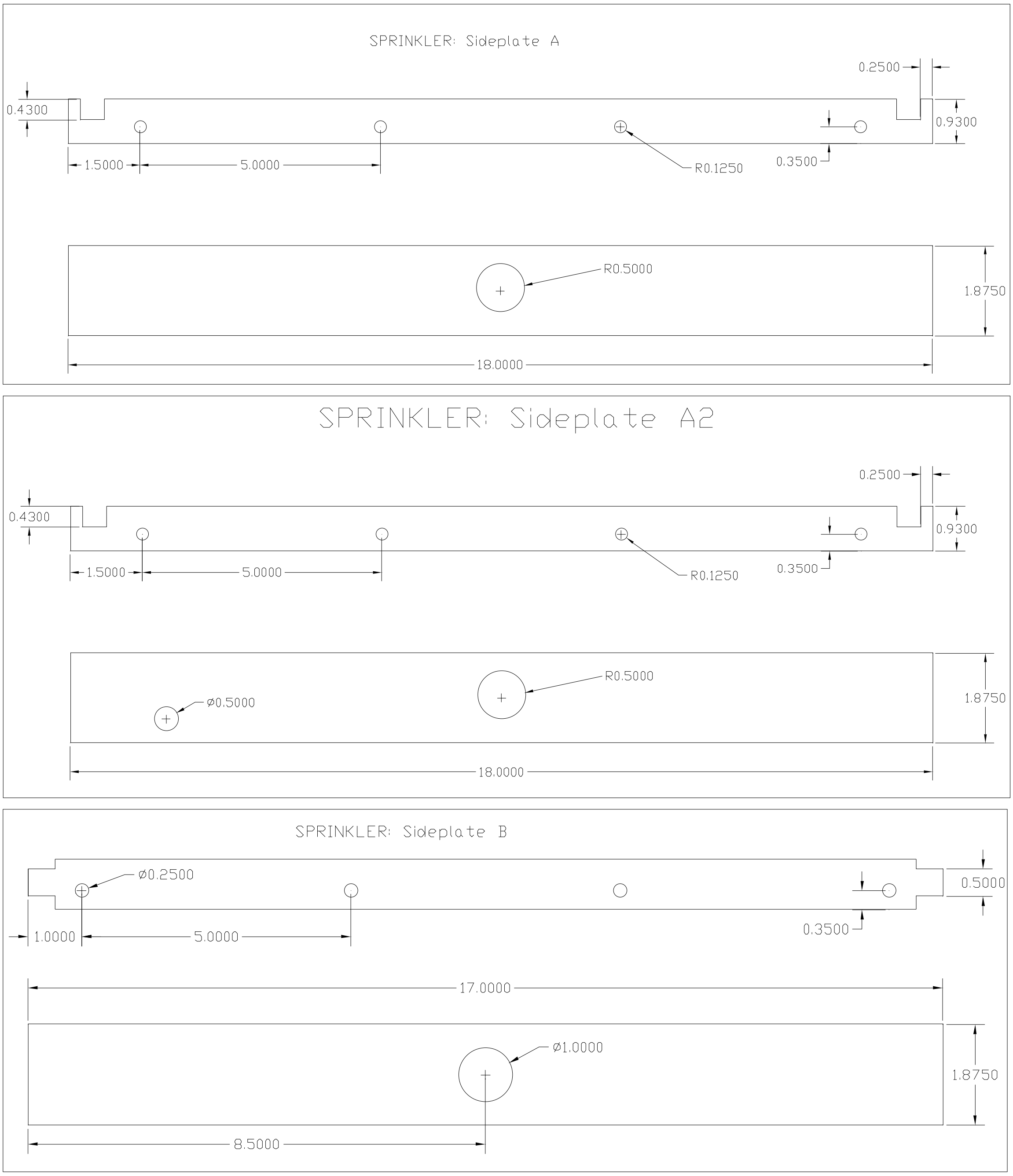

Figure A.5: The sideplates of the Sprinkler. These pieces form the walls of the Sprinkler. They fit together by tongue-and-grove joints (similar to the box). They are bonded by Weld-on acrylic cement applied using capillary forces to wet the joint.

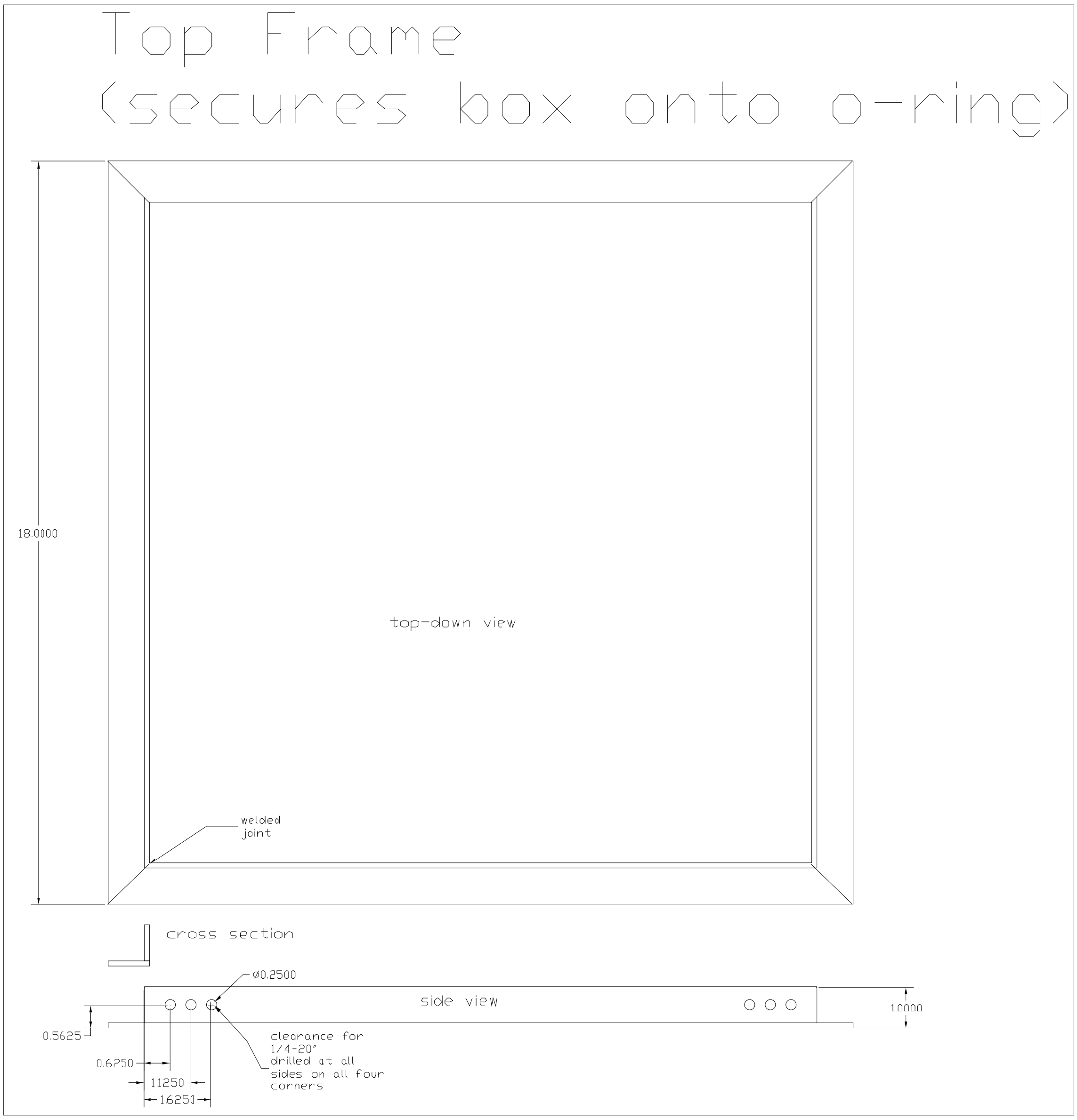

Figure A.6: The top box frame. This is used to apply uniform pressure on the acrylic box to seal against the o-ring on the top plate of the Sprinkler. The frame is made from welded 304 stainless steel angle stock.

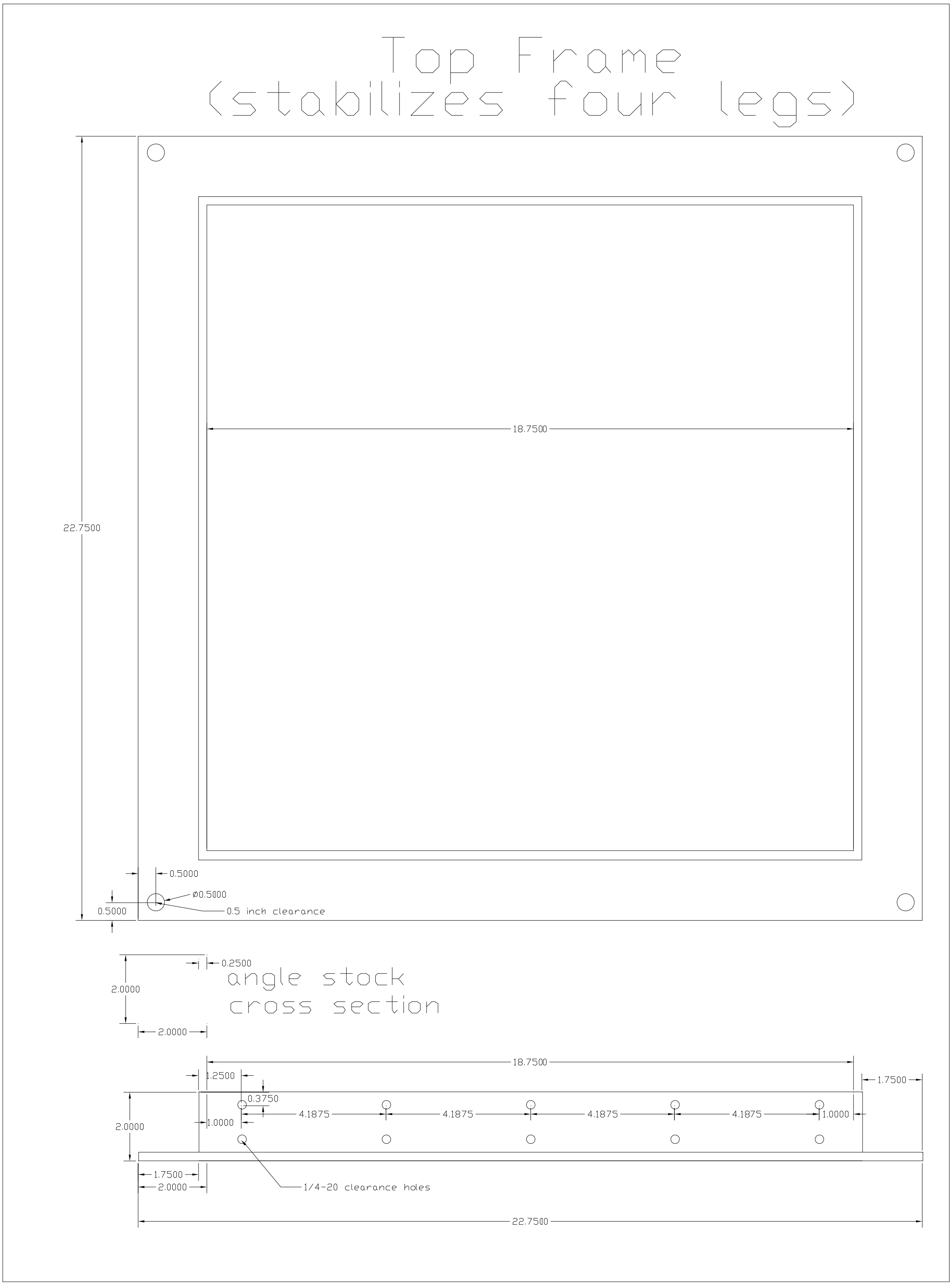

Figure A.7: The top stability frame. This frame is attached to the top of the four angle legs to provide stabilizing support. This frame is made from A36 steel angle stock. It is painted flat black to reduce reflections and protect against rust.

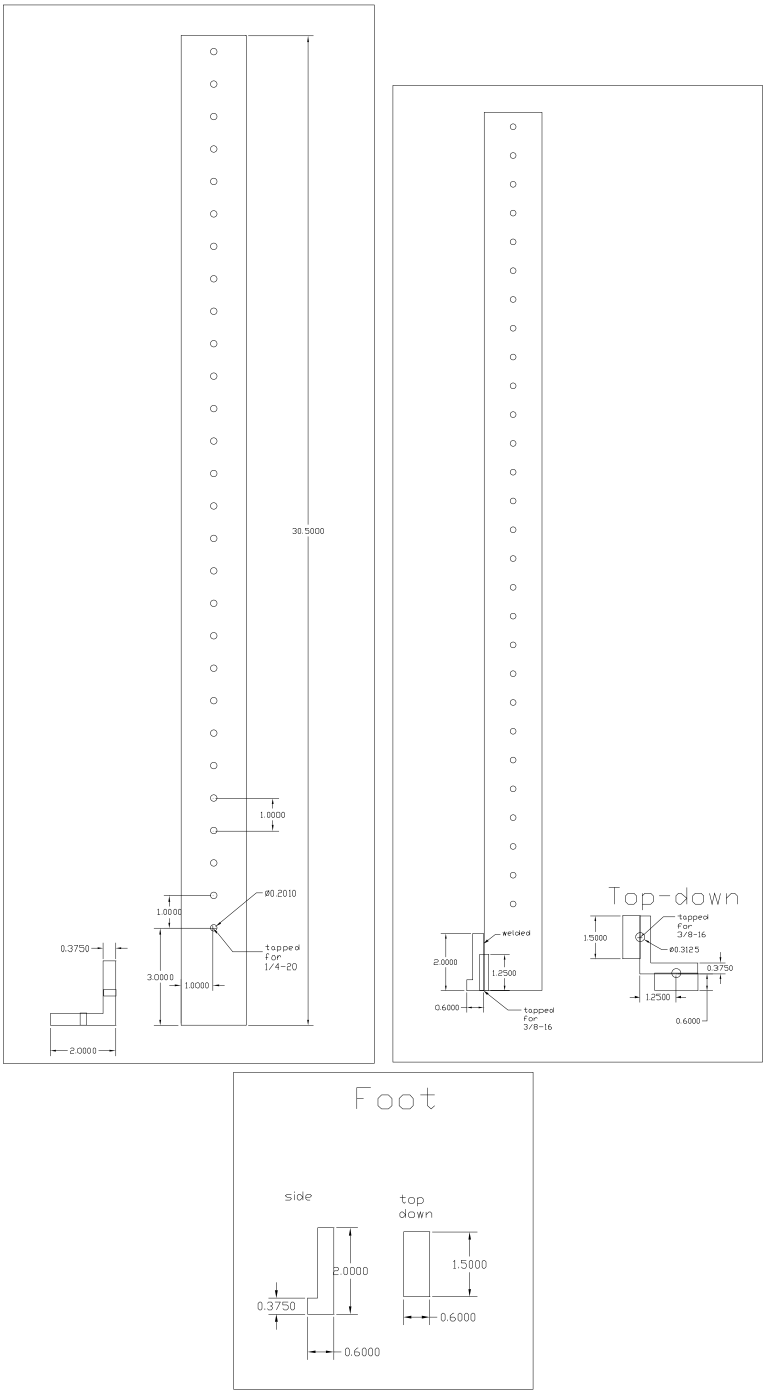

Figure A.8: The supporting side angle “legs”. The legs are made from 304 stainless steel angle stock. The “feet” are welded onto the tall angle pieces. Tapped holes at the bottom of the feet allow the legs to be fastened to the brass plate that the Sprinkler sits on.

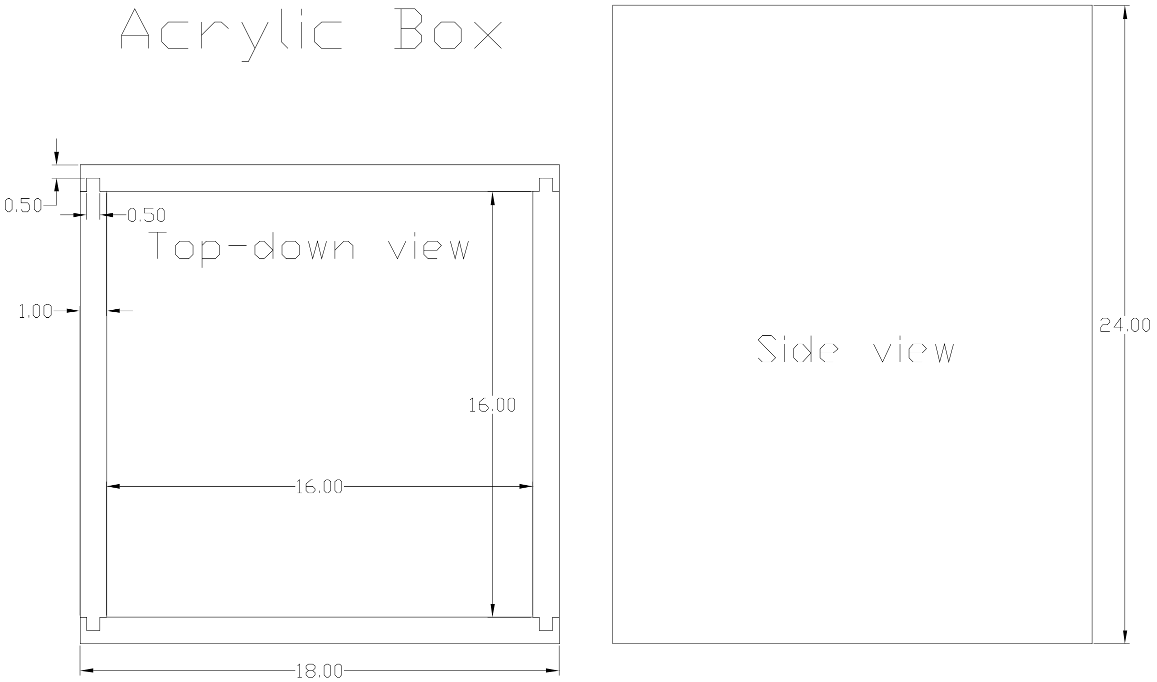

Figure A.9: The acrylic box. The box sits on top of the top plate of the Sprinkler. The sides of the box are glued together by Weld-on acrylic cement. The box is made from 1 inch (nominal) acrylic stock.

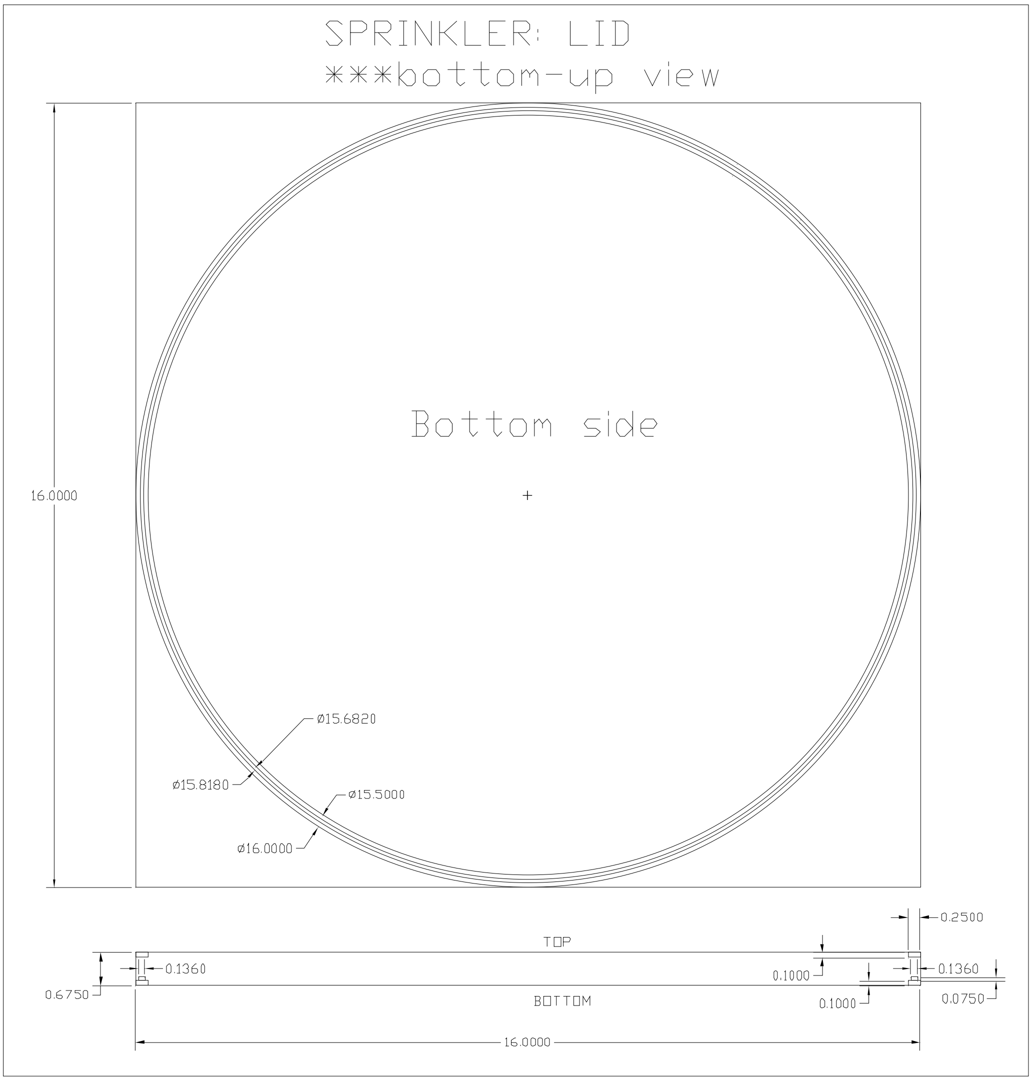

Figure A.10: The lid for the new Sprinkler design. A recess grove allows for a good fit on the cylinder. An o-ring groove inside the recess allows the cylinder to be sealed against the lid. The lid is made from acrylic stock.

Appendix B

More on Okubo-Weiss and POD

In this appendix, we include some results of the application of the Okubo-Weiss criterion and the Proper Orthogonal Decomposition (POD), not included in the main text.

B.1 The Okubo-Weiss criterion and its validity

Here we examine the results from the Okubo-Weiss criterion as applied to the 0.4 Hz 426 cm^3/s pumping data set analyzed in chapter 5.

The centers of large vorticity amplitude are selected as the coherent regions, since the Okubo-Weiss criterion compares strain and vorticity. The way it operates, the criterion cuts holes in the field shown in figure B.1. This leaves a significant amount of large amplitude vorticity behind in the “edges” of the excised regions.

The criterion does a mediocre job of capturing the PDF of the total field, over-sampling the tails and under-sampling the middle, as shown in figure B.2. The skewness, however, seems to be reasonably captured, as shown in table B.1, and the remainder gives a result which is close to Gaussian. This may indicate that the vortices are responsible for the non-zero skewness in our vorticity PDF, since the centers of the vortices are primarily what the decomposition selects. The kurtosis, however, is not well captured by the decomposition.

The reconstructed velocity fields from the decomposition are shown in figure B.3.

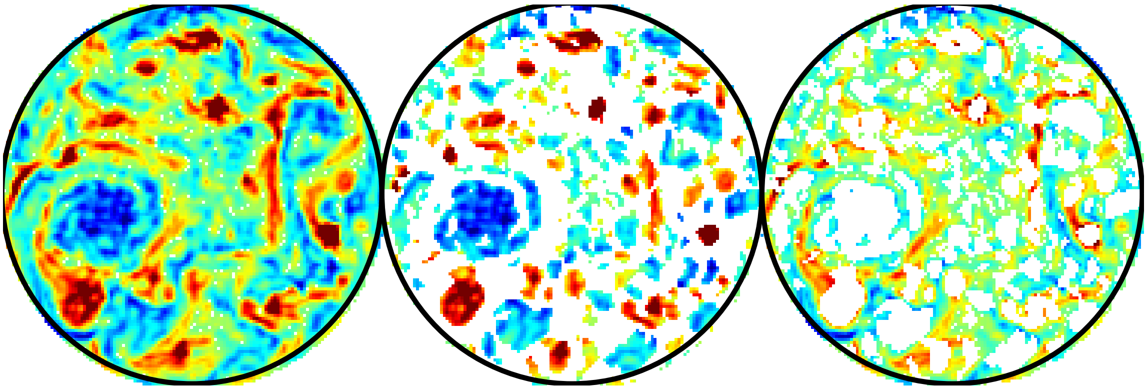

Figure B.1: Sample vorticity field with the Okubo-Weiss criterion decomposition. From left to right are the total, coherent, and remainder fields.

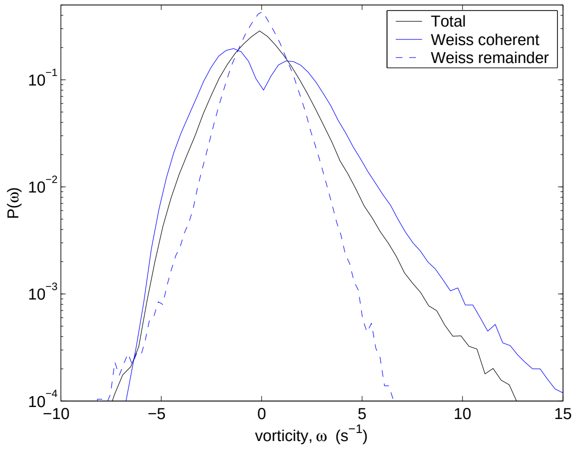

Figure B.2: Vorticity PDF for the Weiss decomposition taken over 50 independent fields.

The criterion does not do as bad of a job as expected, possibly indicating that the large vorticity in the centers of the vortices dominates the flow velocity. This seems to be more true in the jet region than in a vortex where the reconstructed velocity deviates significantly from the original field.

As noted, the assumption of the Okubo-Weiss criterion is not valid over the entire field. Basdevant and Philipovitch demonstrated that the hypothesis is only valid where the pressure field is nearly isotropic. A validity parameter can be constructed based upon the curvature of the pressure,

$$R = \frac{(\lambda_1 - \lambda_2)^2}{(\lambda_1 + \lambda_2)^2} \tag{B.1}$$

where λ_1 and λ_2 are the eigenvalues of the Hessian of the pressure [15]. The pressure field being isotropic corresponds to regions where $\lambda_1 \approx \lambda_2$ and hence R $\ll$ 1.

Applying the validity criterion results in a much smaller region where the Okubo-Weiss criterion can be applied. This was consistent with the numerical results of Basdevant and Philipovitch [15]. The results for some stricter criteria are shown in figures B.4 and B.5, and in table 5.1.

Decomposition Quantity	Total	Weiss Criteria coherent-incoherent		Weiss Criteria R < 0.5 coherent-incoherent		Weiss Criteria R < 0.1 coherent-incoherent	
coefficients retained (%)	100	59.8	40.2	13.7*	86.3*	5.4*	94.6*
Enstrophy/field ($s^{-2} \times 10^4$)	4.33	3.22	1.12	2.37*	3.23*	1.03*	4.59*
Vorticity skewness	0.78	0.73	-0.02	1.75*	0.98*	1.83*	1.68*
Vorticity flatness	7.09	4.71	4.95	7.82*	7.00*	8.17*	13.52*

Table B.1: Statistical properties of the decomposed vorticity fields using Weiss criterion. * indicates for a single field.

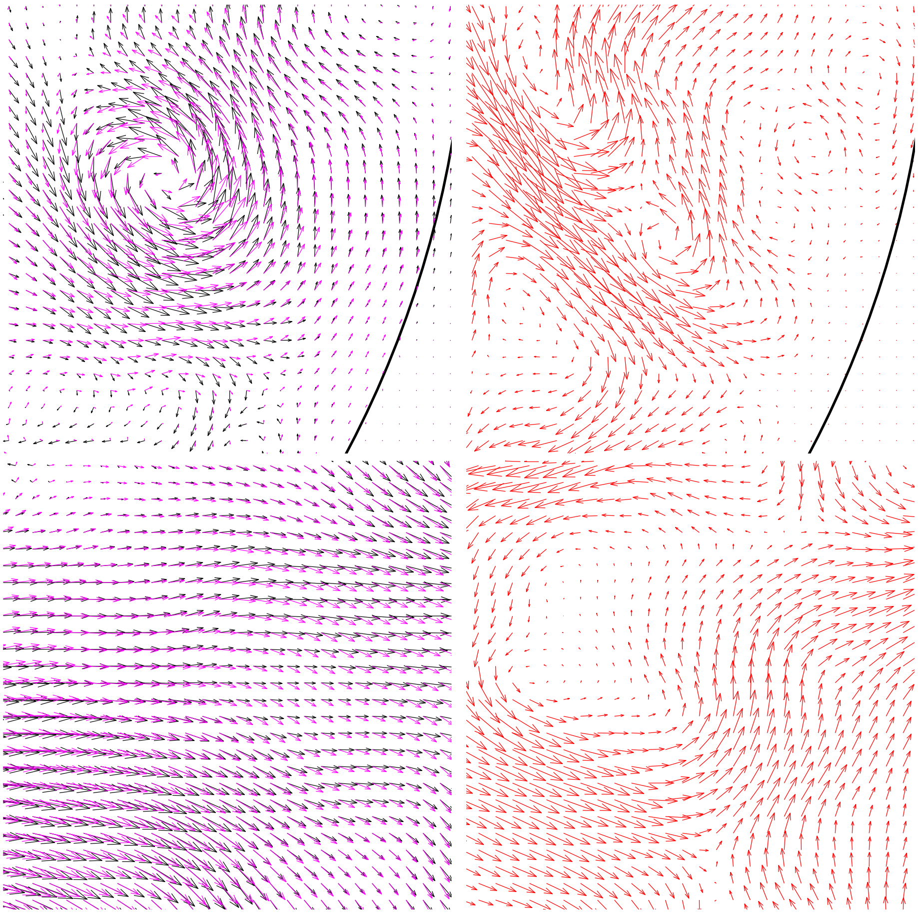

Figure B.3: Velocity fields reconstructed from the vorticity of the Okubo-Weiss criterion separation taken at two different locations. TOP: Close-up of vortex near the wall. BOTTOM: In a cyclonic jet region between vortices. LEFT: Total in black and coherent in magenta. RIGHT: Incoherent remainder in red. The velocity vectors in the remainder are scaled by 5 times larger than they would appear unscaled if plotted with the coherent velocity.

Quantity	Vort.	Weiss criterion Coherent	 Incoherent
Total difference	0.03	0.12	0.84
Magnitude	0.02	0.07	0.64
Angle	0.72	0.94	1.23

Table B.2: RMS pointwise deviations between the original field and reconstructed fields decomposed by the Okubo-Weiss criterion.

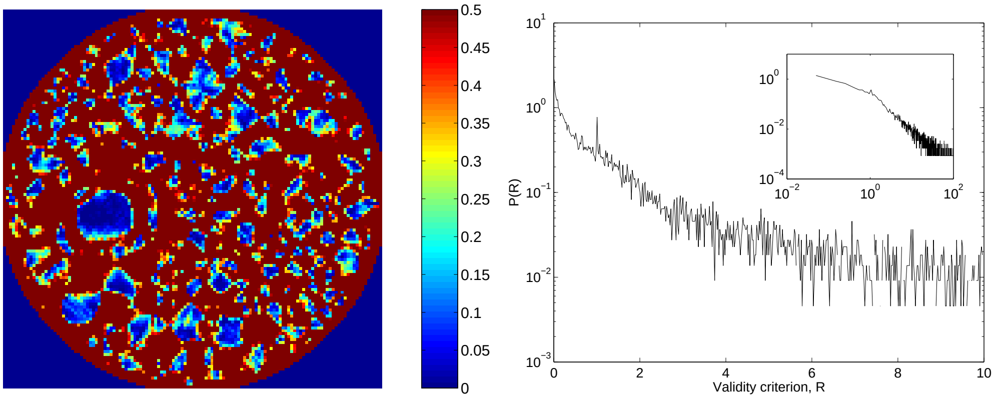

Figure B.4: Validity of the Weiss criterion. LEFT: Validity criterion R in the tank for a single field. RIGHT: PDF of the validity criterion R for the Weiss decomposition for a single field. The PDF is taken for values less than 10 (11192 out of 13372 total points in the field) in the semilog plot and for values less than 100 (12677 out of 13372 total points in the field) in the log-log inset plot.

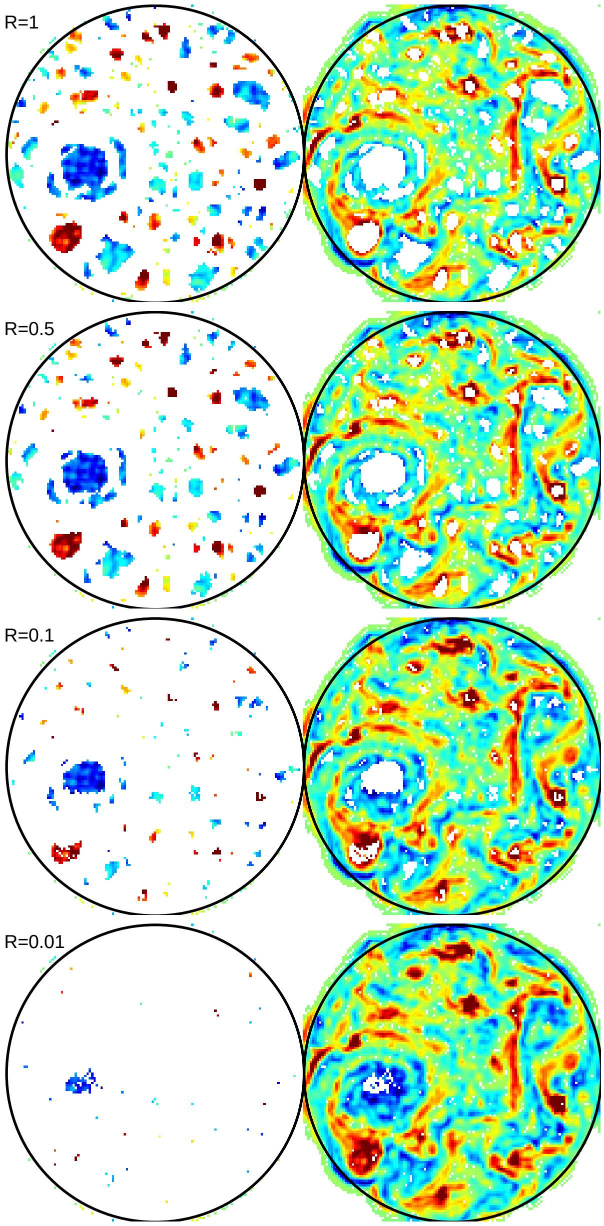

Figure B.5: Separated fields, including the validity of the Weiss criterion. Downward is increasing strictness.

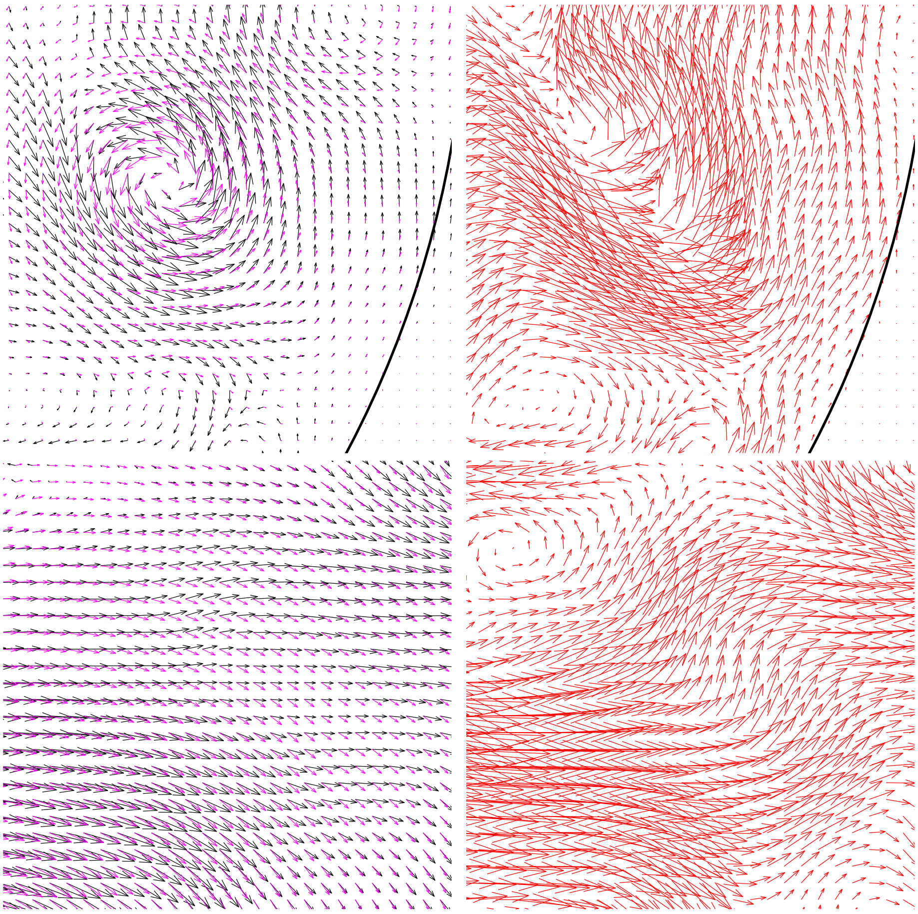

Figure B.6: Reconstructed velocity fields with slightly stricter criterion, R < 0.5 taken at two different locations in the tank. TOP: Close-up of vortex near the wall. BOTTOM: In a cyclonic jet region between vortices. LEFT: Total in black and coherent in magenta. RIGHT: Incoherent remainder in red. The velocity vectors in the remainder are scaled by 5 times larger than they would appear unscaled if plotted with the coherent velocity.

B.2 Some results from POD

Here we present some results of POD applied to the applied to the 0.4 Hz and 426 cm^3/s pumping data set analyzed in chapter 5, corresponding to a Reynolds number of approximately 1000 and Rossby number 0.3. The POD is applied to the vorticity field using the method of snapshots.

Two data sets taken under the same flow conditions were analyzed. The first data are 50 snapshots of the velocity and vorticity field taken over 25 minutes, each separated by 30 seconds. The fields from this long time series are uncorrelated. The second set of data are 300 snapshots taken over 20 seconds, each separated by 1/15 seconds. The fields from this short time series are well correlated with one another. A single snapshot and the mean field of the two data sets are shown in figure B.7.

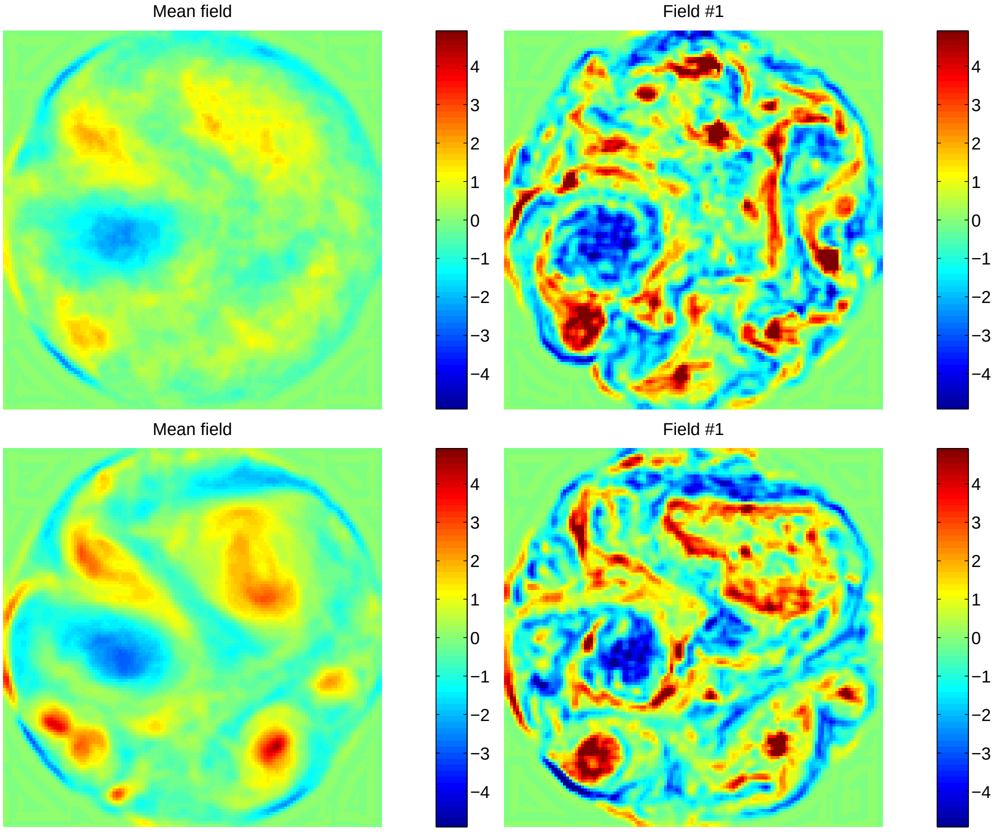

Figure B.7: Our vorticity fields. Left: Mean field Right: single snapshot. TOP: long time series (uncorrelated fields) BOTTOM: short time series (well correlated fields)

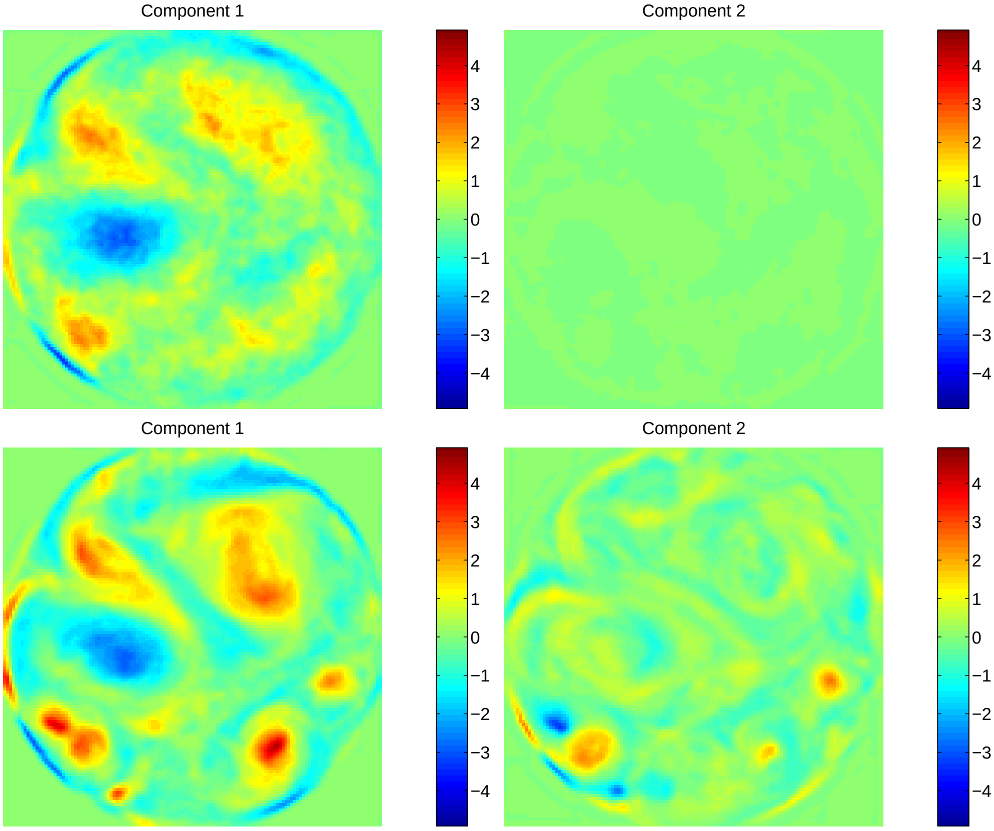

Figure B.8: The first two principal components. Left: first Right: second component. Top: Short time series. Bottom: Long time series.

The 'coherent' component is defined as the reconstructed field from the N largest principal components. The decomposition results in 50 (300) principal components for the long (short) time series, each of which is an entire field. The 'incoherent' remainder is the difference between the coherent and the total field. The first two principal components are shown in figure B.8. The first component appears to roughly correspond to the mean field.

The amplitudes of the principal components are shown in figure B.9. The amplitudes do not behave as we would expect. The mean of the magnitudes stays roughly constant instead of decreasing steadily with larger number of principal components. They also fluctuate rapidly so that the mean amplitude of the later principal components is close to zero.

The results of the POD in terms of convergence are really quite bad (actually worse

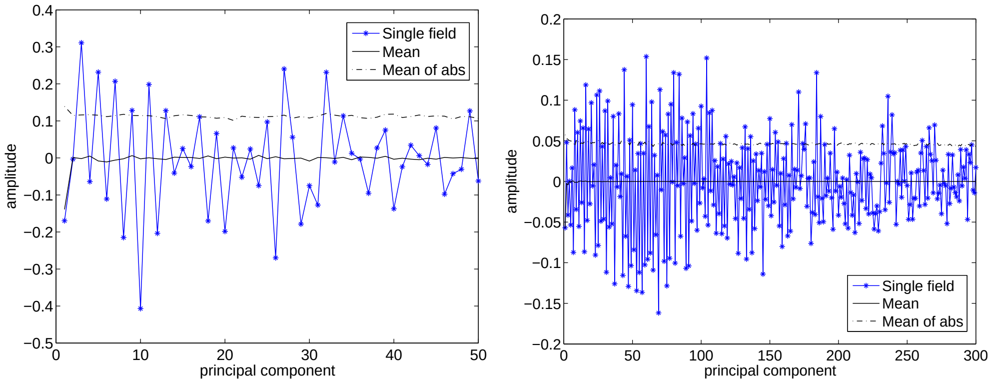

Figure B.9: Amplitudes of the principal components LEFT: for the uncorrelated long time series, RIGHT: for the correlated short time series. Plotted are the amplitudes for a single snapshot, the mean across the snapshots, and the mean of the magnitude of the amplitudes.

at convergence than our JPEG). The compression of the enstrophy is very slow and appears far inferior to the discrete wavelet packet (DWPT), as seen in figure B.10. The convergence of the short time series is much better. However, for this time series the snapshots are well correlated and so each snapshot will be much closer to the mean (i.e. a single component) than for the uncorrelated snapshots of the long time series.

The convergence of the skewness and kurtosis is shown in figure B.11 for the uncorrelated snapshots from the long time series and figure B.12 for the correlated snapshots from the short time series. The convergence to the statistics of the total field is much slower than that of the DWPT. There is almost no comparison for the uncorrelated fields. Additionally, the remainder of the POD does not rapidly converge to Gaussian statistics.

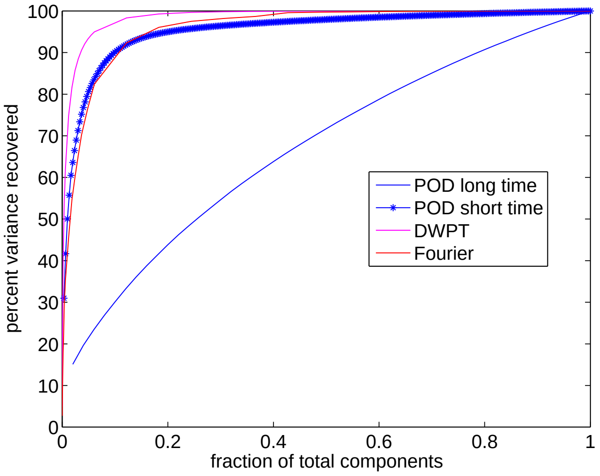

Figure B.10: Compression curve of the enstrophy in the vertical vorticity field. Shown for comparison is the results of the DWPT (magenta curve).

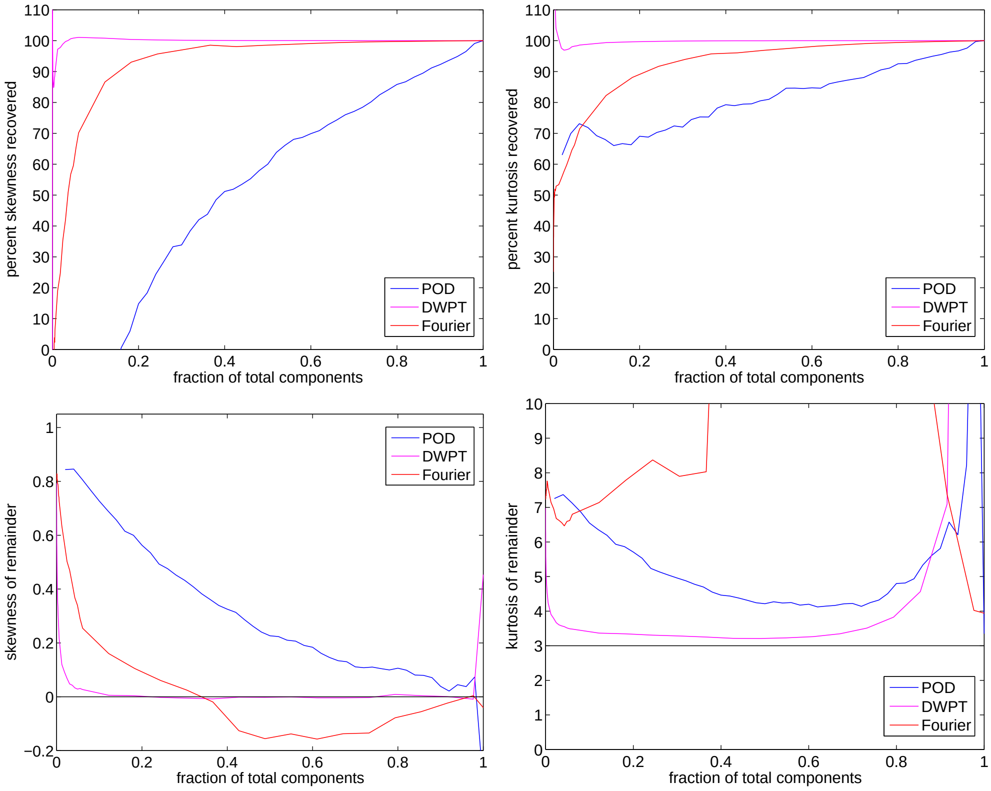

Figure B.11: Convergence of statistics for the long time uncorrelated snapshots. LEFT COLUMN: skewness and RIGHT COLUMN: kurtosis. The top row shows the convergence of the 'coherent' component. The bottom row shows the convergence of the 'incoherent' remainder.

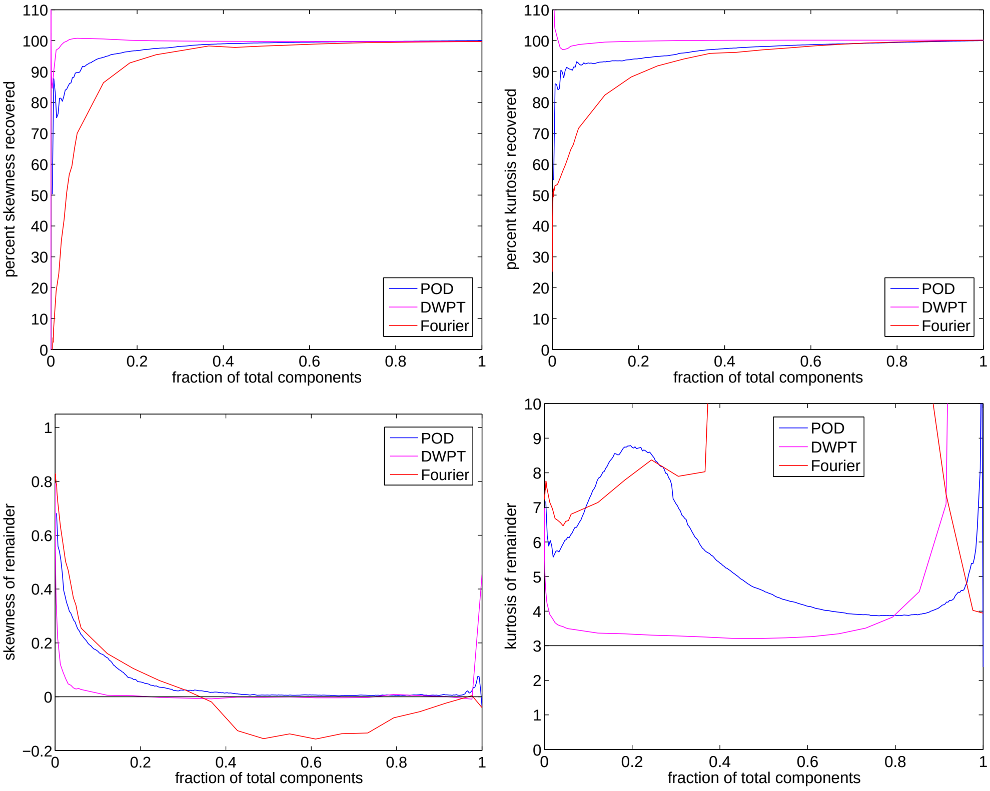

Figure B.12: Convergence of statistics for the short time correlated snapshots. LEFT COLUMN: skewness and RIGHT COLUMN: kurtosis. The top row shows the convergence of the 'coherent' component. The bottom row shows the convergence of the 'incoherent' remainder.

Bibliography

[1] `http://jpeg.org/jpeg2000/index.html`.

[2] decmpfields.avi. See EPAPS Document No. E-PLEEE8-71-103504 for a movie comparing the time evolution of the coherent and incoherent fields produced by the various extraction methods.

[3] NOAA / NESDIS interactive GOES archive. `http://wist.ngdc.noaa.gov/wist/goes.html`.

[4] Particle image velocimetry standard project. `http://piv.vsj.or.jp/piv/image-e.html`.

[5] pscalar.avi. See EPAPS Document No. E-PLEEE8-71-103504 for a movie of the evolution of a numerically integrated passive scalar in the coherent and incoherent field.

[6] Visible Earth. `http://visibleearth.nasa.gov/Oceans/Ocean_Winds/Vorticity.html`.

[7] vorticity.avi. See EPAPS Document No. E-PLEEE8-71-103504 for a movie of the time evolution of the vorticity field.

[8] T. Acharya and P.-S. Tsai. *JPEG 2000 Standard for Image Compression.* Wiley-Interscience, Hoboken, New Jersey, 2005.

[9] R. J. Adrian. Particle-imaging techniques for experimental fluid mechanics. *Annu. Rev. Fluid Mech.*, 23:261–304, 1991.

[10] Y. D. Afanasyev. Stratified vortex dipoles. `http://www.physics.mun.ca/~yakov/dipoles.html`, 2005. From book: Vortex Structures in a Stratified Fluid: Order from chaos, First Edition.

[11] C. D. Andereck, S. S. Liu, and H. L. Swinney. Flow regimes in a circular couette system with independently rotating cylinders. *J. Fluid Mech.*, 164:155–183, 1986.

[12] C. N. Baroud. *Transitions from three- to two-dimensional turbulence in a rotating system.* PhD thesis, University of Texas at Austin, Austin, Texas, December 2001.

[13] C. N. Baroud, B. B. Plapp, Z.-S. She, and H. L. Swinney. Anomalous self similarity in a turbulent rapidly rotating fluid. *Phys. Rev. Lett*, 88:114501/1–114501/4, 2002.

[14] C. N. Baroud, B. B. Plapp, H. L. Swinney, and Z.-S. She. Scaling in three-dimensional and quasi-two-dimensional rotating turbulent flows. *Phys. Fluids*, 15(8):2091–2104, 2003.

[15] C. Basdevant and T. Philipovitch. On the validity of the weiss criterion in two-dimensional turbulence. *Physica D*, 73:17–30, 1994.

[16] G. K. Batchelor. Computation of the energy spectrum in homogeneous two-dimensional turbulence. *Phys. Fluids*, 12(II):233–239, 1969.

[17] C. Beta, K. Schneider, and M. Farge. Wavelet filtering to study mixing in 2d isotropic turbulence. *Communications in Nonlinear Science and Numerical Simulation*, 8:537–545, 2003.

[18] C. Beta, K. Schneider, M. Farge, and H. Bockhorn. Numerical study of mixing of passive and reactive scalars in two-dimensional turbulent flows using orthogonal wavelet filtering. *Chem. Eng. Sci.*, 58:1463–1477, 2003.

[19] F. P. Bretherton and J. S. Turner. On the mixing of angular momentum in a stirred rotating fluid. *J. Fluid Mech.*, 32:449–464, 1968.

[20] J. M. Burgess, C. Bizon, W. D. McCormick, J. B. Swift, and H. L. Swinney. Instability of the Kolmogorov flow in a soap film. *Phys. Rev. E*, 60(1):715–721, 1999.

[21] J. W. M. Bush, H. A. Stone, and J. Bloxham. Axial drop motion in rotating fluids. *J. Fluid Mech.*, 282:247–278, 1995.

[22] D. R. Caldwell and C. W. Van Atta. Characteristics of ekman boundary layer instabilties. *J. Fluid Mech.*, 44(1):79–95, 1970.

[23] C. Cambon, R. Rubinstein, and F. S. Godeferd. Advances in wave turbulence: rapidly rotating flows. *New J. Phys.*, 6(73):1–29, 2004.

[24] C. C. Cambon, N. N. Mansour, and F. S. Godeferd. Energy transfer in rotating turbulence. *J. Fluid Mech.*, 337:303–332, 1997.

[25] V. M. Canuto and M. S. Dubovikov. A dynamical model for turbulence. v. the effect of rotation. *Phys. Fluids*, 9(7):2132–2140, July 1997.

[26] V. M. Canuto and M. S. Dubovikov. Physical regimes and dimensional structure of rotating turbulence. *Phys. Rev. Lett.*, 78(4):666–669, 1997.

[27] V. M. Canuto and M. S. Dubovikov. Response to “some remarks concerning recent work on rotating turbulence” [phys. fluids 10, 3242 (1998)]. *Phys. Fluids*, 10(12):3245–3246, 1998.

[28] A. Colin de Verdiere. Quasi-geostrophic turbulence in a rotating homogeneous fluid. *Geophys. Astrophys. Fluid Dyn.*, 15:213–251, 1980.

[29] Y. Couder and C. Basdevant. Experimental and numerical study of vortex couples in two-dimensional flows. *J. Fluid Mech.*, 173:225–251, 1986.

[30] B. Cushman-Roisin. *Introduction to Geophysical Fluid Dynamics.* Prentice-Hall, New Jersey, 1994.

[31] W. Dansgaard, J. W. C. White, and S. J. Johnsen. The abrupt termination of the younger dryas climate event. *Nature*, 339:532–534, 1989.

[32] I. Daubechies. *Ten Lectures on Wavelets*. SIAM, Philadelphia, 1992.

[33] G. Delerce. `http://www.civproject.org/`. Website for the CIV algorithm.

[34] S. C. Dickinson and R. R. Long. Oscillating-grid turbulence including the effects of rotation. *J. Fluid Mech.*, 126:315–333, 1983.

[35] F. V. Dolzhanskii and D. Yu. Manin. On the effect of turbulent ekman layer on global atmospheric dynamics. *Geophys. Astrophys. Fluid Dyn.*, 72:93–105, 1993.

[36] P. W. Duck and M. R. Foster. Spin-up of homogeneous and stratified rotating fluids. *Annu. Rev. Fluid Mech.*, 33:231–266, 2001.

[37] A. J. Faller. An experimental study of the instability of the laminar ekman boundary layer. *J. Fluid Mech.*, 15:560–576, 1963.

[38] M. Farge. Farge's wavelets research webpage. `http://wavelets.ens.fr/`.

[39] M. Farge. Wavelet transforms and their applications to turbulence. *Annu. Rev. Fluid Mech.*, 24:395–457, 1992.

[40] M. Farge, E. Goirand, Y. Meyer, F. Pascal, and M. V. Wickerhauser. Improved predictability of two-dimensional turbulent flows using wavelet packet compression. *Fluid Dyn. Res.*, 10:229–250, 1992.

[41] M. Farge, K. Schneider, and N. Kevlahan. Non-gaussianity and coherent vortex simulation for two-dimensional turbulence using an adaptive orthogonal wavelet basis. *Phys. Fluids*, 11(8):2187–2201, 1999.

[42] M. Farge, K. Schneider, G. Pellegrino, A. A. Wray, and R. S. Rogallo. Coherent vortex extraction in three-dimensional homogeneous turbulence: Comparison between cvs-

wavelet and pod-fourier decompositions. *Phys. Fluids*, 15(10):2886–2896, October 2003.

[43] A. Fincham and G. Delerce. Advanced optimization of correlation imaging velocimetry algorithms. *Exp. Fluids*, 29(Suppl.):S13–S22, 2000.

[44] A. M. Fincham and G. R. Spedding. Low-cost, high resolution dpiv for measurement in turbulent fluid flows. *Exp. Fluids*, 23:449–462, 1997.

[45] R. Fjørtoft. On the changes in the spectral distribution of kinetic energy for twodimensional, nondivergent flow. *Tellus*, 5:225–230, 1953.

[46] Robert W. Fox and Alan T. McDonald. *Introduction to Fluid Mechanics, Fifth Edition.* John Wiley & sons Inc., New York, 1998.

[47] U. Frisch. *Turbulence: The Legacy of A.N. Kolmogorov.* Cambridge University Press, 1995.

[48] F. S. Godeferd and L. Lollini. Direct numerical simulations of turbulence with confinement and rotation. *J. Fluid Mech.*, 393:257–308, 1999.

[49] H. P. Greenspan. *The Theory of Rotating Fluids.* Cambridge University Press, Great Britan, 1968.

[50] H. P. Greenspan and L. N. Howard. On the time dependent motion of a rotating fluid. *J. Fluid Mech.*, 17:385–404, 1963.

[51] P. Holmes, J. L. Lumley, and G. Berkooz. *Turbulence, Coherent Structure, Dynamical Systems and Symmetry.* Cambridge University Press, New York, 1996. chapter 3.

[52] E. J. Hopfinger. Turbulence and vortices in rotating fluids. In P. Germain, M. Piau, and D. Caillerie, editors, *17th International Congress on Theoretical and Applied Mechanics*, pages 117–138, Grenoble (France), 1989. IUTAM, Elsevier Science Publishers B. V.

[53] E. J. Hopfinger, F. K. Browand, and Y. Gagne. Turbulence and waves in a rotating tank. *J. Fluid Mech.*, 125:505–534, 1982.

[54] E. J. Hopfinger and G. J. F. van Heijst. Vortices in rotating fluids. *Annu. Rev. Fluid Mech.*, 25:241–289, 1993.

[55] M. Hossain. Reduction in the dimensionality of turbulence due to a strong rotation. *Phys. Fluids*, 6(3):1077–1080, 1994.

[56] Lasiris. *Magnum 500mW DS Instruction Manual*, 2000.

[57] J. C. R. Hunt. Industrial and environmental fluid-mechanics. *Annu. Rev. Fluid Mech.*, 23:1–41, 1991.

[58] A. K. M. F. Hussain. Coherent structures - reality and myth. *Phys. Fluids*, 26(10):2816–2850, 1983.

[59] A. K. M. F. Hussain. Coherent structures and turbulence. *J. of Fluid Mech.*, 173:303–356, 1986.

[60] A. Ibbetson and D. J. Tritton. Experiments in turbulence in a rotating fluid. *J. Fluid Mech.*, 68:639–672, 1975.

[61] L. Jacquin, O. Leuchter, C. Cambon, and J. Mathieu. Homogeneous turbulence in the presence of rotation. *J. Fluid Mech.*, 220:1–52, 1990.

[62] A. N. Kolmogorov. The local structure of turbulence in incompressible viscous fluid for very large Reynolds numbers. *Dokl. Akad. Nauk SSR*, 30:301–305, 1941.

[63] R. H. Kraichnan. Inertial range transfer in two-dimensional turbulence. *Phys. Fluids*, 10:1417–1423, 1967.

[64] R. H. Kraichnan and D. Montgomery. Two-dimensional turbulence. *Rep. Prog. Phys.*, 43:547–619, 1980.

[65] J. Lighthill. *Waves in fluids.* Cambridge University Press, 2002.

[66] J. T. C. Liu. Coherent structures in transitional and turbulent free shear flows. *Annu. Rev. Fluid Mech.*, 21:285–315, 1989.

[67] J. Lumley and P. Blossy. Control of turbulence. *Annu. Rev. Fluid Mech.*, 30:311–327, 1998.

[68] J. L. Lumley and A. M. Yaglom. A century of turbulence. *Flow Turbul. Combust.*, 66:241–286, 2001.

[69] T. S. Lundgreen. The vortical flow above the drain-hole in a rotating vessel. *J. Fluid Mech.*, 155:381–412, 1985.

[70] N. N. Mansour, C. Cambon, and C. G. Speziale. *Studies in Turbulence*, chapter Theoretical and computational study of rotating isotropic turbulence, pages 59–75. Springer-Verlag, Berlin, 1992.

[71] P. S. Marcus. Private Communication.

[72] P. S. Marcus. Jupiter's Great Red Spot and other vortices. *Annu. Rev. Astron. Astrophys.*, 31:523–73, 1993.

[73] P. S. Marcus. Prediction of a global climate change on Jupiter. *Nature*, 428:828–831, 2004.

[74] P. S. Marcus, T. Kundu, and C. Lee. Vortex dynamics and zonal flows. *Phys. Plasmas*, 7(5):1630–1640, 2000.

[75] T. Maxworthy, E. J. Hopfinger, and L. G. Redekopp. Wave motions on vortex cores. *J. Fluid Mech.*, 151:141–165, 1985.

[76] A. D. McEwan. A laboratory demonstration of angular momentum mixing. *Geophys. Fluid Dyn.*, 5:283–311, 1973.

[77] A. D. McEwan. Angular momentum diffusion and the initiation of cyclones. *Nature*, 260:126, 1976.

[78] J. C. McWilliams. The emergence of isolated coherent vortices in turbulent flow. *J. of Fluid Mech.*, 146:21–43, 1984.

[79] J. C. McWilliams. The vortices of 2-dimensional turbulence. *J. Fluid Mech.*, 219:361–385, 1990.

[80] O. Métais, C. Flores, S. Yanase, J. J. Riley, and M. Lesieur. Rotating free-shear flows .2. numerical simulations. *J. Fluid Mech.*, 293:47–80, 1995.

[81] S. D. Meyers. *Laboratory studies of coherent structures in quasi-geostrophic flows.* PhD thesis, University of Texas at Austin, May 1990.

[82] E. E. Michaelides. Review - the transient equation of motion for particles, bubbles, and droplets. *J. Fluid Eng.*, 119:233, 1997.

[83] C. Morize, F. Moisy, and M. Rabaud. Decaying grid-generated turbulence in a rotating frame. *submitted to Phys. Fluids*, 2004.

[84] K. Okamoto, S. Nishio, T. Saga, and T. Kobayashi. Standard images for particle-image velocimetry. *Meas. Sci. Technol.*, 11:685–691, 2000. This work describes image generation for PIV/CIV algorithm evaluation.

[85] A. Okubo. Horizontal dispersion of floatable particles in the vicinity of velocity singularities such as convergences. *Deep Sea Research and Oceanographic Abstracts*, 17(3):445–454, June 1970.

[86] J. Paret, D. Marteau, O. Paireau, and P. Tabeling. Are flows electromagnetically forced in thin startified layers two dimensional? *Phys. Fluids*, 9(10):3102–3104, 1997.

[87] J. Paret and P. Tabeling. Experimental observation of the two-dimensional inverse energy cascade. *Phys. Rev. Lett.*, 79(21):4162–4165, 1997.

[88] J. Pedlosky. *Geophysical Fluid Dynamics, Second Edition.* Springer-Verlag, New York, 1987.

[89] A. K. Prasad. Stereoscopic particle image velocimetry. *Exp. Fluids*, 29:103–116, 2000.

[90] A. K. Prasad and R. J. Adrian. Stereoscopic particle image velocimetry applied to liquid flows. *Exp. Fluids*, 15:49–60, 1993.

[91] W. H. Press, B. P. Flannery, S. A. Teukolsky, and W. T. Vetterling. *Numerical Recipes in C: The Art of Scientific Computing*. Cambridge University Press, New York, 1988.

[92] J. Proudman. On the motions of solids in a liquid possessing vorticity. *Proc. R. Soc. Lond. A*, 92, 1916.

[93] A. Provenzale. Transport by coherent barotropic vortices. *Annu. Rev. Fluid Mech.*, 31:55–93, 1999.

[94] M. Raffel, C. Willert, and J. Kompenhans. *Particle Image Velocimetry, A Practical Guide*. Springer-Verlag Berlin Heidelberg, 1998.

[95] P. L. Read. Transition to geostrophic turbulence in the laboratory, and as a paradigm in atmospheres and oceans. *Surv. Geophys.*, 22:265–317, 2001.

[96] J. J. Riley and M. P. Lelong. Fluid motions in the presence of strong stable stratification. *Annu. Rev. Fluid Mech.*, 32:613–657, 2000.

[97] M. Rivera and X. L. Wu. External dissipation in driven two-dimensional turbulence. *Phys. Rev. Lett.*, 85(5):976–979, 1999.

[98] S. K. Robinson. Coherent motions in the turbulent boundary-layer. *Annu. Rev. Fluid Mech.*, 23:601–639, 1991.

[99] J. E. Ruppert-Felsot. Dissipation in a rotating turbulent flow. Master's thesis, The University of Texas at Austin, May 2003.

[100] J. E. Ruppert-Felsot, O. Praud, E. Sharon, and H. L. Swinney. Extraction of coherent structures in a rotating turbulent flow experiment. *to appear in Phys. Rev. E*, 2005.

[101] L. Z. Sansón and G. J. F. van Heijst. Nonlinear Ekman effects in rotating barotropic flows. *J. Fluid Mech.*, 412:75–91, 2000.

[102] H. Schlicting. *Boundary Layer Theory.* McGraw-Hill, 1979.

[103] C. Schram and M. L. Riethmuller. Vortex ring evolution in an impulsively started jet using digital particle image velocimetry and continuous wavelet analysis. *Meas. Sci. and Technol.*, 12:1413–1421, 2001.

[104] P. Schwartz and D. Randall. An abrupt climate change scenario and its implications for United States national security. Technical report, The Pentagon, 2003.

[105] A. Siegel and J. B. Weiss. A wavelet-packet census algorithm for calculating vortex statistics. *Phys. Fluids*, 9(7):1988–1999, 1997.

[106] L. Sirovich. Turbulence and the dynamics of coherent structures part I: coherent structures. *Quarterly of Applied Mathematics*, 45(3):561–571, 1987.

[107] L. M. Smith, J. R. Chasnov, and F. Waleffe. Crossover from two- to three-dimensional turbulence. *Phys. Rev. Lett.*, 77:2467–2470, 1996.

[108] L. M. Smith and F. Waleffe. Transfer of energy to two-dimensional large scales in forced, rotating three-dimensional turbulence. *Phys. Fluids*, 11(6):1608–1622, June 1999.

[109] L. M. Smith and V. Yakhot. Bose condensation and small-scale structure generation in a random force driven 2d turbulence. *Phys. Rev. Lett.*, 71(3):352–355, 1993.

[110] T. H. Solomon, E. R. Weeks, and H. L. Swinney. Observation of anomalous diffusion and lvy flights in a two-dimensional rotating flow. *Phys. Rev. Lett.*, 71:3975–3978, 1993.

[111] J. Sommeria, S. D. Meyers, and Swinney H. L. A laboratory simulation of Jupiter's Great Red Spot. *Nature*, 331:689–693, 1988.

[112] J. Sommeria and R. Moreau. Why, how, and when, mhd turbulence becomes two-dimensional. *J. Fluid Mech.*, 118:507–518, 1982.

[113] K. R. Sreenivasan. Fluid turbulence. *Rev. of Mod. Phys.*, 71(2):S383–S395, 1999.

[114] D. Stipp. The Pentagon's weather nightmare. *Fortune*, 149(3):100, February 2004.

[115] J. K. Sveen. *PIV 1.6 Manual*, 1.6 edition. available at `http://www.math.uio.no/~jks/matpiv/`.

[116] J. K. Sveen. `http://www.math.uio.no/~jks/matpiv/`. internet website.

[117] P. Tabeling. Two-dimensional turbulence: a physicist approach. *Phys. Reports*, 362:1–62, 2002.

[118] P. R. Tatro and E. L. Mollo-Christensen. Experiments on ekman layer instability. *J. Fluid Mech.*, 28(3):531–543, 1967.

[119] G. I. Taylor. Experiments with rotating fluids. *Proc. R. Soc. Lond. A*, 100(703):114–121, 1921.

[120] G. I. Taylor. Experiments on the motion of solid bodies in fluids. *Proc. R. Soc. Lond. A*, 104(725):213–218, 1923.

[121] C. V. Tran and J. C. Bowman. On the dual cascade in two-dimensional turbulence. *Physica D*, 176:242–255, 2003.

[122] L. N. Trefethen. *Spectral Methods in MATLAB.* SIAM, Philadelphia, 2000.

[123] D.J. Tritton. *Physical Fluid Dynamics.* Oxford Science Publications, 1998.

[124] T. Weber. 2D and 3D turbulence in a rotating tank with a vertically oscillating grid. Master's thesis, University of Texas at Austin, August 2000.

[125] E. R. Weeks, Y. Tian, J. S. Urbach, K. Ide, H. L. Swinney, and M. Ghil. Transitions between blocked and zonal flows in a rotating annulus with topography. *Science*, 278:1598–1601, 1997.

[126] J. Weiss. The dynamics of enstrophy transfer in two-dimensional hydrodynamics. *Physica D*, 48:273–294, 1991.

[127] M. V. Wickerhauser. *Adapted Wavelet Analysis from Theory to Software.* A K Peters, Ltd. Wellesley, MA, 1994.

[128] R. A. Wigeland and H. M. Nagib. Grid generated turbulence with and without rotation about the streamwise direction. *IIT Fluid and Heat Transfer Rep.*, 1978.

[129] S. Yanase, C. Flores, O. Métais, and Riley J. J. Rotating free-shear flows .1. linear-stability analysis. *Phys. Fluids A*, 5(11):2725–2737,, 1993.

[130] P. K. Yeung and Y. Zhou. Numerical study of rotating turbulence with external forcing. *Phys. Fluids*, 10(11):2895–2909, 1998.

[131] B. W. Zeff, D. D. Lanterman, R. McAllister, R. Roy, E. J. Kosttelich, and Lathrop D. P. Measuring intense rotation and dissipation in turbulent flows. *Nature*, 421:146–149, 2003.

[132] X. Zhang, D. L. Boyer, and H. J. S. Fernando. Turbulence-induced rectified flows in rotating fluids. *J. Fluid Mech.*, 350:97–118, 1997.

[133] Y. Zhou. A phenomenological treatment of rotating turbulence. *Phys. Fluids*, 7:2092, 1995.

[134] Y. Zhou, C. G. Speziale, and R. Rubinstein. Some remarks concerning recent work on rotating turbulence. *Phys. Fluids*, 10(12):3242–3244, 1998.

Vita

Jori Elan Ruppert-Felsot was born in Champaign, Illinois on November 4, 1978, the son of Judy Rosmary Ruppert and Allan Stan Felsot. In 1990 he entered into the University Laboratory High School at the University of Illinois at Urbana-Champaign. In the spring of 1991, he left with his family to live in Cyprus for six months and attended the International School of Cyprus in Nicosia, Cyprus. The following fall semester he returned to Illinois. However, he again moved with his family to Eastern Washington state shortly afterwards, in 1993. He graduated from Kamiakin High School in Kennewick, Washington in 1995. He returned to Illinois and attended the University of Illinois at Urbana-Champaign, graduating with a Bachelor's of Science in Engineering Physics from the Engineering college in May, 1999. During the following Summer he started research at the University of Texas at Austin in the Center for Nonlinear Dynamics of the Physics department, officially entering into The Graduate School in the Fall of 1999. He completed a Master's in physics from the University of Texas at Austin in May, 2003.

Permanent Address: 92505 Chelsea
Kennewick, Washington 99338

This dissertation was typeset with LaTeX 2_ε[1] by the author.

---

[1] LaTeX 2_ε is an extension of LaTeX. LaTeX is a collection of macros for TeX. TeX is a trademark of the American Mathematical Society. The macros used in formatting this dissertation were written by Dinesh Das, Department of Computer Sciences, The University of Texas at Austin, and extended by Bert Kay, James A. Bednar, and Ayman El-Khashab.